



HAL
open science

Development and characterization of an optical coherence tomography micro-system : Application to dermatology

Stéphane Perrin

► **To cite this version:**

Stéphane Perrin. Development and characterization of an optical coherence tomography micro-system : Application to dermatology. Signal and Image processing. Université de Franche Comté, 2016. English. NNT: . tel-03085671

HAL Id: tel-03085671

<https://hal.science/tel-03085671>

Submitted on 21 Dec 2020

HAL is a multi-disciplinary open access archive for the deposit and dissemination of scientific research documents, whether they are published or not. The documents may come from teaching and research institutions in France or abroad, or from public or private research centers.

L'archive ouverte pluridisciplinaire **HAL**, est destinée au dépôt et à la diffusion de documents scientifiques de niveau recherche, publiés ou non, émanant des établissements d'enseignement et de recherche français ou étrangers, des laboratoires publics ou privés.



SPIM

Thèse de Doctorat



UFC

école doctorale sciences pour l'ingénieur et microtechniques
UNIVERSITÉ DE FRANCHE-COMTÉ

Development and
characterization of an optical
coherence tomography
micro-system

Application to dermatology

■ STÉPHANE PERRIN

SPIM

Thèse de Doctorat

UFC

école doctorale **sciences pour l'ingénieur et microtechniques**
UNIVERSITÉ DE FRANCHE-COMTÉ

N° X | X | X

THÈSE présentée par

STÉPHANE PERRIN

pour obtenir le

Grade de Docteur de

l'Université Bourgogne Franche-Comté

Spécialité : **Sciences pour l'Ingénieur**

Development and characterization of an optical coherence tomography micro-system

Application to dermatology

Soutenue publiquement le 24 juin 2016 devant le Jury composé de :

PAUL MONTGOMERY	Rapporteur	Directeur de recherche CNRS à l'Institut ICube, Strasbourg
ARNAUD DUBOIS	Rapporteur	Professeur à l'Université Paris-Sud - Institut d'Optique Graduate School, Palaiseau
JONAS KÜHN	Examineur	Chercheur, ETH Zurich, Zürich
CHRISTOPHE GORECKI	Directeur de thèse	Directeur de recherche CNRS à FEMTO-ST
LUC FROEHLI	Encadrant de thèse	Chargé de recherche CNRS à FEMTO-ST
NICOLAS PASSILLY	Encadrant de thèse	Chargé de recherche CNRS à FEMTO-ST

A la mémoire de mon grand-père,

"L'Homme est fou. Il adore un Dieu invisible et détruit une nature visible, inconscient que la Nature qu'il détruit est le Dieu qu'il vénère." Hubert Reeves,

RÉSUMÉ EN FRANÇAIS

Titre : Développement et caractérisation d'un microsysteme de tomographie par cohérence optique plein champ à balayage en longueur d'onde - Application à la dermatologie

Les prévisions de l'année 2015 avançaient trois millions de nouveaux cas de cancer de la peau diagnostiqués aux États-Unis. Un diagnostic précoce peut permettre de réduire le nombre d'actes chirurgicaux pratiqués aujourd'hui en vue d'effectuer le diagnostic. D'après la Société Américaine de Cancérologie, il est important de mettre en avant que seulement 20% des pathologies qui ont nécessité une opération chirurgicale sont malignes. Les autres sont donc opérées inutilement. De plus, si le diagnostic s'avère positif, les séquelles seront minimisées. Afin de proposer des traitements appropriés et de bonnes perspectives de thérapie, il existe aujourd'hui un besoin important pour des systèmes de diagnostics non-invasifs.

Habituellement, le diagnostic des tumeurs cutanées est réalisé à partir d'une biopsie suivie d'une procédure histologique. Cependant, il s'agit d'un acte invasif et potentiellement traumatisant pour le patient. Des systèmes d'imagerie non-invasifs ont été développés, tels que l'échographie haute fréquence ou la microscopie confocale. Mais, leurs performances restent insuffisantes (faible résolution pour l'échographie ou faible profondeur d'imagerie pour la microscopie confocale) pour fournir un diagnostic fiable. Une technique d'imagerie de milieux biologiques, la tomographie par cohérence optique (OCT, de l'anglais optical coherence tomography), a récemment fait son apparition dans le domaine de la dermatologie. Elle apporte une réelle avancée pour la visualisation des pathologies de la peau car elle permet d'imager tri-dimensionnellement un échantillon avec une résolution cellulaire (environ 5 μm) sur 1 mm de profondeur. De plus, les mesures sont effectuées selon des coupes transverses à la surface de la peau de manière similaire à l'histopathologie. Actuellement, des systèmes OCT commerciaux existent et sont déjà utilisés en dermatologie comme outils de diagnostic. Cependant, ces systèmes sont encombrants et relativement chers, et sont donc réservés aux grands centres hospitaliers. Ce projet a donc pour but d'améliorer cette situation en proposant un système d'imagerie à coût réduit développé à partir des techniques de micro-fabrication afin de le rendre abordables pour des dermatologues privés. Ce système permettrait

donc d'apporter une aide à la décision médicale pour le professionnel de santé et un diagnostic plus rapide. Ce travail de thèse repose sur la conception et le développement d'un système capable d'imager en volume les différentes couches superficielles de la peau. Le système est une combinaison entre les microsystèmes (MOEMS) et la technique OCT.

L'OCT est une technique d'imagerie qui bénéficie des avantages de la microscopie confocale et de l'interférométrie à faible cohérence. L'interférométrie à faible cohérence permet de sélectionner les photons balistiques porteurs de l'information de profondeur. Ceci est possible grâce à la fonction de cohérence temporelle de la source lumineuse. Par rapport à l'imagerie confocale, la profondeur d'imagerie est nettement améliorée tout en maintenant une résolution axiale acceptable pour visualiser la structure des couches superficielles de la peau. La résolution axiale et la résolution latérale d'un système OCT dépendent des paramètres de la source lumineuse et des composants optiques. Elles sont relativement proches de l'histologie, sans avoir recours à l'excision de tissus. Dans ce projet, la technique OCT à balayage en longueur d'onde a été retenue lors de la conception du système. Contrairement à l'OCT traditionnelle, c'est-à-dire dans le domaine temporel, les signaux d'interférences sont acquis dans le domaine fréquentiel. Ceci a pour but d'améliorer le rapport signal à bruit ainsi que la sensibilité du système, paramètres fondamentaux pour l'imagerie biologique. En outre, le dispositif optique repose sur une configuration plein champ et multicanaux. Il comprend ainsi une matrice de micro-interféromètres de Mirau illuminée par une source large-bande dans le domaine du proche infra-rouge, basée sur une diode super-luminescente DSL. La source employée balaie successivement un spectre en longueur d'onde relativement large générant un faisceau dont la largeur de raie est étroite. Les composantes spectrales des interférogrammes de chaque canal sont enregistrées par une caméra rapide. Ensuite, les interférogrammes sont reconstruits séquentiellement en deux dimensions. L'aspect plein champ ne nécessite donc pas de balayage de la tête optique. Chaque interféromètre comprend un doublet de microlentilles et un miroir de référence supporté par trois bras permettant son actionnement. La tête optique, comprenant les interféromètres de Mirau, est réalisée par une intégration verticale de substrats de microcomposants optiques. Cette approche permet de réduire drastiquement le coût de fabrication ainsi que le volume du système tout en gardant les performances optiques requises. Le schéma du montage optique est représenté dans la Fig. 1.

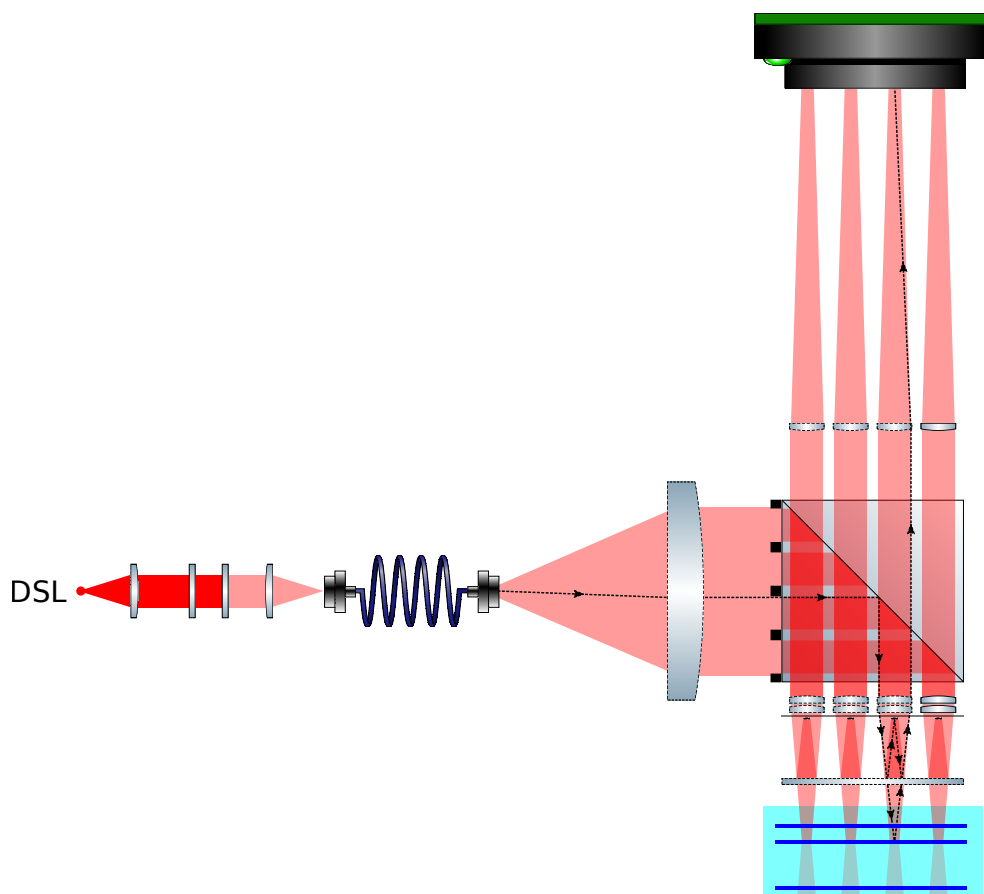


Figure 1: Schéma optique du microsysteme de tomographie par coherence optique.

Afin de répondre aux attentes médicales, la conception du microsysteme d'imagerie a été envisagée. Les spécifications requises, telles que la résolution, la taille du champ de vue et le coût du dispositif final, ont apporté des restrictions sur la fabrication des micro-composants optiques ainsi que sur celles de la source lumineuse et de la caméra. En effet, les performances des éléments du système sont dépendantes les unes des autres.

Aussi, la reconstruction de l'image, en interférométrie spectrale, est faite en traitant le signal interférométrique par une transformée de Fourier. Cependant, cette opération apporte des termes artéfacts, en particulier les termes conjugués et les termes d'autocorrélation. La matrice de miroirs de référence est donc actionnée pour permettre la détection basée sur l'interférométrie à décalage de phase et ainsi obtenir une profondeur d'imagerie complète, comme illustré dans la Fig. 2. Ici, la technique de décalage de phase suit un mouvement sinusoïdal du miroir. Contrairement à l'interférométrie à décalage de phase traditionnelle (linéaire ou par niveau), l'interférométrie à décalage de phase sinusoïdale requiert un algorithme plus complexe de reconstruction du signal interférométrique.

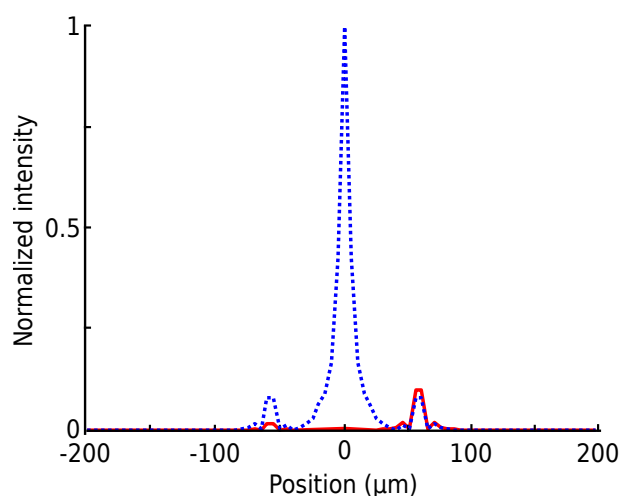


Figure 2: Comparaison de deux profils résultants de la transformée de Fourier du signal interférométrique spectral avec (en ligne continue rouge) et sans (en ligne pointillée bleue) l'application de l'algorithme de décalage de phase.

En parallèle, deux systèmes de caractérisation de microcomposants optiques ont été mis en œuvre afin d'évaluer la qualité des microcomposants et ainsi s'assurer que leurs performances sont conformes aux exigences de la conception. Ils ont permis d'étudier la qualité optique des microcomposants individuellement et de la tête optique des interféromètres de Mirau après assemblage. Le premier de ces systèmes est un profilomètre optique standard basé sur l'interférométrie à faible cohérence. Il donne accès à la topographie bidimensionnelle, comme illustré dans la Fig. 3 (a), ainsi qu'à la rugosité de surface de l'échantillon. Le deuxième système est plus original et est basé sur la mesure directe du volume focal généré par le microcomposant (Fig. 3 (b-d)). A partir de ce volume, la longueur focale, le rapport de Strehl et, via la fonction de transfert de modulation, le pouvoir de résolution sont déduits. En appliquant un algorithme de reconstruction de phase à ce volume, le front d'onde produit par le microcomposant, peut être dérivé et les aberrations optiques quantifiées. La Fig. 4 montre la matrice des objectifs de Mirau et ses principaux composants, tels que les doublets de microlentilles et les micromiroirs, qui ont été caractérisés par ces deux systèmes.

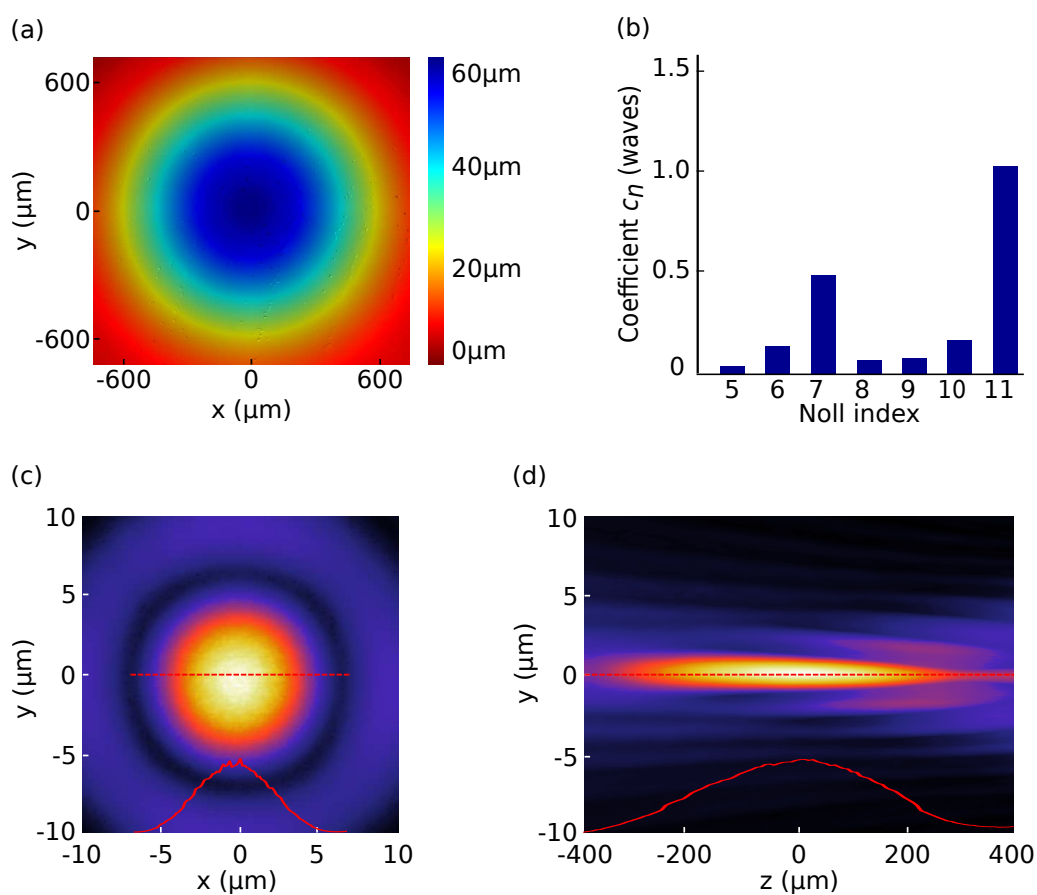


Figure 3: Caractérisations de microlentilles par (a) la mesure de topographie et (b-d) la mesure directe du volume focal.

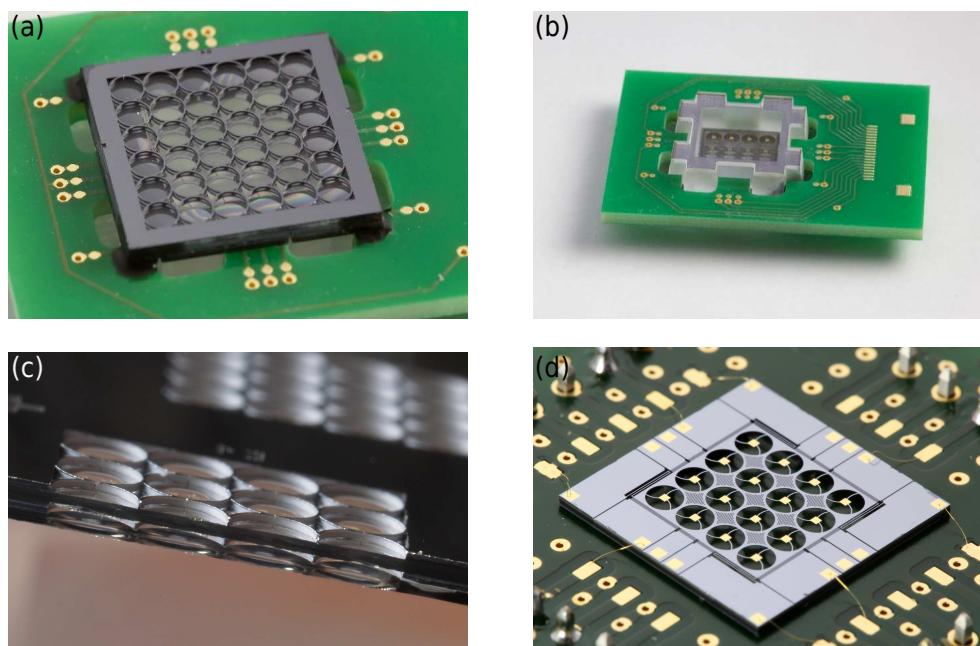


Figure 4: Photographie de la matrice d'interféromètres de Mirau (a) vue du dessus et (b) vue du dessous. Chaque interféromètre est composé (c) d'un doublet de microlentilles et (d) d'un miroir de référence actionné.

Après avoir été caractérisée, la matrice de micro-interféromètres de Mirau est placée dans un macro-système afin d'obtenir les signaux interférométriques et ainsi d'évaluer sa capacité à générer des informations de profondeur comme illustré dans la Fig. 5.

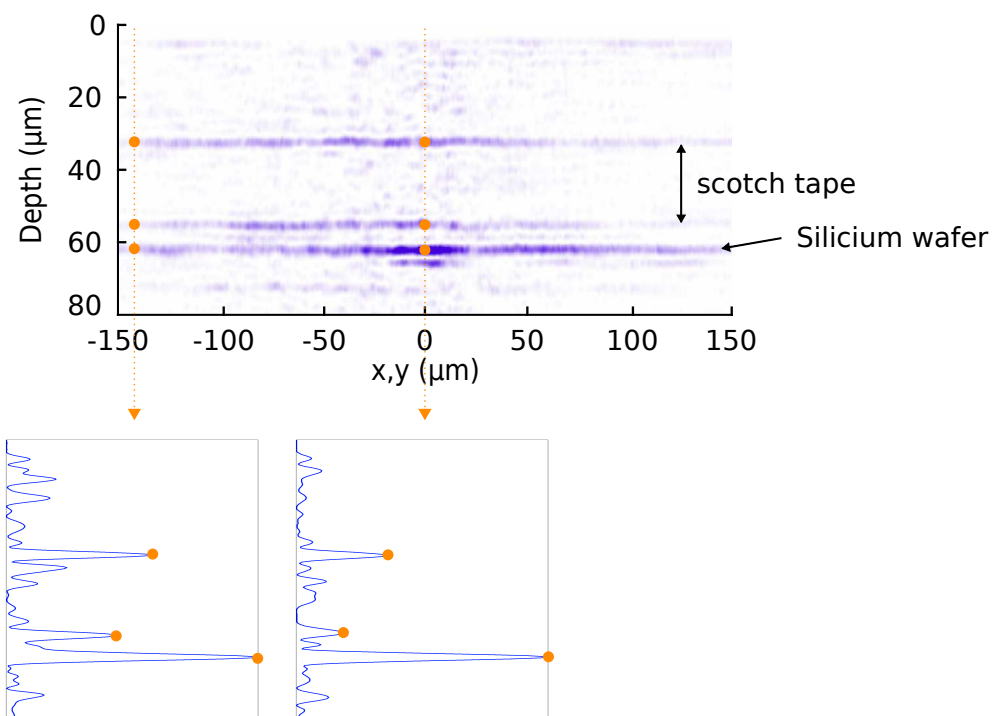


Figure 5: B-scan d'un objet réalisé à partir d'une couche de scotch appliquée sur un substrat de Si.

La matrice est ensuite intégrée aux autres composants optiques afin de réaliser le premier démonstrateur basé sur la tomographie par cohérence optique plein champ à balayage en longueur d'onde avec une matrice de micro-objectifs de Mirau pour la dermatologie.

Ce travail de thèse de doctorat porte sur le développement et sur la caractérisation d'un micro-système OCT pour le diagnostic précoce des pathologies de la peau et plus particulièrement des cancers cutanés. Dans un premier lieu, la conception optique des deux parties du micro-système d'imagerie a été réalisée. Simultanément, deux systèmes de caractérisation de microcomposants ont été développés afin de garantir la bonne qualité des microcomposants répondants aux exigences médicales. Après fabrication et caractérisation des micro-composants optiques, la matrice de micro-interféromètres a été implémentée au sein d'un macro-système de tomographie par cohérence optique plein champ à balayage en longueur d'onde afin d'obtenir les premiers signaux interférométriques. Pour cela, le logiciel de contrôle et d'asservissement des appareils (source lumineuse et caméra) ainsi que le logiciel de reconstruction des images ont été développés via une interface graphique (LabVIEW, National Instruments).

ACKNOWLEDGMENTS

Foremost, I would like to thank my PhD supervisor, Prof. Christophe Gorecki, for giving me the great opportunity of performing my thesis and of working in the MOEMS Group. I want to thank him for having directed and supported my thesis work. Also, I would like to thank particularly Dr. Nicolas Passilly and Dr. Luc Froehly, my PhD co-supervisors. It has been a pleasure to work with them and I really appreciated their contributions and their pertinent ideas during my researches. Their competence and their patience allowed me to get methodologies for my research and to learn two new fields, optical coherence tomography and micro-optics.

I thank the members of my thesis committee, Prof. Paul Montgomery and Prof. Arnaud Dubois, as well as Dr. Jonas Kühn and Prof. Wolfgang Osten for taking their time to review this thesis and for accepting to be in the examination jury.

Sincere thanks go to the members of the MOEMS Group for their contribution to my personal and my professional time: Dr. Maciej Baranski who always has the pertinent question, Dr. Jorge Albero (thank you again for bringing back my motorbike), Sophie Marguier who has a great open-mindedness, Dr. Sylwester Bargiel, Dr. Jaroslaw Rutkowski and Patricia Gorecki. Furthermore, I will never forget my office colleagues, a deeply thank for José Vincente Carrion Perez and Vincent Maurice. It has been a great pleasure to do my thesis work by your side in this pleasant work environment and friendly ambiance. And, my thanks go specially to Justine Lullin, for all the discussions about science (or not) and for her good mood during these almost four years.

Many thanks to other colleagues from FEMTO-ST institute, and in particular my colleagues from MN2S and Optics departments, for their helpful discussions whether it be experimental or theoretical. I want to name: Olivier Gaiffe, Sarah Benchabane, Thibaut Sylvestre, Jean-Charles Beugnot, Remo Giust, Maxime Jacquot, Emmanuel Dordor, Gil Fanjoux, Luca Furfaro. Furthermore, I want to thank all the members of the FEMTO-ST Student Chapter for organizing scientific and pedagogic events. It was a great experience which was highly supported by the direction of FEMTO-ST institute.

This thesis work has been supported by the European Commission (VIAMOS, FP7-ICT-

2011-8). I thank thus the seven partners of the collaborative project for their participation and the discussions we had concerning the medical requirements, the design of the device and the manufacture of the components. Moreover, I would like to thank the team of Superlum company for their efficiency work and their serious.

Finally, I would like to thank my friends I have met in this nice city, Besançon: Yannick (petit frère) and Gloria, Justine (le pire! c'est Uptown Funk) and Pierre, Antonio (Curry), José and Coralie (Gaspard et Balthazar), Abel (la classe espagnole), Sandrine (carotte) and Alex, Julien (la roulade), Mathieu, Clément, Baptiste and Aude, and Ludo. My final special thoughts for my family: my parents, my brother Thomas and my sister Charlène were an unconditional support throughout my life.

CONTENTS

General introduction	3
1 Optical coherence tomography	15
1.1 Time domain optical coherence tomography	16
1.2 Frequency domain optical coherence tomography	20
1.3 Artifact removal in frequency domain optical coherence tomography	24
1.4 Noise analysis and sensitivity	28
1.5 Performances of optical coherence tomography	32
1.6 Towards full field swept source optical coherence tomography	36
2 Specifications and optical design of the OCT micro-system	39
2.1 Architecture of the micro-imaging system	41
2.1.1 Mirau interferometers	43
2.1.2 Imaging part	46
2.1.3 Illumination part	50
2.1.4 Lateral and axial stitching	54
2.2 Sinusoidal phase shifting	56
2.3 Optical power losses - Sensitivity	60
2.4 Fabrication of micro-components	62
2.4.1 Microlens	63
2.4.2 Micro-reference mirror and micro-actuator	65
2.4.3 Planar beam-splitter	66
2.4.4 Assembly of the array of Mirau micro-interferometer	67
2.5 Synthesis	68
3 Characterization of optical micro-components	71

3.1	Characterization techniques	72
3.1.1	Surface quality through coherence scanning interference microscopy	72
3.1.2	Optical performance evaluation through point spread function . .	79
3.1.3	Wavefront quality through phase retrieval method	86
3.2	Inspection of the Mirau micro-interferometer	91
3.2.1	Characterization of the doublet of microlens	92
3.2.2	Characterization of the micro-scanner	95
3.2.3	Characterization of the Mirau micro-interferometer	97
3.3	Conclusion and perspectives	103
4	Towards the first Mirau-based FF-SS-OCT micro-system	105
4.1	Experimental setup of the Mirau-based FF-SS-OCT system	106
4.2	Software of the Mirau-based FF-SS-OCT system	108
4.3	Results of the FF-SS-OCT system using micro-interferometer	110
4.4	Assembly of the FF-SS-OCT micro-system	115
4.5	Discussion and perspectives	117
	General conclusion	119
	Appendix	127

LIST OF FIGURES

1	Schéma optique du microsystème de tomographie par cohérence optique.	xi
2	Comparaison de deux profils avec et sans algorithme de décalage de phase	xii
3	Caractérisations de microlentilles par la mesure de topographie et la mesure directe du volume	xiii
4	Photographie de la matrice d'interféromètres de Mirau	xiii
5	B-scan d'un objet réalisé à partir d'une couche de scotch appliquée sur un substrat de Si.	xiv
6	Inspection of an amelanotic melanoma with a polarized and an unpolarized dermatoscopy device	4
7	Histology slice of a normal skin and histopathology slices of cutaneous tumors	6
8	Principle of the ultrasound imaging technique	7
9	Principle of the photo-acoustic microscopy	8
10	Principle of the confocal scanning microscopy	9
11	Performances of the non-invasive high-resolution imaging technologies in dermatology	10
1.1	Normalized intensities of the interference signal from a coherent light source and from a low coherence light source	18
1.2	Principle of the time domain optical coherence tomography	19
1.3	Principle of the frequency domain optical coherence tomography	21
1.4	Frequency domain optical coherence tomography interferometric signal .	23
1.5	Depth profiles resulting of the Fourier transform of FD-OCT interferometric signals	26
1.6	Depth profiles resulting in the Fourier transform of complex phase shifted spectral intensity	28

1.7	Scheme of the noise contribution onto the resulting A-scan in frequency domain optical coherence tomography	30
1.8	Noise levels as a function of the irradiance onto the photo-detector	31
1.9	Axial resolution of an optical microscope and an OCT system.	33
1.10	Scheme of a single point frequency domain optical coherence tomography system	35
1.11	Principle of the full-field swept-source optical coherence tomography	37
2.1	Architecture of the full field swept source optical coherence tomography micro-system	42
2.2	Schematics of interferometric objectives	43
2.3	Zemax analyses of a single microlens and a doublet of microlenses	44
2.4	Schematic of the array of Mirau micro-interferometers	46
2.5	Layout of the imaging system	47
2.6	Impact of the cross-talk distribution between each channel	49
2.7	Measured transmission peaks from the piezo-based FPI over the 50 nm of spectral tuning range.	52
2.8	Comparison of the illumination system through the speckle reducer device.	53
2.9	Concept of the stitching of the optical head	55
2.10	Stitching actuation system for the motion of the optical head following three axes	56
2.11	Spectral interferogram signal using sinusoidal phase shifting technique	58
2.12	Fourier transform of the spectral interferogram signal with respect of time	59
2.13	A-scan resulting of the sinPSI algorithm	59
2.14	Quantum efficiency and noise standard deviation of the camera	62
2.15	Flowchart of the microlens fabrication process	64
2.16	Photographs of the wafer stack with matrices of microlens doublets and the cross section of a matrix of lens doublets	64
2.17	Flowchart of the reference mirror and spiders fabrication process	65
2.18	Photograph of an array of reference mirrors held by spiders	66

2.19	Evolution of the system sensitivity as a function of the transmission coefficient of the planar beam splitter.	67
2.20	Design concepts of the Mirau interferometer integration	67
3.1	Interferograms resulting of the object displacements at three different axial positions	74
3.2	Principle of the coherence scanning interferometry microscopy equipped with a Mirau interferometric microscope objective	75
3.3	Surface topography characterization using the coherence scanning interference microscope	77
3.4	Surface topography characterization of a micro-ball lens using the CSIM technique	79
3.5	Scheme and photograph of the experimental setup based on the PSF measurement	81
3.6	Measurement of the radius of curvature of a microlens	84
3.7	Photograph and zoom-view of the ball micro-lens	84
3.8	Measurement of ball microlens using the PSF technique	85
3.9	Diagram of the principle of the IPR algorithm	89
3.10	Wavefront distributions of the simulation, the coherent interferometric and the IPR techniques	91
3.11	Characterization of individual microlenses and doublet of microlenses . .	93
3.12	Normalized modulation transfer function of the doublet of microlenses . .	94
3.13	Two dimensional distribution of the refractive index after thermal processing of glass inside the silicon cavity	95
3.14	Characterization of the axial micro-scanner	97
3.15	Characterization of the Mirau micro-interferometer	99
3.16	Photograph of the optical setup for the off-axis CTF measurement	100
3.17	Characterization of the Mirau micro-interferometer to provide an off-axis cellular resolution	101
3.18	Square wave modulation transfer function of the Mirau micro-interferometer	102

4.1	Spectrum of the Superlum swept light source at 802 nm and 880 nm wavelengths	106
4.2	Photographs and zoom view of the on-bench FF-SS-OCT setup	107
4.3	Spectral interferometric signal from the Mirau micro-interferometer and the resulting depth profile	111
4.4	Impact of the sampling onto the depth profile with an object at 68 μm OPD.	112
4.5	Impact of the sampling onto the SNR with an object at 26 μm OPD.	113
4.6	B-scan of a layer of varnish onto a painting.	114
4.7	B-scan of the object which consists of a scotch-layer placed onto a silicon wafer.	115
4.8	Package of the imaging part of the FF-SS-OCT micro-system.	116
4.9	Volume stop, the spacer and of the imaging part of the FF-SS-OCT micro-system	116
4.10	Photograph of the prototype of the FF-SS-OCT micro-system	117
4.11	Anti-reflective coatings behaviour as a function of the wavelength	118
4.12	Photographs of the wafer stack and the cross section of a matrix of lens doublets	123
4.13	Photograph of the test chip of the electrostatically actuatable reference mirrors platform.	123
4.14	Characterization of the complete Mirau micro-interferometer.	124
4.15	B-scan of an object which consists of a scotch-layer placed onto a silicon wafer recorded with the integrated Mirau interferometer objective.	125
4.16	Producer consumer structure for the coherence scanning interference microscope	129
4.17	Data acquisition code of the full field swept source optical coherence tomography macro-system	130
4.18	Incoherent transfer function concept of an aberration-free optical system .	136
4.19	Coherent transfer function concept of an aberration-free system	139

LIST OF TABLES

1.1	Relation between the shape of the spectrum and the temporal coherence length.	17
2.1	Interferometric microscope objective technical specifications.	46
2.2	Imaging part technical specifications.	50
2.3	Illumination system technical specifications.	54
2.4	Acquisition block technical specifications.	60
3.1	Relation between the shape of the lens profile and the conic constant value.	78
3.2	Performances of the coherence scanning interference microscopy technique.	79
3.3	Relation between the Strehl ratio and the root mean square of the wavefront.	83
3.4	Acquisition block technical specifications.	102
4.1	Acquisition block technical specifications.	108
4.2	Zernike orthogonal circle polynomials	134
4.3	Summary of the resolution criteria in microscopy using an incoherent or a coherent light source.	138

LIST OF ALGORITHMS

1	Signal processing of the coherence scanning interference microscopy system	76
2	Sinusoidal phase shifting interferometry algorithm	110
3	Aberration coefficients calculation	133

LIST OF SYMBOLS

LATIN LETTERS

c	Speed of the light in a medium
e	Complex amplitude of the electric field
h	Planck constant with $h \approx 6.62606957 \times 10^{-34} \text{J}\cdot\text{s}$
I	Intensity of the electric field
j	Imaginary unit with $j^2 = -1$
k	Wavenumber vector of the light with $k = \frac{2\pi}{\lambda}$
\mathcal{N}	Noise power
n	Refractive index of a medium
\mathcal{P}	Polarization degree
\Re	Real part of a complex number
\mathcal{S}	Signal power
S	Spectral density

GREEK LETTERS

$\delta_{x,y}$	Lateral resolution of an imaging system
δ_z	Axial resolution of an imaging system
η	Detector responsivity
γ	Magnification of an optical system
Γ	Temporal coherence function of light source
λ	Wavelength of the light
ν	Temporal frequency
ρ and θ	Radial and azimuthal coordinates
τ	Exposure time of the photo-detector
ω	Angular frequency of a sin function

MATHEMATICAL OPERATORS

$\langle \cdot \rangle$	Time average operator
\otimes	Convolution operator
\mathbb{C}	Complex set
δ	Dirac delta function
\mathcal{F}	Fourier transform operator
\mathbb{R}	Real set
Σ	Sum operator

ACRONYMS

CCD	Charge-coupled device
CMOS	Complementary metal-oxide semiconductor
CSIM	Coherence scanning interference microscopy
FD-OCT	Frequency domain optical coherence tomography
FF-SS-OCT	Full field swept source optical coherence tomography
FOV	Field of view
FT	Fourier transform
FWHM	Full width at half maximum
IMO	Interferometric microscope objective
IPR	Iterative phase retrieval
LCI	Low coherence interferometry
MOEMS	Micro-opto-electro-mechanical systems
MTF	Modulation transfer function
NA	Numerical aperture
OCT	Optical coherence tomography
OTF	Optical transfer function
PSF	Point spread function
PSI	Phase shifting interferometry
RMS	Root mean square
RoC	Radius of curvature
ROI	Region of interest
SD-OCT	Spectral domain optical coherence tomography
SLD	Super-luminescent diode
SNR	Signal to noise ratio
SS-OCT	Swept source optical coherence tomography
TD-OCT	Time domain optical coherence tomography

GENERAL INTRODUCTION

Cancer, also called malignant tumor, results in a growth of abnormal cells within an organ - e.g., the human skin - following by their proliferation inside this organ. Unlike the benign lesions, cancerous tumors may also bring metastases leading to a spread of anomalous cells inside the organism, through the blood vessels. The body being made up of millions cells, many types of cancers exist. In this manuscript, we will focus in particular on skin cancer. The cutaneous cancers can be divided into two categories. The first type of skin cancers, the malignant melanoma, which is the most important cancer in terms of "years of potential life lost per death", is developed from the melanin-producing cells: the melanocytes. Melanin is the pigment-containing cell responsible of the skin color. In 2012, melanoma was the 19th most common cause of cancer death in Europe, with around 22,200 deaths [1]. Furthermore, there were around 55,500 deaths from malignant melanoma worldwide (0.7% of total cancer deaths). Due to the localization and the skin prototypes, Australia and New Zealand have the highest rates. In France, in 2012, melanoma skin cancer was the 9th, with 5 429 cases, and the 7th, with 5747 cases, most commonly diagnosed type of cancers for males and for females, respectively [2]. The second type of skin cancers is the non-melanoma cancer, including the basal cell carcinoma and the squamous cell carcinoma. These cancers derive their name from the cells in which they originate within the epidermis or the outer layers of the skin. The basal cell carcinoma comes from an abnormal reproduction of the basal and the squamous cells. It is twenty times more common than melanoma cancer. But, it has a substantially better prognosis than the more aggressive melanomas and hence, it rarely produces a life-threatening for the patient. However, when the patient care is inappropriate, he has a non-negligible potential of tissue damaging, leading to aesthetic sequels.

Nowadays, the main proposed screening procedure is the visual examination of the skin. Indeed, for a primary inspection of the human skin pathology, the dermatologists use the dermatoscopy, also called dermoscopy or surface microscopy. Dermatoscopy is widely employed in the clinical setting especially, for the differentiation of types of skin cancers [3]. This visual examination technique consists in looking at spots and moles through a magnification optical device. However, this technique only proposes the visualization of the skin surface. For imaging the subsurface structures, a liquid interface is placed

between glass plate of the dermatoscopy device and the stratum corneum (outermost layer of the epidermis). This index matching liquid reduces the light reflection from the skin surface and allows increasing the light penetration below the corneal layer. Recently, such dermatoscopy devices have been introduced to obtain tissue information of subsurface structures by combining polarized and multi-wavelength illumination [4, 5]. These techniques provide high quality images with an enhanced contrast. Furthermore, polarizing the probing light beam increases the depth of imaging up to 100 μm [6]. In such a case, the skin surface reflects the probing light beam by maintaining its unidirectional polarization which is rejected by the detector, whereas, the back-scattered light from the deeper skin layers is randomly polarized. Figure 6 shows the amelanotic melanoma visualized with a polarized (a) and an unpolarized (b) dermatoscopy device [7].

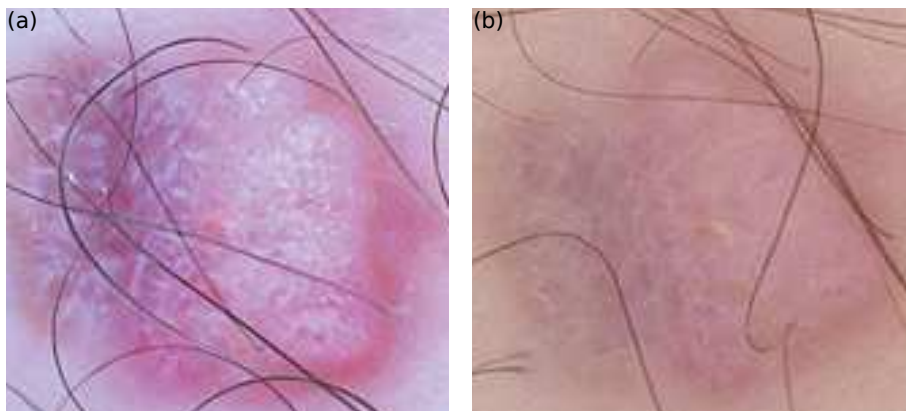


Figure 6: Inspection of an amelanotic melanoma with a polarized (a) and an unpolarized (b) dermatoscopy device. This figure is reproduced from [7].

An important warning sign for melanoma diagnosis is the appearance of a new lesion on the skin surface or a mole which is changing in color, shape or size. Dermatologists employ the well-known ABCDE criterion in order to distinguish a mole from a melanoma [8]. In the acronym, A stands for the asymmetry (asymmetrical shape), B for the border (irregular or blurred edges), C for the color (non uniform pigmentation), D for the diameter (larger than 6 mm) and E for the evolving (evolution of the size, color or new symptom). Nowadays, dermatoscopy is considered as a basic *in-vivo* tissue inspection that can predict a pathology such as a malignant melanoma. However, a diagnosis with dermatoscopy technique is limited by an inspection of the skin surface along the time [9] - i.e., at a given time, dermatoscopy does not provide information of the suspected lesion. Furthermore, a universal method should be established for the correlation of the results between dermatologists.

Currently, when a melanoma or a non-melanoma tumor is suspected, a sample of

the diseased tissue is removed from the body by partial biopsy, by biopsy exeresis or during a surgery. The sample is placed into a fixative to stabilize the tissues and to prevent its decay. After it is sliced, a pathologist examines the thin layers of the sample under a standard optical microscope and determines the spot signs of the pathology. The pathologist measures the margin, the size and the shape of the tumor and provides the type of the pathology. This process, named histopathology, is today the gold standard technique for the diagnosis of skin pathologies [10]. This technique can also be used to detect if a residual tumor is left into the patient's skin. Figure 7 shows histopathology slices of normal skin and diseased skin samples. As it can be seen, in Fig. 7 (a), the normal skin consists of three main layers: stratum corneum, epidermis and dermis. Here, the forth layer, called subcutis, is not illustrated. The layers, as well as the dermo-epidermal junction, are clearly distinguishable. Nevertheless, in case of cutaneous lesions, the surface of the skin is modified and its layers appear disordered. Symptoms depend on the type of cancer - e.g., pearl-shaped nodules for the basal cell carcinoma (see in Fig. 7 (b)), or proliferation of atypical melanocytes for nodular melanoma (see in Fig. 7 (d)). Furthermore, symptoms may vary following the stage of the cancer. For example, during the first stage, *in-situ* melanoma involves only the surface of the skin. While, in the second stage, the thickness of the tumor remains under 1 mm and the surface of the tumor appears broken down.

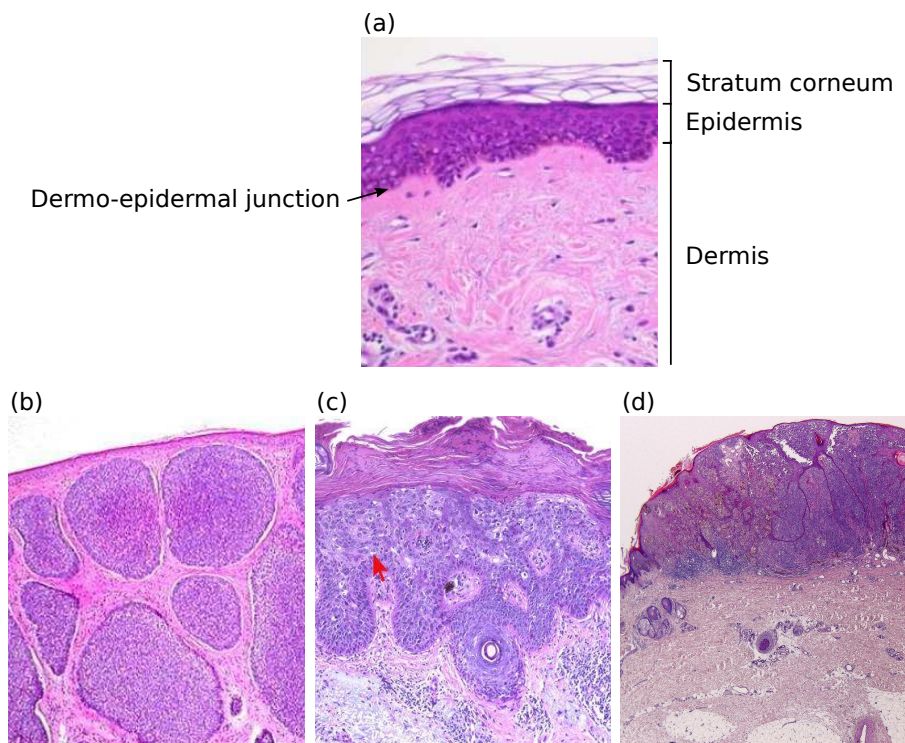


Figure 7: Histology slice of (a) a normal skin and histopathology slices of (b) a basal cell carcinoma below the epidermis, (c) a squamous cell carcinoma and (d) a *in-situ* nodular melanoma. These images are reproduced from websites (a) <http://proteinatlas.org>, (b) <http://studyblue.com>, (c) <http://vivosightatlas.com> and (d) <http://melanocytopathology.com>.

Nevertheless, histopathology suffers from several drawbacks, such as a long process time (2-3 weeks) and invasiveness procedure. Moreover, skin biopsy alters the original skin morphology since releasing of stress and elastic fibers can lead to wavy structure. Consequently, non-invasive imaging methods have been employed for clinical use [11]. They can be divided in two main categories: the spectroscopic techniques - e.g., the Raman scattering, hyper spectral imaging and near infrared absorption - and the structural imaging techniques - e.g., high-frequency ultrasounds, confocal microscopy and more recently photo-acoustic tomography and the optical coherence tomography. The interest of this thesis work is to perform an imaging system allowing visualizing the *in-vivo* structure of the skin layers and the layout of skin cells. Similar to the histopathology procedure, it will inform on the presence of skin pathology and its type. Thus, in the following, only structural non-invasive imaging techniques are retained and reviewed. Moreover, their applications for clinical dermatology is discussed and their performances are compared.

Usually, ultrasound is an imaging technique used in both industry, for the non-destructive testing, and medical - e.g., for the pregnancy ultrasound scans. In medical

domain, it is also called ultrasonography or sonography. Figure 8 is a scheme of the principle of the ultrasound imaging technique. Based on the time delay measurement between the emitted ultrasound wave, in red color, and the back reflected waves from each layers of the sample, in blue color, it provides a depth information subsequently employed to build a two or three dimensional image of the sample.

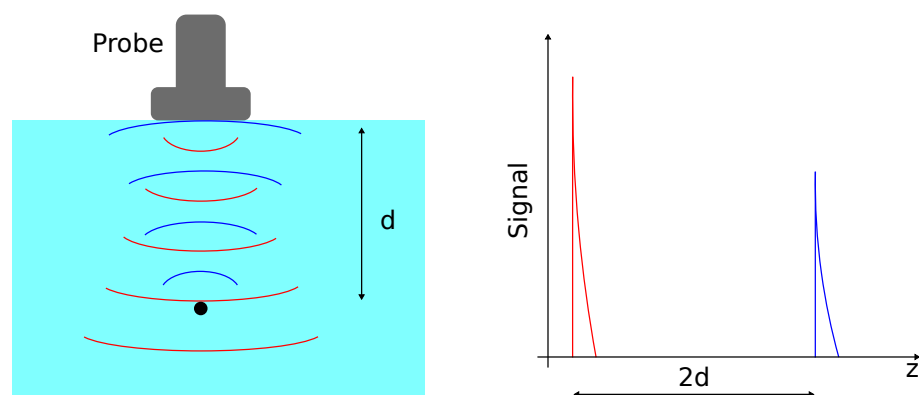


Figure 8: Principle of the ultrasound imaging technique. Red and blue color waves are the emitted and the reflected ultrasound waves, respectively.

Evaluation of the cutaneous lesions requires higher frequency sound waves [12]. Indeed, higher is the frequency of the signal, better is the resolution. Typically, for 100 MHz high-frequency ultrasound wave, the resolution of the ultrasound technique is about $40 \mu\text{m}$ [13]. Furthermore, depending on the frequency of the mechanical wave, the depth of penetration varies from 4 cm, for 7.5 MHz frequency, to 15 mm, for 100 MHz frequency. resolution limitation comes from the fact that higher ultrasound wave frequency may damage a living tissue by causing overheating. Consequently, this imaging technique is restricted to the visualization of skin layers, to recognize the morphology of skin tumors and to measure the tumor thickness.

More recently, a new medical imaging technique appeared, the photo-acoustic tomography (PAT) or photo-acoustic microscopy (PAM) for high resolution [14]. PAT/PAM is related to the photo-acoustic physical effect [15]. This effect occurs inside the sample by a thermoelastic expansion due to the absorption of a electromagnetic field (optical, radio-frequency or micro waves) and therefore, a temperature rise, typically in the millikelvin range. During the thermal relaxation process, pressure is induced leading to the generation of a mechanical wave - i.e., a high frequency acoustic wave. The time delay of the detected ultrasonic wave yields a depth information of the object position. Two or three dimensional surface scans offer a two or three dimensional lateral information about the photo-acoustic source and thus, a tomographic image [16]. Figure 9 shows the scheme of the photo-acoustic microscopy principle.

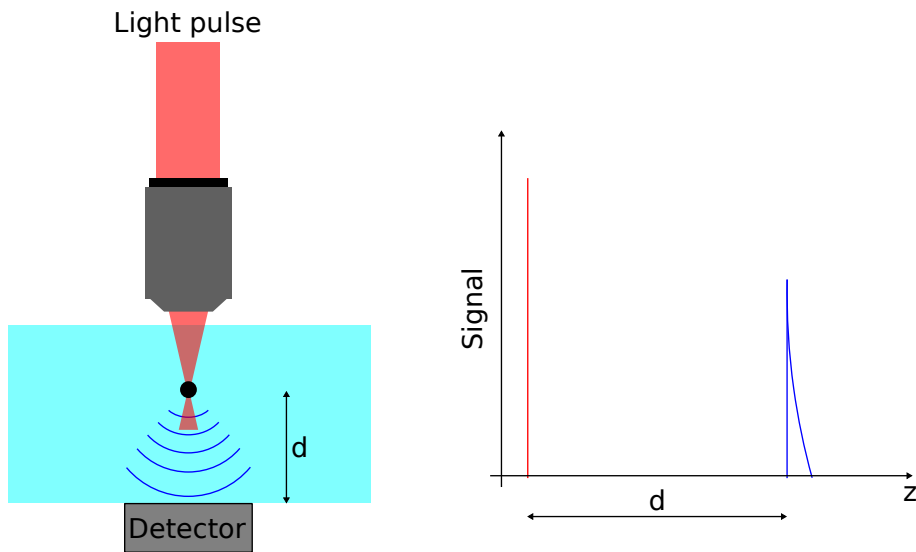


Figure 9: Principle of the photo-acoustic microscopy.

The spatial resolution of PAT is related to the emitting photo-acoustic signal - i.e., higher is the frequency, better is the spatial resolution of the imaging system. For example, a high-frequency photo-acoustic signal with 50 MHz central frequency, results approximately in a $40 \mu\text{m}$ resolution with 3 mm imaging depth - i.e., as for high frequency ultrasound technique - [17]. PAM provides better resolution than PAT because of the focused electromagnetic wave into a small size volume through a microscope objective. In this case, the resolution is similar to the optical resolution (few micrometers)[18]. Nevertheless, despite a good resolution, this technique requires a long acquisition time. Furthermore, the scanning system limits the field of view (FOV) of the imaging area. And, in dermatology, the short pulse laser radiation from the light source is restricted by the maximum permissible exposure irradiance in human biological tissues.

Confocal scanning microscopy (CSM) is an optical imaging technique based on a point light source and a point photo-detector [19]. Figure 10 shows the principle of the CSM through the standard optical architecture. The light beam is spatially filtered by a pinhole P to assure a point light source. Collimated by a lens C, the beam is oriented by the beam-splitter BS and is focused by the microscope objective MO at a specific depth in the sample. The back-reflected (or back-scattered) beam is collected by the MO and imaged onto the detector D by the lens L. A second pinhole is placed in the conjugate plane of the focal plane, before the photo-detector. This insures the recording of single point with a higher axial resolution than traditional microscopy, and allows avoiding the reflected or the fluorescence light from the "out-of-focal-planes" (dotted lines). To obtain a two or three dimensional image, an optical scanning of the sample or of the optical head is required.

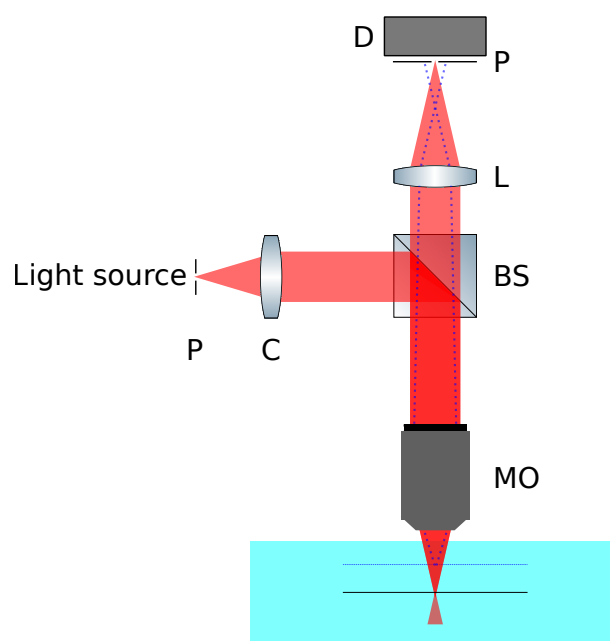


Figure 10: Principle of the confocal scanning microscopy.

The current commercial *in-vivo* CSMs [20] provide $1\ \mu\text{m}$ and $5\ \mu\text{m}$ of lateral and axial resolutions, respectively. These resolutions are sufficient to resolve skin cell. However, the depth of penetration is low (approximately $200\ \mu\text{m}$) and, in some cases, struggles to image the epidermal layers up to the dermo-epidermal junction [21]. This prevents the visualization of the depth invasion of skin tumors. Furthermore, the lateral FOV of CSM is limited by the scanning procedure. Recently, R.R. Anderson *et al.* have developed a polarized sensitive and multi-spectral CSM [22] in order to overcome this FOV limitation, but to the detriment of the resolution ($30\ \mu\text{m}$).

Finally, optical coherence tomography (OCT) is an emerging technique based on the principle of low coherence interferometry. This non-invasive technique is quite similar to the ultrasound imaging technique but in the optical range. However, due to the high speed of light, the optical pulse-echos (back-reflected signals from the object) cannot be distinguished with current detectors. Thus, the technique consists in recording an interference signal between a reference and the object beams. OCT can provide three dimensional images of a sample with a cellular resolution up to $2\ \text{mm}$ depth of penetration. The principle of OCT is detailed in the first chapter.

Figure 11 summarizes the performances of these four current imaging techniques used in dermatology by exposing the depth of penetration as a function of the resolution. As it can be seen, OCT is the only imaging technique which can reach a skin cellular resolution while keeping a sufficient imaging depth for dermatology. This promising

imaging technique seems to be an efficient tool for the discrimination between healthy and cancerous skin samples. Hence, the need of surgery in many useless cases could be eliminated.

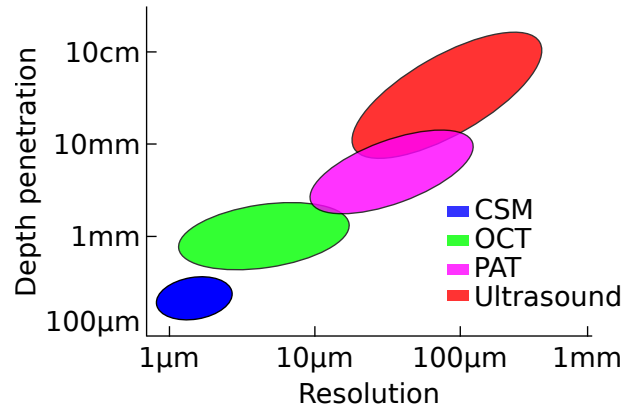


Figure 11: Performances of the non-invasive high-resolution imaging technologies in dermatology. The figure shows the imaging penetration depth as a function of the resolution. Both axes are in logarithm scale.

CONTEXT

Optical coherence tomography is a well recognized technique used for medical imaging in particular, since early 90's, in the field of ophthalmology. OCT has also recently been demonstrated to be a useful diagnostic tool for skin cancers. Here, superficial layers of skin surface can be seen *in-vivo* without need of skin surgery. Market of medical devices for the diagnosis of skin pathologies is growing rapidly through non-invasive and hand-held skin imaging solutions for dermatologists. Currently, in Europe, two main companies share out the OCT commercial market in dermatology [23], namely: Michelson Diagnostics Ltd. (Orpington, United Kingdom) and AGFA HealthCare (Belgium). Up to now, they are the only ones which obtained the agreement for *in-vivo* clinical use. Both of them provide bulk OCT systems that perform a non-invasive "optical biopsy" of the skin. These are well adapted for clinical use, especially in the hospitals. Michelson Diagnostics Ltd. (Orpington, United Kingdom) have developed the *Vivosight* OCT system. This system resolves objects whose size is lower than 10 μm until 1 mm depth of penetration [24]. Thanks to a large volumetric FOV (6 mm \times 6 mm \times 1mm), *Vivosight* is able to indicate the margins and the size of a tumor. The latter are important parameters for the skin cancer diagnosis. *Skintell* OCT system, from AGFA HealthCare company (Belgium), provides a better resolution (3 μm) but a lower penetration depth in tissue (0.5 mm) [25]. Also, the lateral FOV is smaller and equals 1.8 mm \times 1.5 mm. Consequently, dermatologists often use *Skintell* OCT system to diagnose precisely skin

lesions because of its much higher resolution that allows to better distinguish cells. Nevertheless, these commercial OCT devices are not affordable for private physicians and hence, are not sufficiently employed as an early diagnosis tool. Therefore, this situation limits the generalization of this powerful early diagnosis technique. Indeed, skin cancers have to be diagnosed as early as possible because of their "out-of-control" proliferation on the surface (non-melanoma) and in the tissues (melanoma) and, at worst, in the body (metastases).

During the last five years, a real enthusiasm to overcome this issue appeared within the scientific community. Indeed, start-up companies have been founded after research works or projects. DAMAE Medical (Paris, France) patented a technique which combined OCT and CSM and will propose, in some months, an hand-held OCT system for the *in-vivo* skin visualization [26]. In September 2015, Dermalumics (Madrid, Spain) received CE Mark approval in Europe, for the NITID OCT system [27]. Both of them will be able to provide a transverse slice of the *in-vivo* human skin.

The purpose of this research work is to develop a portable, miniaturized and low-cost OCT system, made available for dermatologists, as an early medical examination of *in-vivo* skin pathologies [28] - e.g., epithelial tumors in the first and the second stages. Consequently, in term of imaging performances, the OCT system has to provide cellular resolution over at least 500 μm imaging depth. Also, a large lateral FOV is required to detect the borders of the lesions. Thus, a trade-off subsists between both the performances and the hardware of the system. The manufacturing of the OCT system benefits from advanced micro-opto-electro-mechanical systems (MOEMS) technologies, which enable the generation of new miniature instruments [29] for decreasing the cost and the size. The development of the current device is supported by the VIAMOS (Vertically Integrated Array-type Mirau-based OCT System) collaborative project of the European Commission (FP7-ICT-2011-8, grant N°318542)¹. It involves 7 partners having complementary expertises in optical design, micro-optics, dermatology and system integration. Institut für Technische Optik of the University of Stuttgart (Germany) and FEMTO-ST institute (France) are in charge of the optical design of the VIAMOS system. Furthermore, assisted by Fraunhofer Institute für Elektronische Nanosysteme (Germany) and Stalice (France), FEMTO-ST works on the micro-optical components fabrication and the assembly of the final system. The light source and the camera are achieved by VTT Technical Research Centre (Finland) and Centre Suisse d'Electronique et de Microtechnique (Switzerland), respectively. Validation is realized in the Hospital University of Besançon (France). Dermoscan GmbH (Germany) is responsible of the

¹European project website: www.viamos.eu [Online] (2015).

exploitation of the future product.

THESIS OUTLINE

This manuscript consists of four chapters:

Chapter 1 introduces the principle of OCT method through the different declinations, such as time domain optical coherence tomography and frequency domain optical coherence tomography. A noise analysis is exposed to compare these two OCT techniques. Afterwards, the performances of OCT systems are summarized in terms of axial and lateral resolutions as well as imaging depth. The geometrical and spectral limits of the axial field of view are opposed. Then, the retained OCT approach of the project - i.e., full-field swept-source optical coherence tomography - is presented.

Chapter 2 reports the optical design of the miniaturized full-field swept-source optical coherence tomography micro-system according to the medical specifications. The choice of the components - i.e., their optical performances - and of the measurement strategies are detailed in order to provide a cellular resolution over large lateral and axial field of views. Required performances are exposed through the two blocks of the micro-device - i.e., both illumination and imaging parts - as well as its interferometric architecture - i.e., Mirau-based micro-interferometers. To compensate the empty measurements between each channel, the head is laterally displaced and axially stitched to perform a high imaging depth. A sinusoidal phase shifting method has been implemented to remove the artifacts from the Fourier transform operation and is presented. Afterwards, a study of the optical power losses and the sensitivity of the micro-imaging system is described. Finally, according to the requirements of the design, the fabrication of the optical micro-components and the assembly of the matrix of Mirau micro-interferometers are shown.

Chapter 3 exposes the characterization procedure of the micro-optical elements. Therefore, two characterization systems have been developed in order to evaluate the MOEMS components where their parameters are related to the design. The first system is coherence scanning interference microscope which allows measuring the surface topography and then deriving the radius of curvature and the roughness of the sample. The second characterization system is based on the measurement of the through-focus generated by the micro-element. This system can provide the resolution, the depth of field, the numerical aperture and the focal length of the micro-focusing component.

Furthermore, an enhancement of this technique, related on the phase retrieval technique, has been performed and allows estimating the generated optical aberrations. Here, the optical components of the Mirau-based micro-interferometer, as well as the entire interferometric system, have to be characterized.

Chapter 4 focuses on the implementation of the Mirau-based full-field swept-source optical coherence tomography micro-system. After being assembled and characterized, the array of micro-interferometers is placed into a macro-system in order to obtain the first spectral interferometric signals. The optical setup and the reconstruction algorithm are presented. Then, the micro-interferometer head is integrated on the micro-system.

NAMING CONVENTIONS

In this manuscript, the amplitude and the intensity of electromagnetic fields are used for the description of the interferometric signal of the optical coherence tomography system. For this purpose, the amplitude terms are written in small letters - i.e., $e(x, y, z)$ - while, the intensity terms are in capital letters - i.e., $I(x, y, z)$.

In physics and in particular in the optical field, the definition of the optical signal detected by a sensor is often incorrectly employed and is confusing [30]. Indeed, a distinction has to be done between the optical signal emitted from the light source, which is called the intensity, and the signal collected by the sensor, which is known as the irradiance. By definition, the intensity is the capacity of a light source to emit a radiant energy in the different directions and is expressed in Watt per steradian. While, the irradiance is the radiant flux which is received by a detector per unit surface. Its SI unit is the Watt per square meter.

OPTICAL COHERENCE TOMOGRAPHY

In the nineties, the advances in optics enabled the development of a novel non-invasive optical imaging technique, optical coherence tomography (OCT). Indeed, derived from optical low coherence reflectometry in the telecommunication industry, OCT was investigated by a wide number of research groups worldwide for medical imaging. The method of OCT was introduced by Fercher *et al.* [31]. Fujimoto *et al.* took the benefits of OCT for an ophthalmologic application with the two dimensional mapping of an *ex-vivo* human retina in 1991 [32]. After many improvements and *in-vivo* results, OCT was applied to dermatology in 1997 and in 2000 [33, 34]. OCT is related to the low (time) coherence interferometry method for biological tissue imaging. Formerly, this method was called the coherence gated imaging technique. It relies on the detection of ballistic photons, that are back-scattered from the object and which maintain a coherence degree with the photons from the reference beam. This interferometric technique filters the photons reflected by a layer whose position corresponds to the position of the reference mirror and, hence, rejects the scattered photons from multiple collisions and diffused photons by another layer.

This chapter introduces the general principles of OCT and the different implementations of the technique. In particular, we focus in detail on the time domain optical coherence tomography method and its enhancement - i.e., the frequency domain optical coherence tomography method. A comparison of the performances of these two techniques, in terms of resolution and depth of penetration, is presented. Furthermore, a noise analysis of both interferometric techniques is described. The sensitivity of an OCT instrument is critical and determines the trade-off between the image acquisition procedure and the image quality. Thus, the notion of sensitivity of an OCT system is introduced. Finally, full-field swept-source optical coherence tomography (FF-SS-OCT) which is the method chosen for the imaging micro-system, is described.

1.1/ TIME DOMAIN OPTICAL COHERENCE TOMOGRAPHY

Low coherence interferometry, also named white light interferometry, is an interferometric technique in which the light source is temporally incoherent - i.e., the spectral width of the light source is large. By definition, the temporal coherence length is the propagation distance for which two fields are available to interfere with each other - i.e., the length where the degree of correlation between the fields is maintained. Assuming a Gaussian spectral density of the light source $S(k)$ described by

$$S(k) = \exp \left[- \left(\frac{k - k_0}{\Delta k} \right)^2 \right], \quad (1.1)$$

with the wavenumber k , the central wavenumber k_0 and the half-width of the spectral density at $1/e$ of its maximum Δk of the light source. Thus, the full width at half maximum (FWHM) of the spectrum is written $\Delta k_{FWHM} = 2 \sqrt{\ln(2)} \Delta k$. As a function of wavelength, this yields to

$$\begin{aligned} \Delta k &= \frac{\Delta k_{FWHM}}{2 \sqrt{\ln(2)}} \\ &= \frac{k_{max} - k_{min}}{2 \sqrt{\ln(2)}} \\ &= \frac{\pi}{\sqrt{\ln 2}} \left(\frac{1}{\lambda_{max}} - \frac{1}{\lambda_{min}} \right) \\ &= \frac{\pi}{\sqrt{\ln 2}} \left(\frac{\Delta \lambda}{\lambda_{max} \lambda_{min}} \right), \end{aligned} \quad (1.2)$$

with λ_{min} , λ_{max} and $\Delta \lambda$, the minimal and the maximal wavelength and the FWHM of the light source spectrum [35]. Because of their Fourier transform relation [35, 36], the temporal coherence function $\Gamma(\Delta z)$ is Gaussian and is computed as

$$\Gamma(\Delta z) = \mathcal{F} \{ S(k) \}, \quad (1.3)$$

where \mathcal{F} is the Fourier transform operator according to the optical path difference Δz . This relation is known as the Wiener-Khinchin theorem. By replacing the function 1.1 in Eq.1.3, the temporal coherence function is

$$\Gamma(\Delta z) = \frac{\Delta k \sqrt{\pi}}{2\pi} \exp \left[- \left(\frac{\Delta k}{2} \Delta z \right)^2 \right] \quad (1.4)$$

The definition of the coherence length l_c of a light source is rather arbitrary and depends on the application [36]. In optical coherence tomography, the coherence length is commonly defined as the FWHM of the temporal coherence function $\Gamma(\Delta z)$. By replacing Δk

from the expression in Eq. 1.2, this leads to

$$l_c = \frac{4\sqrt{\ln 2}}{\Delta k} = \frac{4\ln 2}{\pi} \frac{\lambda_{max}\lambda_{min}}{\Delta\lambda} \quad (1.5)$$

The product of λ_{min} and λ_{max} may be approximated to the square of the central wavelength λ_0 , corresponding to the central wavenumber k_0 . The coherence length is thus defined by the ratio of the squared central wavelength λ_0 to the bandwidth of the spectrum $\Delta\lambda$ of the incident light source. For a Gaussian spectral density, the coherence length can be simplified and yields to

$$l_c = \frac{4\ln 2}{\pi} \frac{\lambda_0^2}{\Delta\lambda} \quad (1.6)$$

Note that the coherence length is inversely proportional to the bandwidth of the light source. However, the coherence length depends also on the shape of the spectrum of the light source. Table 1.1 summarizes the temporal coherence length of three main spectral density shapes: Gaussian, Rectangular and Lorentzian [36].

Spectral density shape	Coherence length l_c
Gaussian	$\frac{4\ln 2}{\pi} \frac{\lambda_0^2}{\Delta\lambda}$
Rectangular	$\frac{\lambda_0^2}{\Delta\lambda}$
Lorentzian	$\frac{1}{\pi} \frac{\lambda_0^2}{\Delta\lambda}$

Table 1.1: Relation between the shape of the spectrum and the temporal coherence length.

In coherent interferometry techniques, such as holography [37], the interference signal should not decrease until few centimetres of optical path difference depending on the linewidth of the light source (Fig. 1.1 (a)), so that the interference signal is considered locally perfectly sinusoidal. However, in LCI, the intensity of the interference signal is gated by the temporal coherence function $\Gamma(\Delta z)$ (Fig. 1.1 (b)) and appears temporally localized. The interference pattern can only be detected when the optical path difference Δz , between the reference and the object arms, is less than the coherence length l_c . This results in a constructive interference and produces an intensity peak envelope modulated by a sinusoidal interference signal. Unlike coherent interferometry, the LCI does not provide directly the phase information.

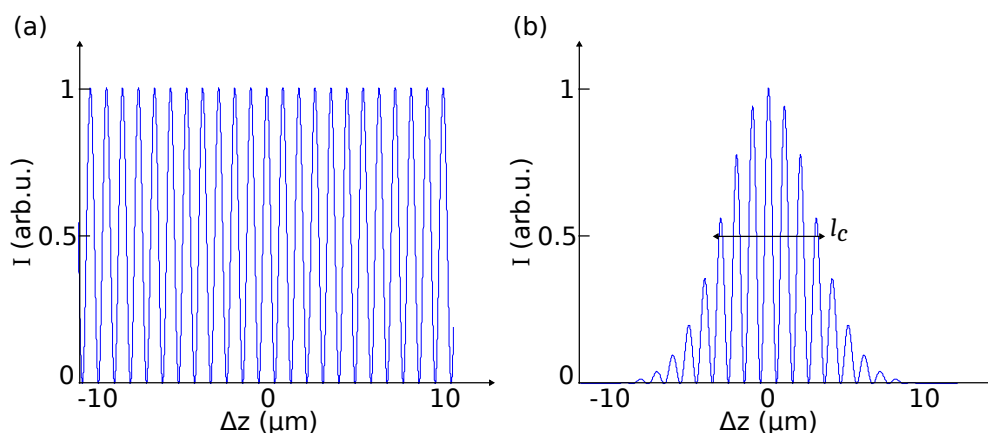


Figure 1.1: Normalized intensities of the interference signal from (a) a coherent light source and (b) from a low coherence light source as a function of the optical path difference Δz .

Time domain optical coherence tomography (TD-OCT) is actually an application of the LCI for biological imaging. Using the coherence property of a broadband light source, the measurement of the time delay (or the distance Δz), between both the reference position z_m and a layer position z_r , can be performed with an axial resolution related to the coherence length l_c . Figure 1.2 exposes the optical schematic of the TD-OCT. The configuration of TD-OCT consists essentially of a broadband light source BLS and a Michelson interferometer. The incident beam from the light source is divided into two parts by the beam-splitter cube BS which are directed toward the reference and object arms. The beams are reflected by the reference mirror M on one side and by the layers within the sample on the other side. Afterwards, the reflected beams are combined by the beam-splitter cube which directs them toward the photo-detector D. The photo-detector records the intensity signal I_{TD-OCT} resulting of the summation of both the reference electric field e_r and the back-reflected electric field $e_s(z_m)$ of each layers m . When the optical path difference $\Delta z = z_r - z_m$ is less than the coherence length l_c , an intensity peak results. Hence, the reference mirror is axially scanned along the z axis. The interference intensity signal I_{TD-OCT} is commonly called interferogram. By isolating the background light and detecting the maximal intensity peak values, TD-OCT provides the one dimensional positions z_m of the layers, called A-scan. In order to obtain a cross-sectional (B-scan) or a volumetric image of the sample, the incident beam on the tissue is laterally scanned and a series of A-scans are collected.

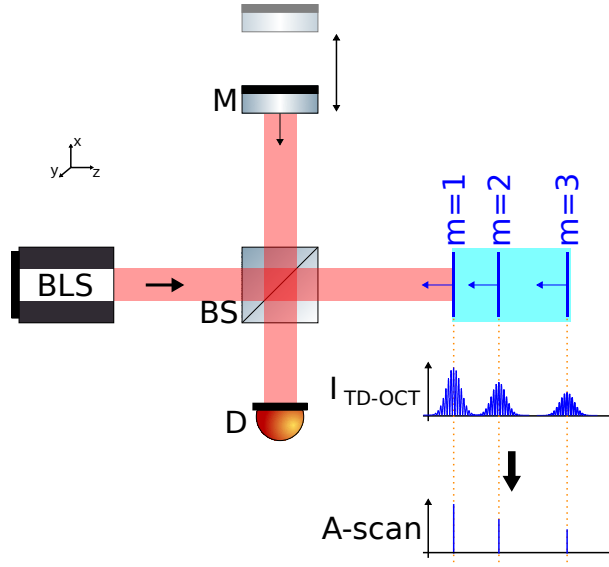


Figure 1.2: Principle of the time domain optical coherence tomography.

The mathematical treatment of the interferometric signal in TD-OCT results on the superposition of two partially coherent waves e_r and $e_s(z_m)$. The expression of the irradiance of the interference signal I_{TD-OCT} , collected by the detector, is proportional to the modulus-squared time average of the sum of the complex fields e_r and $e_s(z_m)$ and can be written as

$$I_{TD-OCT} = \eta \langle |e_r + e_s(z_m)|^2 \rangle, \quad (1.7)$$

with η , the detector responsivity. $\langle \rangle$ denotes the time-average operator over the exposure time of the detector. Developing Eq. 1.7 yields to

$$\begin{aligned} I_{TD-OCT} &= \eta [(e_r + e_s(z_m)) (e_r + e_s(z_m))^*] \\ &= \eta [|e_r|^2 + |e_s(z_m)|^2 + e_r^* e_s(z_m) + e_r e_s(z_m)^*] \end{aligned} \quad (1.8)$$

Both terms $|e_r|^2$ and $|e_s(z_m)|^2$ are the intensity signals from the reference and the sample beams. The sum of these terms is called direct current (DC) and contains only information about the reflectivity from the reference mirror and from the layers of the sample. These terms are independent on the optical path difference - i.e., they do not provide any information about the distances z_r and z_m . Whereas, the interferometric term, $e_r^* e_s(z_m) + e_r e_s(z_m)^*$, contains information of the optical path difference between the two beams. By developing the interferometric signal and replacing $|e_r|^2$ by I_r and $|e_s(z_m)|^2$ by

$I_s(z_m)$, the TD-OCT intensity signal is

$$\begin{aligned}
 I_{TD-OCT} &= \eta \left[I_r + I_s(z_m) + 2 \sqrt{I_r I_s(z_m)} \Gamma(\Delta z) \cos(k_0 \Delta z) \right] \\
 &= \eta \left[I_r + I_s(z_m) + 2 \sqrt{I_r I_s(z_m)} \exp \left[- \left(\frac{2 \sqrt{\ln 2}}{l_c} \Delta z \right)^2 \right] \cos(k_0 \Delta z) \right] \quad (1.9)
 \end{aligned}$$

The interferometric signal results from the product between the temporal coherence function of the light source and a sinusoidal carrier wave modulated at the central wavenumber k_0 and the optical path difference Δz between both arms (Fig. 1.1 (b)). When, Δz equals to zero - i.e., $z_r = z_m$ - the irradiance onto the detector is $I_r + I_s(z_m) + 2 \sqrt{I_r I_s(z_m)}$. Note that, in the equations, the temporal angular frequency $\exp[-j\omega t]$ has been eliminated because the frequency of the oscillations are faster than the response time of the standard detectors [35]. For example, for a wavelength $\lambda = 800 \text{ nm}$, the temporal frequency equals $\nu = 375 \text{ GHz}$.

1.2/ FREQUENCY DOMAIN OPTICAL COHERENCE TOMOGRAPHY

Few years after the TD-OCT has been proposed, Fercher *et al.* [38] have reported the implementation of another OCT method, so-called frequency domain optical coherence tomography (FD-OCT). The first *in-vivo* demonstration of FD-OCT was reported for retinal imaging in 2002 [39]. This spectral interferometric method is based on the Wiener-Khinchin theorem which relates both the spectral interference signal and the depth profile by a Fourier transform [35, 40, 41]. Instead of moving the reference mirror, the interferogram is spectrally recorded as a function of the wavenumber k whereas the reference mirror remains fixed. Furthermore, the FD-OCT method can be divided in two sub-categories according to their optical configuration and their detection technique. The first category is the spectral domain optical coherence tomography (SD-OCT), also called spectrometer based OCT or spatially encoded FD-OCT, where the light source and the detector are a broadband light source and a spectrometer, respectively. The second category of FD-OCT method, implemented by Chinn *et al.* [42], is the swept-source optical coherence tomography (SS-OCT), also known as temporally encoded FD-OCT. Here, instead of simultaneously acquiring the signal by using a spectrometer, the broadband light source is tuned in wavenumber k and, a single-point photo-detector sequentially records each irradiance of the spectral interferometric signal.

Figure 1.3 shows the optical architecture of the FD-OCT. The incident beam from the broadband light source BLS is divided into the reference and the sample arms. The

beams back-reflected by each layers m of the sample $e_s(k, z_m)$ and the beam from the reference arm $e_r(k)$ are combined and directed onto the spectrometer. The spectrometer consists of a diffraction grating G and a lens L which images simultaneously the spectral intensity I_{FD-OCT} as a function of the wavenumber k onto the line detector LD . Each pixel of LD records consequently a component of the spectral interference signal.

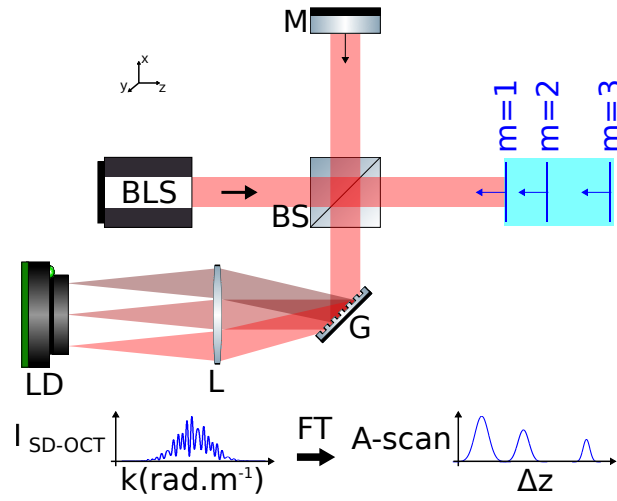


Figure 1.3: Principle of the frequency domain optical coherence tomography.

The amplitudes of the electric fields returning from the reference $e_r(k)$ and the sample $e_s(k, z_m)$ arms are written $e_r(k) = \frac{s(k)}{\sqrt{2}} r_r \exp[j2kz_r]$ and $e_s(k, z_m) = \frac{s(k)}{\sqrt{2}} \sum_{m=1}^M r_m \exp[j2kz_m]$, respectively. $S(k) = |s(k)|^2$ represents the spectral density of the light source and M is the number of layers within the sample. Both terms r_r and r_m are the electric field reflectivities of the reference mirror and the layer m . As in TD-OCT, the temporal component has been eliminated because of its faster oscillation frequency than the acquisition frequency of real detectors. The recorded intensity I_{FD-OCT} , also called A-line, is written as the modulus-squared time average of the sum of the reference and sample fields,

$$\begin{aligned} I_{FD-OCT} &= \eta [(e_r + e_s(z_m)) (e_r + e_s(z_m))^*] \\ &= \eta [e_r e_r^* + e_r e_s(z_m)^* + e_r^* e_s(z_m) + e_s(z_m) e_s(z_m)^*], \end{aligned} \quad (1.10)$$

which leads to a four-terms equation.

$$\begin{aligned}
I_{FD-OCT} = \eta \left[\frac{S(k)}{2} R_r + \frac{S(k)}{2} r_r \exp(j2kz_r) \sum_{m=1}^M r_m \exp(-j2kz_m) \right. \\
+ \frac{S(k)}{2} r_r \exp(-j2kz_r) \sum_{m=1}^M r_m \exp(j2kz_m) \\
\left. + \frac{S(k)}{2} \sum_{m=1}^M r_m \exp(j2kz_m) \sum_{m=1}^M r_m \exp(-j2kz_m) \right] \quad (1.11)
\end{aligned}$$

Where $R_r = |r_r|^2$ and $R_m = |r_m|^2$ are the reference and the sample power reflectivities, respectively. Eq. 1.11 can be simplified into:

$$\begin{aligned}
I_{FD-OCT} = \eta \frac{S(k)}{2} \left[\left(R_r + \sum_{m=1}^M R_m \right) \right. \\
+ \sum_{m=1}^M \sqrt{R_r R_m} \exp(j2k(z_r - z_m)) + \sum_{m=1}^M \sqrt{R_r R_m} \exp(-j2k(z_r - z_m)) \\
\left. + \sum_{m \neq p=1}^M r_m r_p \exp[j2k(z_m - z_p)] \right] \quad (1.12)
\end{aligned}$$

Moreover, using the Euler formula, the second and the third terms of Eq. 1.12 may be written in the form of a sinusoidal function. Similarly the fourth term can be written as a co-sinusoidal function instead of a complex exponential function, since only the real part of the interferogram is recorded by the detector. The spectral intensity of the interference signal is now given by

$$\begin{aligned}
I_{FD-OCT} = \eta \frac{S(k)}{4} \left[\left(R_r + \sum_{m=1}^M R_m \right) \right. & \text{Continuous term} \\
+ 2 \sum_{m=1}^M \sqrt{R_r R_m} \cos(2k(z_r - z_m)) & \text{Cross-correlation between } e_r \text{ and } e_s \\
+ \sum_{m \neq p=1}^M \sqrt{R_m R_p} \cos(2k(z_m - z_p)) & \text{Cross-correlation between } e_s \\
\left. \right] \quad (1.13)
\end{aligned}$$

As it can be seen, the irradiance of the SD-OCT signal results as a sum of a continuous, a cross-correlation and a low frequency terms. The continuous term (DC), sometimes called auto-correlation, is proportional to the intensities reflected by the reference mirror and back-scattered from each layer of the sample. This is independent on the optical path difference and can be associated to an offset. The cross-correlation term between the reference and the sample beams, also called interferometric signal, provides information on the phase difference and thus on the depth profile. It is proportional to the square

root of the reflectivity from each layers and the reference mirror. This is the desired component in FD-OCT. Finally, the cross-correlation term between the layers themselves, resulting from the product between $e_s(k, z_m)e_s(k, z_m)^*$, describes the interference signal between each layers of the sample [43]. This term obviously brings noise and is not desired. It can be written as $\frac{S(k)}{2} \left[\sum_{m=1}^M R_m + \sum_{m \neq p=1}^M r_m r_p \exp [j2k(z_m - z_p)] \right]$, where z_p is the position of the layer p within the sample, different from the position z_m , with a power reflectivity $R_p = |r_p|^2$. The first term is a part of the DC, while the second term is a noise which occurs when the coherence length of the light source is higher than the distance $z_m - z_p$ between both respective layers m and p . In digital holography, this last term is called coherent noise [44]. Despite a smaller optical intensity than the other terms of Eq. 1.13, it can be further reduced by increasing the optical power of the reference beam [35, 38].

As an example, Fig. 1.4 shows spectral interferograms as a function of the wavenumber k resulting from a sample with one reflector, in Fig. 1.4 (a), and with multiple reflective layers, in Fig. 1.4 (b). The intensity signal from multiple reflector can be interpreted as a sum of sinusoidal oscillations with a frequency proportional to $\Delta z / \pi$.

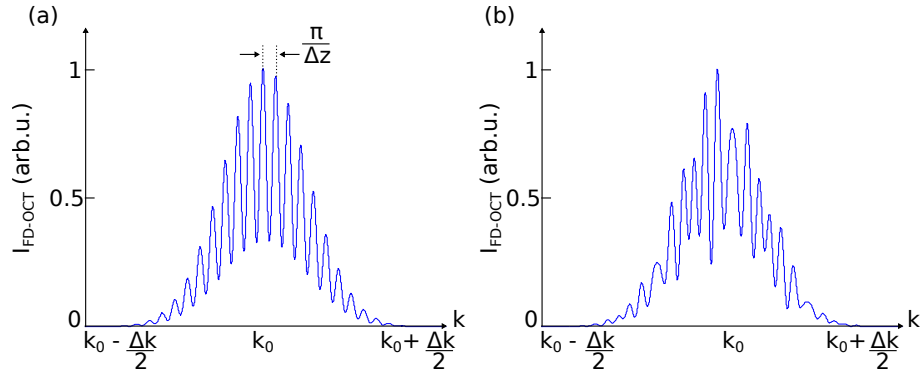


Figure 1.4: Frequency domain optical coherence tomography interferometric signal as a function of the wavenumber k , obtained with (a) a unique reflective layer sample and (b) a multiple layers sample.

By performing an inverse Fourier transform of the spectral interferogram, the one dimensional depth profile can be derived and information about the relative position of the

layers is retrieved.

$$\begin{aligned}
\mathcal{F}^{-1} [I_{FD-OCT}] = & \frac{\eta}{4} \left[\Gamma(\Delta z) \left(R_r + \sum_{m=1}^M R_m \right) \right. \\
& + \Gamma(\Delta z) \otimes \sum_{m=1}^M \sqrt{R_r R_m} [\delta(z - 2\Delta z) + \delta(z + 2\Delta z)] \\
& \left. + \Gamma(\Delta z) \otimes \sum_{m \neq p=1}^M \sqrt{R_m R_p} [\delta(z - 2(z_m - z_p)) + \delta(z + 2(z_m - z_p))] \right] \quad (1.14)
\end{aligned}$$

\mathcal{F}^{-1} is the inverse Fourier transform operator and δ is the Dirac delta function. The Dirac delta function results in the Fourier transform of the cosinusoidal function. Due to the properties of the Dirac delta function, the convolution $\Gamma(\Delta z) \otimes \delta(z - 2\Delta z)$ can also be written as $\Gamma(z - 2\Delta z)$. This means that the coherence function appears for each zero value of optical path difference. Moreover, it has been shown that using the phase information of the Fourier transform operation, provides "en-face" images with high resolution [45].

However, by applying the Fourier transform on the real interferometric signal, two components of the cross-correlation terms appear. Indeed, both a positive and a negative terms are generated. This effect can be illustrated by the Fourier transform of the cosine function.

$$\mathcal{F}^{-1} [\cos(2k\Delta z)] = \frac{1}{2} [\delta(z - \Delta z) + \delta(z + \Delta z)] \quad (1.15)$$

Finally, only one component out of six from Eq.1.14 is meaningful for A-scan retrieval. Hence, others components (DC, mirror image and cross-correlation between each layers of the sample) should be suppressed. Section 1.3 shows implementations used to remove these artifacts and to keep only the desired cross-correlation term.

1.3/ ARTIFACT REMOVAL IN FREQUENCY DOMAIN OPTICAL COHERENCE TOMOGRAPHY

First, as it was explained in the last section, several terms exist when the inverse Fourier transform is applied to the spectral interferometric signal (see Eq. 1.14). First, the back-reflected intensities from the reference mirror and the scattering layers of the sample yields to a continuous term which can be interpreted as an offset. Moreover, interference between layers themselves provides a noise term. These terms are not useful to derive an A-scan and are thus considered as artifacts in FD-OCT. In addition,

both the continuous and the cross-correlation between the sample terms affect the signal-to-noise ratio (SNR), hence, the sensitivity of the system [46] and may blur the true object structure. More details of the noise analysis of OCT systems are presented in the next section. Furthermore, due to the Hermitian symmetry, the Fourier transform of a real interferometric signal provides complex conjugate terms. This leads to a positive and a negative images around the zero time delay line [47]. These complex conjugate terms limit the imaging depth of the system [48].

As an illustration, Fig. 1.5 shows the outcome of the Fourier transform applied to a real spectral interferometric signal resulting from the investigation of a sample made of two layers. As it can be seen, five intensity peaks appear. The cross-correlation within the sample terms are neglected. The higher intensity peak, displayed in black color, is the continuous term. The cross-correlation terms including both the negative, in red color, and the positive, in blue color, provide a lower intensity peak. In Fig1.5(a), the easier manner to obtain the cross-correlation free of mirror artifacts, is to digitally remove the left part of the signal although this treatment decreases the axial imaging range by a factor two. However, this is viable because the zero optical path difference is located before the layers. When it is not the case, as in Fig. 1.5(b), the effect of the Fourier transform leads to a mixing of the positive and negative peaks, making this rough method non-practical. In spectral interferometry, several techniques, including the polarization demodulation method [49], heterodyne interferometry [50], 3x3 fiber coupler based method [51] and phase shifting interferometry (PSI), have been implemented in order to resolve the complex conjugate ambiguity and to obtain a depth profile free of artifacts. In this work, due to the optical architecture of the micro-interferometer, the PSI technique has been chosen. The aim of PSI is to add a known optical phase delay ϕ_{PSI} between both the reference and the sample beams for several acquisitions [48, 52]. The reference electric field is hence modified to

$$e_r(k) = \frac{s(k)}{\sqrt{2}} r_r \exp [j2kz_r + \phi_{PSI}] \quad (1.16)$$

By rewriting the Eq. 1.13, the spectral interferogram recorded by the detector becomes

$$\begin{aligned} I_{FD-OCT}(\phi_{PSI}) = \eta \frac{S(k)}{4} & \left[\left(R_r + \sum_{m=1}^M R_m \right) \right. \\ & + 2 \sum_{m=1}^M \sqrt{R_r R_m} \cos (2k (z_r - z_m) + \phi_{PSI}) \\ & \left. + \sum_{m \neq p=1}^M \sqrt{R_m R_p} \cos (2k (z_m - z_p)) \right] \quad (1.17) \end{aligned}$$

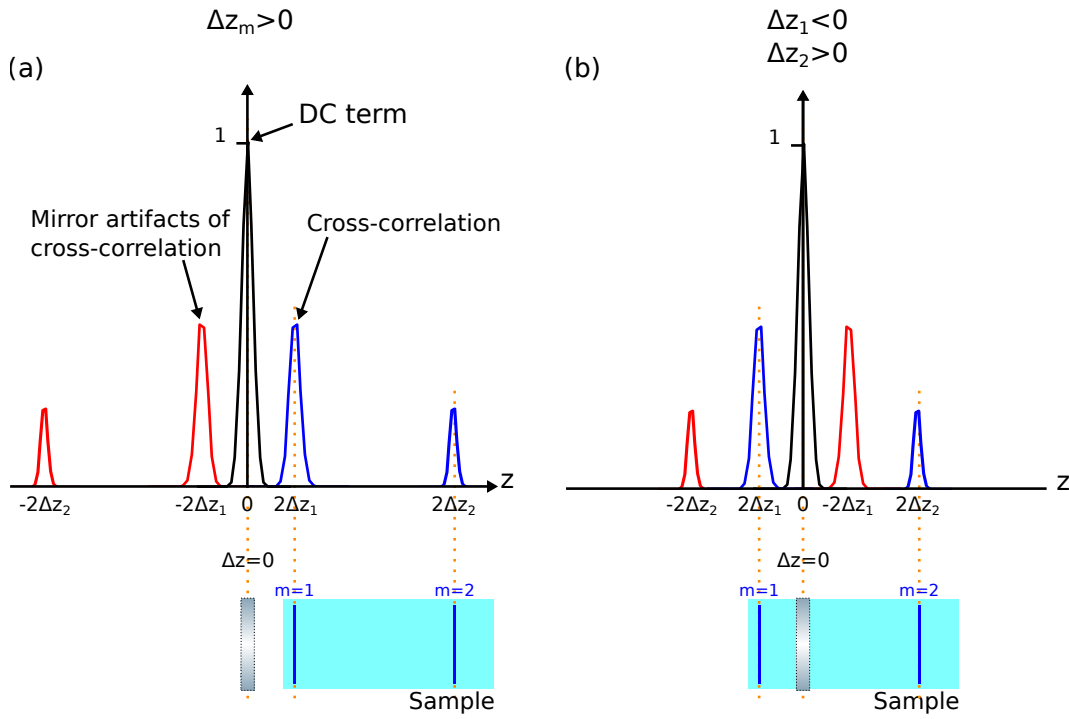


Figure 1.5: Depth profiles resulting of the Fourier transform of FD-OCT interferometric signals. In (b), the optical path difference between the reference mirror and the layer $m = 1$ is negative and is positive for the layer $m = 2$.

Where the phase delay appears only in the cross-section term - i.e., the term of interest. Hence, if a phase delay $\phi_{PSI} = \pi$ between two phase shifted irradiance is implemented, the continuous and the cross-correlation into the sample terms can be eliminated by calculating the difference between the two interferograms. In details, by subtracting the phase delayed ($\phi_{PSI} = \pi$) from the non-phase delayed ($\phi_{PSI} = 0$) irradiances, the resulting spectral intensity is

$$I_{FD-OCT}(\phi_{PSI} = 0) - I_{FD-OCT}(\phi_{PSI} = \pi) = \eta S(k) \sum_{m=1}^M \sqrt{R_r R_m} \cos(2k(z_r - z_m)) \quad (1.18)$$

This is called the two-step algorithm [53] (or differential spectral OCT). The only terms to subsist, the cross-correlation terms, are increased by a factor of two. However, the complex conjugate terms are still present. In order to remove the entire non-interferometric and complex conjugate terms, four phase shifted images have to be recorded. The phase delay between two respective irradiances is then $\phi_{PSI} = \frac{\pi}{2}$. The mathematical treatment

provides a complex interference signal.

$$\begin{aligned}
 I_{PSI} &= [I_{FD-OCT}(\phi_{PSI} = 0) - I_{FD-OCT}(\phi_{PSI} = \pi) \\
 &\quad + j \left[I_{FD-OCT}(\phi_{PSI} = \frac{\pi}{2}) - I_{FD-OCT}(\phi_{PSI} = \frac{3\pi}{2}) \right] \\
 &= \eta S(k) \sum_{m=1}^M \sqrt{R_r R_m} \exp[-2jk\Delta z]
 \end{aligned} \tag{1.19}$$

The Fourier transform of the spectral interferogram, ensuing from the four-steps algorithm [53], leads to an intensity depth profile.

$$\mathcal{F}^{-1}[I_{PSI}] = \eta \sum_{m=1}^M \sqrt{R_r R_m} \Gamma(2\Delta z) \tag{1.20}$$

An example of phase shifting implementation performed onto a spectral interferometric signal similar to the one of Fig. 1.5, is exposed in Fig. 1.6. As it is shown, the complex conjugate resulting from the Fourier transform, the continuous and the cross-correlation from the layers in the sample terms disappear wherever the zero optical path difference location is. Moreover, by using the PSI algorithm, the imaging depth is doubled. This corresponding depth is called the full-range imaging depth.

The four-step PSI technique is relatively simple to implement and provides a good suppression ratio of the DC and the complex conjugates - i.e., around 20 dB of the complex conjugate artifacts rejection [54]. However, LCI requires the use of a broadband light source. The accuracy of the algorithm is thus limited by the polychromatic phase error, originated from the wavelength dependence on the phase delay ($\phi_{PSI} = f(\lambda)$). To compensate this error and, hence, to perform a quasi-achromatic measurement, PSI techniques have been developed including in particular the iterative least-square PSI where 20 dB mirror term rejection was reported [55], the B-M method which lead to 45 dB suppression ratio of mirror terms [56] and the complex spectral OCT (or five-steps PSI algorithm) providing 7.5 dB signal-to-noise ratio improvement [48]. Although the polychromatic phase error is corrected, these techniques require a long acquisition time or are not well adapted for *in-vivo* diagnosis. Besides, the phase-stepping techniques need a good stability of the reference mirror position. In this work, instead of applying an incremental step or a linear phase delay between both arms of the interferometer, the reference mirror is actuated following a sinusoidal motion. Despite a more difficult implementation, a sinusoidal phase shifting (sinPSI) guarantees a stable, high-speed and repeatable displacement of the reference mirror along the acquisition process as well as an achromatic measurement of the FD-OCT signal. The implementation of the sinPSI, in terms of hardware and algorithm, is described in Sec. 2.1 and Sec. 2.2.

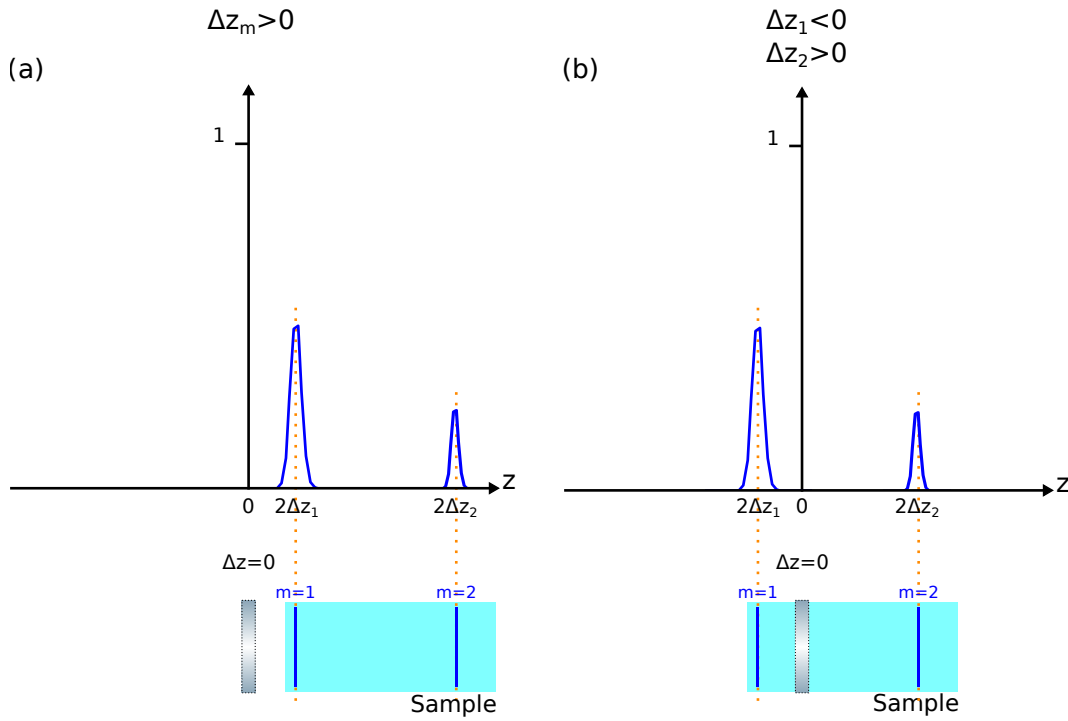


Figure 1.6: Depth profiles, as a function of the axial distance z , resulting in the Fourier transform of complex phase shifted spectral intensity where (a) the optical path difference between the reference mirror and each layer m positions are positive and when (b) the optical path difference between the reference mirror and the layer $m = 1$ is negative and is positive for the layer $m = 2$. The four-step algorithm has been applied in order to remove the non-interferometric (continuous and complex conjugate artifacts) and the cross-correlation within the sample terms.

1.4/ NOISE ANALYSIS AND SENSITIVITY OF OPTICAL COHERENCE TOMOGRAPHY

In optical coherence tomography, the “useful” signal to be detected is unavoidably modulated with noises. Those undesirable components arise from the light source, from the photo-detector and from the environment [35]. They have consequently to be taken into account from the design of the imaging system. In this section, a description of the noise sources in FD-OCT is presented. Both signal and noise terms are expressed as a function of the number of photo-electrons generated by the photo-detector. Usually, in FD-OCT configuration, the interferometric signal is recorded by a camera, in particular a line CCD camera. Assuming a line CCD camera with N pixels, by Fourier transform the spectral interferometric signal, in Eq. 1.13, the amplitude of the FD-OCT signal can be written as [35],

$$\langle \mathcal{S}_{FD-OCT} \rangle = \frac{\eta \tau}{h\nu_0} P_0 \sqrt{R_r R_m}, \quad (1.21)$$

where η and τ are the quantum efficiency and the exposure time of the photo-detector, respectively. h and ν_0 are the Planck constant and the central frequency of the spectrum, respectively. Assuming that the entire bandwidth of the light source is imaged onto the N pixels, the resolution of the photo-detector is given by $\delta k = \Delta k/N$. Thus, $P_0 = \sum_{n=1}^N S(k_n)\Delta k$ is the integrated optical power of the light source over Δk - i.e., over N pixels. R_r and R_m are the reference and the sample power reflectivities, respectively.

Uncorrelated noise contributions \mathcal{N}_{FD-OCT} are described as a summation of the squared standard deviation of each noise [57, 58]. The amount of generated noise per photo-detector pixel is conveniently expressed in terms of the number of noise-equivalent accumulated electrons. Three main types of noise can be defined where each of them gathering different noise sources.

First, the receiver noise \mathcal{N}_{rec} consists of several noises that are not proportional to the received signal - e.g., the thermal noise, which is due to the thermally generated electrons, and the read noise, which is partially due to both the charge conversion (analog to digital conversion) and the amplification processes. Reset noise can be assimilated to a read noise. The receiver noise can be approximated to a white noise [35] and stays constant along the acquisition time.

Secondly, the optical source is also responsible for noises, in particular, the photon shot noise \mathcal{N}_{shot} and of the excess noise \mathcal{N}_{exc} . The shot noise originates from the quantum nature of the incident light radiation and conveys the statistical variation in the arrival rate of photons incident onto the detector - i.e., the fluctuation of the number of photo-electrons during the exposure time. This obeys a Poisson distribution where its variance equals

$$\langle \mathcal{N}_{shot}^2 \rangle = \frac{\eta\tau}{h\nu_0} P_0 \left(R_r + \sum_{m=1}^M R_m \right) \quad (1.22)$$

In biological sample, such as in human skin, the power of the back-scattered beams from the sample arm is considered much lower than that of the reference arm ($R_m \ll R_r$). Thus, shot noise equation can be simplified as

$$\langle \mathcal{N}_{shot}^2 \rangle \approx \frac{\eta\tau}{h\nu_0} P_0 R_r \quad (1.23)$$

The excess noise originates from the fluctuations of the light source intensity along the time [58]. Also dependent of the optical power of the light source, it can be considered as a noise over the shot noise. It follows the Bose-Einstein distribution. Defined as a function of the polarization degree \mathcal{P} and the frequency bandwidth of the light source

$\Delta\nu$, the excess noise is given by

$$\langle \mathcal{N}_{exc}^2 \rangle = \frac{1 + \mathcal{P}^2}{2\Delta\nu} \left(\frac{\eta\tau}{h\nu_0} \right)^2 P_0^2 (R_m + R_r)^2 \approx \frac{1 + \mathcal{P}^2}{2\Delta\nu} \left[\frac{\eta\tau}{h\nu_0} P_0 R_r \right]^2 \quad (1.24)$$

Sometimes, the mechanical motions of the optical components of the OCT system are also included in the excess noise statistics [59].

It subsists another important noise source which is called Flicker noise or 1/f noise. In FD-OCT, due to the short integration time of the detector - i.e., less than 1 ms - used to record the full interferometric signal, this noise is usually neglected [46].

In FD-OCT, the noise, provided by each pixel of the spectrometer, contributes to the noise of one Fourier transform bin, in the spatial domain [46]. This mathematical transform improves the noise level of the bin by a factor \sqrt{N} which is the squared standard deviation of the pixel noise. Nevertheless, a N^{-1} normalization term has to be taken into account for the calculation of the global noise term due to the Fourier transform operation [60]. A schematic of the noise distribution is exposed in Fig. 1.7.

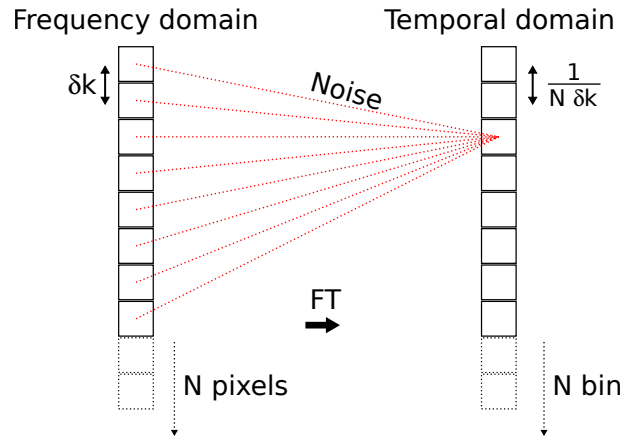


Figure 1.7: Scheme of the noise contribution onto the resulting A-scan in frequency domain optical coherence tomography. The noise of the A-scan results of the noise contribution from each pixel, in the Fourier plane (spectrometer). Consider N pixels spectrometer with a resolution of δk , this occurs to a spatial increment of $\frac{1}{N\delta k}$ in the spatial domain.

Usually, the measurement performance is achieved through the calculation of the ratio between both the signal \mathcal{S}_{FD-OCT}^2 and the combined noise \mathcal{N}_{FD-OCT}^2 powers. By defini-

tion, the signal to noise ratio (SNR) is expressed in decibel (dB).

$$\begin{aligned} SNR &= 10 \log \left(\frac{\langle \mathcal{S}_{FD-OCT}^2 \rangle}{\left(\frac{\sqrt{N}}{N} \right)^2 \langle \mathcal{N}_{FD-OCT}^2 \rangle} \right) \\ &= 10 \log \left(\frac{\left(\frac{\eta\tau}{h\nu_0} \right)^2 P_0^2 R_r R_m}{\frac{1}{N} \left(\mathcal{N}_{rec}^2 + \frac{\eta\tau}{h\nu_0} P_0 R_r + \frac{1+\mathcal{S}^2}{2\Delta\nu} \left[\frac{\eta\tau}{h\nu_0} P_0 R_r \right]^2 \right)} \right) \end{aligned} \quad (1.25)$$

Shot noise limited detection is only achieved if the shot noise dominates the receiver noise and if the excess noise remains negligible [35]. Figure 1.8 shows a scheme of the noise power as a function of the irradiance onto the photo-detector. As it can be seen, for low irradiance powers, the constant receiver noise is predominant. Then, by increasing the irradiance, the shot noise level increases and, further, the relative intensity noise occurs. Occasionally, in the literature, the term relative intensity noise is employed to describe the summation of the shot noise, the thermal noise and the excess photon noise [61].

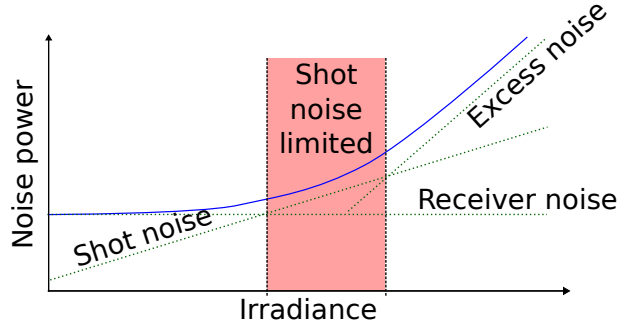


Figure 1.8: Noise levels as a function of the irradiance onto the photo-detector. The solid blue color line represents the entire noise power and the green dotted line the different noise sources. The red color area define the shot noise limited detection range.

Thus, assuming a shot noise limited detection, the SNR expression can be simplified.

$$SNR = 10 \log \left(N \frac{\eta\tau}{h\nu_0} P_0 R_m \right) \quad (1.26)$$

In TD-OCT, considering N axial displacements of the reference mirror, the interferometric signal \mathcal{S}_{TD-OCT} is similar to \mathcal{S}_{FD-OCT} . However, the noise term \mathcal{N}_{TD-OCT} differs. The factor $\frac{\sqrt{N}}{N}$ disappears [46, 61, 62, 63] yielding to a lower SNR than in FD-OCT - e.g., for $N=100$, SNR_{FD-OCT} is 20 dB higher than SNR_{TD-OCT} .

$$SNR_{FD-OCT} = 10 \log(N) + SNR_{TD-OCT} \quad (1.27)$$

Nevertheless, in FD-OCT, other types of artifacts, such as the chromatic dispersion and

the non-resampling of the signal before applying the Fourier transform [64], occur and may decrease the signal to noise ratio.

The sensitivity of the OCT system can be deduced from the SNR. The sensitivity is the minimum reflectivity of the sample $R_{m,min}$ that can be detected by the photo-detector - i.e., when the signal power equals the noise level. This leads to a SNR equals to unity or 0 dB. In the human skin, the sensitivity provides the maximal imaging depth or the minimum refractive index contrast that can be detected. In case of a shot noise-limited OCT system, the minimum sample reflectivity equals

$$R_{m,min} = N \frac{h\nu_0}{\eta\tau P_0} \quad (1.28)$$

As it can be seen, the minimum detectable reflectivity is inversely proportional to the optical power of the light source and the exposure time of the photo-detector. To be noted, in *in-vivo* medical imaging, a SNR of at least 80 dB is required [65]. Hence, with such SNR value, an OCT system could detect a surface that back-reflects at least 1.10^{-8} of the incident light.

1.5/ PERFORMANCES OF OPTICAL COHERENCE TOMOGRAPHY

The performances of optical coherence tomography are both related to the light source and to the characteristics of optical components which compose the optical setup. Both axial and lateral resolutions as well as the imaging depth of the OCT system are linked to the wavelength range and the numerical aperture of the microscope objective. Indeed, the use of microscope objectives is required in order to improve the lateral resolution of an OCT system.

Listed in Annex 4.5, many criteria exist in order to define the lateral resolution of an optical imaging system [66]. In this manuscript, the Abbe resolution criterion - i.e., the cut-off frequency of the modulation transfer function (for a spatially incoherent light source) or of the amplitude transfer function (for a spatially coherent light source) - has been chosen in order to describe the lateral, or transverse, resolution of OCT systems [67]. The notion of spatial coherence can be assimilated as the phase difference between two fields along their propagation. Assuming two point-light sources, if their phase difference is constant along the propagation, the two points are spatially coherent and can interfere among themselves. The lateral resolution $\delta_{x,y}$ of an imaging system can be

computed from the following equations:

$$\delta_{x,y} = 0.5 \frac{\lambda_0}{NA}, \quad \text{Spatially coherent detection} \quad (1.29)$$

when the light source is coherent, and from the following equation:

$$\delta_{x,y} = \frac{\lambda_0}{NA}, \quad \text{Spatially incoherent detection} \quad (1.30)$$

when the light source is incoherent. Only a constant term differs from both equations. NA is the numerical aperture of the microscope objective and is defined by $NA = n \sin(\theta)$, with n , the refractive index of the medium and θ , the half-angle of the cone of light that can enter or exit the lens. The use of higher numerical aperture microscope objective - i.e., microscope objective able to resolve sub-cellular features - leads to a variant of conventional OCT, the so-called optical coherence microscopy [35, 68]. This technique achieves *en-face* images - i.e., transverse to the optical axis images - with high lateral resolution through the coherence gated detection.

In standard confocal microscopy, both lateral and axial resolutions are related to the wavelength and the NA of the microscope objective. For example, a microscope objective with $NA=0.36$ is required to obtain an axial resolution of $6.4 \mu\text{m}$, as illustrated in Fig. 1.9 (a).

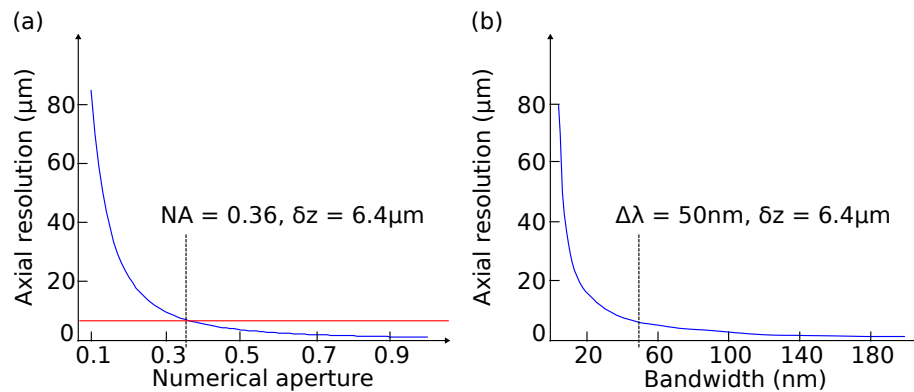


Figure 1.9: Axial resolution of (a) a conventional optical microscope, depending on the numerical aperture of the microscope objective, and (b) an optical coherence tomography system, defined by the spectral characteristics of the light source. In both cases, the central wavelength of the light source equals 850 nm .

While, in OCT, axial and lateral resolutions are decoupled from one another since the axial resolution depends on the coherence length l_c - i.e., the central wavelength λ_0 and the bandwidth $\Delta\lambda$ of the light source [69]. Assuming a limited temporal coherence gate,

the axial resolution δz of an OCT system is given by

$$\delta z = \frac{l_c}{2n} = \frac{2 \ln 2}{n\pi} \frac{\lambda_0^2}{\Delta\lambda} \quad (1.31)$$

In air, the axial resolution equals half of the coherence length of the light source. Then, the higher is the bandwidth of the light, the better is the resulting axial resolution. For example, if the bandwidth and the central wavelength equal 50 nm and 850 nm, respectively, the axial resolution in air is 6.4 μm as shown Fig. 1.9 (b). A sub-micrometer axial resolution has been achieved by using a broadband femto-second pulsed laser ($\Delta\lambda \approx 400 \text{ nm}$) [70]. The use of broadband light source requires large bandwidth achromatic optical components and dispersion compensation elements in order to compensate the chromatic dispersion and thus to avoid a widening of the interference signal peak. The axial resolution can also be increased by matching the refractive indexes of both the microscope objective's working medium n and the sample.

An important limitation of the imaging depth of an OCT system is the attenuation of the beam by tissue diffusion. In biological tissue imaging, the imaging depth depends on the ability to penetrate deeply in the diffusing and absorbing medium. In this case, the spectral wavelength range is crucial to avoid a strong absorption [71]. The imaging depth can reach 2 mm in human tissues for wavelength centered on $\lambda_0 = 1.3 \mu\text{m}$ [72] although resolutions are better for smaller wavelengths. The depth of field of the system is also related to geometrical and spectral parameters. In paraxial approximation, the imaging depth FOV_z of an imaging system is inversely proportional to the square of the numerical aperture [73].

$$FOV_z = \frac{1.77 n \lambda_0}{NA^2} \quad (1.32)$$

Outside this depth of field, the transverse resolution decreases drastically thereby limiting the axial measurement range. Thus, a trade-off between the transverse resolution and the axial measurement range occurs through the NA of the microscope objective. To note that, in case of single-point illumination, the axial imaging depth can be assimilated to the Rayleigh length [74]. It corresponds to the range over which the focused beam radius, or the beam waist, is not increased over a factor of $\sqrt{2}$.

In FD-OCT, the axial imaging depth is also limited by the wavenumber sampling - i.e., the detector resolution - or the linewidth of the narrow swept wavelengths [75]. Indeed, the temporal coherence function of each narrow-band wavelength $\delta\lambda$ has to maintain a good visibility along the imaging depth. The smaller is $\delta\lambda$, the higher is the

imaging depth. Assuming a Gaussian form of the spectrum, the maximum imaging depth of an FD-OCT system is limited by the spectral resolution.

$$FOV_{spectral} = \frac{4 \ln 2}{\pi} \frac{\lambda_0^2}{\delta \lambda} = \frac{N}{2} l_c \quad (1.33)$$

$\delta \lambda$ is the linewidth of an individual spectral channel of the swept light source and N is the number of evenly spaced wavenumbers [65]. This assumes that $N \delta \lambda = \Delta \lambda$.

Figure 1.10 summarizes the performances of a single-point OCT system. Both lateral and axial resolutions are shown. As it can be seen, the linewidth $\delta \lambda$ of the swept light source limits the axial FOV. This means that the imaging depth is independent of the numerical aperture of the objective lens. The lateral FOV was not considered, but in scanning single point devices, in order to obtain a three dimensional image of the sample, the beam has to be tilted of an angle θ . This task may be achieved using galvanometric mirrors which provide a lateral $FOV_{x,y}$ depending onto the focal length f of the lens and the angle scanning θ .

$$FOV_{x,y} = 2f\theta \quad (1.34)$$

This configuration is called the f-theta scanning system.

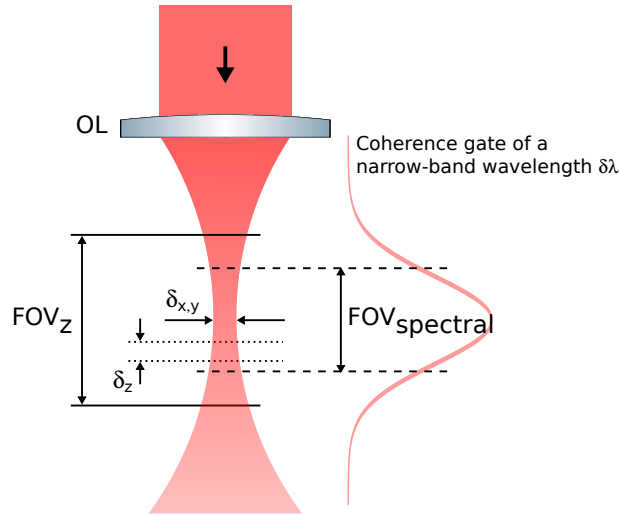


Figure 1.10: Scheme of a single point frequency domain optical coherence tomography system. This configuration assumes a cylindrical symmetry of optical component and a single point illumination. The sample beam is focused by an objective lens OL which leads to a lateral resolution $\delta_{x,y}$. The axial resolution δ_z depends on the bandwidth of the light source.

Nevertheless, the quality of the focused beam is often decreased because of the optical scattering into the sample and of the chromatic dispersion. For OCT systems, this yields

to a loss of the lateral resolution. However, recent works have shown that resolution or the imaging depth limitations, and further optical aberrations, can be overcome by using the principle of adaptive optics - e.g., continuous tracking of the focal [76], the complex wavefront shaping [77] or digital correction during data processing [78].

1.6/ TOWARDS FULL FIELD SWEEPED SOURCE OPTICAL COHERENCE TOMOGRAPHY

In SS-OCT, the spectral interferometric signal is time-encoded - i.e., is recorded sequentially along the time. A sweeping wavelength laser source along with a single point photo-detector are used for this task. Then, a Fourier transform of the spectral interferometric signal (A-line) is calculated in order to retrieve a depth profile (A-scan). To provide a two dimensional (B-scan) or a three dimensional image of the sample, the object beam has to be laterally scanned. However, despite a higher SNR than TD-OCT, this technique brings some drawbacks - e.g., the need of high sweeping rate (leading to fast synchronization between electronic components), the compromise between the lateral FOV and resolutions, the limitation of the lateral FOV due to the scanning procedure and the mechanical jitter [79, 80] (leading to a lateral non-uniformity of the image).

The advances of high-speed light sources and ultrahigh-speed two dimensional photo-detectors (CMOS or CCD camera) have led researchers to investigate the full-field OCT configuration in time domain [81, 82] and in frequency domain [83]. In SD-OCT, the use of a two-dimensional camera - i.e., a highly parallel spectrometers - limits the reconstruction of one B-scan of the sample [84]. Since the advent of the SS-OCT technique, a parallel acquisition of the components of the multiple spectral interferometric signal has been considered using a camera [79]. Indeed, full-field swept-source optical coherence tomography (FF-SS-OCT) is a spatially and temporally multiplexed acquisition technique and can thus avoid the requirement of scanning mechanism. The FF-SS-OCT configuration has been introduced by Drexler *et al.* [79]. In 2010, Bonin *et al.* have reported a FF-SS-OCT system equipped with a high speed CMOS camera for ophthalmology application [85]. They have demonstrated an acquisition rate of 1.5 million A-scan per second with 72 dB of sensitivity by multiplexing 640×24 pixels (frame rate of 100,000 fps) and sweeping 512 lines along 50 nm spectral bandwidth of the light source.

The standard FF-SS-OCT setup consists of a broadband light source illuminating a Linnik interferometer shown in Fig. 1.11.

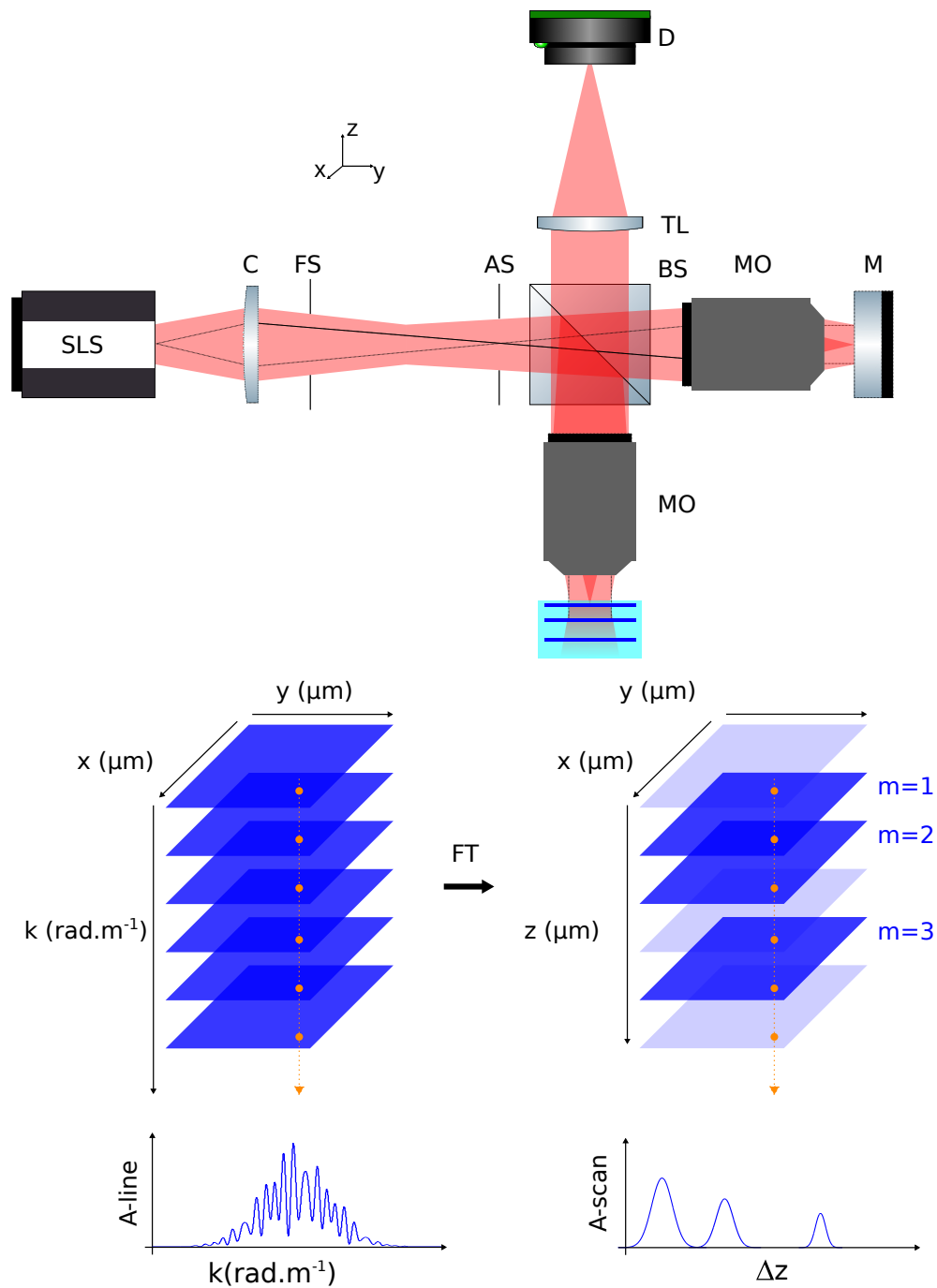


Figure 1.11: Principle of the full-field swept-source optical coherence tomography. The Köhler illumination arrangement consists of the field and the aperture stops FS and AS, the collector lens C and microscope objectives MO. Each component of the A-line is sequentially recorded by the two dimensional detector D through the tube lens TL. Then, a Fourier transform of parallel A-line signals is applied in order to get a three-dimensional image of the sample.

By placing a microscope objective MO in each arm, it allows compensating the dispersion and furthermore, improving the lateral resolution. This configuration is quite similar to

the traditional SS-OCT configuration. However, in FF-SS-OCT, the swept source light source is spatially incoherent in order to make parallel the line field OCT detection and to reduce the cross-talk [86]. The beam emerging from the spatially incoherent swept light source passes through a Köhler illumination system and is directed, by the beam-splitter cube BS, into the reference and into the sample arms. The Köhler arrangement, classically used in standard microscopy, provides an uniform illumination of the sample [86, 87]. The beams back-reflected by the sample and the reference mirror are collected by the MO's. A spatial coherence occurs between two points from the reference and the sample beams, at a given lateral and axial positions. Then, the BS combines the two beams and the tube lens TL images sequentially the two dimensional spectral irradiance onto the camera.

For *in-vivo* imaging of human skin, a swept source with at least 1100 nm of central wavelength, is usually chosen because a higher depth penetration and a reduced multi-scattering occur at these wavelengths [71, 88]. However, the silicon-based cameras cannot transform such radiations into an electric current because of vanishing quantum efficiency. Because of their better sensitivity, indium gallium arsenide (InGaAs) area detectors could be a solution in infrared. Nevertheless, in addition to their high cost, they offer much lower frame rates than Si cameras. In real-time *in-vivo* medical imaging, this relative slowness could lead to a blurred image due to the motion of the sample. Instead, in this work, the central wavelength of the swept light source has been chosen at 840 nm. Despite a higher tissue diffusion, around 800 nm wavelength, the image contrast appears higher because of better lateral and axial resolutions [88].

In our project, the illumination system is quite similar to the one exposed in Fig. 1.11. Indeed, a broadband light source - i.e., a superluminescent diode - is wavelength-swept and is then made spatially incoherent. However, the imaging part differs. Instead of using a Linnick architecture, the interferometric architecture consists of a vertical interferometric microscope objective, the so-called Mirau microscope objective. In this architecture, the reference mirror is located within the interferometric objective by a vertical alignment with beam-splitter and lens [89]. This allows reducing the size of microscope objective so that several interferometers can be located next to each other. By doing so, sixteen interferometers - i.e., an array of 4×4 interferometers - are combined. This achieves a large lateral field of view of $8 \text{ mm} \times 8 \text{ mm}$. As for the recording detector, a high speed CMOS camera is employed. The chapter 2 presents the design of the OCT micro-system.

SPECIFICATIONS AND OPTICAL DESIGN OF THE OPTICAL COHERENCE TOMOGRAPHY MICRO-SYSTEM

Existing optical coherence tomography (OCT) devices are strongly dominated by fiber optics interferometers which are combined often with massive scanners and bulk optical components. Through the fabrication techniques, these building blocks appear expensive and, thus, are only accessible by Hospitals. Indeed, the cost of such systems is about 100,000 euros. Here is proposed an alternative to conventional manufacturing technologies by using micro-opto-electro-mechanical systems (MOEMS) technologies. The unit price of the OCT micro-system should be much lower thanks to the low-cost hardware solution, while miniaturizing the size of the components. By maintaining similar performances to standard systems, MOEMS components offers a particular potential for the feature of imaging systems. Indeed, various applications of MOEMS exist in everyday life and in the world of research, with development of light sources - e.g. vertical-cavity surface-emitting lasers -, microscopes and telecoms devices [90]. Indeed, exploiting the advantages of micro-systems and the progress in optical technologies, the development of novel miniaturized imaging devices appears such as confocal microscopes [91, 92], digital holographic microscopes [93], interferometric microscopes [94] and fluorescence microscopes [95]. Recently, the miniaturization of medical imaging devices has shown a great interest and potential for patients and doctors. MOEMS-based systems response to the commercial need of the miniaturized and cheap optical imaging devices - i.e., hand-held, low-cost and low-energy consumption [96] - such as photo-acoustic microscopes [97]. MOEMS technology has been implanted in optical coherence tomography (OCT) technique, in order to integrate and miniaturize the systems [98, 99, 100], to make OCT-fiber-based endoscopes [101], to improve the scanning speed [80, 102] or to enhance the imaging depth and the resolution [103]. Even

in the current life, combination of OCT and MOEMS can be found for self-diagnosis [104].

Particularly true when a new MOEMS-based imaging system is heading for the development, the optical design is an important task to insure its good performances while taking into account the constraints of the manufacturing [105, 106]. Indeed, the design of the optical system is adapted to consider, on the one hand, the tolerances of the fabrication processes - e.g., fabrication of micro-elements or multi-wafer bonding - and, on the other hand, the imaging quality required - e.g., the resolutions or the imaging depth.

Here, the design is based on medical specifications. Indeed, the micro-system aims to provide a three dimensional image of the skin in order to analyze epithelial tumors. Cutaneous cancers emerge from the skin surface and, then, cancerous cells proliferate in depth within the epidermis. During the first and the second stage, the global size of suspect toxic molds does not exceed 1 mm of depth. Also, its lateral size is similar to a benign mole. Thus, according to the dermatologists, the axial field of view (FOV) of the system has to provide an imaging depth until at least the dermo-epidermal junction - i.e., between 100 μm and 500 μm of epidermis height on average and at the fingertips, respectively [107]. In addition, the lateral FOV should be of $8 \times 8 \text{ mm}^2$. Moreover, the device aims at visualizing cells whose normal size varies from 10 μm to 50 μm [108]. Thus, a cellular resolution is needed (5 μm of voxel size). Following table summarizes the requirements of the research project.

Requirements	Targeted values
Volume of view	$8 \times 8 \text{ mm}^2 \times 500 \mu\text{m}$
Resolutions	5-10 μm

The resulting architecture of the micro-system is the optimal compromise of three conditions which are the micro-machining, the optical performances and the cost of the device [109]. MOEMS components are actually adapted since they can provide high resolution at a limited working distance. However, a large lateral FOV is required and constrains to employ a matrix arrangement. This chapter shows the design of the micro-system. It is demonstrated that the proposed approach is a key enabling technology for low cost fabrication of a new generation of OCT micro-systems. The imaging system architecture is detailed through its illumination and its imaging part. Also, the sinusoidal phase shifting technique, used for removing the artifacts of the frequency domain optical coherence tomography system, is exposed in terms of both hardware and algorithm.

Then, the optical power losses and the sensitivity of the micro-system are estimated. Finally, the fabrication processes of MOEMS components are presented according to the medical specifications. For the simulation and the analyses, the ray tracing software Zemax (Zemax LLC) and MacroSim (Technische Optik, University of Stuttgart) were used.

Institut für Technische Optik of the University of Stuttgart and FEMTO-ST institute were in charge of the design of the FF-SS-OCT micro-system. By responding to the expectations of the project and by considering the manufacture of the elements of the micro-system, they worked in collaboration with VTT Technical Research Centre for the development of the light source, with Centre Suisse d'Electronique et de Microtechnique for the development of high-frame-rate camera and with Stacice for the building of the lateral and axial stitching device as well as the packaging. Furthermore, FEMTO-ST was in charge of the fabrication of micro-optical components with Fraunhofer Institute für Elektronische Nanosysteme. Finally, the software for the control and for the data processing as well as the algorithm for the phase shifting, were developed by FEMTO-ST. In this part, I contributed to the optimization of the design - i.e., the illumination part, the array of microlenses, the optical head stitching - and also, I developed the sinPSI algorithm according to the specifications.

2.1/ ARCHITECTURE OF THE MICRO-IMAGING SYSTEM

In this section, the architecture of the full field time-encoded frequency domain OCT micro-system to achieve a three dimensional image of the sub-surface of the skin, is reported. Indeed, full field swept source optical coherence tomography (FF-SS-OCT) appears as a good compromise between fast acquisition to perform a *real-time* large FOV visualization of the pathology and the MOEMS-based assembly. The architecture can be divided in two main blocks:

- The illumination part and
- The imaging part

The numerical aperture of the microlens, the total track length to achieve a compact micro-system, the optical imaging properties and the requirement on the maximal acquisition time define the merit function for the microlens's FOV, the lens pitch, the lens size, the focal length and the number of lateral head stitching.

The concept of the proposed FF-SS-OCT setup is schemed in Fig. 2.1. The illumi-

nation system consists of a super-luminescent diode SLD generating a broad spectrum which is subsequently filtered by a Fabry Perot interferometer FPI. A multimode optical fiber MF and a collimator lens C provide an uniform illumination onto the beam-splitter cube BSC directing the beam toward the array of interferometric microscope objectives IMO. Each interferometer is made of a 4×4 array of doublets of microlenses DML and of reference mirrors M, as well as a beam-splitter layer BS. An array of Mirau interferometers is considered for the vertical space-saving and the large lateral FOV required. This is the key element of the system allowing parallel imaging. Furthermore, the reference mirrors are actuated to implement the phase shifting technique, suppressing the mirror term due to the Fourier transform operation and hence increasing the measurement range by a factor of two. Afterwards, each FOV of Mirau interferometers is acquired by a two dimensional detector D through an array of tube lenses TL.

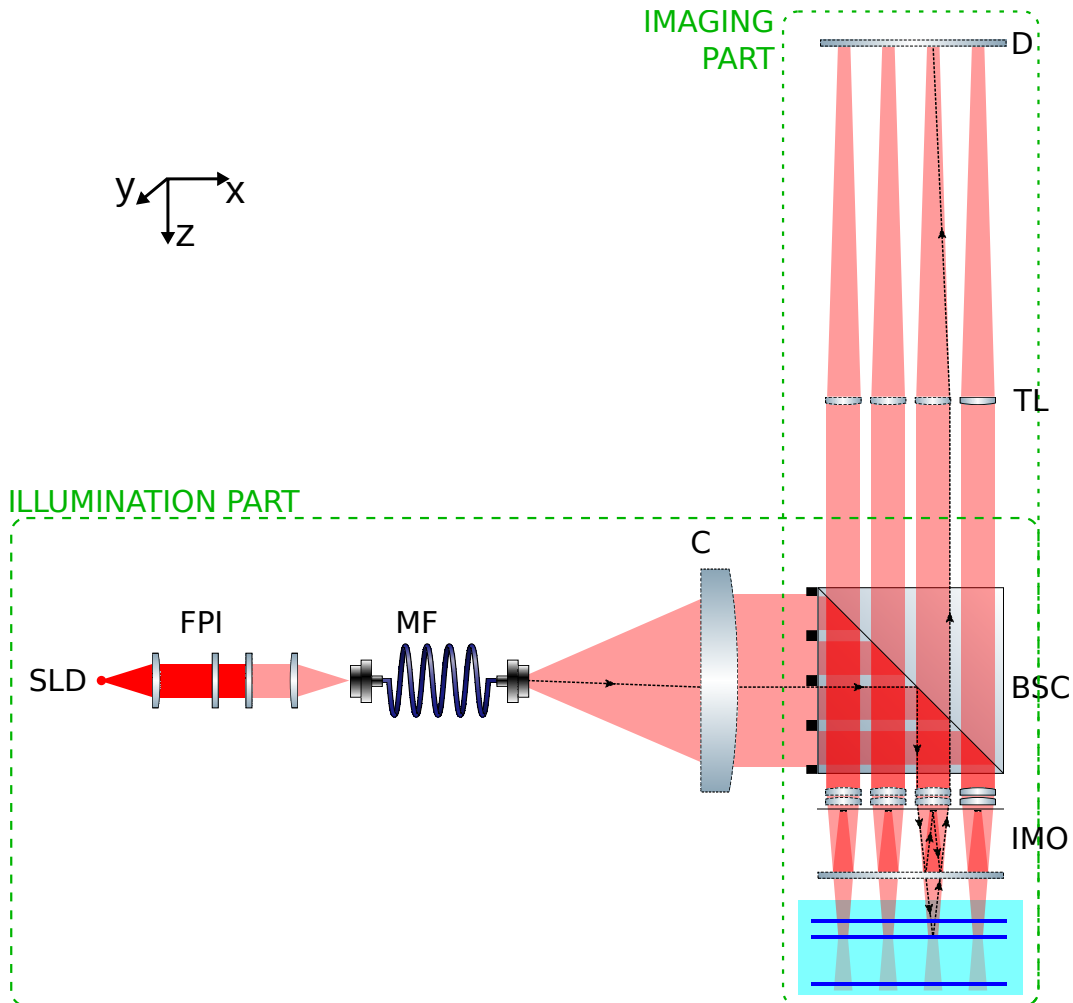


Figure 2.1: Architecture of the full field swept source optical coherence tomography micro-system.

The two dimensional concept allows recording the spectral interferograms from each in-

ferrometric channel. By implementing a signal processing based on a Fourier transform operation, the depth profile of the sample is retrieved from the frequencies of the spectral signal.

2.1.1/ MIRAU INTERFEROMETERS

Commercially available IMO's use basically three types of configuration - i.e., Michelson, Linnik and Mirau - which are schemed in Fig. 2.2 [110]. Common configuration for

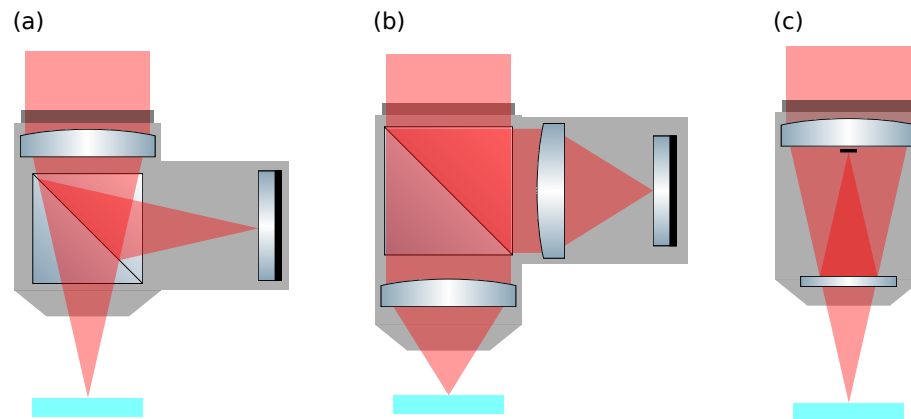


Figure 2.2: Schematics of interferometric objectives: (a) Michelson, (b) Linnik and (c) Mirau.

interferometry - i.e., Michelson interferometric objective - consists of a lens which is located prior to a beam-splitter cube. This configuration is suitable for small magnifications. Indeed, the working distance is limited by the finite size of the beam-splitter cube. Thus, Michelson IMO is only used for low numerical aperture microscope objective, typically 0.1. Linnik double objective configuration is an enhancement of the Michelson configuration. Both of the arms are composed of objective lenses. This allows improving the numerical aperture and, hence, the lateral resolution. However, the adjustment of this type of interferometric objective is not trivial. The two objective lenses have to perform a minimum-aberrated wavefront and high fringe contrast [111]. Finally, Mirau configuration is a coaxial optical configuration. It is characterized by a vertical architecture where the reference and the object arms are vertically aligned. The reference mirror is then placed in the center of the objective lens whereas the beam splitter is planar.

Here, Mirau architecture, which is the highest possible compactness configuration [111], has been retained to collect the two-dimensional spectral interferometric signal. Indeed, since the reference arm is coaxial with the incident illumination beam, the interferometer footprint is limited by the size of the objective lens. This gives the advantage to make a full-field array of IMO and, hence, improving the lateral field of view as

requested. Furthermore, from a MOEMS technology point of view, this architecture allows a vertical integration of different wafers - i.e., optical and mechanical wafers - carrying the different micro-optical components all arranged along the wafer surface. This can perform a high precision and a packaging using the approach of multi-wafer bonding [112].

The aim of the interferometer is to provide an isotropic cellular resolution. In OCT, the lateral resolution is linked to the axial one by the central wavelength of the light source. In this work, the central wavelength λ_0 has been fixed to 840 nm in order to use a standard silicon-based chip for the camera and to perform a high contrast image of the early skin pathology. According to the Abbe-based criterion, defined in Eq. 1.30, the numerical aperture (NA) of the DML equals 0.13, yielding to $6.2 \mu\text{m}$ of lateral resolution. By knowing the NA of the lens, the geometrical axial FOV can be retrieved. According to Eq. 1.32, it equals $114 \mu\text{m}$ (with $n = 1.3$).

One important requirement is to image all FOV points without changing the resolution. Assuming a single microlens where its geometric conditions - i.e., effective focal length and diameter - are equivalent to the ones of a DML, the latter produces higher optical performances in terms of resolutions and wavefront quality. Furthermore, due to the large FOV, off-axis points has to be considered in the analysis. The effect has been shown by implementing a Zemax simulation of the imaging system where the IMO consists of (a) a single lens and (a) a doublet. The results are exposed in Fig. 2.3.

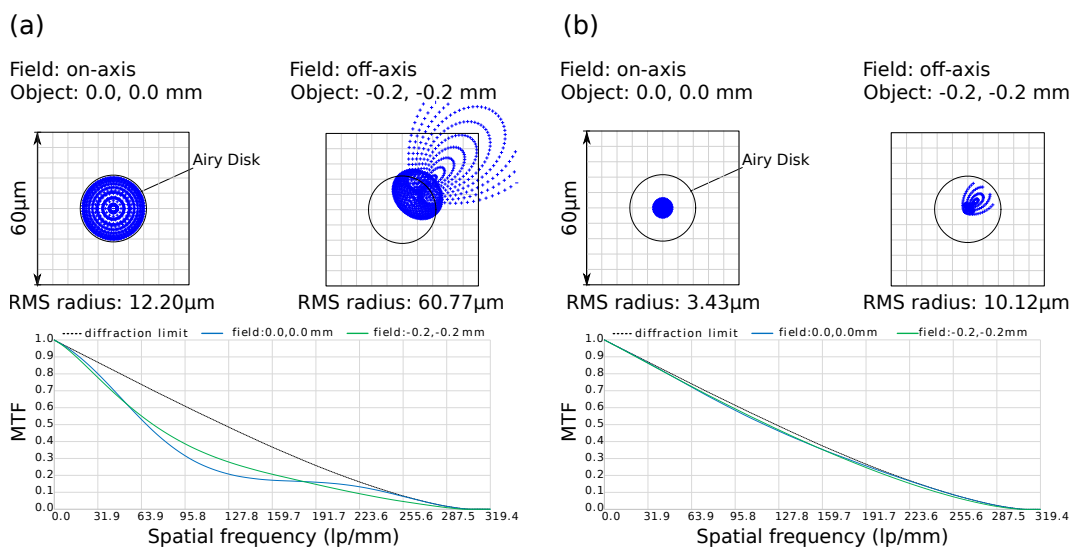


Figure 2.3: Zemax analyses of (a) a single microlens and (b) the doublet of microlenses. The spot diagram and the MTF of two object points - i.e., in the center and at the edge of the FOV - are represented. J. Krauter, ITO.

As it can be seen, the on-axis rays from the single lens are located within the Airy spot diameter, where the geometric radius equals $12.2 \mu\text{m}$. However, it is not the case for off-axis rays where the spot shape is no longer circular and the radius much higher. The modulation transfer function (MTF) shows in addition rather low contrasts. For instance, the MTF contrast for an object structure of $6 \mu\text{m}$ is 0.16 and 0.13 for the on-axis and off-axis field points, respectively. Secondly, a DML made of two identical plano-convex lenses with twice less refractive power than the previous lens is considered. The DML increases clearly the optical performance since the geometric spot radius for the off-axis field point is reduced from $60 \mu\text{m}$ to $10 \mu\text{m}$ and since the MTF shows a nearly diffraction-limited curve for the whole FOV. The contrast for an object structure of $5 \mu\text{m}$ was increased from 0.13 to 0.22. Furthermore, it allows reducing the refraction power of each lens, leading to less optical aberrations, in particular spherical aberrations [96, 105]. The RMS wavefront error generated by the doublet is only around $\lambda/5$ whereas it is 1λ for the equivalent single lens. An experimental characterization of the two configurations have been performed and the comparison of the results is reported in Sec. 3.2. The experimental values of the RMS wavefront error from the single and the doublet are 1.6λ and 0.7λ , respectively [113]. Consequently, assembling two lenses with less refractive power instead of a single lens reduces significantly the generated aberrations so that such system can lead to a homogeneous imaging performance for the whole FOV. Furthermore, the reduction of the refraction power reduces the requirements on the positioning [112]. Two stacked wafers of plano-convex objective lens arrays have been chosen to make the array of DML and were designed with equal dimensions - i.e., the thickness, the radius of curvature and the diameter - in order to have less variety for the manufacturing process.

The specifications require a large lateral FOV which can only be achieved using a high diameter IMO or an array of IMO. For a space saving, the optical head consists of an array of 4×4 Mirau micro-interferometers as exposed in Fig. 2.4. Each IMO consists of a doublet of microlenses DML, a reference mirror vertically actuated, for the modulation phase shifting (see Sec. 2.2), and a planar beam-splitter.

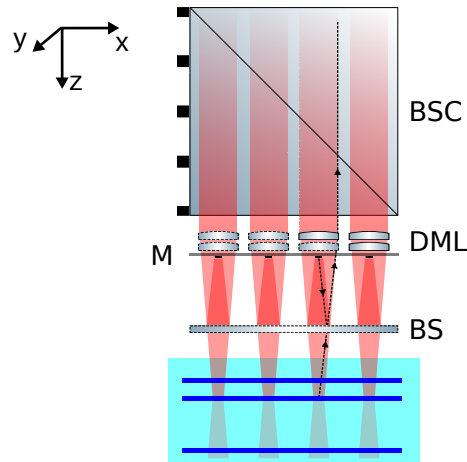


Figure 2.4: Schematic of the array of Mirau micro-interferometers

For the moment, only the NA of the DML has been estimated, leading to the lateral resolution and axial FOV which are two parameters dependent of the geometry of the lens. Others parameters, relying on the camera specifications and the illumination part, are determined in following sections.

Technical specifications	Targeted values
Interferometric architecture	Mirau
Number of interferometric channels	4×4
Numerical aperture of the IMO	0.13
Lateral resolution	$6.2 \mu\text{m}$
Vertical field of view of the IMO	$88 \mu\text{m}$ (in air)

Table 2.1: Interferometric microscope objective technical specifications.

2.1.2/ IMAGING PART

After being collected by a micro-interferometer, the two-dimensional spectral component is recorded onto a camera through a tube lens. The arrangement of the tube lenses is similar to the IMO - i.e., a 4×4 array of tube lenses and each tube lens is vertically aligned with an IMO. Figure 2.5 shows the layout of the imaging system through only one channel. The fabrication of the sensor chip of the camera brings constraints of the design in terms of pixel size and combination between both the frame rate and the number of pixels used to record the interferometric signal. According to the manufacturer of the

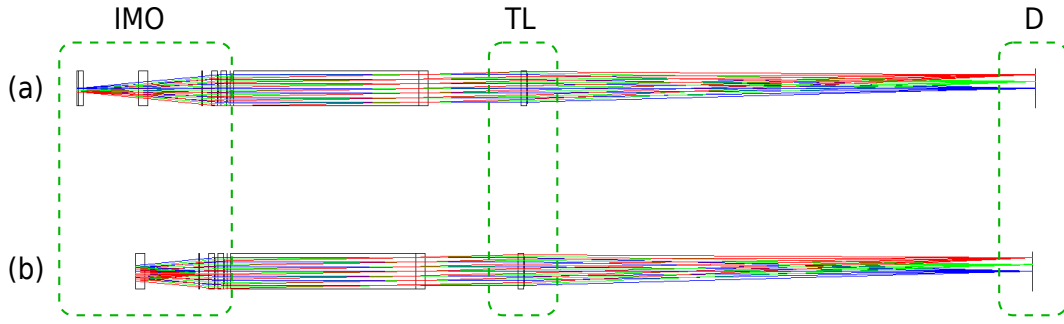


Figure 2.5: Layout of the imaging system which consists of the interferometric microscope objective IMO, the tube lens TL and the camera D, with the (a) object ray path and (b) the reference ray path. J. Krauter, ITO.

camera (CSEM), the pixel size is $12 \mu\text{m}$. According to Nyquist sampling criterion where the smallest intensity peak has to be sampled by minimum two pixels, the lateral resolution size in the image plane - i.e., onto the camera - should be $24 \mu\text{m}$. This criterion limits the magnification of the imaging system.

$$\gamma = \frac{2\Delta x}{\delta_{x,y}} = \frac{24}{6.2} = 3.9 \quad (2.1)$$

The maximum frame rate of the camera is limited by the number of pixels, which have to be transferred simultaneously. According to the manufacturer, the maximum pixel count for one channel of the 4×4 channels is 128×128 - i.e., 242,064 pixels totally - at a frame rate of 4000 fps, which is the maximum realizable frame rate for the current specifications. The size of the FOV in the image plane results in $1540 \mu\text{m} \times 1540 \mu\text{m}$. Then, the pixel size Δx and the magnification γ define the lateral FOV of the system.

$$FOV_{x,y} = \frac{N \Delta x}{\gamma} = \frac{128 \times 12}{3.9} = 400 \mu\text{m} \quad (2.2)$$

Thus, for a parallel acquisition, each frame consists of 4×4 regions of interest (ROI) having 128×128 pixels each. Also, the lateral FOV determines the size of the reference mirror which has to be similar.

The design of the imaging system aims at the visualization of $8 \times 8 \text{ mm}^2$ lateral FOV. Thus, a compromise between the constraints of micro-fabrication of the microlenses - e.g., the sagittal distance -, the working distance and the diameter of the lens has been taken into account. Indeed, the numerical aperture being chosen, a large diameter leads to a small focal length and, reciprocally, a small diameter leads to a large focal length. Here, the diameter of the lens has been defined to 1.9 mm and the channel pitch is 2 mm. According to the following relation, the geometrical parameters of the DML depend on

the NA.

$$NA = n \sin(\alpha) = n \sin \left[\arctan \left(\frac{D}{2f'} \right) \right], \quad (2.3)$$

where n and α are the refractive index of the medium in which the IOL is placed (in air, $n=1$) and the half-angle of the maximum cone of light that can enter the IOL, respectively. The angle α is expressed as a function of both the diameter D and the focal length f' of the doublet. The focal length of the DML results in 7.5 mm.

The detector is placed in the image focal plane of tube lenses which are placed in an afocal system configuration with the DML. The magnification can also be expressed as a function of the ratio of the focal lengths of the tube lens f'_{TL} and the DML f'_{DML} and described by the relation

$$\gamma = \frac{f'_{TL}}{f'_{DML}} \quad (2.4)$$

Thus, the focal length of the tube lenses equals 28 mm.

Because the micro-system has an array-type configuration, the cross-talk between the respective channels has to be taken into account in the design. The cross-talk can be defined as the rays contributing to the wrong channel on the camera. Although not represented onto Fig. 2.1, a volume stop is placed between the tube lenses and the chip of the CMOS camera in order to avoid this effect and also to reduce the photon-noise. The impact of the volume stop is exposed in Fig. 2.6. These simulations were made with the ray-tracing software ASAP from Breault Research Organization.

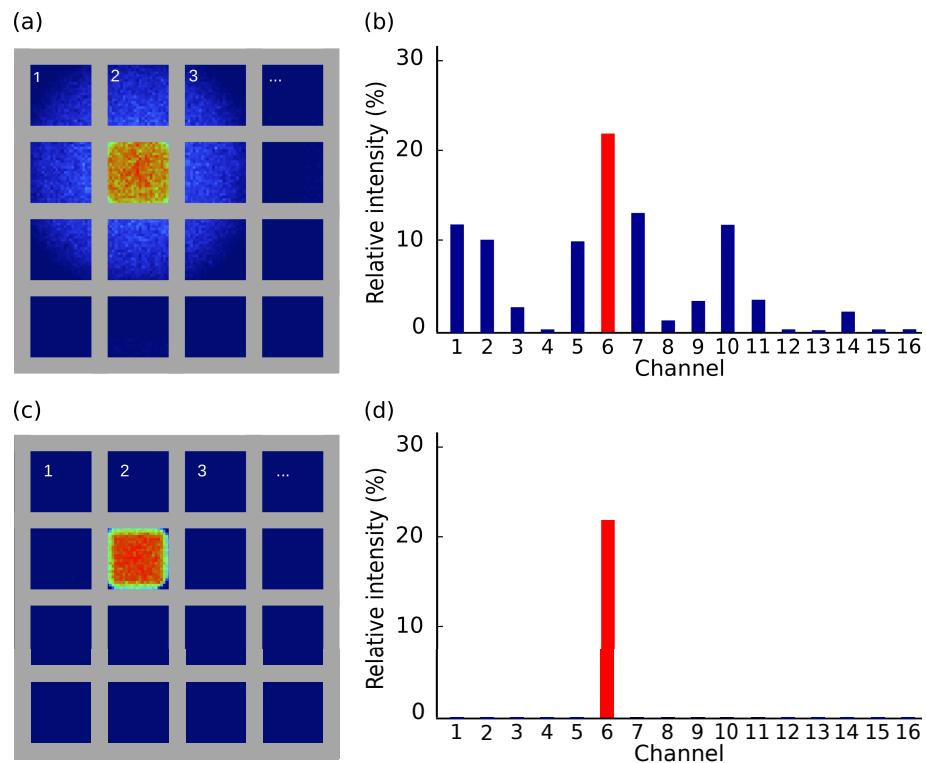


Figure 2.6: Impact of the cross-talk distribution between each channel. When (a) a circled illumination is employed, (b) the resulting relative intensity shows this effect onto the channels neighbourhood. Whereas, by placing a volume stop array, only (c) one channel is illuminated and (d) the neighbouring channels do not collect intensity. In both cases, the channel 6 of the array is illuminated. J. Krauter, ITO.

Because of the high frame rate of the camera, the two dimensional irradiance distribution is read out as a function of both the swept wavelength and the shifted phase, and then directly recorded into the camera-internal memory. The bandwidth of the internal memory - i.e., bus from sensor to memory including field-programmable gate array (FPGA) - is 1500 MPix/s. Whereas the one of the CameraLinkTM interface - i.e., bus between camera and computer via frame grabber - is 320 MPix/s. Hence, this makes possible to increase the frame rate of the camera. When the data acquisition to the camera memory is stopped, the camera memory can be read out to the frame grabber/PC by the CameraLinkTM. It takes less than four seconds to transfer all data to the PC memory. This might vary depending on computer performances and other tasks on PC. To be noticed, data information from sensor is coded on 10 bit. Furthermore, 2 GB RAM are dedicated for frame buffer.

Table 2.2 reports the parameters of the illumination block.

Technical specifications	Targeted values
Pixel size of the camera	$12 \mu\text{m} \times 12 \mu\text{m}$
Image size per channel	128×128 pixels (= $1530 \times 1530 \text{ mm}^2$)
Number of illuminated pixels per acquisition	$4 \times 4 \times 128 \times 128$
Frame rate of the camera	4000 fps
Magnification (DML - TL)	3.9
Lateral field of view of the IMO	$400 \mu\text{m} \times 400 \mu\text{m}$
Reference mirror size	$400 \mu\text{m} \times 400 \mu\text{m}$
Diameter of the tube lens	1.9 mm
Focal length of the IMO	7.5 mm
Focal length of the tube lenses	28 mm

Table 2.2: Imaging part technical specifications.

2.1.3/ ILLUMINATION PART

Swept source optical coherence tomography technique uses a tunable laser system for the illumination. The wavelength of the light source is thus tuned over the broadband spectrum so that only one narrow-band wavelength is emitted at a time. Several techniques have been reported to build a sweeping wavelength light source such as galvanometer scanning mirror [114, 115], polygon rotating mirror [116] and Fabry-Perot cavity (FPI) [117]. The objective of this work was to develop an imaging system for the detection of skin diseases with micro-optical components. Thus, the FPI method has been chosen for a MOEMS-based integration of the swept light source. A tunable FPI is an optical resonator consisting of two partially-reflecting parallel dielectric mirrors. Under normal illumination, the spectral tuning of transmitted wavelengths can be controlled by adjusting the distance between these mirrors. A MEMS-based FPI has already been made by Miranto *et al.* in the visible range with 5.4 nm of full width at half maximum (FWHM) of the transmission signal and with 67% of maximum transmission at 510 nm [118]. One of the challenges of this project was to make a high resolution FPI cavity in the near-infrared range in order to provide a high interference cavity uniformity with micro-machining process and thus a high imaging depth. The micro-fabrication can

offer even further cost reductions due to mass production capability and potential for monolithical construction of the filter devices.

In interferometry, especially in optical coherence tomography, the illumination system plays a crucial part because the performances of the light source are strongly related to the ones of the system. Indeed, in SS-OCT, a trade-off exists between the optical parameters of the swept light source - i.e., the central wavelength, the spectral bandwidth, the linewidth and optical power - and the resolutions, the sensitivity and the depth of penetration. Usually, the wavelength range from 650 nm to 1100 nm is suitable for ophthalmology application because of corresponding low absorption in eyes. Whereas, in dermatology, the longer wavelengths permit less scattering effects and thus deeper tissue penetration [35]. However, the use of long wavelengths decreases the axial and lateral resolution. Due to low imaging depth - i.e., few hundreds micrometers - and to the high contrast which may be obtained, the central wavelength has been fixed to 840 nm [88]. Then, the bandwidth of the spectrum has been chosen in order to achieve a cellular axial resolution of 6.2 μm . According to the resolution relation, detailed in Sec. 1.5, the resulting bandwidth is 50 nm. These were obtained by using a super-luminescent diode (SLD-37-HP, Superlum)[119]. SLD reaches a high optical power over a wide wavelength distribution. In frequency domain OCT, the linewidth of the swept wavelength is critical because it limits the imaging depth. Thus, in order to maintain a coherence over 500 μm and according to equation in Sec. 1.5, the linewidth has to be less than 1.2 nm. This leads to 520 μm of coherent imaging depth.

In the proposed system, this distance is varied by the motion of an electrostatically actuated membrane carrying one mirror, hence modifying the air gap. Primary MEMS-based FPI have been made in order to provide the swept light source. However, despite the FWHM of the output beam from the FPI appears much narrower than previously reported ones in literature for this wavelength range, the optical performances, in terms of linewidth and optical power, exceed the specifications and are not satisfactory for a biological imaging system. Indeed, the FWHM of the transmitted narrow-band beam was 3.6 nm with only 14% of the transmission power. Furthermore, difficulties appeared during the integration process. Therefore, an alternative method to realize miniaturized filter structure, based on the piezo-actuation, was developed. In terms of manufacturing, the optical structure is easier to make than MEMS-based one. However, its production cost is higher - i.e., from 1-20 euros for a MEMS-based FPI to 100-1000 euros for a piezo-based FPI. In 2009, Saari *et al.* have developed a piezo-actuated FPI cavity with 5 nm of spectral resolution over 400 nm of spectral range [120]. Here, the aim is to make a narrow-band transmission FPI over 50 nm of bandwidth of a near-infrared range

spectrum. Figure 2.7 exposes the measured transmission peaks at four mirror positions within the tuning range. The FWHM has been measured and results in 0.9 nm at 846 nm wavelength which is in good agreement with the specifications of the project.

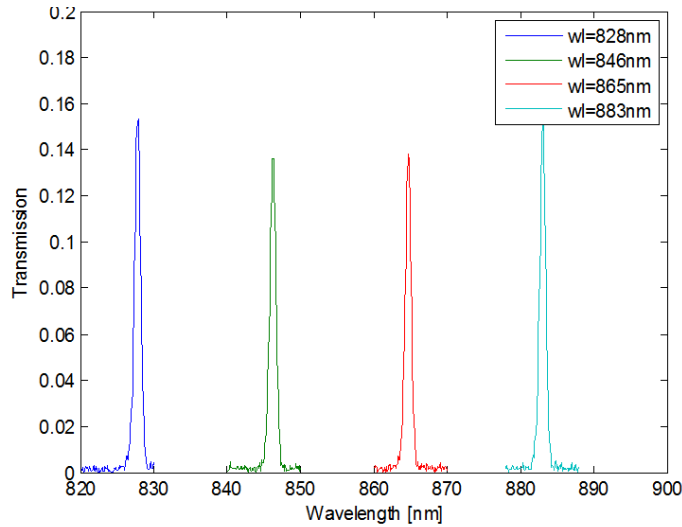


Figure 2.7: Measured transmission peaks from the piezo-based FPI over the 50 nm of spectral tuning range.

However, as it can be seen, the transmitted optical power by the FPI is low - i.e., only 14% of the power of the incident beam passes through the FPI - which does not meet the specifications for the imaging of scattering medium. Furthermore, the rest of the spectrum which is not transmitted, is back-reflected by the FPI, but so that it cannot illuminate back the SLD chip. This is achieved simply by slightly tilting the FPI. It has been shown that an angle of 2° increases the FWHM of the transmission signal to 1.2 nm . Pending the manufacturing of the FPI device by VTT, a commercial swept light source was used. Indeed, the broadband sweeper (BS-840-2-HP, Superlum), based on a tunable semiconductor laser source, has been placed in the FF-SS-OCT system for testing micro-components and developing the software (see Cha. 4). Despite a higher available power, it performs equivalent optical characteristics - e.g., central wavelength, linewidth and bandwidth of the emission spectrum.

Then, the filtered beam from the FPI is focused onto a multimode fiber (MF), with 1.2 mm core diameter (D_{MF}) and 0.37 numerical aperture, in order to make a spatially incoherent illumination. This incoherence avoids the cross-talk - i.e., coherent multiple scattering [121, 122]. However, at the end of a MF, random intensity patterns are observed. This is the result of temporally coherent interferences between the propagation modes. This phenomena is sometimes called speckle although it is not due to the reflection of a rough surface. Several methods have been reported to avoid this granular

appearance and to mean the intensity pattern, such as by vibration of the MF, to mix the electromagnetic modes within the MF, [123, 124] or by rotating a diffuser plate. For space-saving of the system, a LASER speckle reducer (LSR-3005-12D-NIR, Optotune) [125], based on a moving diffuser device, is employed and is placed between the FPI and the MF. The impact of the speckle reducer onto the illumination quality is illustrated in Fig. 2.8. As it can be seen, it guarantees an uniform illumination of the sample. The illumination is smoothed and homogeneous around the field of view.

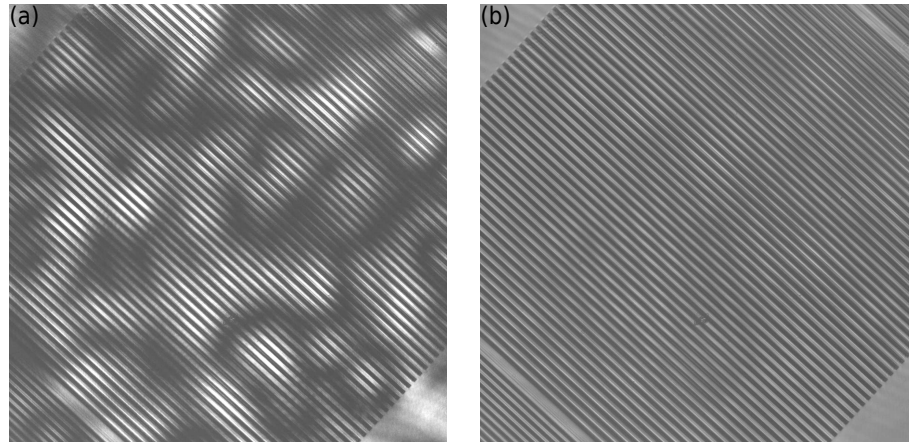


Figure 2.8: Comparison of the illumination system (a) without and (b) without the speckle reducer device. In absence of such system, the intensity distribution is not uniform, whereas with the speckle reducer, it is smoothed.

Afterwards, the lens C (Combination condenser, Qioptic) [126], which is in fact a condenser triplet, collimates the beams and the beam-splitter cube directs them onto the skin, through the array of DML. It can be noted that the BSC is only used to direct the incident beam onto the array of Mirau interferometers and is not a part of the interferometer. Its transmission-reflection ratio is 50:50. Arranged in an afocal system configuration, the combination of the condenser lens and the DML has to provide an illumination over a square of $400 \mu\text{m}$ size. Therefore, the two focal lengths have to match as exposed in the following relation.

$$\begin{aligned} \gamma &= \frac{FOV_{x,y}}{D_{MF}} = \frac{400 \sqrt{2}}{1200} = 0.47 \\ &= \frac{f'_{DML}}{f'_C} = \frac{7.5 \text{ mm}}{16 \text{ mm}} = 0.47 \end{aligned} \quad (2.5)$$

Where f'_C is the focal length of the condenser lens.

These values are summarized in Tab.2.3.

Technical specifications	Targeted values
Central wavelength	840 nm
Bandwidth	50 nm
Axial resolution	6.2 μm
Line-width	1.2 nm
Coherent imaging depth	520 μm
Magnification (Condenser lens - doublet of microlenses)	0.47
Focal length of C	16 mm

Table 2.3: Illumination system technical specifications.

2.1.4/ LATERAL AND AXIAL STITCHING

The lateral as well as the axial FOV equals $400 \times 400 \mu\text{m}^2$ and $88 \mu\text{m}$ (in air), respectively. The value of the axial FOV is not sufficient for the visualization of the dermo-epidermal junction over the entire human body. Therefore, an axial stitching of the optical head has been developed by using motion motors. Furthermore, in order to avoid the unmeasured areas between FOV of IMO, the head is laterally stitched. This allows covering the complete lateral FOV without the requirement of the scanning head during the measurement. To overcome these limitations, a lateral and an axial relative displacements of the optical head has been proposed to perform a complete image volume of the sample - i.e., $8 \text{ mm} \times 8 \text{ mm} \times 500 \mu\text{m}$.

By implementing six axial displacements of the optical head, the imaging depth reaches $530 \mu\text{m}$. Furthermore, to get a good repeatability of the stitching algorithms, the axial FOV_z have to be overlapped of 20% [127] - i.e., $18 \mu\text{m}$. The focal plane of IMO has hence to be moved by $72 \mu\text{m}$ of axial increment ζ_z . This requirement is very high, because the displacement must be done with a mechanical positioning tolerance of $\pm 4 \mu\text{m}$. To be noticed that due to the optical configuration of the imaging system, the magnification does not change during the axial stitching of the Mirau interferometers thanks to the infinite conjugate configuration of the imaging objective. Moreover, to obtain $2 \text{ mm} \times 2 \text{ mm}$ lateral imaging area per IMO, leading to a complete visualization of the sample over $8 \text{ mm} \times 8 \text{ mm}$, the optical system has also to be stitched along x and y axes. Considering the same level of overlapping, the transverse increment $\zeta_{x,y}$ distance

is then $320 \mu\text{m}$. The displacement tolerance is $\pm 20 \mu\text{m}$. During the axial stitching, only the array of Mirau interferometers is moved. Whereas, both the matrix of Mirau interferometers and of tube lenses are displaced for the lateral stitching operation. In this case, the camera remains fixed and only the multiple ROIs are digitally modified during scanning steps. The multiple ROI is applied via USB 2.0 interface.

Figure 2.9 exposes the principle of (a) the axial and (b) the lateral stitching for providing a $8 \text{ mm} \times 8 \text{ mm} \times 500 \mu\text{m}$ imaging volume. In order to clear the scheme, only three stitching steps have been represented - i.e., the first, the second and the sixth steps. Also, to simplify the schematic only the doublet of microlenses have been shown in (b).

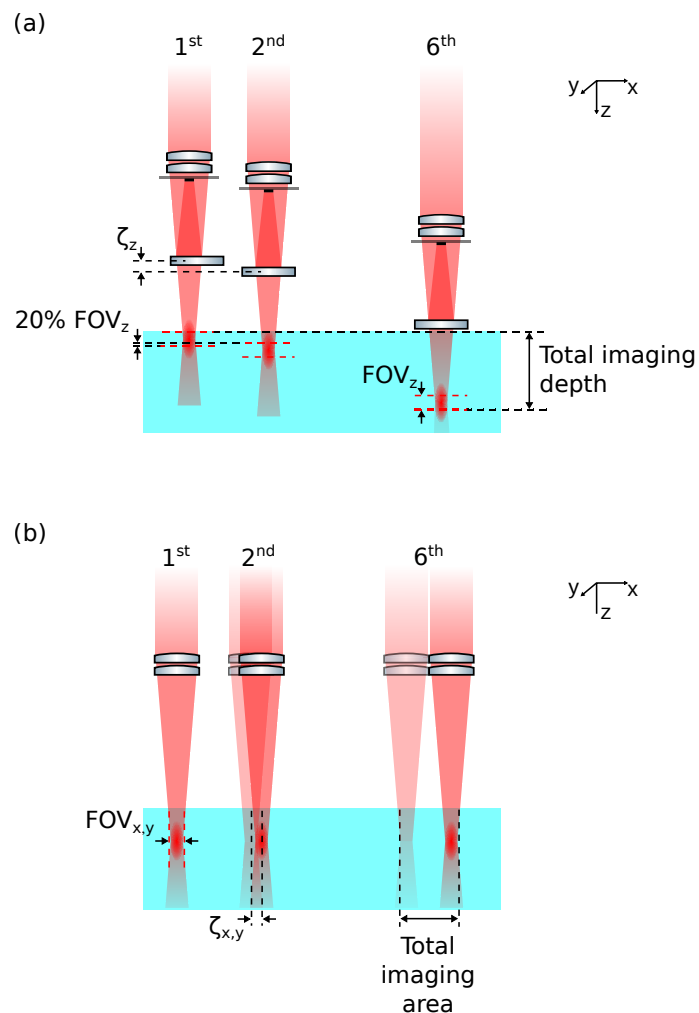


Figure 2.9: Concept of the stitching of the optical head. The principle of the stitching, through only three schematics of the displacement, is divided in two parts: in (a) the axial and in (b) the lateral stitching of the head.

Figure 2.10 shows the scheme of the stitching actuation system. It consists of three DC micro-motors (08016KD12SR, Faulhaber) and magnetic encoders (HEM3-256 W, Faul-

haber). Each axis has his own motion controllers (MCDC 3002 S, Faulhaber). They are equipped with a serial interface and are programmed with a specific software (ASCII code) to implement the displacements.

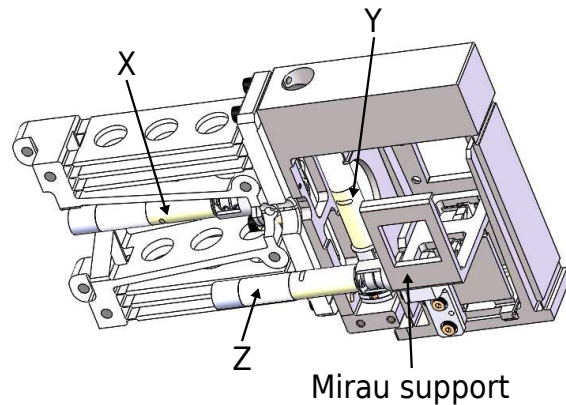


Figure 2.10: Stitching actuation system for the motion of the optical head following three axes. The scheme represents the frame including the motors and the encoders.

A motion test of motors, following x, y and z axes, was performed to ensure the good positioning system and its repeatability, as well as the displacement time of the head. Accuracy of the positioning has been measured around $10\ \mu\text{m}$ which is in agreement with the specifications of the stitching procedure. During the transfer data, from the camera memory to the computer memory, the lateral or the axial stitching of the interferometric head is implemented. It has been showed that due to the small weight of the Mirau head, the displacements time is around 100 ms only. This is shorter than the data transfer time of $4 \times 4 \times 128 \times 128$ pixels which is 350 ms. The acquisition time is then only limited by the data transfer.

2.2/ SINUSOIDAL PHASE SHIFTING

In FD-OCT, after applying a Hermitian Fourier transform operation on the real spectral interferometric signal, artifacts occur - i.e., mirror and continuous terms are generated. They decrease the measuring range and may yield to confusions on the positions of the sample layers. As shown in Sec. 1.3, phase shifting interferometry (PSI) method is a mean to overcome this issue by moving the reference mirror [35, 53]. Principle of PSI is basically to acquire a sequence of images with a phase change between them. Depending on the accuracy and the stability required, several PSI techniques have been reported, yielding to algorithms such as linear or stepped approaches (three-steps [128], four-steps [129] and five-steps [130, 131] PSI). To define the efficiency of a PSI algorithm, the suppression ratio is calculated. The suppression ratio is the ratio between the amplitudes

of both the sample signal and its complex conjugate. In FD-OCT, the linear and the four-steps algorithms provide around 25 dB [132] and 30 dB [133] of suppression ratio of the complex conjugate, respectively. A comparison between the PSI setup implementation [132] was reported. However, these step PSI techniques are not well adapted for the fast imaging because they are limited by their mechanism - i.e., each step must be stabilized before to take an image - and are chromatic dependent. Chen *et al.* have presented a complex method to avoid this poly-chromatic error which consists in moving both the reference mirror and the object [134]. This is called B-M method. Furthermore, a phase-shifter device calibration is often recommended [135, 136]. In the design of the micro-system, the sinusoidal phase shifting interferometric (sinPSI) technique, also called sinusoidal phase modulating interferometry, has been retained. In this approach, the phase delay is made by a sinusoidal displacement of the reference mirror. Despite high algorithm performances, robustness, performing an achromatic detection and being computationally efficient, the sinPSI technique has not dethroned more conventional PSI techniques [137]. This could be explained by the lack of sinusoidal phase-shifting devices.

In 1986, Sasaki *et al.* introduce the first sinPSI in order to measure the surface topography of an object [138] and, further, a theoretical analysis was reported [139, 140] for a random-noise error evaluation of the algorithm. Then, the sinPSI has been applied to the full-range FD-OCT [141, 142] and enhanced for the Doppler full-range FD-OCT [143]. Until 32 dB of suppression ratio of the mirror terms has been experimentally shown [132, 142] which is similar with the one of standard PSI techniques. The sinPSI is not only employed for its achromatic detection since the impact of light source bandwidth should be reasonable. But, it provides a good repeatability along time and a good stability in frequency and in amplitude of the reference mirror while making fast acquisitions. In this work, the MEMS platform which consists of the reference mirror and spider holders, is displaced by an electrostatic actuation following a sinusoidal motion [144].

The frame rate of the camera limits the frequency of the sinusoidal displacement of the reference mirror. Indeed, eight frames per period of actuation are required in the sinPSI algorithm. Thus, the frame rate of the camera being fixed to 4000 fps, the MEMS-based reference mirror is actuated at its resonance frequency of 500 Hz.

$$f_r = \frac{\text{Frame rate}}{8} = \frac{4000}{8} = 500 \text{ Hz} \quad (2.6)$$

Furthermore, the amplitude a of the displacement has to be fixed to 315 nm which is the optimized value for sinPSI [140, 142].

$$a = \frac{3 \lambda_0}{8} = 315 \text{ nm} \quad (2.7)$$

Nevertheless, the sinPSI requires a more complex algorithm than standard PSI techniques. It is based on the Jacobi Anger expansion and multiple Fourier transforms. Indeed, in FF-SS-OCT, the spectral interferogram from each pixel is not only wavelength dependent, like in Eq. 1.13, but is expressed as a function of both time t and wavenumber k

$$I_{sinPSI}(k, t) = \eta \frac{S(k)}{4} \left[\left(R_r + \sum_{m=1}^M R_m \right) + 2 \sum_{m=1}^M \sqrt{R_r R_m} \cos [2k(z_r - z_m) + 2ka \cos(\omega t + \beta)] \right], \quad (2.8)$$

where a , ω and β terms are the amplitude, the angular frequency and the initial phase of the sinusoidal actuation, respectively. ω is given by $2\pi f_r$, with f_r , the frequency of the oscillation. Figure 2.11 shows a sinusoidal phase shifted interferometric signal represented in two dimensions as a function of the time and the wavenumber.

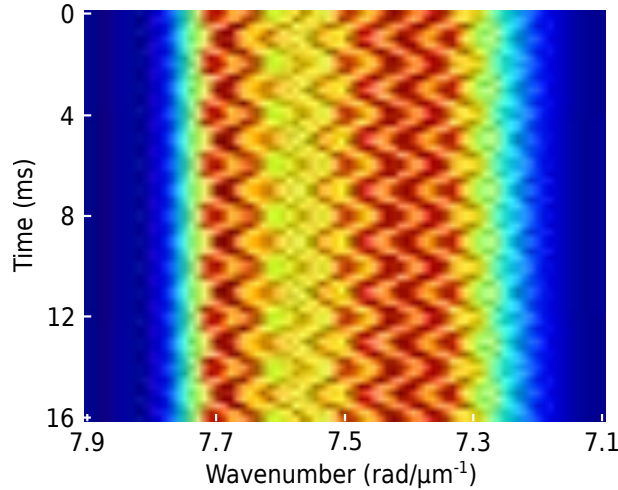


Figure 2.11: Spectral interferogram signal as a function of the time and the wavenumber using sinusoidal phase shifting technique.

Then, a Fourier transform of the acquired interferogram $I_{sinPSI}(k, t)$ along time, is performed. The magnitude of this expression is represented in Fig. 2.12.

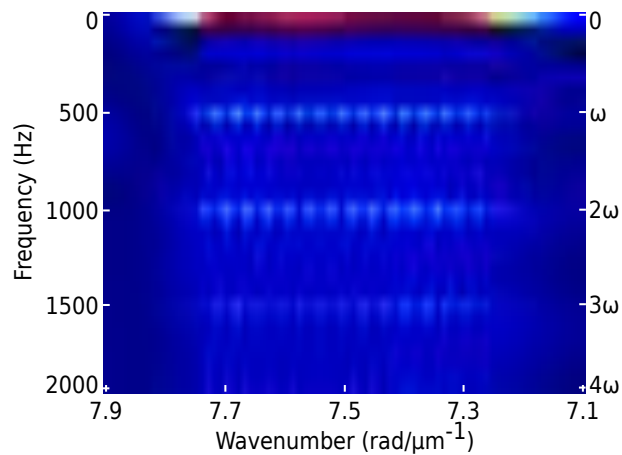


Figure 2.12: Fourier transform of the spectral interferogram signal with respect of time. It is represented as a function of the frequency and the wavenumber.

Two terms are retrieved at the first ω and the second 2ω harmonics of the Fourier transform for each k , respectively. These terms are the solution to reconstruct the complex interferometric signal. Afterwards, the Fourier transform of the complex signal is performed along the wavenumber k , leading to an artifacts-free depth signal. More details on the mathematical treatment of sinPSI is presented in the Annex 4.5.

A MATLAB code (MathWorks) was developed for the FF-SS-OCT micro-system. The simulation, in Fig.2.13, shows the influence of using the sinPSI onto a spectral interferogram. The object is positioned at $60 \mu\text{m}$ from the zero OPD.

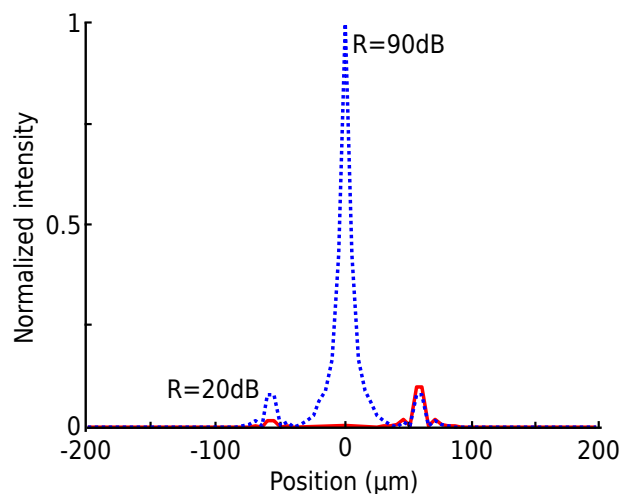


Figure 2.13: Comparison of two A-scans obtained by conventional FD-OCT (in blue dotted color line) and by sinusoidal phase shifting FD-OCT (in solid red color line). The artifact terms are efficiently suppressed.

As it can be seen, the sinPSI allows eliminating the DC term (suppression ratio $R=90 \text{ dB}$)

and reducing the mirror term of at least 20 dB whereas letting unchanged the cross-correlation term. This technique provides good performances for free-artifact imaging skin tissues through FF-SS-OCT. The suppression ratio is dependent on the reference mirror position. For instance, a position error of 50 nm leads to a suppression ratio of 85 dB and 18 dB of the DC and the conjugate terms, respectively. Such a position error is very large compared to the one specified in our system so that such algorithm should be efficient as artifacts suppression method. It has to be underlined that sixty four frames - i.e., eight frames per period over eight periods - are required in order to reconstruct an A-scan free of artifacts [142]. Reducing the number of frames has no impact onto the suppression ratio but onto the signal-to-noise ratio.

Table 2.4 reports the parameters of the sinusoidal actuation of the micro-scanner for the phase shifting.

Technical specifications	Targeted values
Frequency of the reference mirror actuation	500 Hz
Peak-to-peak amplitude of the reference mirror displacement	335 nm
Suppression ratio of the DC component	90 dB
Suppression ratio of the conjugate components	more than 20 dB

Table 2.4: Acquisition block technical specifications.

2.3/ OPTICAL POWER LOSSES - SENSITIVITY

This section describes an estimation of the optical power budget in the FF-SS-OCT micro-system [133]. Figure 2.1 displays all the components which contribute to the calculation of the optical power losses excepted the SLD and the FPI which are replaced by a broadband sweeper. The optical power and the losses are presented in the decibel scale - i.e., dBm and dB. The filtered light coming from the swept light source has an optical power of 16 mW (12 dBm) per sweeping wavelength. Afterwards, the filtered wavelength is coupled into an optical fiber. The transmission of both the coupling and the fiber is assumed to be 60% (-2.2 dB). Then, the beam is collimated by a lens triplet. The beam diameter after collimation is 12 mm. After, the beam is divided into 4×4 channels using an aperture stop array. Each aperture stop has a diameter of 1.5 mm. The transmission of this channel separation is calculated to 40% (-4 dB), which is the ratio

between the area of the collimated beam and the area of 16 aperture stops. then, the beam-splitter cube, which has 50% (-3 dB) of reflectivity ratio, directs the light onto the matrix of Mirau interferometers. Due to obscuration of the reference mirror and spiders, the transmission of the platform is 90% (-0.5 dB). The optical power for the reference and sample path can be adapted by the transmission-reflection ratio of the planar beam splitter of the Mirau interferometer. Here a ratio of 70/30 is assumed (-1.5 dB for object beam and -5.2 dB for reference beam). For the illumination system, this leads to 0.8 dBm and -2.9 dBm in the sample and in the reference arms, respectively.

Then, the optical losses regarding the imaging part have been determined. The reflectivity of the reference mirror, made of gold, is assumed to be 97% (-0.13 dB). Also, the percentage of back-scattered photons from the skin sample is 0.1% (-30 dB) [71]. Both object and reference beams are collected by the array of Mirau micro-interferometers, yielding to -1.5 dB and -5.2 dB of optical losses, respectively. The beams pass once again through the beam-splitter cube (-3 dB) and are focused onto the camera sensor. Thus, the total optical power of the OCT micro-system is estimated to -33.7 dBm from the object and -11.2 dBm from the reference arms.

The number of illuminated pixels per frame is $4 \times 4 \times 128 \times 128$ pixels. Thus, the optical power per pixels is -87.5 dBm and -65 dBm for the sample and the reference arms, respectively. According to the camera specifications, the fill factor is 60% and the quantum efficiency at 840 nm wavelength is around 20% as shown in Fig. 2.14. Depending on the central frequency of the light source ν_0 and the optical power P_0 , the number of generated photo-electrons is given by the following relation.

$$n_e = \frac{\eta \tau P_0}{h \nu_0}, \quad (2.9)$$

where h is the Planck constant. Here, assuming a maximum exposure time τ of 250 μ s, corresponding to 4000 fps frame rate of the camera, the resulting number of photo-electrons from the sample and the reference is 223 and 39474 for one sweep wavelength and one camera pixel, respectively. According to the parameters of the camera, the excess noise should be negligible because its exposure time is longer than the coherence time of the light source. Thus, the camera can be assimilated to a shot-noise limited detector. Figure 2.14 is the noise evolution of the camera depending on its full-well capacity. The camera employed in the FF-SS-OCT micro-system has 40,000 electrons FWC, yielding to around 200 e^- of global noise.

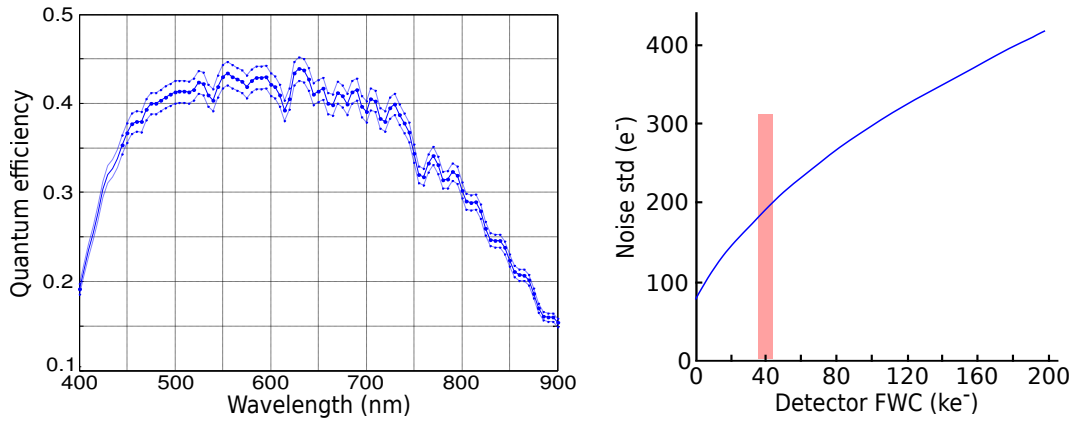


Figure 2.14: Parameters of the high speed camera. The quantum efficiency is represented as a function of the wavelength and the noise standard deviation as a function of the FWC.

The sensitivity of the imaging micro-system is thus estimated at 83 dB at 50 μm of depth and 80 dB at 150 μm . The sensitivity can be also understood as the lowest reflectivity of the sample arm that leads to an SNR of unity. In our case, it can be written

$$R_{min} = \left(\frac{\Delta n}{2n} \right)^2 \quad (2.10)$$

where Δn and n are the local refractive index variation and the average refractive index, respectively. Assuming n equals 1.36, the sensitivity of 83 dB allows measuring a refractive index of 2.10^{-4} .

2.4/ FABRICATION OF MICRO-COMPONENTS OF THE MIRAU MICRO-INTERFEROMETERS

The main element of the FF-SS-OCT micro-system is an array of 4x4 Mirau micro-objectives and the array of tube lenses. After being designed - i.e., knowing the parameters of each MOEMS components - the array of IMO as well as the array of relay lenses have been fabricated with micro-machining processes. As seen previously, each micro-interferometer consists of a doublet of plano-convex microlenses, a vertically actuated reference mirror hold by spiders and a planar beam-splitter. Instead of using a single microlens, a doublet of microlenses reduces the refractive power per lenses and thus decreases the optical aberrations [113]. Also, the reference micro-mirrors are maintained by three curved arms (here, called spiders). A simulation and experimental measurements have shown that this configuration leads to negligible impacts onto the imaging quality [145]. The characterization methods are detailed in Cha. 3.

Each micro-optical component is made at wafer-level, so that the assembly can also be performed at the wafer-level before to release individual components. This miniature OCT system requires the combination of heterogeneous technologies (micro-optical, micro-machining technology, glass, polymer, silicon) and is packaged using the approach of multi-wafer bonding. In this section, the fabrication processes of the micro-optical components, which constitute the array of Mirau interferometers, are described according to the specifications from the optical design.

2.4.1/ MICROLENS

Firstly reported by Merzal *et al.*, where sub-millimeter diameters microlenses were fabricated [146], glass flow process has been here considered for the manufacturing of the array of microlenses. In this process, a glass substrate located on top of cylindrical silicon cavities is heated so that it melts. Convex shapes are obtained in a similar manner than during polymer reflow although they are the consequence of forces due to pressure difference and glass viscosity. This process can be suited for dense matrices of plano-convex microlenses generation and millimetric sized lenses generation with good optical quality. Fabrication of arrays of plano-convex glass lenses where millimeter-range diameters, high NA and high fill factors are required, has been reported [147, 148].

The flowchart of the fabrication process of array of the doublet of microlenses is shown in Fig. 2.15. A 500 μm thick silicon substrate is spin-coated with positive photo-resist. (a) A standard UV photo-lithography is performed with a mask of circular apertures. The photo-resist is patterned in order to define the footprint of the lenses - i.e., the diameter and pitch of the array. Note that the main differences between the single channel case and array case concern the design of the photo-lithography mask. Then, (b) the silicon wafer is etched anisotropically - i.e., perpendicularly to the wafer surface - through the mask apertures by deep reactive ion etching (DRIE). The depth of the obtained cylindrical cavities is fixed to 250 μm . At the end of the step, the photo-resist is removed with acetone in an ultrasound wet bench. Afterwards, (c) a wafer of borosilicate glass (Borofloat®33, Schott) is anodically bonded under vacuum environment at 350°C on top of the cavities. In (d), the silicon-glass set is heated up to a temperature between the annealing and the softening point of the glass (560°C and 820°C, respectively). Basically governed by the ideal gas law and thus the pressure difference between the cavities and the furnace chamber, the glass is attracted towards the bottom of the cavity leading to a nearly spherical shape of the inner side of the membrane. This surface, formed without any contact with silicon, is the convex side

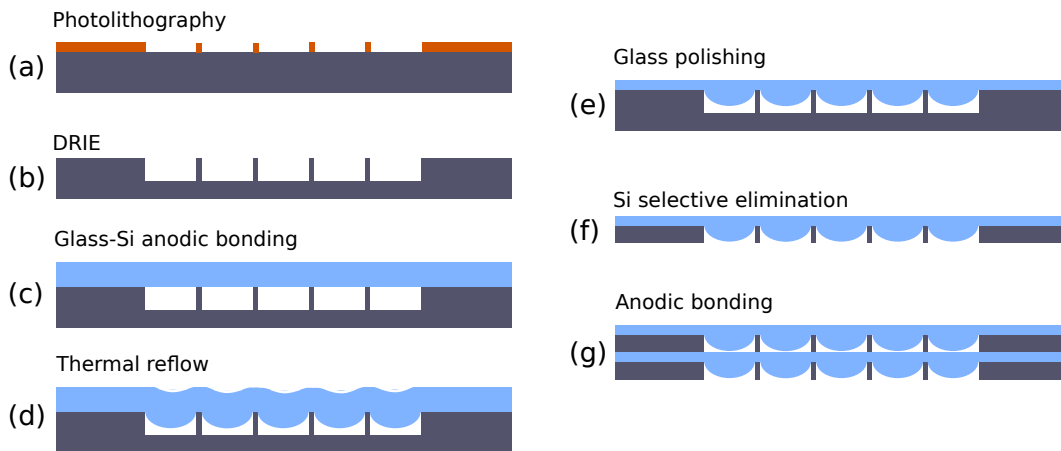


Figure 2.15: Flowchart of the microlens fabrication process. It consists in seven steps.

of the final lens. The high pressure difference between the cavity and the outside is sufficient to avoid an equilibrium situation, so that the cavity would be completely filled by glass after a sufficiently long time. Hence, only time governs the amplitude of the sag. The next step consists in grinding and polishing the backside of the glass in order to obtain the flat side of the plano-convex lenses (e). Finally, (f) the backside of the silicon is also polished down to the desired thickness to release the convex side of the microlenses. Finally, (g) the last step consists in assembling the two similar wafers again by anodic bonding on the top of each other in order to make the DML. Figure 2.16 shows two photographs of the assembly of two wafers of microlens matrices and its cross section after the whole process.

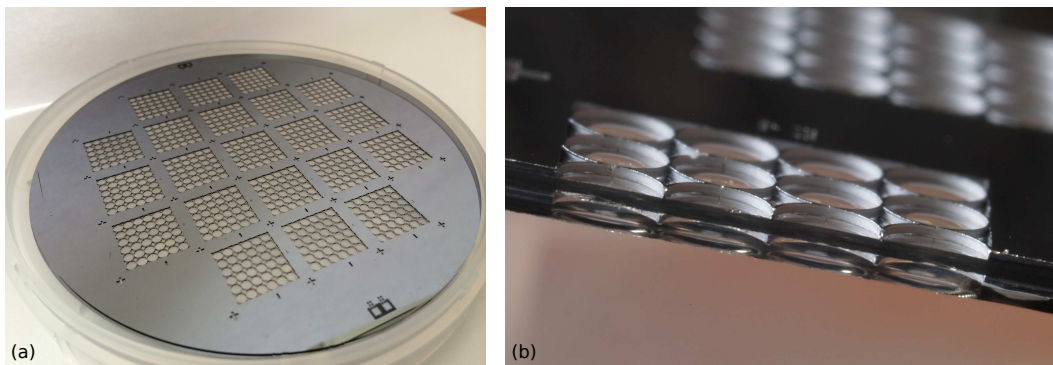


Figure 2.16: (a) Photographs of the wafer stack with matrices of 6×6 microlens doublets and (b) cross section of a matrix of lens doublets. This figure is extracted from [113].

The array of tube lenses has been made following the same fabrication process. Nevertheless, it does not require a doublet assembly because the focal length being higher, aberrations are smaller.

In order to match with the specifications of the design, after being fabricated, the array of objective lenses is characterized. Resolutions, depth of field and wavefront quality are estimated. These results as well as the characterization techniques are presented in Cha. 3.

2.4.2/ MICRO-REFERENCE MIRROR AND MICRO-ACTUATOR

Besides the doublets of microlenses, the Mirau objective includes an array of reference mirrors. In FD-OCT and contrary to TD-OCT, the reference mirror is usually kept fixed. However, in this work, the reference mirror is vertically actuated for phase shifting procedure in order to remove the artifacts terms due to the Fourier transform and follows a sinusoidal motion thanks to a system of comb-drive actuators. The reference mirror is supported by curved suspensions, so-called spiders [144, 149], since in the Mirau architecture, the mirror plane should be transmissive around the reflective mirror area. This technology is mainly based on the silicon structuration. The main steps of the fabrication process are shown in Fig. 2.17. (a-e) The device layer is structured by DRIE with two different masks to create asymmetric comb fingers. Then, in order to protect the front side during the back-side etching, (f) an oxidation of the wafer is applied. In (g) and (h), the back-side is etched down to the buried oxide. Afterwards, the structure is released in vapor (i) and, finally, the pads and the mirrors are deposited using a shadow mask (j).

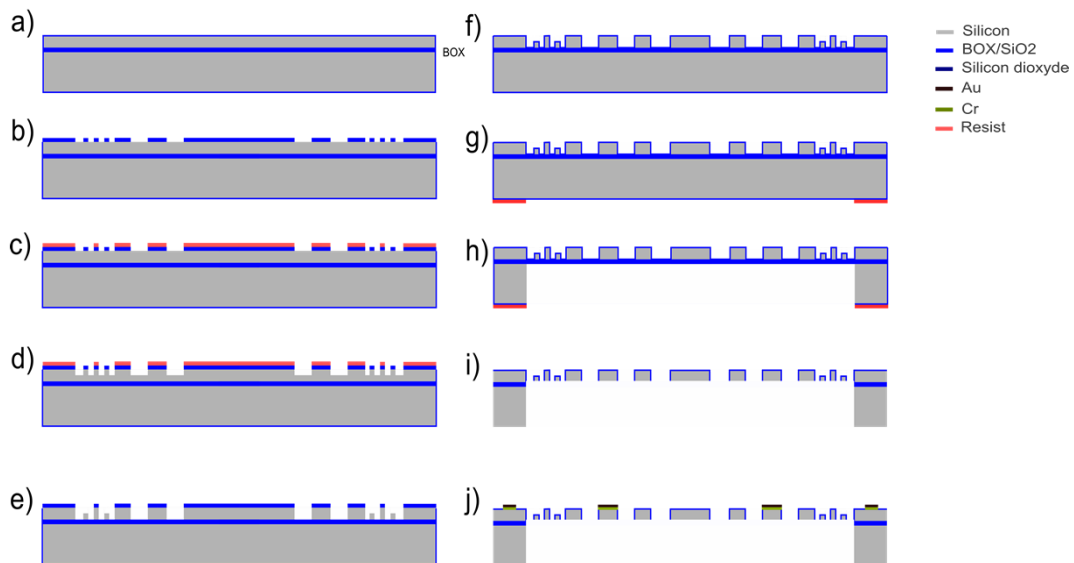


Figure 2.17: Flowchart of the reference mirror and spiders fabrication process. It consists in ten steps. This figure is extracted from [144].

The fabrication process of the reference mirrors and the actuator is detailed in J. Lullin's thesis [150]. It can be noticed that optical simulations have been made to ensure that

the diffraction generated by the spiders is negligible and does not deteriorate the optical signal quality significantly [145]. Figure 2.18 shows the final actuated platform wire-bonded on a PCB chip.

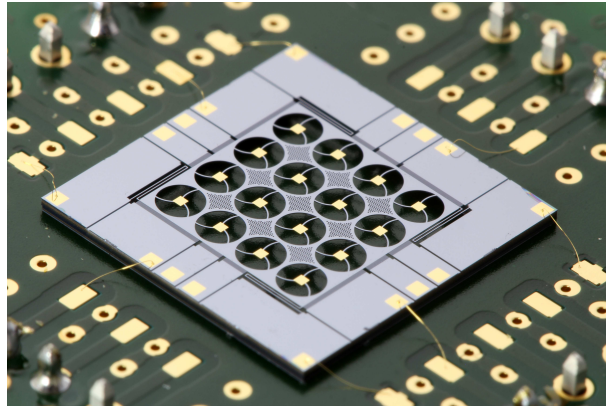


Figure 2.18: Photograph of an array of reference mirrors held by spiders. This figure is extracted from [144].

The quality of the reference mirror surface - i.e., reflectivity, roughness and topography - as well as the displacement parameters - i.e. frequency and amplitude - have been characterized and are reported in Sec. 3.2.2.

2.4.3/ PLANAR BEAM-SPLITTER

The third element of the array of micro-interferometers is the planar beam-splitter which is used to divide the incident beam into both the reference and the object arms. Simulations have been made to find the trade-off between the ratio of reflection to transmission and a good sensitivity for the imaging of biological sample. According to the optical power losses analysis, a sensitivity of 83 dB can be achieved with a ratio of 70:30 - i.e., 70% of light is transmitted into the sample arm whereas 30% is reflected into the reference arm. Figure 2.19 illustrates the sensitivity evolution at different transmission coefficients. Such a ratio can be reached by a single layer if its refractive index is $n = 2.239$ and its height is 95 nm. TiO_2 films present an excellent chemical stability, a good mechanical properties and a non-toxicity in addition to high refractive index. Here, the planar beam-splitter is made of a borosilicate glass wafer covered with a single layer of TiO_2 generated by physical vapor deposition (PVD). Depositions have been performed to set the refractive index. According to the measured value ($n = 2.20$), the target thickness of the layer is 97 nm to correspond to a quarter-wave. In this region of refractive index, the dependence of the T:R ratio to the wavelength varies of 0.2 % along the 50 nm of spectral range and thus is quite small.

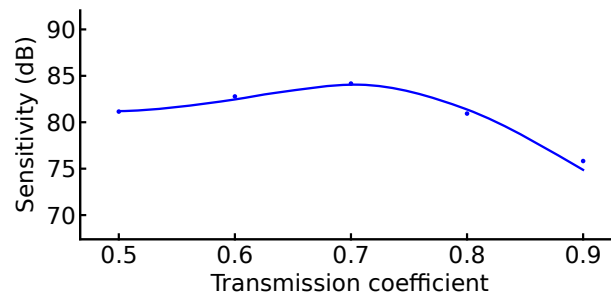


Figure 2.19: Evolution of the system sensitivity as a function of the transmission coefficient of the planar beam splitter.

2.4.4/ ASSEMBLY OF THE ARRAY OF MIRAU MICRO-INTERFEROMETER

Then, the Mirau interferometer is assembled through a multi-wafer bonding technology by taking into account difficulties, such as different materials, residual stress, alignment accuracy and protection of sensitive components [112]. Figure 2.20 shows (a) a schematic and (b-c) front-side and back-side photographs of the integrated array of Mirau micro-objectives after releasing. It consists in seven wafers: four wafers for the lens doublet, one wafer for the micro-scanner - i.e., including the reference mirrors and the spiders - a focus spacer and the planar beam-splitter wafer.

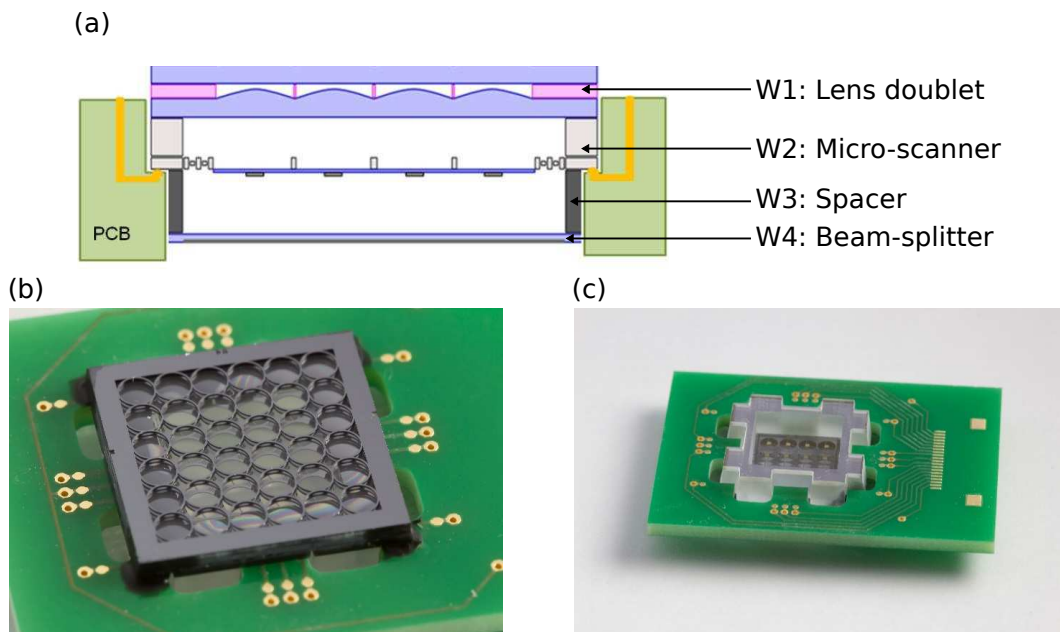


Figure 2.20: Design concepts of the Mirau interferometer integration. This figure is extracted from [112].

2.5/ SYNTHESIS

This chapter reports the design of the full-field swept-source optical coherence tomography micro-system. It describes the architecture of the micro-system through both its illumination and its imaging parts. The system provides a large lateral and axial fields of view ($8 \text{ mm} \times 8 \text{ mm} \times 500 \text{ }\mu\text{m}$) with a cellular resolution in order to visualize a suspect cutaneous tumors. This is the motivation of the project for the diagnosis of skin pathologies at an early stage. The imaging micro-system is based on the combination of swept source optical coherence tomography, in order to spectrally record the interference signals, and the two dimensional acquisition to avoid the beam scanning. Therefore, a sweeping wavelength light source has been developed. However, the performances of the swept light source did not meet the expected ones thus, a commercial broadband sweeper has been retained. The parameters of this light source allows performing an axial resolution of $6 \text{ }\mu\text{m}$ in the same order than lateral one provided by the optical parameters of the micro-interferometers. The optical head is composed of an array of Mirau micro-interferometers (4×4 interferometric objectives). The optical configuration of the interferometers has been chosen for its compactness and its vertical integration compatibility. The lateral and the axial fields of view of each interferometer are $400 \text{ }\mu\text{m} \times 400 \text{ }\mu\text{m}$ and $90 \text{ }\mu\text{m}$ (in air), respectively. It can be noticed that the linewidth of the swept source does not introduce a limitation on the axial field of view. To obtain the large expected imaging volume, the system is laterally translated six times and also six times axially to fill the gaps between adjacent channels of the array. During the moving, data recorded in the internal-camera memory, during the acquisitions, are transferred through a CameraLink bus for a time saving. Instead, the pipeline mode is applied. Each pixel of the camera collects the spectral components of the interferometric signal and a Fourier transform is applied to each A-line for the reconstruction of the depth profile. Nevertheless, mirror and continuous terms occur due to this operation onto a real signal. To avoid these artifacts, a sinusoidal phase shifting interferometric algorithm has been employed. It has been shown that the suppression ratio of the complex conjugate is about 20 dB which is similar to the state-of-the-art of standard phase shifting techniques. According to this design, the estimated duration for the full volume imaging of the pathology is about 75 seconds. However, this long time for *in-vivo* imaging can lead to artifacts due to heart beat or the breathing of the patient. Although three dimensional imaging is a real asset, it is highly probable that dermatologists are more comfortable with the analysis of four cross-section images - i.e., four parallel B-scans - spaced out by 2 mm. This mode, that could be very easily implemented, would require to stitch the optical head along only one direction - e.g., X. In this case, by adapting the ROIs to four lines also, the amount of data would be much smaller and the stitching time would thus be limited to the displacement

duration (100 ms). This leads to an acquisition time between 2 and 6 seconds depending on the number of axial required movements. Such acquisition time seems much more compatible with *in-vivo* imaging. Finally, the fabrication processes of the micro-optical components which constitute the imaging part, are shown.

CHARACTERIZATION OF OPTICAL MICRO-COMPONENTS

The challenge of this research work was to combine micro-structures and micro-opto-electro-mechanical systems (MOEMS) technologies in a free-space platform adapted for new generation of optical coherence tomography (OCT) micro-systems, realizing a real-time *in-vivo* three dimensional imaging of the epidermis and the dermis layers. Thus, micro-optical components of the imaging system - e.g., microlenses and micro-mirrors - have to perform a good imaging quality to meet the specifications. Indeed, a sufficient depth of penetration and a large lateral field of view (FOV) is required with a cellular resolution. Each micro-elements have been fabricated according to the optical design.

In order to assure the good quality of the agreement of the MOEMS components with the design, characterization techniques have been developed in the frame of this work. Moreover, an extensive characterization of micro-optical components is required in order to optimize the fabrication processes and should result from a good reproducibility [151]. Based on the surface topography and on the through focus measurements, two devices allow, on one hand, estimating the parameters and the quality of the surface - e.g., roughness and radius of curvature - and, on other hand, retrieving the optical performances - e.g., resolutions and wavefront deviation - of the micro-optical elements. Firstly, the micro-components are characterized individually and then, after being vertically integrated thank to resorting to a wafer-level fabrication, the array of Mirau micro-objectives is characterized once again.

This chapter summarizes the methods employed for the characterization. Afterwards, the results of the evaluation of the quality of each MOEMS element and of the multi-channels OCT system are presented and compared to the specifications. This is the main work of my thesis. I was in charge of developing and characterizing micro-optical

elements of the FF-SS-OCT system. Therefore, I set up the two characterization devices. Further, all the micro-optical elements have been inspected with them.

3.1/ CHARACTERIZATION TECHNIQUES

Because of the imaging quality required, two optical characterization techniques have been developed. These systems provide information on distinct parameters and are consequently complementary. The first technique, coherence scanning interferometry, allows the measurement of the surface topography of the micro-optical element. Knowing the topography of the micro-optical element is important in order to provide the roughness of the sample and, in the particular case for microlens characterization, the shape parameters such as conic constant and radius of curvature. These two parameters are usually employed for performance evaluation of the component providing that ray tracing is additionally applied. However, the topography information is sometimes not sufficient to determine the quality of the micro-optical components. Indeed, an estimation of its ability to achieve a high quality beam - e.g., diffraction-limited or aberration-free - is also essential. Hence, a second characterization system has been implemented in order to get this information. It requires the measurement of the focal volume generated by the micro-optical element. Through the through-focus measurement, the determination of optical parameters - e.g., lateral and axial resolutions, focal length and modulation transfer function (MTF) - as well as a quantification of the optical aberrations is performed. Indeed, based on the phase retrieval technique and then Zernike polynomial decomposition, the wavefront distribution and the optical aberrations are retrieved. This section presents these different techniques through their implementation and their performances.

3.1.1/ SURFACE QUALITY THROUGH COHERENCE SCANNING INTERFERENCE MICROSCOPY

The inspection of the surface topography of micro-optical elements is a basic evaluation of the quality and an important mean to provide information about the shape and the roughness of the micro-optical components. Indeed, their optical properties are highly related to their shape. For this reason, multiple mechanical or optical techniques, have been developed in order to obtain the profile or the two dimensional map of the object [96, 111].

The simplest device which can provide a height information is the stylus profiler [152]. This mechanical system consists in displacing a small probe across the surface

of the object and measuring the relative position of the object step-by-step. The two dimensional surface information may be retrieved by repeating the lateral scan of the probe at different positions. The mechanical profiler technique can measure the profile along a large surface, up to 200 mm, and up to millimetre of height with around $0.2 \mu\text{m}$ of resolution. Because of the finite size of the stylus profiler probe, the lateral resolution is limited. Despite measuring the profile with a low root mean square noise, this technique suffers of a limitation of the investigation range due to the geometrical shapes of the probe. Indeed, in case of high-sloped objects, the probe cannot provide height information. Furthermore, this tactile method is limited by its potential surface damaging.

Another technique of surface characterization is the scanning probe microscopy. As well as for the stylus profiler technique, a physical probe is laterally displaced along the specimen. The information of height is obtained by the interaction between the tip and the surface of the object. Several types of scanning probe microscopy technique, depending on different measurement principles, exist. For example, the well-known atomic force microscopy [153] and scanning tunneling microscope [154] techniques are based on the atomic repulsion forces between electrons of the object surface and electrons of the tip, and on the concept of quantum tunneling between the surface and the probe, receptively. Both of these techniques can perform a surface topography at the atomic level - i.e., 0.1 nm resolution. Unlike stylus profiler, the scanning probe microscopy techniques are a non-invasive and contact-less technique - i.e., they do not damage the sample during the characterization process. Despite a high resolution, the scanning probe microscopy has a small axial and lateral FOV and, further, is usually slow due to the scanning process. Thus, this technique is often used for the roughness measurement of the object. A comparison in term of precision, between both atomic force microscopy and the mechanical profilometry techniques, has been reported by Bennett *et al.* [155].

Due to the non-contact character and the fast acquisition motivations, optical profilometry techniques gained interest [156]. Among them, confocal scanning microscopy technique detects images corresponding to the focus spot reflected by the surface of the object. Indeed, as well as in biological applications exposed in Fig. 10, the single point detector measure the intensity back-reflected by the surface passing through a pinhole located at the conjugate focal plane [157]. Thus, the pinhole filters in-focus ray so that high resolution can be achieved depending on the microscope objective. Two dimensional lateral and one dimensional axial scans have hence to be performed to get the surface topography of the micro-optical component. A trade-off occurs between the acquisition process time and both the resolution and the FOV of the system.

In order to test the surface quality of micro-optical components, an alternative strategy, named coherence scanning interference microscopy (CSIM), has been developed [158]. This low coherence interferometry technique was introduced by Davidson *et al.* [159]. Since then, various names have been employed in the literature such as vertical scanning interferometry, optical coherence profilometry or white-light scanning interferometry [111]. This technique is similar to the principle of the full-field time domain optical coherence tomography (or *en-face* TD-OCT), in biological imaging [160]. It derives the sample height from an optical signal reflected from the sample surface by using amplitude demodulation of poly-chromatic light. Indeed, the mathematical treatment of each pixel is quite similar to the one of TD-OCT. When the optical path difference Δz , between the reference mirror position and the surface of the object, is smaller than the coherence length l_c , an interference pattern occurs. Then, the low temporal coherence of the light source is used to localized accurately the signal, since the interference signal is gated by the coherence function. The interference pattern provides the information about the relative position of the surface. In order to get the whole surface topography, the object is axially displaced by a scanner device. Figure 3.1 shows the two-dimensional interference pattern recorded by the camera at three different object positions.

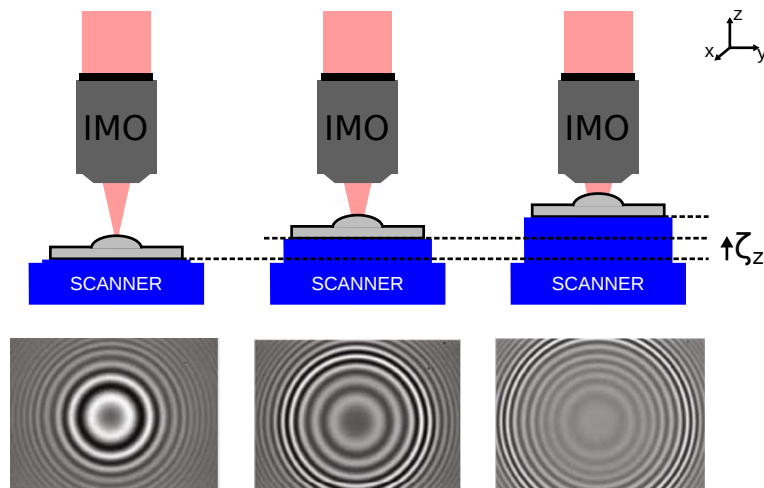


Figure 3.1: Interferograms resulting of the object displacements at three different axial positions. The increment of the scanning system is ζ_z .

The optical arrangement of CSIM is presented in Fig. 3.2 [161]. The incident beam, from broadband light source BLS, passes through the Köhler illumination system, allowing a homogeneous illumination of the object to be characterized [87]. Usually, a halogen lamp is used as the light source ($\lambda_0 \approx 650 \text{ nm}$). The aperture stop AS controls the numerical aperture of the illumination and the field stop FS, the illuminated area of the object surface. Then, the beam-splitter cube BS directs the beam from the Köhler system into

the interferometric microscope objective IMO. The Mirau objective IMO ($\times 10$, $NA=0.3$) is composed of lenses, a mirror and a beam splitter. The intensities of the reference and the object beams are collected by the IMO and imaged onto the camera D through the tube lens TL. The sensor is a CMOS camera from μ Eye with a resolution of 1280×1024 pixels. A piezo-electric device from Physik Instrumente P-622.Z, in closed-loop mode, is used for the vertical motion of the object. Its full range equals $250 \mu\text{m}$ and the axial increment can reach 3 nm. The range of the piezoelectric system has to be higher than height of the object. The lateral resolution of the characterization system has been measured, using an USAF 1951 resolution target, and equals $2.1 \mu\text{m}$. Furthermore, the lateral FOV is $740 \times 550 \mu\text{m}^2$.

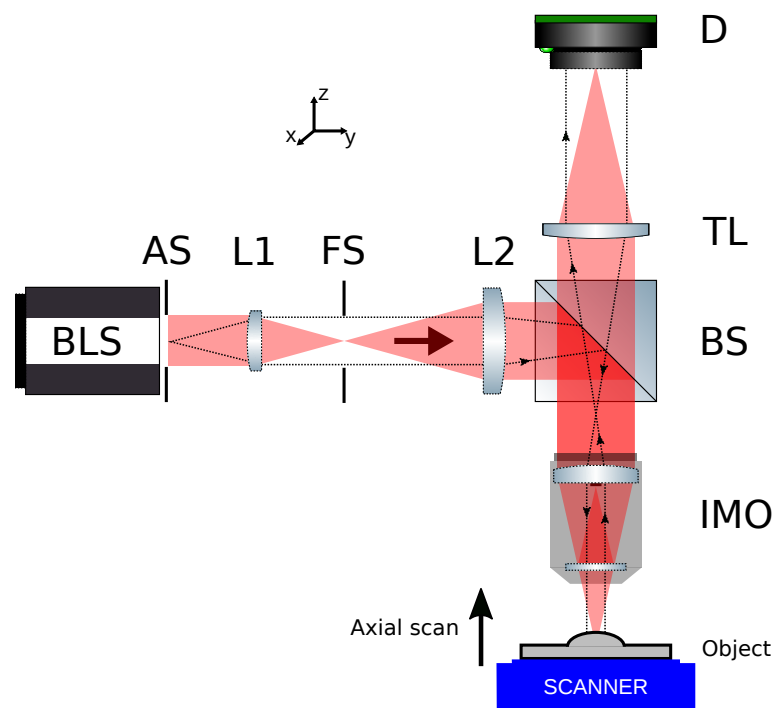


Figure 3.2: Principle of the coherence scanning interferometry microscopy equipped with a Mirau interferometric microscope objective. Broad-band light source BLS, beam-splitter cube BS, tube lens TL, interferometer microscope objective IMO and camera detector D are illustrated. Köhler illumination configuration consists of the aperture and the field diaphragms AD and FD, and two condensers L1 and L2. The object is axially displaced using a piezo-electric scanner.

A home-made LabVIEW (National Instruments) program has been developed on the producer-consumer structure [162]. This structure is geared toward time saving. The processing of the interferogram using modern computerized technique increases the accuracy and the dynamic range of surface topography measurements. The producer-consumer structure is used to communicate data between loops with only computer's RAM limitation. By involving two while-loops, it can also be used to acquire and pro-

cess data in real-time. The structure is shown in Fig. 4.16. The first producer loop allows controlling the motion of the piezoelectric device, acquiring frames and placing interferogram images in the queue. The dynamic libraries have been used to write/read the positions of the piezoelectric system. In parallel, the consumer loop read the image of the interferogram from the queue. Then, it allows processing the data by demodulating the interference pattern, and then reconstructing the topography map of the object. For that, an algorithm of the detection of maximum contrast of the interference fringes - i.e., constructive interference - has been established [163] and exposed in Algo.1 here after. Typically, the profiler records the position of the peak contrast for each point of the FOV [164].

Algorithm 1 Signal processing of the coherence scanning interference microscopy system. The algorithm is based on the reported research [163]. It returns the two dimensional surface topography of the object.

```

1: N = range / increment                                ▷ Number of frame measurements
2: [P,Q] = size(frame)                                ▷ Dimensions of the camera frame in pixels
3: topo = zeros(P,Q)                                  ▷ Initialize the resulting topo array
4: A = zeros(P,Q)                                     ▷ Initialize the queue array
5: B = zeros(P,Q)                                     ▷ Initialize the array of shift register
6: while  $i < N$  do
7:   read A                                           ▷ Read the frame from the queue
8:   read B                                           ▷ Read the frame from the shift register
9:   for  $p := 0$  to  $P$  step 1 do
10:    for  $q := 0$  to  $Q$  step 1 do
11:     if  $A(p,q) \geq B(p,q)$  then
12:      topo(p,q) = topo(p,q) + 1                    ▷ Add one to TOPO(p,q)
13:      B(p,q) = A(p,q)                             ▷ Replace the maximal value of A(p,q) in B(p,q)
14:     else
15:      pass
16:     end if
17:    end for
18:  end for
19:   $i = i + 1$ 
20: end while
21: return topo(p,q)  $\times \zeta_z$                     ▷ Return the topography surface

```

Then, the image processing provides the map of the surface topography. By inspecting this map, the radius of curvature (RoC) of the micro-optical components as well as the

conic constant, can be retrieved. For this task, a LabVIEW (National Instrument) program has been developed. By determining the center of the microlens, the developed code allows determining these parameters through the analysis of multiple line profiles. Figure 3.3 presents the surface topography of plano-convex microlens fabricated following the fabrication process described in Sec. 2.4.1. Here, due to the large required FOV, a Michelson interferometric objective (x4, NA = 0.1) has been employed.

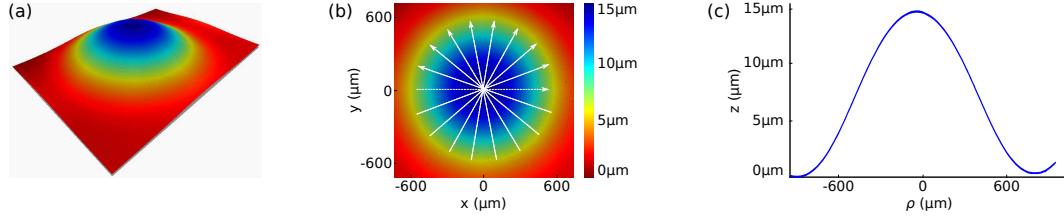


Figure 3.3: Surface topography characterization using the coherence scanning interference microscope. This device allows displaying the false-color maps of the surface in (a) three and (b) two dimensional representations. The line profile, in (c), results of the contribution of several profiles shown in white color arrows in (b).

Assuming a rotational symmetry of the microlens surface with respect to its center, a one dimensional mean profile is provided which is calculated from angle profiles (white color arrows, in Fig. 3.3 (b)). Then, the resulting line profile, also-called the saggital height, presented in Fig. 3.3 (c), is fitted following the conic equation

$$z(\rho) = \frac{c \rho^2}{1 + \sqrt{1 - (k + 1) c^2 \rho^2}} \quad (3.1)$$

Where, c is the apical curvature at the vertex and k is the conic constant (or Schwarzschild constant) in unit-less. z and ρ terms are the depth and the radial coordinates from the apex, respectively. The curvature is determined as the inverse of the radius of curvature (RoC) at $\rho = 0$. By knowing the RoC, the conic constant is extracted according to the fit root mean square error (RMSE) [165]. Indeed, the quality of fit is characterized by evaluating the RMSE between both the fitted function and the one dimensional profile. Then, the conic constant value leads to the type of microlens profile.

Lens profile	Conic constant (unit-less)
Hyperbolic	$k < -1$
Parabolic	$k = -1$
Prolate elliptical	$0 > k > -1$
Spherical	$k = 0$
Oblate elliptical	$k > 0$

Table 3.1: Relation between the shape of the lens profile and the conic constant value.

Over 1 mm diameter, the plano-convex microlens, illustrated in Fig. 3.3, presents an aspherical profile with $k = -1.12$ of conic constant - i.e., hyperbolic microlens profile. The surface topography measurement is a powerful tool for the characterization of micro-optical components. It provides accurate results and, further, assuming an homogeneous distribution of the refractive index of the microlens, the generated wavefront can be retrieved - e.g., by ray tracing. Furthermore, an estimation of the surface roughness R_a over the whole surface can be calculated [166]. However, this technique presents two non-negligible limitations and drawbacks in the case of micro-optical elements characterization. Indeed, this technique allows a quality estimation of only one surface - i.e., it is not adapted for the characterization of optical systems. Also, this technique is sensitive to optical properties of the surface materials [111, 152]. Indeed, if the object surface consists of two different materials, a phase difference will be introduced upon the reflection. This is explained by the imaginary part of their refractive index which is dependent of the wavelength. Nevertheless, this limitation does not exist for non-absorbing dielectric materials (with a null imaginary part of refractive index) [111]. Furthermore, if the thickness of the object is smaller than the coherence length of the light source - i.e., less than $3 \mu\text{m}$ - this could lead to interference artifacts between both layers, yielding to a difficult envelope detection [111]. Finally, this technique is usually geometrically limited to rather low numerical aperture of the measured components. Even if the NA of the objective is higher than the one of the lens under investigation, high slopes avoid distinguishing the interference pattern - i.e., interference fringe spacing decreases - carrying on an incorrect measurement of the contrast [167]. A compromise has to be found between the lateral FOV and the numerical aperture of the microlens. Figure 3.4 shows an example of this effect through the topography measurement of a high numerical aperture micro-ball lens. Here, the NA of the objective lens is 0.1.

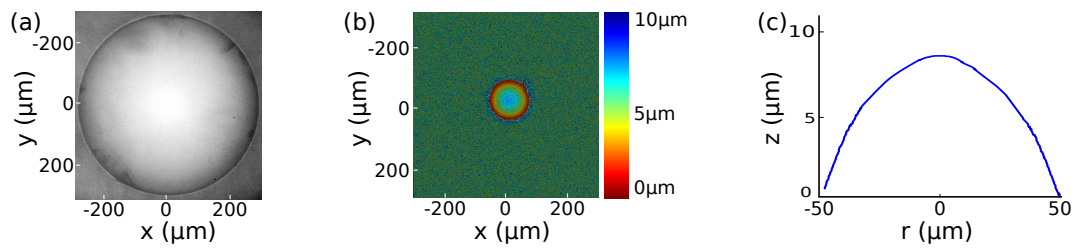


Figure 3.4: Surface topography characterization of a micro-ball lens ($NA = 0.56$) using the CSIM technique. Comparison between (a) a photograph and (b) the surface topography measurement of the microlens reveals the limit. Plot, in (c), shows the spherical profile of the microlens which is typical for ball lens.

The real diameter of the lens is $596 \mu\text{m}$ whereas the measured FOV equals $100 \mu\text{m}$. To be noticed, the diameter from the manufacturer data-sheet, is $600 \mu\text{m}$. Thus, only a small part of the lens surface can be visualized. Moreover, surface topography technique is not sufficient and optical characteristics have to be derived from the measured geometry using optical propagation algorithms (ray-tracing or diffraction theory).

The performances of the CSIM are summarized in Tab. 3.2.

Performances	NA = 0.1	NA = 0.3
Measurement axial range	$250 \mu\text{m}$	$250 \mu\text{m}$
Axial increment	3 nm	3 nm
Lateral FOV	$2.2 \times 1.6 \text{ mm}$	$740 \times 550 \mu\text{m}^2$
Lateral resolution	$4.2 \mu\text{m}$	$2.1 \mu\text{m}$

Table 3.2: Performances of the coherence scanning interference microscopy technique.

3.1.2/ OPTICAL PERFORMANCE EVALUATION THROUGH POINT SPREAD FUNCTION

In order to overpass the limits of the surface topography measurement, we proposed to characterize the micro-optical components by measuring the transmitted (or reflected) generated beam by the focusing optical element itself. Indeed, the capacity of the micro-optical element to transform the incident beam provides information onto its optical performances. This characterization method is then based on the point spread function (PSF) measurement. This direct characterization of focusing response through the measurement of PSF, allows estimation of the optical quality, leading to identification

of aberrations, as well as measurements of parameters such as spot size and radius of curvature (RoC). The PSF has already been employed as a characterization tool for complex transmissive optical systems like confocal microscopes [168, 169] or objectives [170, 171]. In this manuscript, this approach has been adapted to build a simple setup for micro-optics characterization, in particular microlens.

The optical setup, shown in Fig. 3.5, consists of a temporally and spatially coherent light source and an imaging system. Indeed, the beam emerging from the He-Ne LASER source ($\lambda=632.8$ nm) is spatially filtered and expanded in order to get a single source point - i.e., a flat wavefront incident onto the sample. The diameter of the output beam is in the order of few millimeters and is larger than the pupil aperture of the measurement system assuring its uniform illumination. A half-wave plate and a polarizer P are added to adjust the intensity of the incident beam. The expanded probing beam is reflected by two mirrors to be easily directed onto the micro-optical element. The focused spot is collected by the microscope objective MO (Nikon CF Plan, x50/0.45 SLWD) and projected by the tube lens TL ($f' = 125$ mm) onto the CMOS camera (μ Eye UI-1240SE from IDS). The microscope objective, playing the role of collection lens, provides a high numerical aperture (NA) to the imaging system and a large magnification. In order to obtain data about the whole investigated micro-optical element, the numerical aperture of the microscope objective has to be higher than the numerical aperture of the investigated sample. Otherwise, only a part of the sample is characterized. MO, TL and camera are part of the imaging system which is axially displaced in order to acquire the different slices of the through-focus. This translation is achieved by a servo motor (Ealing 37-1104) whose minimum incremental motion and travel range are 50 nm and 25 mm, respectively. The step size is then adjusted depending on the NA of the investigated element in order to record typically 100 to 200 slices around the focal plane. The camera and the motor are controlled by a computer, for which system control and data processing have been programmed in Python language [172]. The image of each focus slice is then recorded by the CMOS camera. Since the dynamic range of the CMOS sensor (8 bits) is not sufficient to register the rapidly changing structure along the optical axis, the dynamic range is improved by recording multiple frames of each focus slices with different exposure times [173]. In here, 6 consecutive frames (with exposures varying from 0.05 ms to 100 ms) are recorded and the final image is reconstructed from multi-exposure data. The reconstruction involves images normalization (according to exposure time) of the different frames, followed by frames averaging with exclusion of saturated or under-threshold pixels. This method allows increasing significantly the dynamic range while minimizing the noise level. To be noticed that, in practice, locating precisely the focal plane can be difficult. When the focal volume data is recorded the

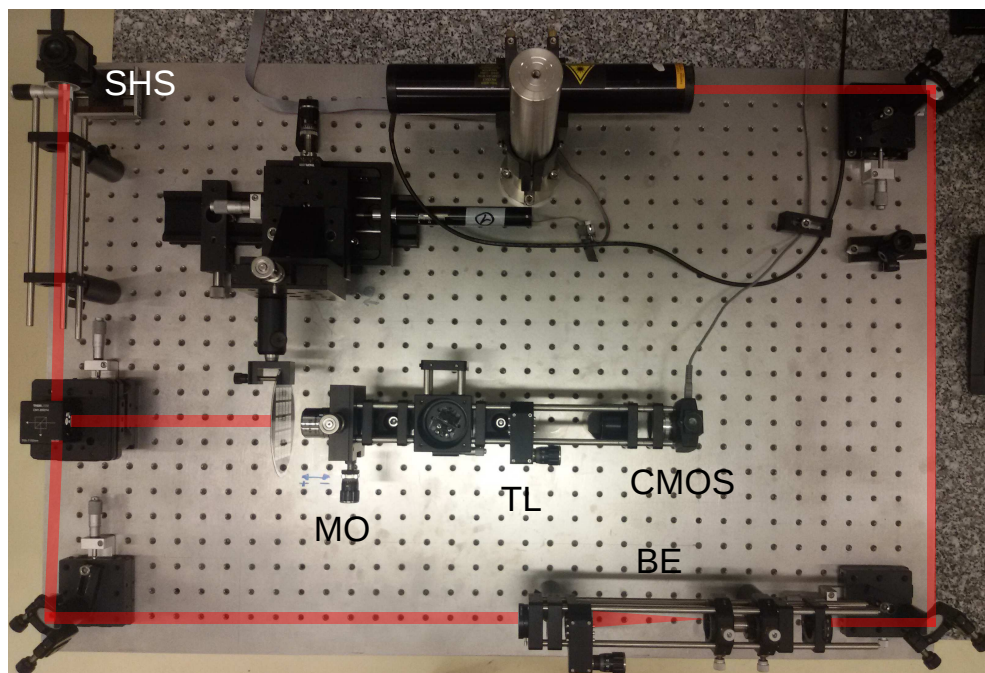
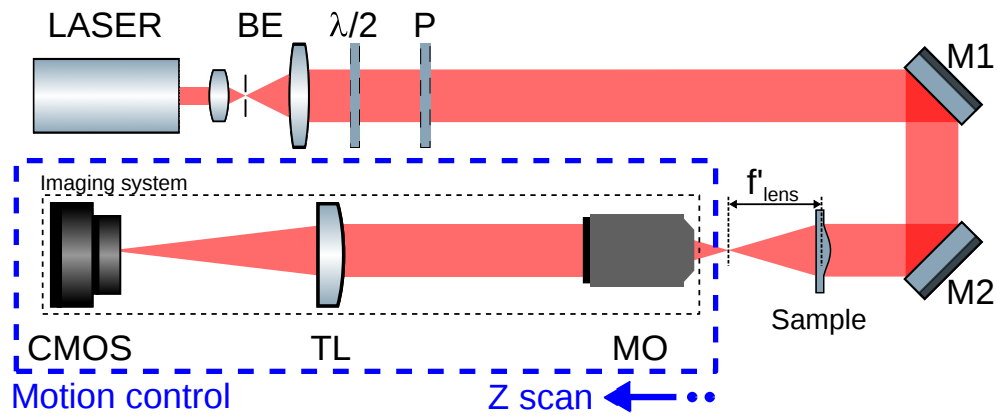


Figure 3.5: Scheme and photograph of the experimental setup based on the PSF measurement. Two mirrors M1 and M2 direct the probing beam, emerging from the point-light source onto the microlens to be tested. Then, the imaging system which consists of a microscope objective MO, a tube lens TL and a CMOS camera, records the transverse intensity distribution at a given position. The imaging system is axially displaced in order to record the focal volume of the microlens. It can be noted that a Shack-Hartmann sensor SHS is added to assure both a flat wavefront and a good quality of the probing beam, although not necessary for the measurements. Thus, experimentally, M2 is changed by a beam-splitter cube.

desired spot radius or Strehl ratio can be calculated for all collected slices and the real position of focal plane can be easily identified.

The recorded focal volume can provide several information about the inspected optical component performances. Indeed, by analysing the PSF geometrical spreading,

the resolution can be derived. The optical resolution can then be defined in different ways such as full width at half maximum (FWHM) or radius encircling a certain amount of energy. The FWHM is given by the relation

$$\delta_{FWHM} = \frac{1.03}{2} \frac{\lambda}{NA} \approx \frac{\lambda}{2NA} \approx \frac{1}{f_c} \quad (3.2)$$

where λ and NA are the wavelength of the light source and the numerical aperture of the optical system, respectively. In this manuscript, the FWHM criterion has been retained to determine the lateral resolution due to its easy deduction from the PSF measurement. By Fourier transform the in-focus PSF, the modulation transfer function (MTF) can be obtained as well as the cut-off frequency f_c . This is the frequency for which the contrast is zero [174, 175]. The expression of the FWHM-based resolution is quite similar to the inverse of the cut-off frequency (Abbe criterion) from the MTF.

Another parameter that can be extracted from the measured PSF data is the Strehl Ratio that quantifies contrast (peak intensity value of the PSF) in comparison to a perfect optical component having the same numerical aperture [176].

$$SR = \frac{\max(PSF)}{P_{tot} \pi \frac{NA_m^2}{\lambda^2}} \quad (3.3)$$

where, $\max(PSF)$ is the peak intensity in the 3D focus pattern, P_{tot} is the total power of the beam and NA_m is the numerical aperture of the micro optical element. Both $\max(PSF)$ and P_{tot} can be obtained from the focal plane frame. Total power is calculated by integrating the intensity over the whole focal plane. To perform this, the total power can be approximated by the sum of the intensity values recorded by the camera [177]. Peak intensity is taken as the maximal value in the measured frame. For an imaging application, it can be considered that a lens should have a SR of at least 0.8 [178]. In this case, according to [179, 180], the optical system is considered as "diffraction-limited". The relation between the criteria and the SR value are reported in Tab. 3.3.

Furthermore, for low aberration systems, it is possible to derive , the root mean square (RMS) of the wavefront generated by the lens, from the SR value. Indeed, the SR is defined by a statistical measure of the aberration function - i.e., the RMS wavefront RMS_Φ related by Maréchal's Strehl approximation [181].

$$SR = e^{-(RMS_\Phi)^2} \quad RMS_\Phi < \lambda/14 \quad (3.4)$$

Sometimes, the Maréchal criterion is defined in term of maximal optical path difference (OPD) error with a spherical fit wavefront and expressed in the peak-to-valley (PV). This is named Rayleigh criterion. The RMS of the wavefront deviation is the most common aberration quantification. Nevertheless, in case of higher wavefront deformation, a calculation error occurs due to the mathematical approximation. Hence, the smaller SR values do not correlate with imaging quality. Table 3.3 presents the relation between the SR and the RMS values according to important criteria.

Strehl ratio (unit-less)	RMS (wave)	Criterion
0.96	$\lambda/32$	
0.82	$\frac{\sqrt{0.2}}{2\pi} \lambda \approx \lambda/14$	Maréchal
0.8	$\lambda/13.4$	Diffraction limited
0.4	$\approx \lambda/7$	

Table 3.3: Relation between the Strehl ratio and the root mean square of the wavefront.

The SR of the microscope objective, used in the imaging system, has been determined to evaluate its quality. It results in 0.96, corresponding to $\sigma_{\Phi} \approx \frac{\lambda}{32}$ [177]. This is most of time negligible compared to the micro-component under test. This value demonstrates the high quality of our imaging system [179].

Moreover, the optical arrangement may be modified in order to provide the real value of RoC through reflective configuration [165, 177, 182]. Therefore, without modification of the optical system, a beam-splitter cube BS2 is placed between the microscope objective and the tube lens of the imaging system. It can be noticed that the beam-splitter cube does not deteriorate the optical beam quality thanks to the infinite conjugate configuration of the imaging objective. Figure 3.6 illustrates the optical arrangement of the reflective configuration and the RoC measurement principle. RoC is the distance between both the confocal and the cat's eye locations. In order to find these positions, the micro-optical component is axially displaced by the same motor than the transmissive measurements. Furthermore, to address the misalignment of the optical system (object and imaging system), the intensity of each recorded frame is numerically integrated over a digital circular pinhole [177]. The diameter of the pinhole is the FWHM of the beam in the focal plane. This task requires to identify the beam center for each recorded intensity slice.

To assure performances of the PSF characterization system, measurements of the

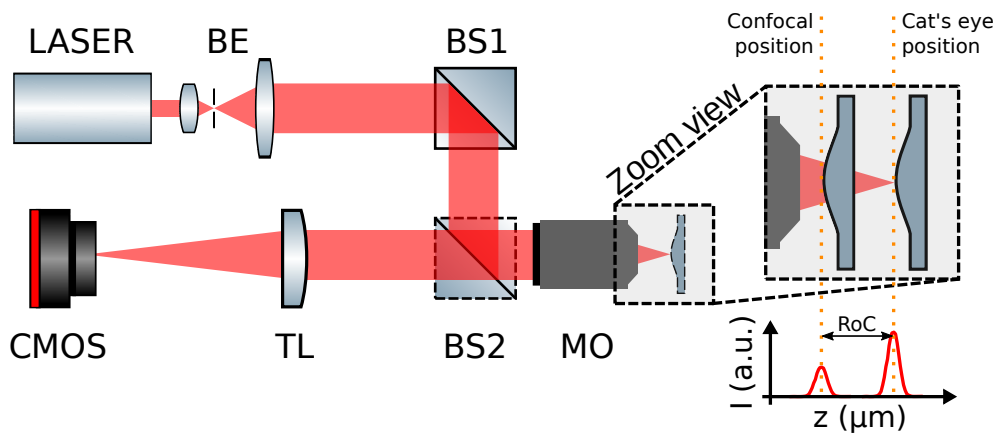


Figure 3.6: Measurement of the radius of curvature of a microlens. This reflective optical arrangement is quite similar to the transmissive one. The probing beam emerging from the LASER and the beam expander BE, is directed by two beam-splitter cubes BS1 and BS2 onto the microlens to be tested. Then, the microscope objective MO and the tube lens TL captures and images each intensity slice onto the CMOS camera, respectively. By axially displacing the object, the confocal and the cat's eye positions are found. The distance between these two locations is called radius of curvature. It can be noted that the lens was used without any additional reflective coatings.

performances of the ball micro-lens used with the CSIM technique, has been performed. According to the manufacturer, the diameter and the NA of the lens are $600 \mu\text{m}$ and 0.56, respectively. A fine needle has been employed to held the ball micro-lens.

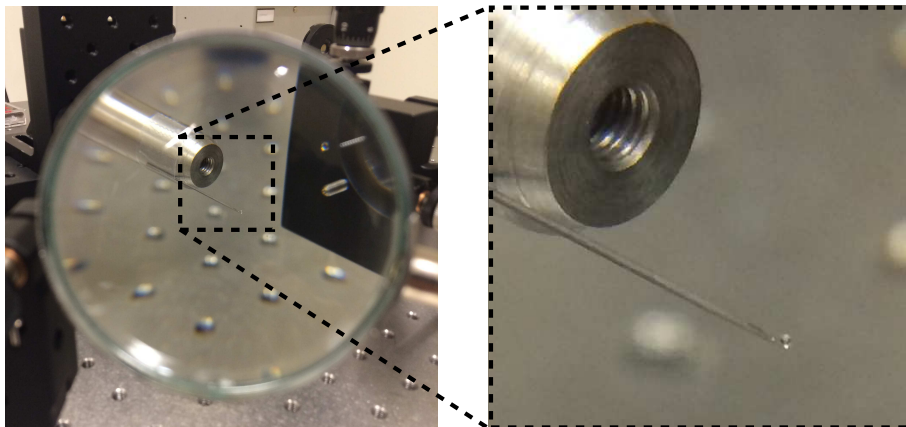


Figure 3.7: Photograph and zoom-view of the ball micro-lens.

Fig 3.8 exposes the measurement results. Here, due to the lower NA of the microscope objective ($\text{NA}=0.45$) than the one of the tested microlens, only a part of the lens is illuminated. It is equivalent to the conditions of use when the lens is illuminated by a probing beam whose the diameter is $300 \mu\text{m}$. The axial, in Fig. 3.8 (a), as well as the transverse, in Fig. 3.8 (b), cross sections allow determining both the axial and the lateral resolutions of the microlens which are $1.0 \mu\text{m}$ and $1.7 \mu\text{m}$, respectively. Also, Fig. 3.8 (c)

is the two dimensional MTF and Fig. 3.8 (d), the cross-sections according to horizontal, vertical and diagonal axes. The NA of the microlens is calculated by retrieving the cut-off frequency f_c . According to the MTF plots, the cut-off frequency equals $0.93 \text{ 1/}\mu\text{m}$, leading to $1.07 \mu\text{m}$ and 0.340 of lateral resolution and numerical aperture, respectively. This results are in good agreement with the FWHM based resolution measurement - i.e., resolution of $1.0 \mu\text{m}$ - and the data provided by the manufacturer - i.e., $\text{NA} = 0.33$ for $300 \mu\text{m}$ diameter. Moreover, the SR value of the micro-ball lens equals 0.26 which is low for an imaging system but acceptable for the main application of this kind of lens - i.e., optical fiber coupling. According to the reflective configuration procedure, the RoC of the micro-ball lens measured equals $296.8 \pm 0.8 \mu\text{m}$. The RoC value is consistent with the expected one given by the manufacturer - i.e., $\text{RoC} = \text{diameter}/2 = 300 \mu\text{m}$.

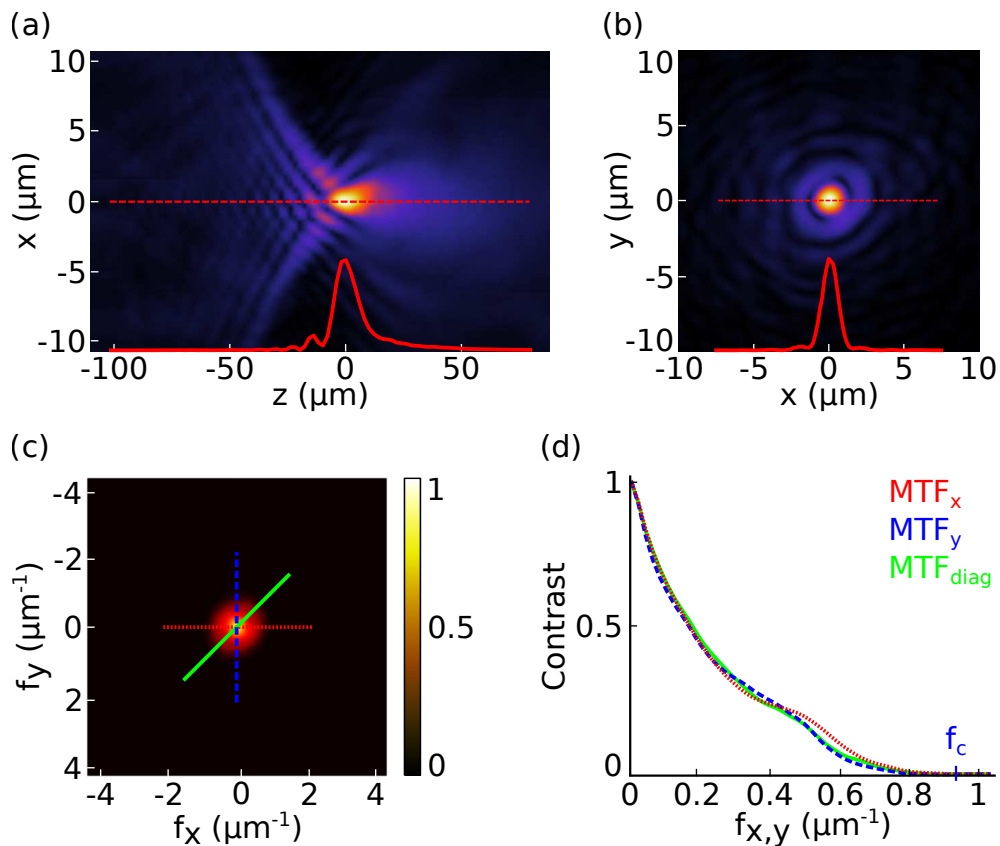


Figure 3.8: Measurement of $600 \mu\text{m}$ diameter ball microlens using the PSF technique. Results of (a) xz and of (b) xy (in focal plane) cross sections of the focal volume are exposed. The red color lines are the intensity distribution according to the red dotted line. The MTF in the focal plane is retrieved by Fourier transform. (c) The two dimensional MTF and (d) the MTF profiles following three angular directions are represented.

By visualizing the longitudinal cross section of the focal volume, a lack of symmetry with respect to the focal plane is attributed to the wavefront aberrations introduced by the microlens. Such strong asymmetry is the signature of a significant spherical aberration.

However, the qualitative (visual) assessment of the PSF shape can only indicate the presence of aberrations.

3.1.3/ WAVEFRONT QUALITY THROUGH PHASE RETRIEVAL METHOD

The PSF characterization technique allows visualizing and qualifying the optical aberrations generated by a micro-optical component or a more complex micro-optical system. This method aims to be simple, not expensive, and easy to setup. Moreover, assuming low aberration optical element, the wavefront RMS, through the calculation of the SR, can be quantified [177]. However, it remains quite qualitative and not enough quantitative. Consequently, in order to quantify the wavefront deformation - i.e., the two dimensional representation of the wavefront distribution - and to derive Zernike coefficients, the PSF technique has been improved by performing an iterative phase retrieval (IPR) algorithm [183]. Wavefront deformation introduced by the microlens is a good criterion to determine the quality of focusing optical elements.

Coherent interferometry provides the wavefront distribution by measuring the phase difference between an object beam and a reference beam [184]. It allows retrieving the wavefront generated by the microlens with high axial and lateral resolutions (few nanometers). However, it usually necessitates a complex optical setup and is highly sensible to external vibrations. Another well-known technique is the direct wavefront sampling using a Shack-Hartmann sensor [185]. Nevertheless, because of the small size of micro-components, the probing beam has to be downsized in order to be equivalent to the microlens size and then, magnified to match, e.g. the Shack-Hartmann sensor aperture [186]. These operations may introduce additional optical aberrations. In this manuscript, a well-known technique has been implemented from the PSF measurements for the measurement of the wavefront generated by microlenses. Indeed, often-used in astronomy, crystallography and optics, we have adapted the iterative phase retrieval method for the characterization of single microlens or more-complex micro-optical system, and then, the determination of the optical aberrations. The IPR technique can provide the phase distribution if at least two separated intensity measurement planes are available. The first phase retrieval algorithms were initially developed for the phase reconstruction using two intensity planes that are Fourier transform pairs [187]. In this work, the through-focus generated by the microlens is considered [188, 189, 190]. This simple approach can be applied for characterizing efficiently and extensively micro-optical components while benefiting from the intuitive and easy setup dedicated to through-focus measurements. Moreover, it provides a comparable accuracy and spatial resolution as digital interferometric techniques [191, 192] although requiring

simpler optical arrangements and cheaper optical components than the ones based on more conventional interferometers or Shack-Hartmann sensors. Furthermore, by decomposing the retrieved wavefront in series of Zernike functions, we show that the optical aberrations can be quantified [193].

Mathematically, the three dimensional propagation of a wave in a free space is described by the Helmholtz equation [194]. In the conditions of paraxial approximation and assuming a plane wave propagating along the z axis, the Helmholtz equation results in a complex electric field $E(\rho, \theta, z)$ given by the relation

$$E(\rho, \theta, z) = \sqrt{I(\rho, \theta, z)} \exp[j\phi(\rho, \theta, z)] \quad (3.5)$$

Both terms ρ and θ are the normalized radial and azimuthal coordinates in the transverse planes. The modulus of the transverse electric field is defined as the square root of the intensity $I(\rho, \theta, z)$ and $\phi(\rho, \theta, z)$ is the phase deviation to recover. The principle of the IPR technique [189] is based on this relationship between the complex electric field $E(\rho, \theta, z)$, and the $\phi(\rho, \theta, z)$ term (Eq. 3.5) and the angular spectrum approach.

$$I(\rho, \theta, z) \propto \left| \mathcal{F}^{-1} \left\{ \left| \mathcal{F} \{ E_0(\rho, \theta, z = 0) \} \right| \exp(jk_z z) \right\} \right|^2 \quad (3.6)$$

Where, \mathcal{F} and \mathcal{F}^{-1} are the Fourier transform and the inverse Fourier transform operators, respectively. In other words, assuming the knowledge of at least two intensity planes, this IPR technique can provide the phase distribution in the pupil plane. However, it is preferable to use multiple intensity measurements in order to increase the calculation robustness and to better converge to the solution of the phase distribution.

Figure 3.9 describes the algorithm flowchart of IPR technique. Starting with an initial phase distribution $\phi_i(\rho, \theta)$ (commonly a two dimensional array of random numbers between π and $-\pi$) and an amplitude, defined as the square root of the intensity of the slice $s = 0$, the transverse electric field in the initial plane $E(\rho, \theta, z = 0)$ is computed. This electric field is propagated in the plane $s = 1$ according to the angular spectrum approach. Preserving the phase $\phi(\rho, \theta)$, the modulus is corrected by the known amplitude value $\sqrt{I(\rho, \theta, z = z_1)}$. Then, the electric field $\tilde{E}(\rho, \theta, z = z_1)$ is back-propagated in the initial plane ($s = 0$). Again, the modulus of the electric field in the initial plane is changed according to $\sqrt{I(\rho, \theta, z = 0)}$. These wavefront reconstruction cycles are repeated depending on the number of intensity planes s . At the end of a complete cycle, both convergence of the algorithm σ and root mean square error (RMSE) are estimated. σ is the difference between the current retrieved phase and the previous one, whereas RMSE is defined between the current retrieved phase $\phi_{current}$ and the predicted one

$\phi_{expected}$ [195]. The RMSE is used to represent the accuracy of the reconstructed phase - i.e., when the RMSE is almost perfectly zero - the correct phase is retrieved.

$$RMSE = \sqrt{\sum(\phi_{current} - \phi_{expected})^2} \quad (3.7)$$

Then, the phase reconstruction procedure is reiterated until a convergence is observed - i.e., σ tends to zero. In addition, in order to extract the optical aberrations, the retrieved phase distribution can be decomposed in a series of N-number Zernike circle polynomial functions $Z_n(\rho, \theta)$ [193, 196, 197].

$$\phi(\rho, \theta) = \sum_{n=0}^N c_n Z_n(\rho, \theta) \quad (3.8)$$

with n , a positive integer corresponding to Noll index, and c_n , the coefficients of the Zernike function Z_n . The first four Zernike modes represent a displacement of the focal plane from its optimal position, whereas, the others modes depict a modification of the shape of the wavefront and thus changes both the lateral and the axial resolutions. More details on the Zernike polynomial decomposition are presented in Annex 4.5.

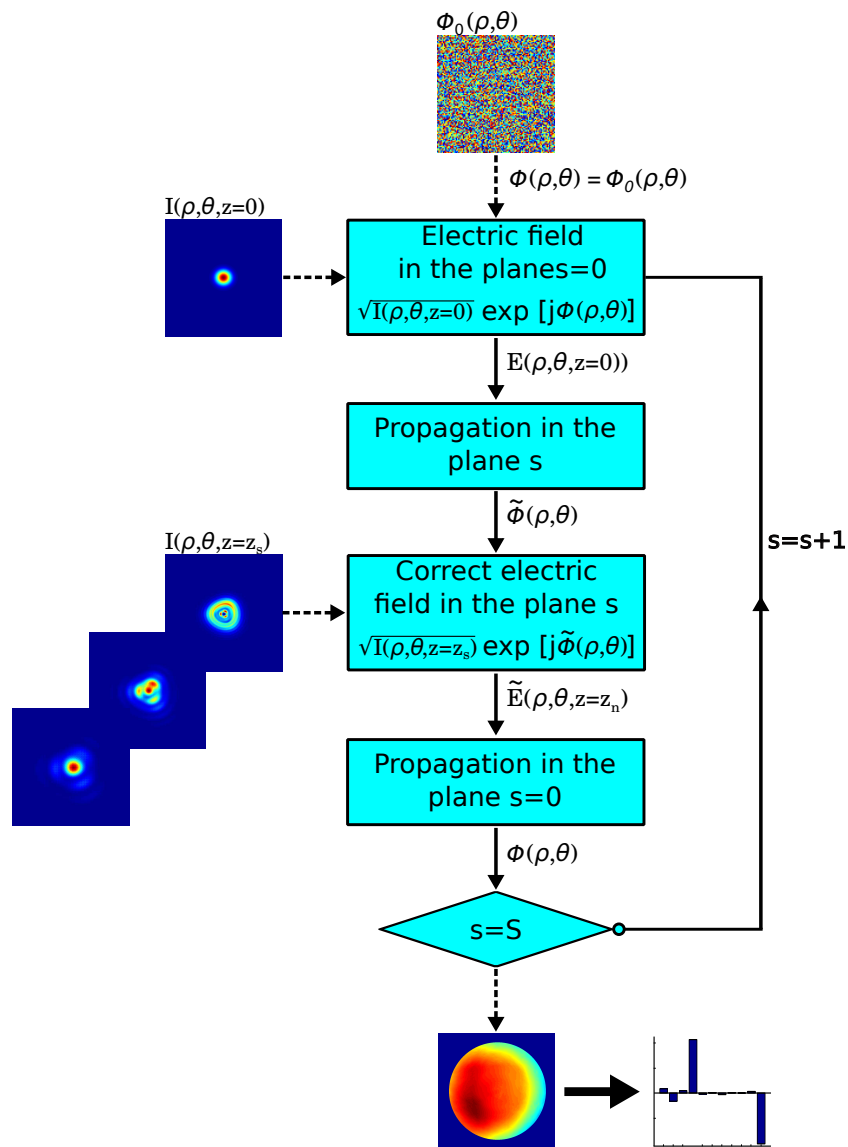


Figure 3.9: Diagram of the principle of the IPR algorithm. Only one iteration cycle on the measurements has been drawn. At the end of the calculation process, this algorithm may be iterate depending onto both RMSE and σ values.

The measurement procedure starts with the recording of through-focus slices according to the method described in the previous section. In addition, in order to retrieve low-frequency wavefront information, five derived intensity planes exponentially-spaced along the optical axis are kept [198, 199]. Then, the IPR algorithm is applied and processed as in Fig. 3.9. The NA of the microlens to be tested is limited by the one of the microscope objective, as well as the sampling of the imaging system. The latter depends onto the detector pixel size Δx , the wavelength λ , the magnification of the imaging sys-

tem γ and the Nyquist sampling Q [200]. It is given by the relation

$$NA_{\text{samp}} \leq \frac{\gamma \lambda}{2 Q \Delta x} \quad (3.9)$$

In our case, the maximal value of NA equals 0.8, which is higher than the maximal NA value of the microscope objective.

A comparison between both the IPR and a more conventional coherent interferometric technique, has been experimentally implemented. The characterized sample is the ball microlens, with 596 μm diameter and 0.56 numerical aperture. We can note that the numerical aperture of the microlens to be tested is not limited by the sampling but only by the NA of the microscope objective of the intermediate imaging system (NA = 0.45). The architecture of the interferometer used for the comparison is Mach-Zehnder - i.e., in transmissive off-axis configuration [184]. Furthermore, a modeling of the beam propagated by the considered microlens has been performed using the ray tracing Zemax software (Zemax LLC). The calculated wavefront as well as the measured ones results, with the interferometry and with the IPR, are exposed in Fig. 3.10 (a), (b) and (c), respectively. The wavefront distribution is unwrapped [201, 202] and normalized to 2π . As it can be seen, despite a small horizontal distortion of the two measured wavefront distributions, they are in good agreement with the simulated prediction. This is attributed to the influence of the holder of the microlens. Indeed, the micro-ball lens has been glued onto a fine needle, leading to a distortion of the transmitted beam. Then, the Noll's coefficients (third order) are then extracted by using the Zernike polynomial decomposition. Zernike Noll's coefficients are shown in blue (simulation), green (interferometry) and red (IPR) color bar [193]. It has to be underlined that the first four Noll terms have been ignored and numerically removed. Indeed, they are related to the misalignment of the microlens during the test [179, 203]. As expected, the ball microlens introduces optical aberrations and in particular spherical aberrations (eleventh Noll index). This reaches one wave of amplitude. Furthermore, due to the distortion of the wavefront, the experimental Noll's coefficients of the vertical astigmatism (sixth Noll index) and the vertical coma (seventh Noll index) are high. Theoretically, the RMS wavefront is 0.92λ , whereas, experimentally, it is 1.03λ and 1.02λ . The results, from interferometry and IPR, are in good agreement with the simulation one. Moreover, despite a much simpler implementation, the IPR is a powerful technique for micro-optical components characterization, which provides similar results compared to interferometric technique.

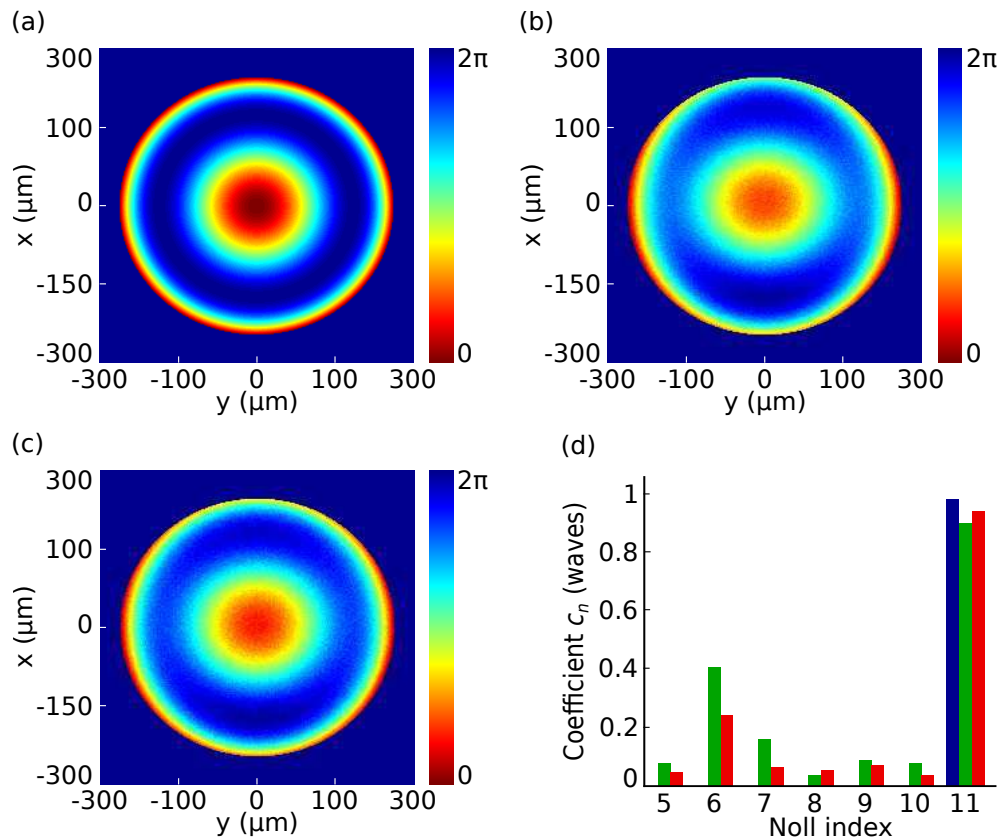


Figure 3.10: Wavefront distributions of (a) the numerical simulation, (b) the coherent interferometric and (c) the IPR techniques. In (d), Noll's coefficients from simulation (blue), from the interferometry (green) and IPR (red) are shown.

3.2/ INSPECTION OF THE MIRAU MICRO-INTERFEROMETER

Using these characterization techniques, the micro-optical components of the Mirau interferometer - i.e., the doublet of microlenses and the reference mirror - were characterized in order to insure a good imaging quality and to agree with the specifications of the optical design. Firstly, the performances of the objective microlenses, in terms of resolutions, of imaging depth and aberrations, are determined. Also, the performances of the micro-scanner which consists on the reference mirror and the spiders, are evaluated. The surface topography of the mirror, the impact of the spiders onto the imaging quality and the displacement parameters are measured. Then, after the vertical assembly of the MOEMS components, the Mirau micro-interferometer has been inspected. Consequently, this section is dedicated to the results of the characterization of both individual micro-optical components and the complete Mirau micro-interferometer.

3.2.1/ CHARACTERIZATION OF THE DOUBLET OF MICROLENS

According to the specifications of the design, the NA of the doublet of microlenses has to equal 0.1. Furthermore, the objective lens has to provide a lateral resolution of $6\mu\text{m}$ over $400 \times 400 \mu\text{m}^2$. Also, the depth of field should be of $90 \mu\text{m}$. Therefore, the optical quality of the doublet of microlenses has been analyzed using the three characterization techniques proposed.

Firstly, the surface topography of the two microlenses of the doublet was measured with the CSIM. The results are exposed in Fig. 3.11 (a). As it was expected, the sagittal height values are not uniform over the entire wafer. This non-uniformity could be explained by the temperature gradient oven during the re-flow process. However, the sag values inside each matrix are similar and vary slightly (standard deviation of the sag measurements is less than 0.02%). In details, the sag of a microlens is around $65 \mu\text{m} \pm 0.5 \mu\text{m}$ within a matrix and $\pm 1.0 \mu\text{m}$ over the wafer. Then, the measured profiles were fitted using a parabolic function to evaluate the maximum usable diameter according to the Maréchal criterion - i.e., to provide a RMS less than $\lambda/14$. The optimal conic constant has been calculated and results in $k = -1.02$. Through this measurement, we can define the microlens type as aspherical. This criterion limits thus the effective diameter to 1.5 mm. Thereafter, an aperture stop is located in front of the lens during the characterization tests.

Secondly, the doublet of microlenses has been characterized with the PSF and the IPR techniques. The optical aberrations, generated by the doublet of microlenses, have been measured using the IPR technique. Figure 3.11 (b) shows the Zernike Noll's coefficients where the first four indexes are not displayed. As it can be seen, the doublet of microlenses still presents non-negligible spherical aberrations. The corresponding RMS of the wavefront deviation equals 0.7λ . They slightly disturb the imaging quality of the micro-system. Nevertheless, it has been shown that it is twice lower than a simple lens of equivalent focal length [113]. In Fig. 3.11 (c), the two dimensional intensity distribution of the focal plane is shown. The lateral resolution of the microlens can be measured using the FWHM criterion. It equals $4.8 \mu\text{m}$. To be noticed that the measurements have been realized with a coherent illumination where the wavelength equals 633 nm. This means that the value is lower than using an incoherent near-infrared illumination as in the OCT system. As exposed in Fig. 3.11 (d), the depth of field of the microlens is $400 \mu\text{m}$ which is higher than the expected one from the design. Despite a reduction of the intensity distribution within the focal volume, leading to a low sensitivity of the OCT signal, the stretched depth of field could avoid to resort on many axial displacements and axial stitching of the Mirau head. Moreover, the Strehl ratio has been evaluated and

equals 0.34 which is low compared to a diffraction limited imaging system [181]. If the SR is higher than 0.4, the contrast at the limit resolution is still considered as visible. In reflective configuration, the RoC and then the focal length were measured. The focal length of the doublet equals 7.65 mm which is higher than the specified one in the design. This slight increase of the focal length as well as the diminution of the effective diameter of the lens could reduce the lateral resolution of the OCT system.

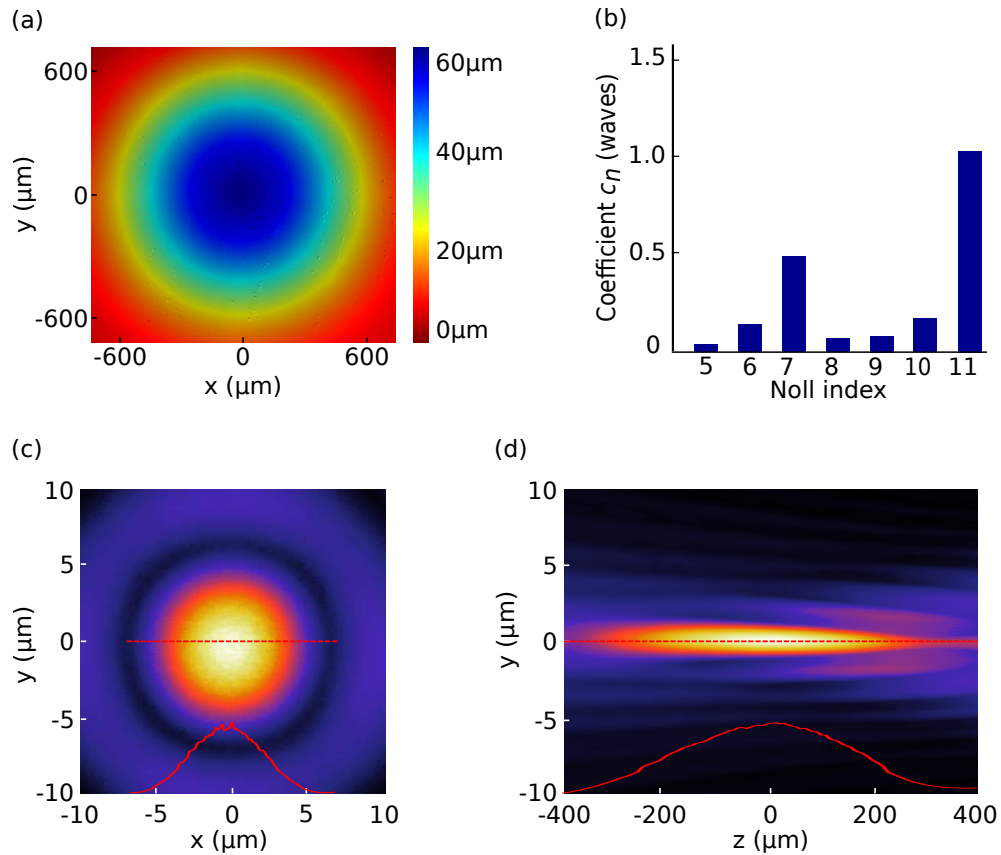


Figure 3.11: Characterization of single microlenses through the (a) CSIM and the doublet of microlenses using the (b) IPR and the (c-d) PSF techniques. This figure is extracted from [113].

Therefore, a measurement of the NA of the doublet has been achieved through the calculation of the MTF. Figure 3.12 illustrates the MTF of the doublet of microlenses from the in-focus PSF.

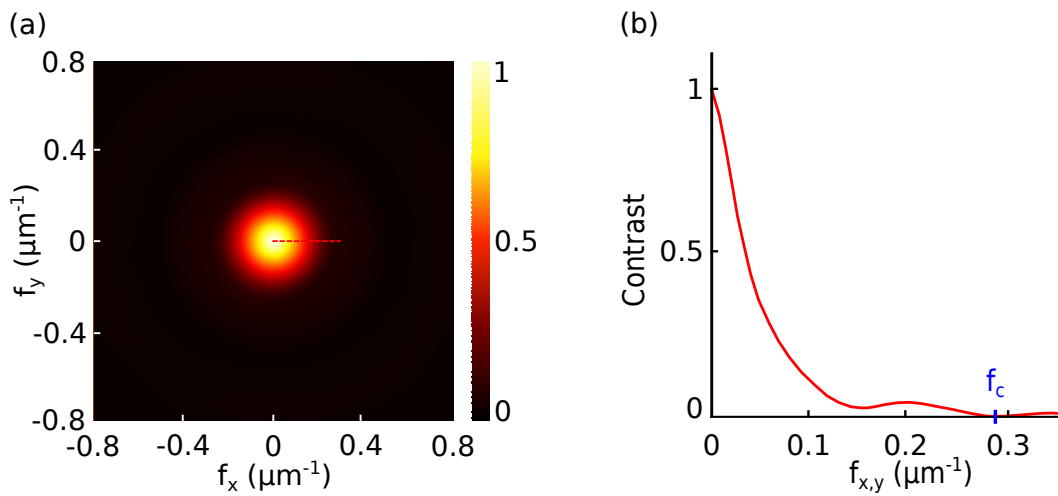


Figure 3.12: Normalized modulation transfer function of the doublet of microlenses. (a) The two dimensional MTF are calculated from the point spread function by Fourier transform and (b) the cross-section is plotted along frequency axis $f_{x,y}$.

The cut-off frequency f_c allows retrieving the NA of the microlens (see Annex 4.5). The measured f_c equals 0.28, yielding to 0.14 of NA. Thus, despite a decrease of the diameter of the lens pupil - i.e., effective diameter of 1.5 mm - the impact of the spherical aberrations [204], the NA is still in agreement with the design of the OCT system. Furthermore, the NA allows providing a lateral resolution which equals thus 6 μm at 840 nm of central wavelength. These results are in agreement with the expected ones presented in the optical design chapter.

The surface topography presents a high quality RMS ($RMS = \lambda/14$) whereas, the wavefront RMS ($RMS = 0.7\lambda$) is ten times higher which is weak for the specifications of an imaging system. For a plano-convex lens and assuming a constant refractive index within the lens, the wavefront distribution should be similar to the shape of the convex dioptré. Therefore, an analysis of the refractive index variation, at the end of the re-flow fabrication process, has been done in order to understand this loss. Hence, in order to evaluate the presence of an index of refraction variation, we compared the wavefront from the surface topography measurements (assuming a constant refractive index of 1.47 @ $\lambda = 632.8 \text{ nm}$) and from the IPR technique. The results is shown in Fig. 3.13 by illustrating the axial refractive index distribution of the lens. Usually, in microlens fabricated by etching or polishing, the refractive index should be constant. In here, because of the re-flow approach, a slight variation appears and the refractive index is reduced radially towards the center of the lens until a value of 1.445. This refractive index variation leads to a higher wavefront deviation and thus, a higher RMS value. This effect has already been reported for heated borosilicate glass [205] and could be due

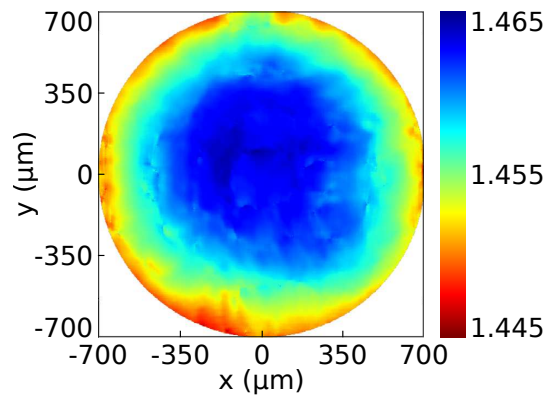


Figure 3.13: Two dimensional distribution of the refractive index after thermal processing of glass inside the silicon cavity. This figure is extracted from the manuscript "Dense arrays of millimeter-sized glass lenses fabricated at wafer-level", Albero [147].

to several reasons [147] such as migration of ions Na^+ , more thermally insulation of the center of the cavity or a local concentrations of other compounds than SiO_2 and B_2O_3 .

3.2.2/ CHARACTERIZATION OF THE MICRO-SCANNER

Afterwards, the micro-scanner - i.e., a platform carrying the reference mirror and vertically actuated by comb-drives - has been characterized to answer to the specifications. It should have a good reference surface quality and perform an axial displacement where the parameters are in compliance with the specified ones. Furthermore, the structure supporting - i.e., the area around the reference mirror - has to be transparent and should not degrade the imaging performances. Two solutions have been identified to carry the mirror, either a transparent glass membrane or suspensions. First solution is a real technological challenge in term of integration onto an actuated structure [150] whereas the second solution may introduce a decrease of the imaging performances. Thus, axial micro-scanner has been characterized to answer to the design requirements.

Firstly, the parameters of the displacement were estimated using the Doppler vibrometry technique (MSA500, Polytec) [206]. Indeed, for the sinusoidal phase shifting implementation, it is important to know the frequency and the amplitude of the displacement of all the mirrors. The dynamic displacement of the actuator and its spectral response have been retrieved. Firstly, the dynamic displacement of the platform at the resonant frequency was investigated at different points of the platform - i.e., at the position of the four micro-mirrors as shown in Fig. 3.14 (a). Therefore, a periodic chirp signal is applied to the four actuators and the vibrational response of the actuator is recorded. Then, by applying a sinusoidal excitation signal, the resonance frequency f_r is measured. The displacement as a function of the time and the spectral response of

the system of the platform are exposed in Fig. 3.14 (b) and (c), respectively. As it can be seen, a small deviation between the amplitude of displacement of each mirror occurs. The displacement error between the first and the fourth mirrors is 70 nm . This variation has no-impact onto the measurements of the OCT signal and onto the calculation of the depth profile. Indeed, the actuation of the reference mirror is made to phase shift the spectral interferometric signal and a variation of displacement leads to an offset which does not affect the phase shifting implementation. Afterwards, the frequency resonance of the platform is identified and equals 543 Hz with a high measured quality factor Q of 50 (at -3 dB). According to the design, the mirrors are actuated at the frequency resonance for low-voltage level and the frequency should be of 500 Hz. This slight difference can be compensated by working at a lower frequency by increasing the voltage value or by improving the frame rate of the camera.

Then, the surface topography of the reference mirrors has been investigated through the white-light interferometric profilometer. The surface profile of the reference mirror is plotted in Fig. 3.14 (d) where the radius of curvature was derived by fitting the curve and equals 700 mm. The deformation height equals 52 nm across the $400 \times 400 \mu\text{m}$ mirror surface. As demonstrated in Sec. 2.2, these variations - i.e., from the surface mirror and between each mirror - have a negligible impact onto the suppression ratio of the artifact terms. Furthermore, the reflection ratio of the gold-based mirror was measured and equals 97 %.

Finally, the impact of the diffraction introduced by the suspensions onto the PSF has been determined through the generated MTF. A compromise between the number, the width and the radius of curvature of arms as well as their obscuration has been first numerically simulated. It has been shown that three spiders configuration, where radius of curvature is $750 \mu\text{m}$ provides good performances in terms of the resolution symmetry and value. The contour profiles of the two dimensional MTF, at 0.8, 0.5, 0.26 and 0.2 contrasts, are shown in Fig. 3.14 (e). Then, experimental measurements were performed to confirm the simulation. As it can be seen in Fig. 3.14 (f), the experimental measurements match the simulation ones. It has been demonstrated that the impact of the diffraction effect has a low influence onto the quality of the PSF of the micro-interferometer.

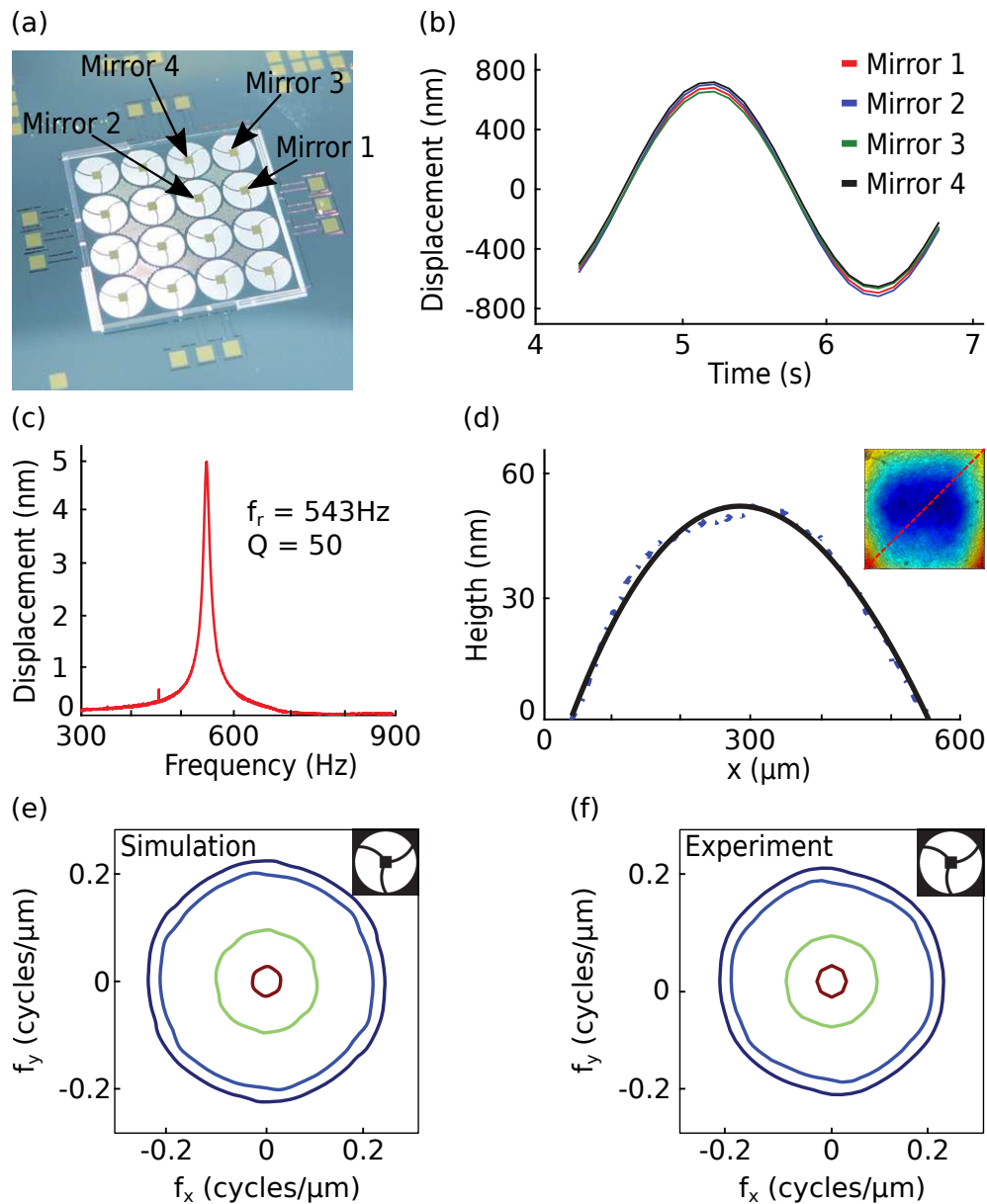


Figure 3.14: Characterization of the axial micro-scanner. Photograph of the micro-scanner is exposed in (a). (b) The axial displacement as a function of the time and (c) the spectral response are measured. (d) The diagonal profile of the surface topography is plotted. Furthermore, (e) the simulated and (f) the experimental MTFs are exposed. These figures are extracted from [145, 144].

3.2.3/ CHARACTERIZATION OF THE MIRAU MICRO-INTERFEROMETER

After analysing individually the micro-optical components, the wafer stack is then integrated by multi-wafer bonding and is diced to release the matrices of the Mirau micro-interferometers. Afterwards, the characterization of the complete interferometric system is realized to insure that the system has not been deteriorated during the assembling processes.

The imaging system is studied with the PSF system in order to determine the quality of its focal volume and in particular the resolution, the depth of focus and the Strehl ratio. The cross-section of the focal volume and the focal plane are displayed in Fig. 3.15 (a-b). The depth of focus of the doublet of microlenses has been determined by calculating the equivalent diameter and the FWHM. It results in $800\ \mu\text{m}$ and $400\ \mu\text{m}$, respectively [177]. The deviation between the two values is due to the optical aberrations generated by the microlenses. Indeed, the equivalent diameter takes into account the rings around the main intensity peak whereas the FWHM ignores them resulting in a smaller depth of focus. Thus, the imaging depth from the geometry is higher than the required one in the optical design which does not bring a limitation of the OCT measurement range. Nevertheless, as it can be seen, the intensity distribution, along the propagation axis, fluctuates. These intensity variations may lead to a degradation of the interferometric signal.

The lateral resolution of the doublet of microlenses equals $5\ \mu\text{m}$ at $632\ \text{nm}$ of wavelength. Compared to the doublet of microlens alone, this slight decrease of lateral resolution could be attributed to the diffraction effect from the reference mirror. Furthermore, the intensity in the first ring is not negligible and decreases the performances of the imaging system, in term of resolution and sensitivity. Indeed, the Strehl ratio is slightly decrease compared to one measured before the assembly of the array of interferometers (SR = 0.34). Here, it equals 0.32.

The potential of vertical actuation of the micro-scanner alone has been previously tested before the vertical integration of the Mirau micro-interferometer. Now, that it is integrated, the first and the second resonance frequencies are measured at $485\ \text{Hz}$ and $724\ \text{Hz}$, respectively. The spectral response of the integrated platform is exposed in Fig. 3.15 (c). The first resonance frequency corresponds to a piston mode motion of the vertical micro-scanner and is the mode used for the actuation of the vertical micro-scanner used as a phase modulator. As shown the resonance frequency is lower than the expected one which should be of $500\ \text{Hz}$. This lower value could allow increasing the exposure time of the camera and thus, improving the sensitivity of the OCT system. Furthermore, the quality factor of the vertical micro-scanner, typically measured around 50 before the integration, is here equal to 64. This high quality factor allows using low voltage of only $3\ \text{V}$ to actuate the reference mirror. The second peak is much higher than the one recorded on other chips before the integration. However, this second peak does not interfere with the dynamic behavior of the micro-scanner when the structure is excited at $485\ \text{Hz}$. The targeted peak to peak amplitude has also been achieved and equals $335\ \text{nm}$ at the first resonance frequency. This amplitude corresponds to an optimal

amplitude with respect to the phase modulation algorithm [144].

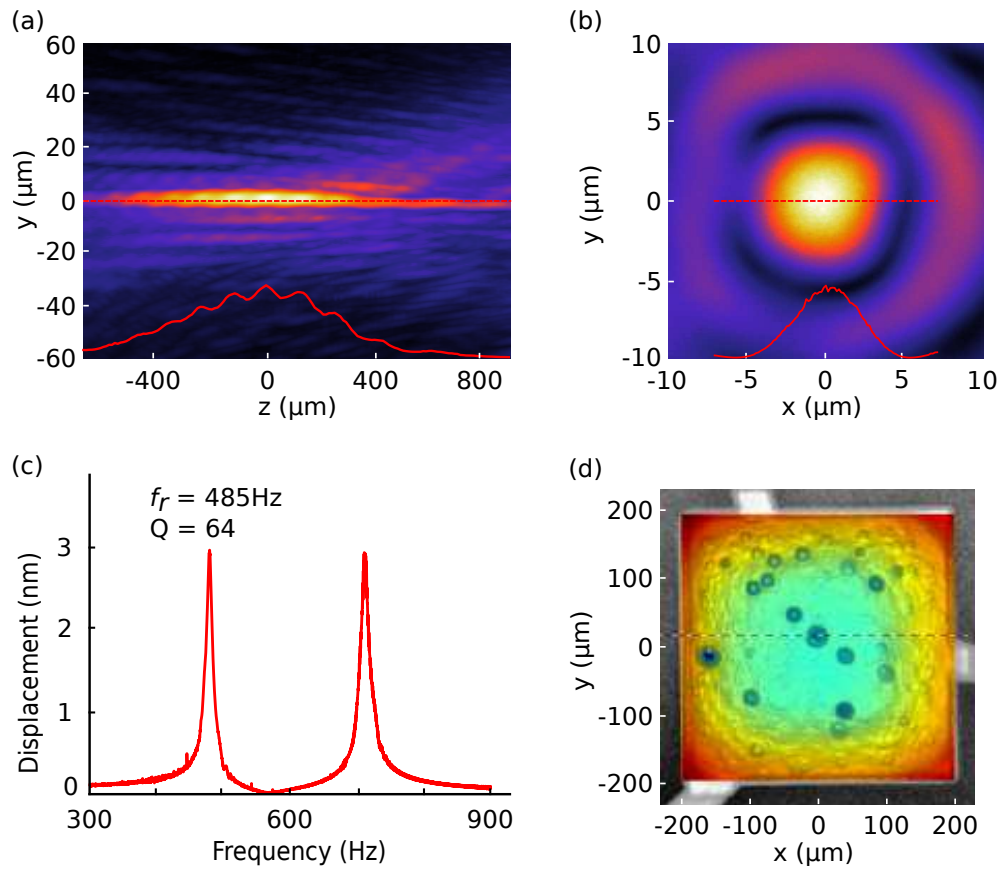


Figure 3.15: Characterization of the complete Mirau micro-interferometer. With the PSF technique, the cross-sections (a) along z-axis and (b) in the focal plane are retrieved. Through the MEMS analyser (MSA500, Polytec), (c) the spectral response of the micro-scanner can be measured. And (d) shows the surface topography of the reference mirror.

The two dimensional surface topography of the reference mirror is also measured and is shown in Fig. 3.15 (f). A good surface quality of the reference mirror leads to a good imaging performances of the Mirau system. The mirror is imaged through the planar beam-splitter where the thickness is of $500\ \mu\text{m}$. Thus, this thickness is compensated by placing a glass slide in the reference arm of the interferometric objective of the profiler. A substantial degradation of the micro-mirror quality with the apparition of black dots is observed after assembly of the Mirau interferometer. It is important to note that this degradation is not observed for all the micro-mirrors and further tests must be conducted to clearly understand the phenomena. The surface roughness of the micro-mirrors equals $3.1\ \text{nm}$ and $6.5\ \text{nm}$ before and after the bonding processes, respectively, with a cut-off wavelength of $0.25\ \text{mm}$. In comparison with the deformation of the mirror, this can be negligible.

Then, the capacity of the Mirau micro-interferometers to collect a two dimensional signal over the required lateral FOV - i.e., $400 \mu\text{m} \times 400 \mu\text{m}$ - is characterized by measuring the distortion of the image and the off-axis resolution. For this task, a 4F imaging system, which consists in the doublet of microlenses, a tube lens ($f' = 25 \text{ mm}$) and a camera, has been developed. Fig. 3.16 shows the optical setup. The incident beam is from a monochromatic spatially incoherent light source where the wavelength is 633 nm.

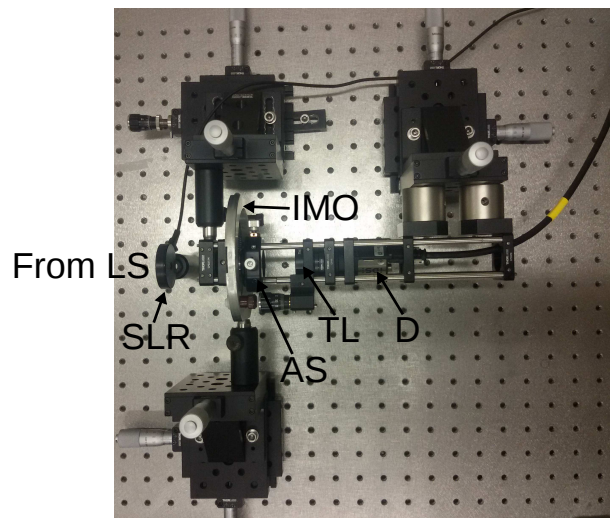


Figure 3.16: Photograph of the optical setup for the off-axis CTF measurement. The Ronchi ruling target or the distortion grid is illuminated by a monochromatic and spatially incoherent light source LS using a He-Ne LASER and a speckle laser reducer SLR. The microlens of the Mirau objective IMO collects the irradiance and image the pattern onto the camera D through the tube lens TL. An aperture stop AS is placed between IMO and TL.

Firstly, as shown in Fig. 3.17 (a), the Mirau objective lens yields to a distortion of the image of the grid ($50 \mu\text{m}$ pitch). The width of the lines is smaller in the center of the image than in the corner. As seen in Fig. 3.11, the doublet of microlenses presents spherical aberration (Z_{11}). These terms are not negligible for an imaging system and could lead to a distortion of the image as obtained here. Furthermore, depending on the orientation of the lines, the width is different at a given position. This could be explain by the combination of both the coma (Z_7) and the astigmatism (Z_{10}) aberrations. The optical aberrations provide a distortion of the image and thus affect the contrast transfer function (CTF) - i.e., contrast function using a square wave object (see Annex 4.5) - and the resolution of the system. In order to show the impact of the aberrations onto the contrast and the resolution loss, a Ronchi ruling pattern placed in the object focal plane of the imaging system. Figure 3.17(b) and (c) show the image of the Ronchi target with 80 l/mm and 140 l/mm intervals, respectively. As shown previously, the optical

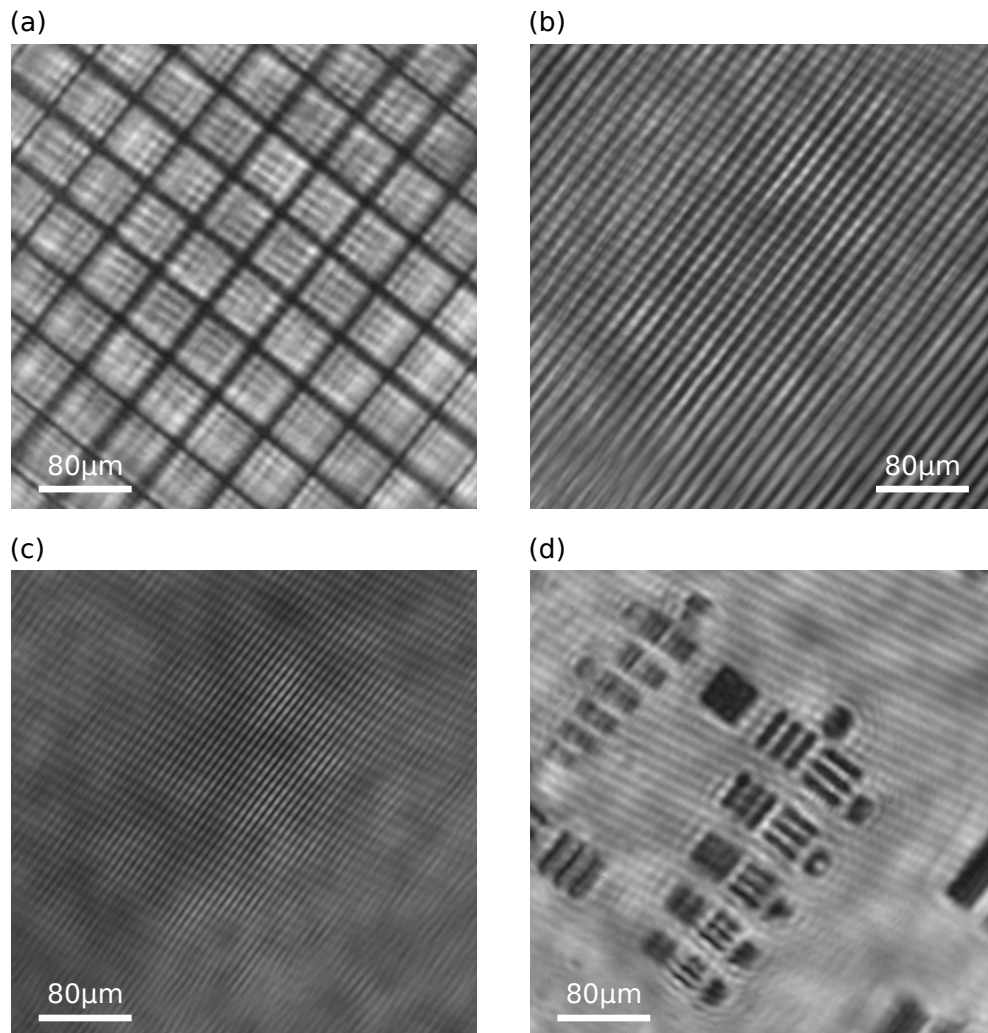


Figure 3.17: Characterization of the Mirau micro-interferometer to provide an off-axis cellular resolution. The effect of aberrations onto (a) the image distortion is shown using a grid as object. A Ronchi ruling target, with (b) 80 l/mm and (c) 140 l/mm intervals, is used to measure the degradation of the resolution in the corners of the image - i.e., at +200 μm ; +200 μm . In (d), an USAF 1951 target allows determining experimentally the resolution of the system in the center and in the extreme corner.

aberrations decrease the off-axis contrast and hence the lateral resolution. The on-axis resolution power of the Mirau interferometer is 140 l/mm leading to 7.1 μm period. This value can be retrieved in Fig. 3.17 (d) through the image of the Element 3 of the Group 6 (6.9 μm) of an USAF 1951 target. Despite optical aberrations, the resolution in the center of the image reaches 6.9 μm with a contrast of 30% and 10 μm at the border of the FOV - i.e., +200 μm ; +200 μm . Furthermore, a degradation of the resolution according to the orientation of the motif can also be found in Element 4 of the Group 6 and others. To notice that, in Fig. 3.17 (c) and (d), an interference pattern overlaps the image. This is due to the two dioptres of the infrared protection glass of the camera.

Figure 3.18 shows the modelling of the Mirau micro-interferometer through the CTF. The simulated resolution value, in the center of the FOV, equals $6.4 \mu\text{m}$ which is in good agreement with the measured value. However, in border of the FOV, the lateral resolution should be $6.7 \mu\text{m}$. Due to the optical aberrations, the lateral resolution decreases of around 50%.

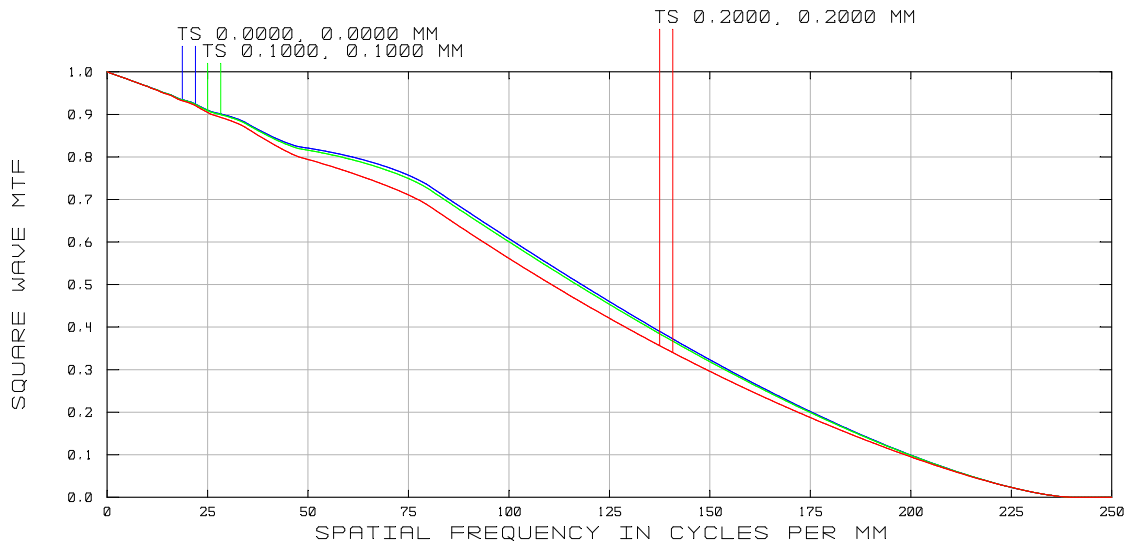


Figure 3.18: Square wave modulation transfer function in the center and in the border of FOV of the Mirau micro-interferometer.

Despite non-negligible optical aberrations generated by the doublet of microlenses, the interferometric micro-objective provides a cellular resolution (less than $10 \mu\text{m}$).

In Tab. 3.4 are summarized the performances of the Mirau interferometric lens.

Technical performances	Measured values
Axial FOV (at 633 nm)	$400 \mu\text{m}$
Numerical aperture of the doublet of microlens	0.14
Lateral resolution (at 633 nm)	$6.9 \mu\text{m}$
Lateral FOV	$400 \mu\text{m} \times 400 \mu\text{m}$
Frequency of the reference mirror actuation	485 Hz
Peak-to-peak reference mirror displacement	335 nm

Table 3.4: Acquisition block technical specifications.

3.3/ CONCLUSION AND PERSPECTIVES

This chapter reports the implementation of two characterization systems developed in the framework of this thesis. They have been used for quantification of the performances of the optical micro-components - i.e., microlenses and reference mirrors - and Mirau interferometers. A cellular resolution over a large lateral FOV ($400 \mu\text{m} \times 400 \mu\text{m}$) and a deep axial FOV ($90 \mu\text{m}$ in air) are specified in the design of the imaging system. Therefore, all along the fabrication processes, the quality of each individual elements as well as of the entire matrix of micro-interferometers is estimated.

The two characterization systems are made to be complementary. The first one is an optical profilometer based on the low coherence interferometry. This system allows retrieving the two dimensional surface topography of the micro-component. Through this information, the roughness as well as the radius of curvature, and thus the focal length, of the micro-elements can be estimated. However, surface topography is often not sufficient and optical characteristics have then to be derived from the measured geometry using optical propagation algorithms. Furthermore, this technique is usually geometrically limited to rather low numerical apertures - i.e., suitable only for moderate slopes. We have hence developed a new system for characterization of single optical micro-elements or of optical micro-systems based on several optical micro-components. The method is based on the direct measurement of the probing beam focused by the micro-optical elements. It allows characterizing transmissive and reflective components. Through this technique, the lateral and axial resolutions as well as the Strehl ratio - i.e., yielding to the standard deviation of the wavefront - and the estimation of the optical aberrations can be derived. Moreover, by implementing a phase retrieval algorithm onto the slices of the through focal volume, the map of the phase distribution is calculated and the optical aberrations quantified using the Zernike polynomial decomposition.

The single components - i.e., the doublet of microlens and the micro-mirrors - and the entire array of Mirau interferometers has been inspected with these techniques. The performances obtained are in good agreement with the required ones from the optical design. Indeed, the lateral resolution of the micro-system reaches $6 \mu\text{m}$ in the center of the image and decreases to maximum $10 \mu\text{m}$ at the extreme border of the FOV. This is due to the spherical aberrations which have been measured not negligible in this case. The optical aberrations are also responsible of a higher depth of focus ($400 \mu\text{m}$) than expected which should allows reducing the number of axial displacements. Furthermore, the performances of the reference mirror - i.e., the amplitude and the frequency of displacement - are similar to the specified ones for suppressing the artifact terms from

the Fourier transform operation.

An alternative optical configuration has recently been developed in our group in order to minimize the optical aberrations generated by the doublet of microlenses [207]. Indeed, despite providing lower aberrations than transmissive lens, Schwarzschild reflective micro-objective presents several advantages such as a free poly-chromatic dependence, an extension of the working distance and a compatibility with the Mirau architecture. Indeed, the obscuration from the reference mirror is not anymore an additional loss source [208]. This configuration could be used to implement an aberration-free Mirau interferometer.

TOWARDS THE FIRST MIRAU-BASED FULL-FIELD SWEPT-SOURCE OPTICAL COHERENCE TOMOGRAPHY MICRO-SYSTEM

After being designed, fabricated and characterized, the optical micro-components were implemented into a full-field swept-source optical coherence tomography (FF-SS-OCT) macro-system allowing more degrees of freedom for illumination and detection alignments. The architecture of the FF-SS-OCT macro-system is similar to the one designed and exposed in Cha. 2. This optical setup allows testing the Mirau-based micro-interferometers to provide the parallel spectral interferometric signals and also, to develop the software for the reconstruction of the depth information.

This chapter exposes the first imaging results of the Mirau micro-interferometers into a FF-SS-OCT macro-system. Indeed, due to a late delivery and manufacturing complexities of the swept-light source and the high-speed camera, only the Mirau micro-interferometers have been tested so far. Also, both developed swept light source and camera were replaced by commercial ones. The evaluation of the micro-interferometers consists in determining the quality of the spectral interference pattern following the parameters required in the design - e.g., linewidth of the swept light source -, measuring the sensitivity of the OCT system and estimating the error onto the OCT signal of the positioning of the Micro-interferometer components. Therefore, the sampling of the interferometric signal has been changed and its impact onto the interference signal and thus, onto the depth profile is investigated. Furthermore, the sensitivity at different depth positions in air and in scattering media has been evaluated. In parallel of this work, the assembly of the prototype of the FF-SS-OCT micro-system has begun based on

a provided package made by Statice (partner of the project).

4.1/ EXPERIMENTAL SETUP OF THE MIRAU-BASED FULL-FIELD SWEPT-SOURCE OPTICAL COHERENCE TOMOGRAPHY SYSTEM

A bulky FF-SS-OCT setup, based on a vertical architecture, has been implemented in order to test the Mirau micro-interferometers as well as to develop the programming software. The array of micro-interferometers is introduced in a bench optical macro-setup where a commercial swept-light source is used for the illumination, and the spectral components of the interferometric signal are recorded by a camera. Indeed, the manufacture of the swept light source, presented in Sec. 2.1.3, did not lead to the expected specifications - i.e., output power is few micro-Watts and the linewidth is higher than 1.2 nm. The broadsweeper light source (BS-840-2-HP, Superlum) is composed of a broadband superluminescent diode and a narrow-band acousto-optic tunable filter as a selective intracavity element for tuning and sweeping the wavelength. It provides 78 nm bandwidth around 841 nm central wavelength. Also, the linewidth of the swept wavelength is 0.12 nm. Furthermore, the output optical power can reach up to 15 mW for one spectral channel by using an additional optical power booster. The value of the optical power can be adjusted depending on the sample as well as the sweep speed through a serial interface. As it can be seen in Fig. 4.1, the spectrum of the light source is carried by a continuous signal. This is due to the amplified spontaneous emission of the booster which emits an intensity of about 1 mW for the whole spectrum.

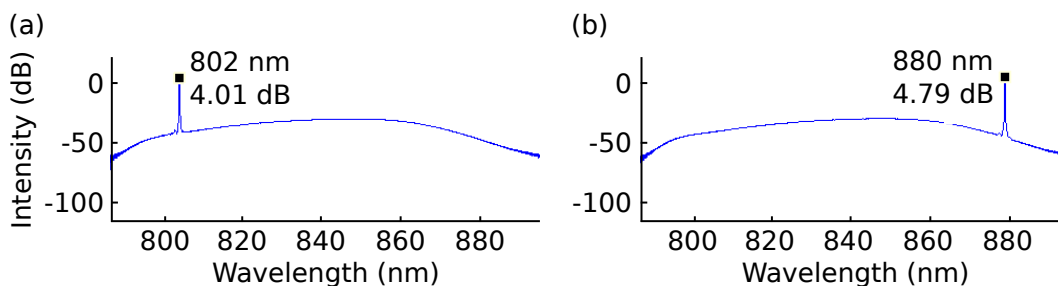


Figure 4.1: Spectrum of the Superlum swept light source at (a) 802 nm and (b) 880 nm wavelengths.

Furthermore, the high-speed camera was not delivered in time. Thus, a high-frame rate camera from Photonfocus (MV-D1024-160-CL, Photonfocus) has been employed. The resolution (1024×1024 pixels) as well as the pixel size ($12 \mu\text{m}$ length on each side) of the camera is similar to the designed one. In addition, its dynamic is also 10 bit. However,

the frame rate is only 160 fps. To be noticed, due to the lower frame rate of the camera compared to the actuation frequency applied to the reference mirror, the reference mirror is actuated in static mode and not at the resonance frequency.

The FF-SS-OCT system is shown in Fig. 4.2. The output beam is guided from the light source to the optical setup using a single mode fiber SMF and then collimated to pass through an actuated optical diffuser. This allows performing a spatially incoherent illumination of both the sample and the reference mirror. The beam from the diffuser is collimated by a condenser lens C and directed within the Mirau micro-interferometers IMO by the beam-splitter cube BSC. The arrangement between C and IMO provides $400 \mu\text{m} \times 400 \mu\text{m}$ lateral field of view (FOV) similarly to the miniature device.

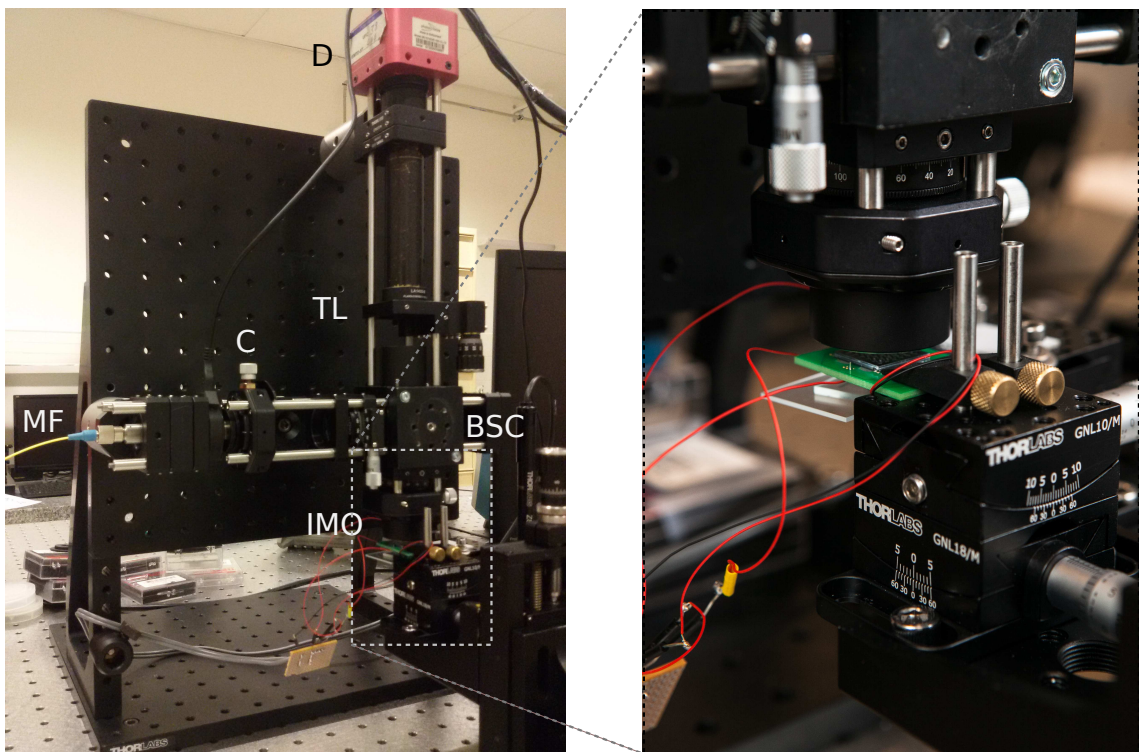


Figure 4.2: Photographs and zoom view of the on-bench full-field swept-source optical coherence tomography setup. Multimode fiber MF, collimator lens C, beam-splitter cube BSC, array of Mirau interferometric microscope objectives IMO, tube lens TL and camera detector D are shown. Photo credit: Ludovic Godard - UFC / Institut FEMTO-ST.

Firstly, only one IMO of the array is used. Thus, the diameter of the entrance pupil is reduced, by means of an additional aperture stop, in order to match the 1.5 mm diameter of the microlenses doublet. The beams from both the object and the reference mirror are coupled together by the planar beam-splitter with a ratio of T:70-R:30. The tube lens TL (LA1433-B, Thorlabs) images the back-reflected irradiances onto the camera D. As primary test, the magnification is different than the designed one - i.e., $\gamma = 3.8$ -

since we use only one channel. In this experiment, the magnification equals 18. Thus, a back-scattered point which is discernible by the IMO, is recorded onto 11 pixels.

The performances of the FF-SS-OCT system using a Mirau micro-interferometer have been experimentally evaluated and are summarized in the following Tab.4.1. The lateral resolution was experimentally measured using an USAF 1951 target. However, the vertical FOV was theoretically estimated.

Specifications	Values
Lateral resolution	6.9 μm
Lateral FOV	400 $\mu\text{m} \times 400 \mu\text{m}$
Axial resolution	2.5 μm
Axial FOV (from geometry of lenses)	400 μm
Magnification (IMO - TL)	18
Pixel size of the camera	12 $\mu\text{m} \times 12 \mu\text{m}$
Central wavelength	841 nm
Bandwidth	78 nm

Table 4.1: Acquisition block technical specifications.

4.2/ SOFTWARE OF THE MIRAU-BASED FULL-FIELD SWEEPED-SOURCE OPTICAL COHERENCE TOMOGRAPHY SYSTEM

A software has been developed in order to control the hardware devices of the optical system as well as to process the data and to reconstruct images of the sample. The tasks of the software are summarized in the following list.

- to control the sweeping wavenumber from the light source,
- to control the grabber of the camera and to acquire data,
- to control the displacement of the phase shifting device (MEMS platform),
- to process the data and
- to reconstruct the image volume of the sample

It is made in such a way as to be modular and modifiable following the hardware - e.g., if a new devices is employed, the software can be modified without changing its

architecture. This can be used if the system is upgraded by new device such as the camera from CSEM (VIAMOS partner).

Usually, in SS-OCT, the spectral components of the interferometric signal are recorded as a function of the wavelength. However, this requires a re-sampling of the OCT signal in wavenumber domain before applying the Fourier transform operation. The wavenumber being inversely proportional to the wavelength, several methods have been reported for the re-sampling such by optical arrangement [209] or by numerical non-uniform Fourier transform [210, 211]. In this work, the light source is swept linearly in wavenumber instead of in wavelength. This allows avoiding the re-sampling of spectral interference signal and hence reducing the processing time [212].

The software is developed with the graphical language LabVIEW (LabVIEW 2010 64bit, National Instruments) onto a HP workstation (Intel Xeon CPU E5 2.80 GHz, 8GB RAM and Windows 7 64bit OS). It provides advantages compared to other languages such as the interfacing of hardware and performing parallel control/acquisition and data processing. Previously, this powerful language has already been used for FF-SS-OCT [213, 83]. Here, the developed software distinguishes from other codes by a sinusoidal phase shifting implementation. The LabVIEW diagram of data acquisition part is shown in Annex Fig. 4.17. The producer-consumer structure has been retained to get data from camera and, simultaneously, to process data [162]. Furthermore, three independent loops allow estimating the memory progression, stopping the software and opening the camera configuration application.

After collecting the stack of spectral irradiances as a function of the wavenumber, the data are processed in order to calculate the complex interferometric signal according to the phase shifting algorithm. Assuming a sinusoidal phase shifting (sinPSI) algorithm, as presented in Sec. 2.2, the mathematical treatment requires Fourier transform operation according to the measurement time. The algorithm, which appeals LabVIEW MathScript RT Module (National Instrument), is shown in Alg.2.

Before applying the Fourier transform along the time, the spectral signal has to be shaped in order to minimize the noise and to improve the resolution of the resulting A-scan. Therefore, a zero-padding function is implemented. Also, the Fourier transform assumes a periodicity of the signal. A window function has also been applied to the spectral intensities $I(k,t)$. Otherwise, a discontinuity between the last sample and the repeated first sample causes artifacts in the result. Furthermore, a cosine tapered window function is applied to the signal as an enhancement of the dynamic range [214].

Algorithm 2 Sinusoidal phase shifting interferometry algorithm. The algorithm is based on the reported research [141]. It returns the depth profile.

- 1: $F(k, \omega) = \text{FT}[I(k, t)]$ ▷ Fourier transform of $I_{\text{sinPSI}}(k, t)$ with respect to time t
 - 2: $F_{kw} = \text{abs}(F(k, \omega))$ ▷ Keep half of the modulus of Fourier transform
 - 3: $\text{ReFW} = \text{real}(F_{kw}(k, \Omega))$ ▷ Keep term at the first harmonic Ω
 - 4: $\text{ReF2W} = \text{real}(F_{kw}(k, 2\Omega))$ ▷ Keep term at the second harmonic 2Ω
 - 5: $J_1(k), J_2(k)$ ▷ Define first and second order Bessel functions
 - 6: $A = -\text{ReF2W} / (J_2 \cos(2 \cdot \text{teta}))$ ▷ Calculate real part
 - 7: $B = -\text{ReFW} / (J_1 \cos(\text{teta}))$ ▷ Calculate imaginary part
 - 8: $Is = A + j B$ ▷ Complex spectral interferogram
 - 9: **return** $\text{abs}(\text{iFT}(Is))$ ▷ inverse Fourier transform of Is . Return the depth profile
-

4.3/ RESULTS OF THE FULL-FIELD SWEEP-SOURCE OPTICAL COHERENCE TOMOGRAPHY SYSTEM USING A MIRAU MICRO-INTERFEROMETER

As primarily test, the array of IMO has been replaced by a single Mirau micro-interferometer where its performance is equivalent - i.e., $NA = 0.15$ and 8 mm focal length. Furthermore, the camera has been employed as a single-point photo-detector through a selected subset of pixels to acquire the spectral components from one A-line without phase shifting implementation. In this configuration, the moving diffuser and the collimator lens C are removed from the optical setup to perform a spatial coherent illumination. The object is placed in the focal plane of the IMO and is characterized by a high reflection. It has been placed at $26 \mu\text{m}$ of the reference mirror by using a step motor. Figure 4.3 (a) shows the spectral interferometric signal plotted as a function of the wavelength. The red points are the measured irradiances of the OCT signal whereas in green is the fit curve with a polynomial of degree 6. This operation allows reducing the continuous term after applying the Fourier transform as exposed in Fig. 4.3 (b). As it can be seen, the processing operations allow retrieving the depth profile. Also, the relative position of the mirror which is determined by the peak, corresponds to the expected one.

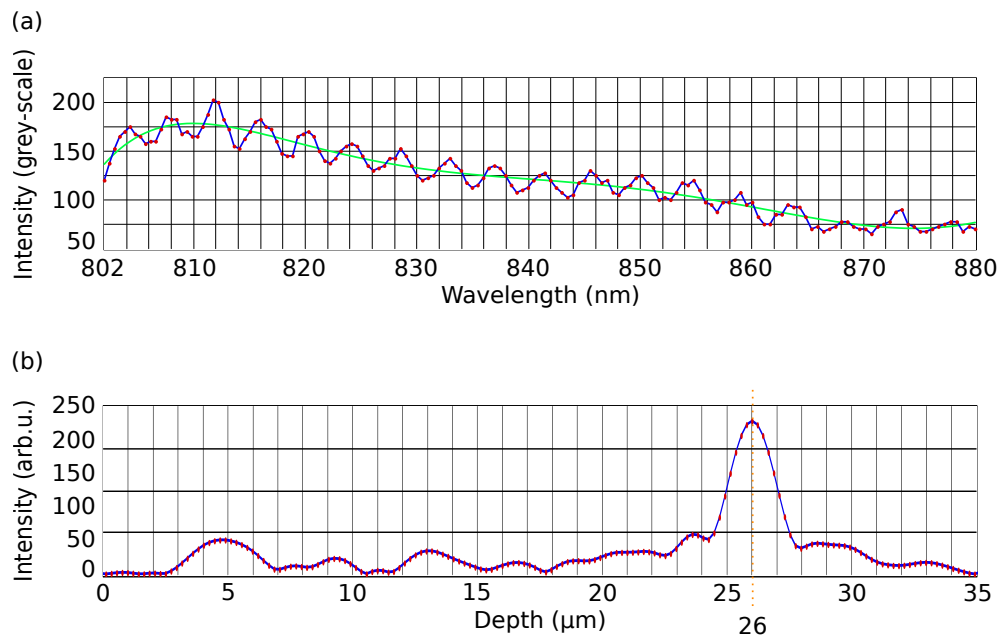


Figure 4.3: (a) Spectral interferometric signal as a function of the wavelength using the Mirau micro-interferometer and (b) half range of the resulting depth profile.

Furthermore, the impact of the number of spectral components recorded has been studied. Indeed, assuming an object positioned far from the zero optical path difference (OPD), the frequency of the sinusoidal function in wavenumber domain is high. Thus, it requires a large sampling. Figure 4.4 shows three A-scans of the object positioned at $68 \mu\text{m}$ OPD retrieved according to the number of recorded data.

As it can be seen, when only 50 sampling points are employed to record the spectral data, the A-scan is not reconstructed and the position of the object is not retrieved. In case of 78 sampling points, the A-scan is reconstructed. However, the position of the peak does not correspond to the position of the object. This effect is due to the folding of the Fourier transform operation. Indeed, when the number of sampling is insufficient to measure the OCT signal, a frequency aliasing occurs. With 78 points and a complete sweeping of the spectrum, the linewidth equals 1 nm which is quite similar with the requirements of the design ($\delta\lambda = 1.2 \text{ nm}$).

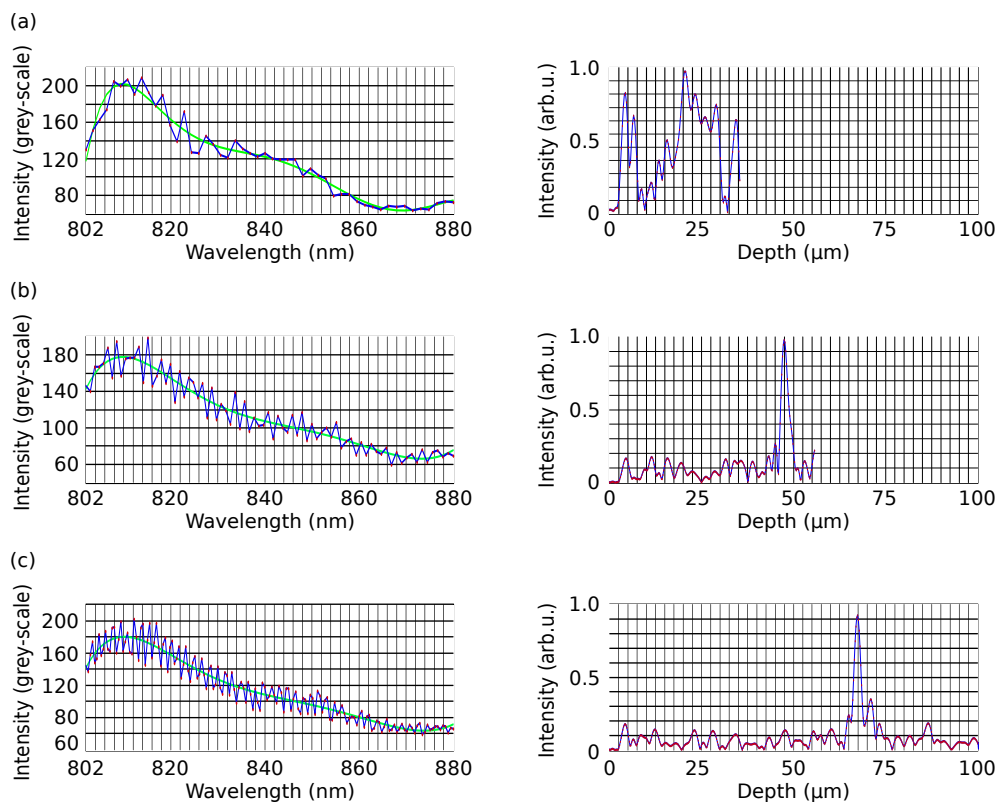


Figure 4.4: Impact of the sampling onto the depth profile with an object at $68 \mu\text{m}$ OPD. On the left are shown the interferograms and on the right the depth profiles. (a), (b) and (c) were reconstructed with a sampling of 50, 78 and 156 points, respectively.

In order to provide a good quality A-scan of $\pm 45 \mu\text{m}$ range - i.e., geometrical limitations of the microlens recommended in the design - the number of points should be 78, as exposed in Fig. 4.4 (b). However, the characterization of microlenses have shown a higher axial field of view - i.e., $\pm 200 \mu\text{m}$. The use of 156 sampling points could perform a $\pm 100 \mu\text{m}$ imaging depth with our microlenses and thus, reducing the number of axial stitching of the optical head.

Moreover, even with an object positioned close to the zero OPD, the sampling of the acquisition has an impact onto the signal-to-noise ratio (SNR). It has been shown that with 50, 78, 156 and 312 points, the SNR increases according to N sampling as it was detailed in Sec. 1.4. However, increasing the number of points could lead to a higher acquisition time. Figure 4.5 displays the impact of the sampling onto the SNR where the object has been placed at $26 \mu\text{m}$ OPD. As it was expected in Fig. 3.15, the optical aberrations of the Mirau objective leads to intensity fluctuations of the A-scan. Due to their time-free dependence, they were not taking into account for the SNR calculation.

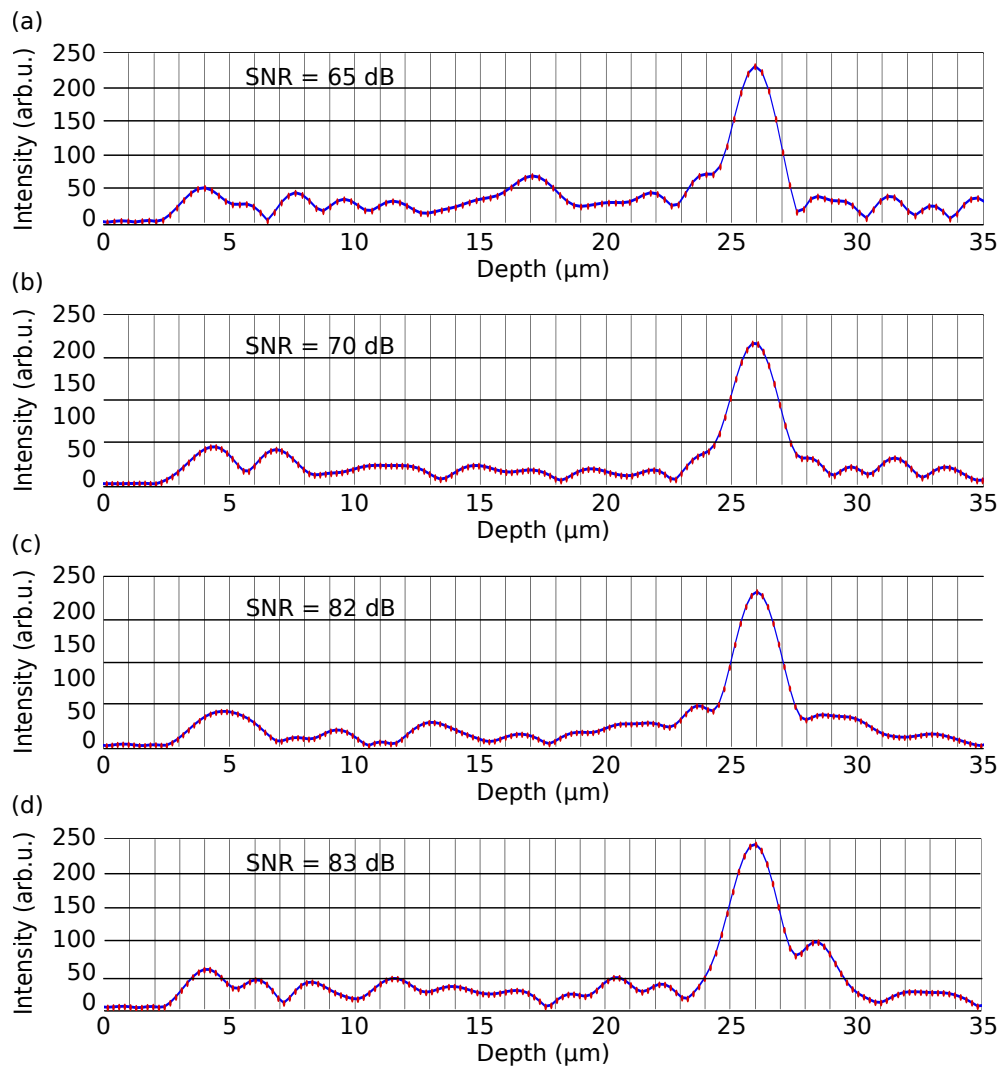


Figure 4.5: Impact of the sampling onto the SNR with an object at 26 μm OPD. (a), (b), (c) and (d) are the depth profile with a sampling of 50, 78, 156 and 312 points, respectively.

Then, by implementing a displacement of a sample, a depth image of a layer of varnish onto a painting has been obtained. Although strongly diffusing, a cross-section image of the sample has been made with 80 dB of sensitivity. The measurement range is 4 mm with 10 μm of lateral increment. The result is exposed in Fig. 4.6.

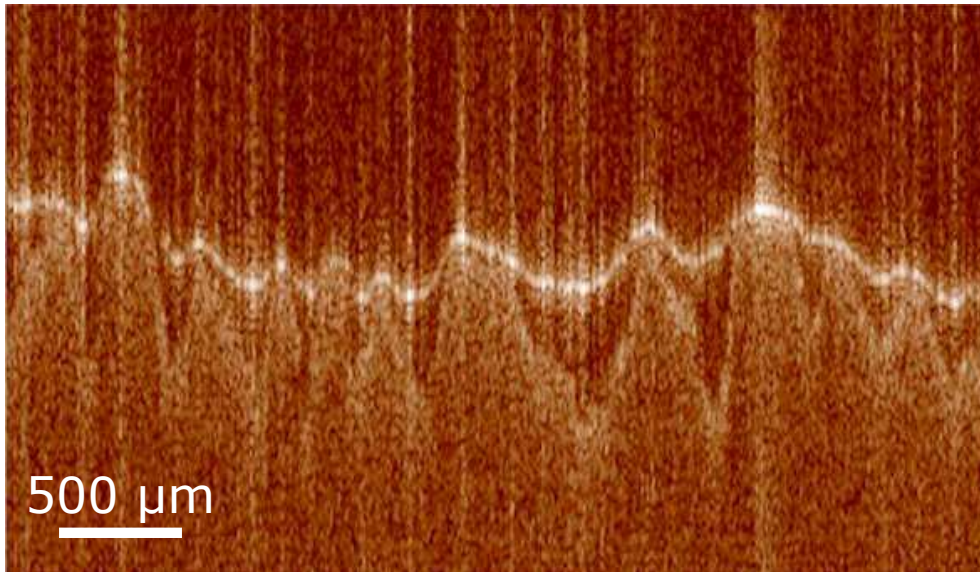


Figure 4.6: B-scan of a layer of varnish onto a painting obtained by using a micro-Mirau interferometer in SS-OCT configuration. The sensitivity equals 80 dB.

Afterwards, the non-assembled and planar beam-splitter have been replaced by the fabricated array of integrated micro-interferometers. Hence, the matrix of IMO has been placed in the FF-SS-OCT system and a full-field acquisition has been performed. Operation of the full-field acquisition was demonstrated by imaging a scotch tape located onto a silicon wafer. Figure 4.7 shows the provided cross-section image where the three layers appears. The image has been obtained over $300 \mu\text{m} \times 300 \mu\text{m}$ lateral FOV. However, as it can be seen, the edge of the image presents a non-negligible decrease of the sensitivity. The decrease of the SNR at the border has been calculated [215] and equals about -5 dB compared to the main peak, corresponding to the signal from the wafer layer. This loss of SNR could be explained by the intensity variations provided by the spherical aberrations, as shown in Fig. 3.15. This effect can also be seen on the A-scan plots extracted from the center and from the edge of the image. Artifact peaks appear around the three main ones represented in orange dots. Despite this SNR loss, the two dioptres of the scotch-tape and the surface of the wafer can be retrieved. The height of the scotch-tape should be about $20 \mu\text{m}$. Whereas, the measured one equals $22 \mu\text{m}$. Here, the difference is smaller than the axial resolution of the imaging system.

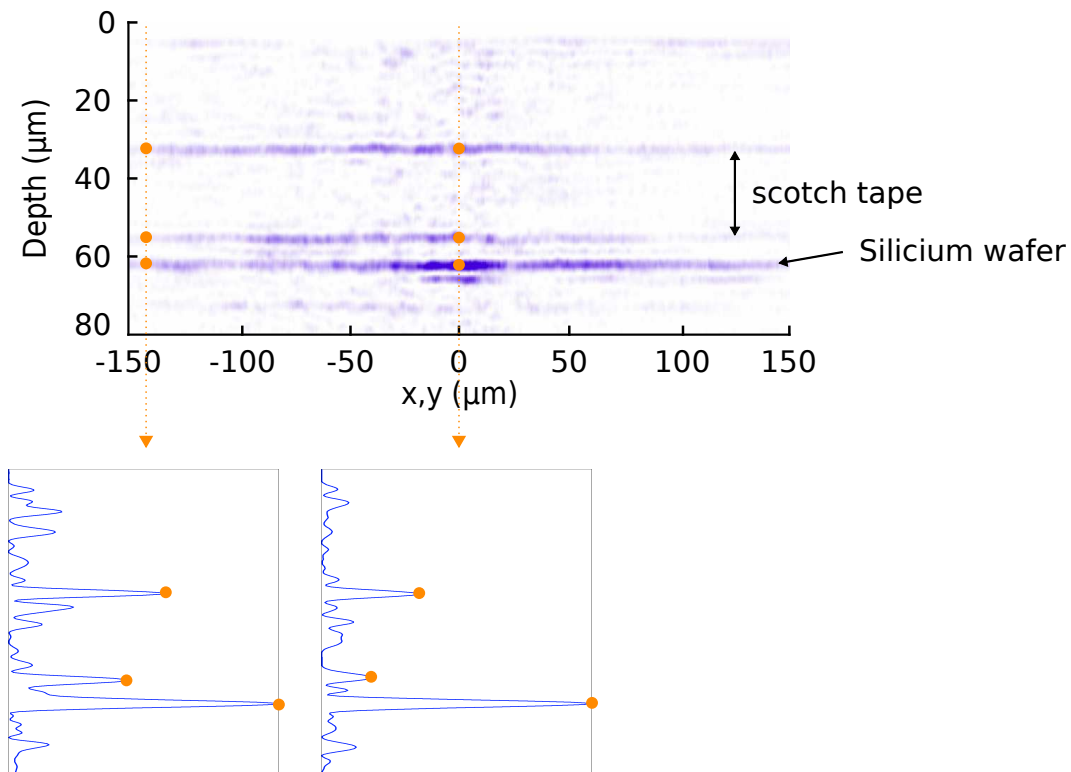


Figure 4.7: B-scan of the object which consists of a scotch-layer placed onto a silicon wafer.

4.4/ ASSEMBLY OF THE FULL-FIELD SWEEP-SOURCE OPTICAL COHERENCE TOMOGRAPHY MICRO-SYSTEM

All the micro-components of the imaging micro-system - i.e., array of microlenses, beam-splitter layer, spacers and micro-scanner - being fabricated and characterized, the prototype of the FF-SS-OCT micro-system is thus under assembly. The task consists first in the alignment of the micro-components of the imaging part and then, placing them into the package with the illumination part. The assembly of such micro-components requires high accuracy alignment. Therefore, several optical setups for the optical alignment of micro-elements were developed. Here are exposed the photographs of the prototype integration of the complete Mirau-based MOEMS interferometers. Figure 4.8 shows the photograph of the package of the imaging part. It consists of the array of Mirau interferometers, the beam-splitter cube where two arrays of aperture stops are glued on, the spacer between the cube and the array of tube lenses, and finally, the volume stops.

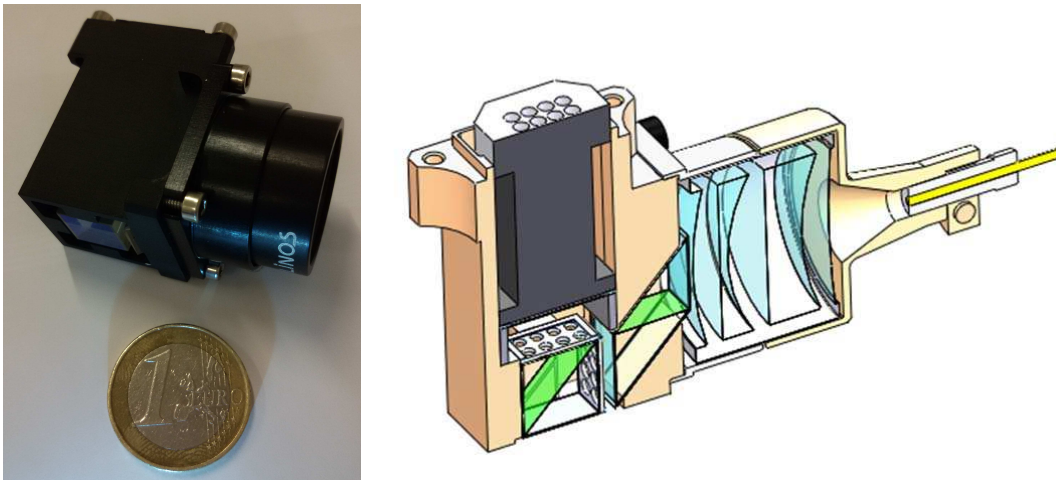


Figure 4.8: Package of the imaging part of the FF-SS-OCT micro-system.

Also, the collimator lens is fixed on the right of the support. The array of Mirau interferometer objectives, illustrated in Fig 2.20, will be placed below the package. The volume stop as well as the beam-splitter cube are displayed in Fig. 4.9.

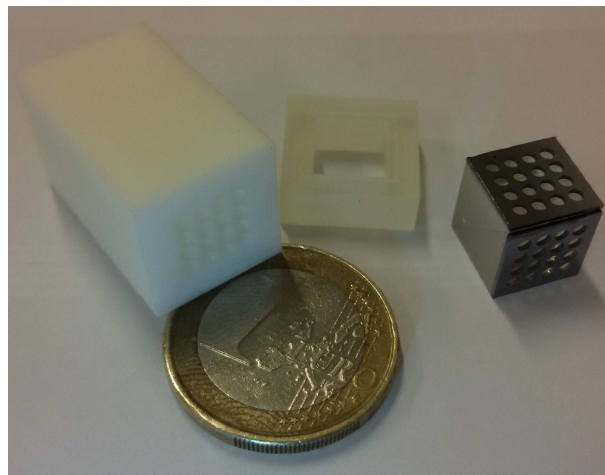


Figure 4.9: Volume stop (on the left), the spacer (in the center) and (on the right) of the imaging part of the FF-SS-OCT micro-system.

The prototype of the device is shown in Fig. 4.10 where the three motors for the optical head stitching are enclosed in the white dotted rectangle. Encircled by a white dotted line, the optical head appears small in comparison with the prototype size. Indeed, the high-frame-rate camera prototype requires large electronic cards. By reducing the bulk of the cards, the size of the prototype FF-SS-OCT system could match with the one of the white dotted rectangular which is about $10 \times 10 \text{ cm}^2$.

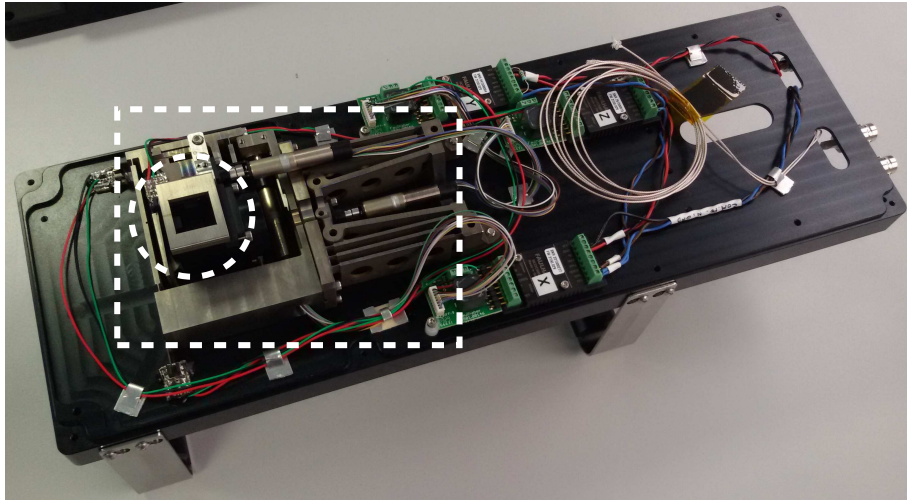


Figure 4.10: Photograph of the prototype of the FF-SS-OCT micro-system. The three stitching motors are integrated to perform lateral and axial displacements of the optical head.

4.5/ DISCUSSION AND PERSPECTIVES

This chapter exposes the implementation of the full-field swept-source optical coherence micro-system. In order to have more degree of alignments, the micro-elements were tested one after another. Firstly, a single micro-lens equivalent to the ones of the array of micro-interferometers where a mirror is deposited on its backside, was integrated into a vertical FF-SS-OCT macro-system for testing the acquisition of frequency domain OCT signal. Afterwards, it was replaced by the matrix of Mirau micro-interferometers. The configuration of the FF-SS-OCT macro-system is made according to the optical design of the micro-system. Due to large delays for the manufacture of the swept light source and high-frame-rate camera, commercial devices have been employed. The Mirau micro-objectives were tested on totally and partially reflective multi-layers sample. A study of the sampling - i.e., the number of acquisition points - has been performed and it has been shown that 156 points are necessary to provide a depth profile according to the optical design. Despite optical aberrations generated by the doublet of microlenses, depth profiles were found to be in agreement with the specifications of the design.

Simultaneously, the assembly of the prototype of the FF-SS-OCT micro-system has started. This complicated task has required the build up of optical benches for the alignment of the micro-elements. The first parts of the imaging system were integrated.

During the test of the Mirau micro-interferometers, it has been seen that the diop-
tres such as the convex surface of the doublet of microlenses or the back-side of the

reference mirror, yield to reflections from the incident beam and can disturb the acquisition of the OCT signal, leading to a higher SNR. Thus, an anti-reflective coating could be applied onto the microlenses to avoid these reflections. Since the spectrum bandwidth of the light source is not very wide, only two layers deposited onto microlens can be effective to reduce the reflectivity as in Fig. 4.11.

- first layer with 121 nm height and 1.77 refractive index (for 850 nm wavelength)
- second layer with 146 nm height and 1.45 refractive index (for 850 nm wavelength)

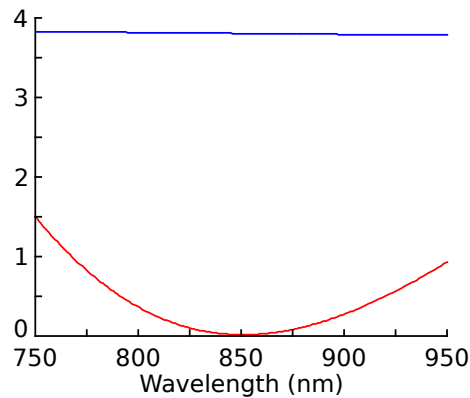


Figure 4.11: Anti-reflective coatings behaviour (red line) as a function of the wavelength compared to uncoated BF glass (blue line).

In perspective, an acquisition of the spectral interferometric signals should be performed through the 4×4 imaging channels. Already developed, the multiple region of interest algorithm for the acquisition of the spectral data should be integrated into the main control software. However, a modification of the processing program is required for the reconstruction of the multi-channels data. Also, static and dynamic acquisitions with the sinusoidal phase shifting technique has to be made using the camera from Photonfocus or the camera developed by the partner CSEM. The post-processing algorithm has already been developed and integrated in the main software. Finally, the assembly of the different components of the prototype has to be achieved with respect of the alignment precision and the motion control and data acquisition programs have to be tested using *ex-vivo* and *in-vivo* biological samples.

CONCLUSION

If skin is the largest human organ, it is also the one for which the largest number of diseases has been numbered so far. Indeed, about three thousands different diseases can affect skin and, in some countries, until two-third of people suffer from skin pathologies. Among this large number of pathologies, many of them are analyzed by investigating the skin morphology and its changes over time - i.e., ABCDE criterion. In particular, this concerns the follow-up of moles that can eventually evolve in cancers. Usually, screening is made by surface inspection, and when several criteria converge toward a possible risk, the mole is examined by histo-pathology. Unfortunately, histo-pathology involves invasive surgery or biopsy and, in addition, requires time to process the samples. But most of all, this standard diagnostic technique leads to 80 % of useless procedures - i.e., investigation and destruction of healthy tissues. Consequently, in recent years, new non-invasive systems have been tested for skin inspection, such as high frequency ultra-sonography or confocal microscopy. Regarding trade-off between the imaging contrast, the resolution and the depth of penetration, optical coherence tomography (OCT) seems to be better adapted to skin examination. Indeed, it provides a cellular resolution (few microns of range) at penetration depths that can reach one millimetre. These are actually close to the features of histo-pathology and hence probably easier to interpret for practitioners, especially because OCT provides B-scans which are slices orientated perpendicularly to the skin surface. Several commercial OCT devices dedicated to dermatology have then been released and demonstrated their efficiency. However, due to their bulk and cost, only several systems per country have been sold so far, and mostly to large hospital services. Hence, using OCT as an early detection tool is still far from being a standard situation, despite a real need.

The solution lies probably in being able to provide to the practitioners a cost-effective and easy-to-use device that would be affordable by most of independent dermatologists. For this purpose, the system would be based on micro-opto-electro-mechanical-systems (MOEMS) technologies allowing wafer-level components fabrication and collective integration. This approach would lead to a massive reduction of the systems size and cost. In addition, it is particularly interesting for dermatology because although the lateral field of view to be investigated has to be large, the depth of penetration remains reasonable, and is thus compatible with working distance of micro-optics. In order to

fill the large field of view specification, it is then possible to arrange micro-systems in dense arrays in order to perform parallel inspection. This is typically the situation where collective fabrication of MOEMS becomes very attractive - i.e., the use of advanced MOEMS technologies to generate a miniature and cost-efficient OCT system for skin inspection.

OCT technique can be compared to ultra-sonography - i.e., measuring the time delay of the back-reflected wave from a layer. However, measuring such an echo pulse duration is impossible at optical frequencies because of the high speed of light. Therefore, low coherence interferometry and, specifically, reflectometry has been enhanced for medical application. When the optical path difference between the reference wave and the back-scattered wave from a layer is zero, a constructive interference occurs leading to an intensity peak. Indeed, a correlation exists between the two waves. Subsequently, the depth profile can be retrieved by displacing the reference mirror along the propagation axis. This technique is called time domain optical coherence tomography (TD-OCT). Nowadays, most of the systems work in the frequency-domain (FD-OCT) for which the reference mirror displacement is replaced by the acquisition of a spectral interferogram. This is achieved by either a spectrometer located just before the detector, or by sweeping the source in order to tune sequentially its wavelength (SS-OCT). Then, the Fourier-transform of this spectral signal corresponds to the reflectivity profile (A-scan) of the sample. In both cases, FD-OCT presents higher sensitivity and lower acquisition time than TD-OCT. The SS-OCT, in addition, gives the possibility to perform parallel detection, usually referred to as full-field approach, provided that a fast enough image sensor is employed (FF-SS-OCT).

This thesis presents the development of a MOEMS-based FF-SS-OCT system for the early diagnosis of skin pathologies. The design is detailed according to the different part of the imaging system. Then optical micro-components used in the system are extensively characterized to check if their features match the specifications fixed by the design. For this purpose, characterization devices have been implemented and are presented as well. Finally, the integration of the OCT system and the preliminary results are exposed.

According to the dermatologists, the FF-SS-OCT system should provide an image of the sample with a cellular resolution over a lateral field of view similar to the size of a mole and a depth penetration allowing the visualization of the dermo-epidermal junction. Thus, the first challenge was to design an optical interferometer able to image a volume of view of basically $0.5 \times 8 \times 8 \text{ mm}^3$ with a high enough resolution. The

performances of the optics of the FF-SS-OCT system have to be in agreement with these specifications. In the framework of MOEMS technologies, fabrication tolerances have to be taken into account. In other terms, the system cannot be too small to ensure large enough field of view and fabrication tolerances.

One of the assets of OCT is to decouple the lateral and axial resolutions since lateral resolution is linked to the geometry of the optics whereas the axial resolution depends on the spectral bandwidth of the source. A numerical aperture of 0.13 and 50 nm bandwidth at 840 nm central wavelength lead to a voxel of $6.2 \mu\text{m}$ size. Note that the central wavelength is chosen in the near-infrared range because quantum efficiency of imaging sensors is still substantial, although biological tissues have lower diffusion at $\lambda=1.3 \mu\text{m}$. The numerical aperture seems to be a trade-off between aberrations control, lateral resolution and depth of field which equals thus $90 \mu\text{m}$ (in air). However, the linewidth of sweeping wavelength limits also the imaging depth through a coherence gate. Here, 1.2 nm linewidth has been retained and yields to $520 \mu\text{m}$. According to the Nyquist criterion, the image should be sampled by at least two pixels. Since the pixel size of the image sensor is $12 \mu\text{m}$, the magnification should be about 4. The image sensor has 1024×1024 pixels, but can be used by sequential activation of regions-of-interest (ROI). In order to be compliant with the typical size of micro-optical components, the device is based on 4×4 interferometers, each channel using a ROI of 128×128 pixels allowing imaging an area in the object space of $400 \mu\text{m} \times 400 \mu\text{m}$.

The interferometers are based on a Mirau architecture for which the reference mirror is located within the incident light path and hence, minimizing the footprint. Furthermore, it is compatible with vertical integration. Because of MOEMS fabrication concerns, the array is then made of 4×4 interferometers of 1.9 mm aperture arranged with a pitch of 2 mm. The effective diameter of the lens is limited by an aperture stop of 1.5 mm diameter to minimize the effect of spherical aberrations induced by lens borders. The focal length is then equal to 7.5 mm. The imaging part is a infinitely corrected objective lens in combination with a tube lens (28 mm focal length). This provides a large lateral field of view of $8 \times 8 \text{ mm}^2$. Also, the planar beam-splitter is made of a borosilicate glass wafer covered with a single layer of TiO_2 generated by physical vapor deposition. The beam splitting ratio of the planar beam splitter is 70:30, i.e. 70% of light is transmitted into the sample arm whereas 30% is reflected into the reference arm.

One drawback of FD-OCT is the generation of additional terms due to the Hermitian character of the Fourier transform operation. The raw A-scan is thus symmetric to the zero-delay position. If an accurate adjustment of the latter outside the inspection range is performed, the mirror terms could not superpose with the cross-correlated (of interest) terms. But the range is then halved. Another possibility is to rely on phase-shifting techniques. By introducing a variable single pass phase delay between the reference

and the object beams, complex conjugate artifacts can be removed. However, it requires the acquisition of several frames corresponding to different positions of the reference mirror. For this purpose, the reference mirrors are then actuated following a sinusoidal function and eight interferograms are recorded to derive an A-scan. Since the frame rate of the image sensor is fixed to 4000 fps, the mirrors is actuated at 500 Hz. According to the algorithm, the micro-mirror peak-to-peak displacement amplitude is set to 352 nm. Hence, acquisition of the full spectrum (50 spectral channels) is performed at 10 Hz. Thanks to the full-field approach, this acquisition frequency concerns 242,000 pixels simultaneously.

Finally, to be able to record B-scans, or eventually a 3D image, the array of interferometers is laterally moved so that each one of them can record an area covering the gap between two adjacent channels. This gap corresponding to the pitch of the interferometer array is 2 mm. Taking into account an overlap of 20% for stitching, six lateral movements of the array are performed to record continuous 8 mm long B-scans.

The key component of the system is the wafer-level fabricated and assembled array of Mirau interferometers. It has three main stages, namely, an array of glass lens doublets, an array of actuated reference mirrors and a planar beam-splitter. All these three stages, involving 7 substrates totally, have been then anodically bonded at wafer-level. Dicing of the different chips was achieved by laser cutting in order to release the 5 mm-thick Mirau-interferometers arrays. Flip-chip bonding onto a PCB board then allows connecting electrically the mirrors actuators and holding the Mirau chips.

The glass lens doublets are employed to ensure that the imaging performance is quasi diffraction limited for the whole field of view. The lenses are fabricated at wafer-level by thermal reflow of a glass wafer anodically-bonded under vacuum on top of silicon cavities. After the convex lens sides are generated by reflow, grinding and polishing of both stack sides allow, on the first hand, to form the planar lens backside and, on the other hand, to open the silicon cavity. Nevertheless, silicon frames are kept and thinned down to form well-controlled and auto-aligned spacers between the lenses. It is then used for the doublet generation where multi-wafer anodic bonding is applied. The latter ensures a high level of alignment both laterally and axially since no additional material is required. Thanks to polishing, the generated lens doublets are then as thin as several hundreds of microns - i.e., $870 \mu\text{m}$ - as shown in Fig. 4.12. The generated optical module is then robust and provides improved optical performances thanks to the lens splitting technique where the focusing power is divided between two optical components. Indeed, theoretically, two stacked lenses with similar features and spherical profiles can be almost diffraction limited whereas a single lens characterized by the same numerical aperture than the doublet presents five times higher wavefront error.

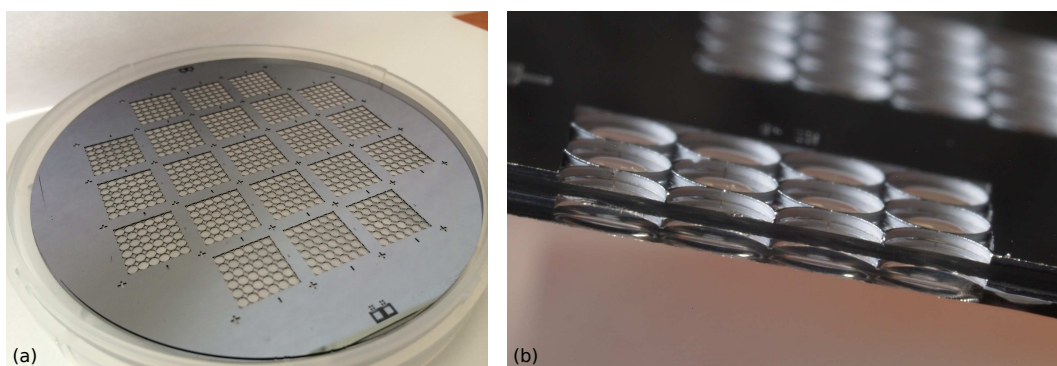


Figure 4.12: (a) Photographs of the wafer stack with matrices of 6×6 microlens doublets and (b) cross section of a matrix of lens doublets.

Such glass lens doublets are then assembled onto another substrate where a platform carries the 4×4 array of mirrors (Fig. 4.13). The challenge for this component is to reflect light only at the mirror location whereas it has to transmit light elsewhere. Hence, the area surrounding the mirror should be transparent. The optical influence of mirror suspensions was then studied and a configuration based on three curved silicon springs was chosen to minimize the non-symmetric effects of obscuration and diffraction. The mirrors are squared in order to make easier the digital processing of acquired X/Y images, and their size is of $400 \mu\text{m} \times 400 \mu\text{m}$, corresponding to the area measured within each channel. The obscuration is hence about 10%. The platform generated in the $40 \mu\text{m}$ thick device layer of a silicon-on-insulator wafer ($40/1.5/500 \mu\text{m}$) supports the array of mirrors and has a honeycomb structure to ensure a high stiffness but low mass. Whereas asymmetric multi-folded silicon springs designed to be stiff in the in-plane directions are located around the platform, out-of-plane actuation is performed by comb-drives also located all around the platform. The asymmetric comb-fingers are generated by a two-steps DRIE performed with two different masks.

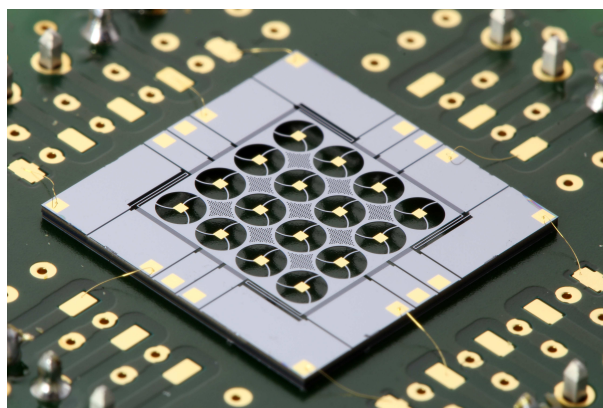


Figure 4.13: Photograph of the test chip of the electrostatically actuatable reference mirrors platform.

Then, the characterization of the integrated micro-optical elements has been performed in order to assure that their performances meet the requirements. Results are shown in Fig. 4.14. As it can be seen, the transmitted beam presents optical aberrations (Fig. 4.14 (a-b)). This optical aberrations - spherical and coma - generated by the doublet of microlenses are not negligible and should affect the performances of the imaging system. They have been quantified using point spread function (PSF) measurements and by applying an iterative phase retrieval algorithm. The measured RMS wavefront error was 0.7λ . The PSF of the Mirau chip have also been used to estimate the depth of field (Fig. 4.14 (a)). Based on the measured axial FWHM, the depth of field equals $400\ \mu\text{m}$ and is larger than the theoretical one, due to both optical aberrations and obscuration of the mirror. Through the modulation transfer function (MTF) calculation, the numerical aperture of the objectives has been evaluated and equals 0.14. Thus, the measured lateral resolution is $6.9\ \mu\text{m}$ at $633\ \text{nm}$ - i.e., about $9\ \mu\text{m}$ at $840\ \text{nm}$ - which meets the specifications of the system.

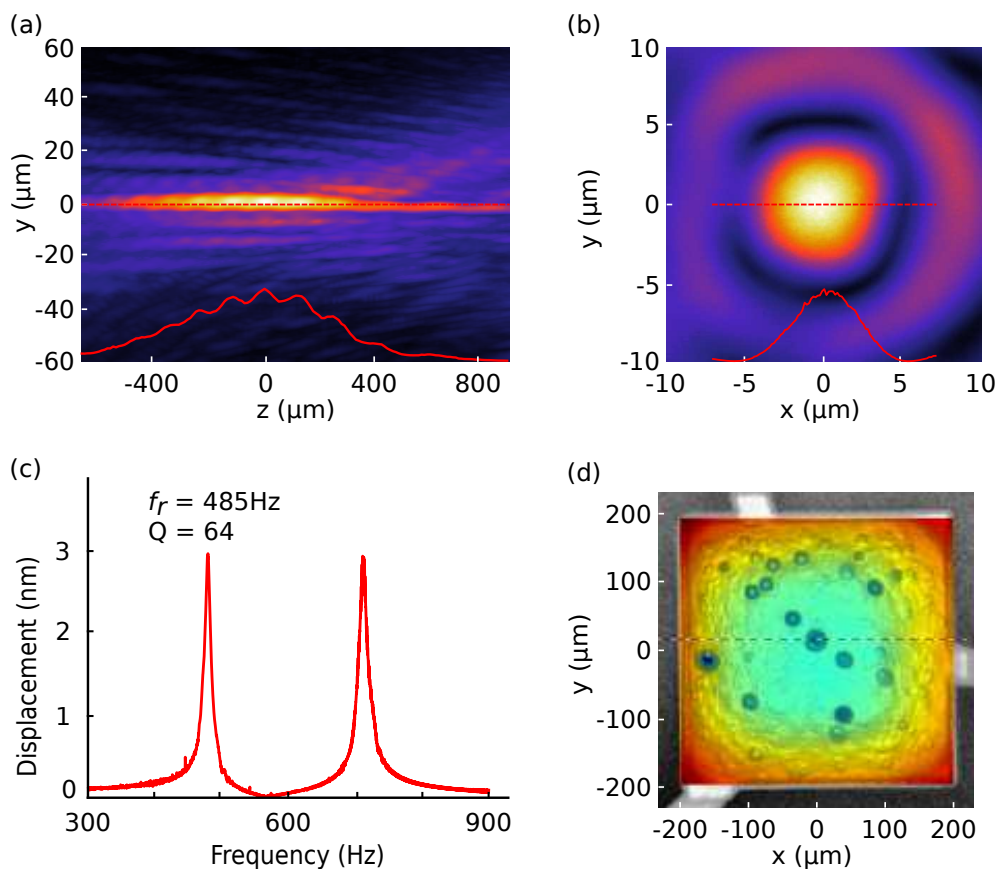


Figure 4.14: Characterization of the complete Mirau micro-interferometer.

The resonance frequency of the mirror platform has been measured equal to 485 Hz with 64 quality factor (Fig. 4.14 (c)). It can be mentioned that with a such quality factor, only few volts are necessary to actuate the micro-scanner.

The results from the characterization of the Mirau micro-interferometers have shown that the performances of the optical components are in agreement with the specifications of the optical design despite the optical aberrations.

Afterwards, the array of Mirau-based MOEMS interferometers has been placed into a FF-SS-OCT macro-system. It has been shown that 156 sampling points are required to perform 90 μm of imaging depth. Furthermore, despite this complex task due to degree of freedom for the alignment of components, the first spectral interferograms were obtained in one dimension and in two dimensions (Fig. 4.15).

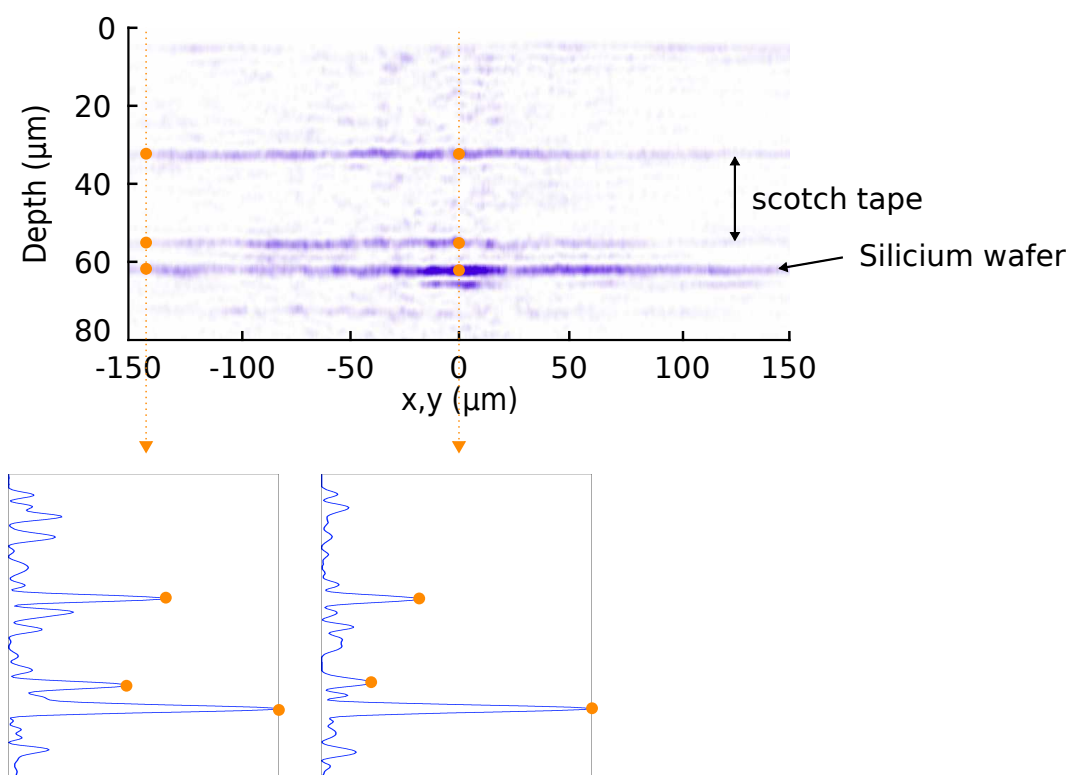


Figure 4.15: B-scan of an object which consists of a scotch-layer placed onto a silicon wafer recorded with the integrated Mirau interferometer objective.

In parallel, the assembly of the prototype of the complete FF-SS-OCT micro-system is in progress gathering elements for the illumination as well as for the imaging.

This MOEMS-based device, designed and fabricated under medical specifications, has a great potential for the imaging of *in-vivo* skin samples and further, for the diagnosis of pathologies such as cutaneous tumors. Moreover, enhancements of the hardware or of the software could yield to a promising medical imaging system. Indeed, the optical aberration could be reduced by using an array of Mirau-based reflective objectives, the size of the device could be minimized by reducing the size of the electronic acquisition

cards, the beam shape of the swept light source could be structured to follow the array of 4×4 channels. It would reduce losses from the gaps between channels and improve the system sensibility. The development of a MEMS-based actuated diffuser matching with the frame rate of the high-speed camera is also an important point to be investigated since standard moving diffusers require relatively long integration times to achieve sufficiently low spatial coherence, leading to a lower acquisition rate. Furthermore, it has been shown that using a circular polarization of the probing beam provides a deeper penetration in scattering medium [S. Rehn, Proc. SPIE **8088**, 80881I (2011)]. This could be implemented providing that polarizing micro-fabricated components are integrated. Also, an improvement of the reconstruction algorithm - e.g., using graphics processing unit - could lead to a lower processing time.

APPENDIX

MATHEMATICAL DEFINITIONS

The electromagnetic fields are formulated as a time-average value in order to represent the recorded irradiance during the exposure time of a detector. The time average operator is denoted by angle brackets. Mathematically, the time-average value of a function $F(x)$, over a given time range T , is determined by

$$\langle F(x) \rangle = \frac{1}{T} \int_0^T F(x) dt \quad (4.1)$$

The Fourier transform is a mathematical operation which allows transforming a temporal (as a function of the time) or a spatial (as a function of the distance) function into a function in the frequency domain [216, 217]. This is a convenient tool which is often used for the analysis of the signal such as the retrieval of its frequencies. For example, the Fourier transform is employed for the calculation of the depth profile through a spectral interferometric signal (see Sec. 1.2). Assuming a spatial continuous function $F(x)$, its Fourier transform $f(\xi) : \mathbb{R} \rightarrow \mathbb{C}$ is defined by

$$f(\xi) = \mathcal{F} \{F(x)\} = \int_{-\infty}^{\infty} F(x) e^{-j2\pi\xi x} dx \quad (4.2)$$

As well, the spatial-domain function $F(x)$ can be determined by the inverse Fourier transform of the frequency-domain function $f(\xi)$.

$$F(x) = \mathcal{F}^{-1} \{f(\xi)\} = \int_{-\infty}^{\infty} f(\xi) e^{+j2\pi\xi x} d\xi \quad (4.3)$$

Where \mathcal{F} and \mathcal{F}^{-1} are the Fourier transform operator and the inverse Fourier transform operator, respectively. j is the imaginary unit, that satisfies the relation $j^2 = -1$. x and ξ are the spatial and the frequency vectors (or continuous variables) such as $x, \xi \in \mathbb{R}$. A special case is the Fourier transform of a Gaussian function which, in this manuscript, is used for the determination of the temporal coherence function of a light source. Assuming a Gaussian function $F(t)$, defined by $F(t) = C \exp -Bt^2$, where both C and B are

constants. Its Fourier transform $f(v)$ is given by [217, 218]

$$\begin{aligned}
 f(v) &= C \int_{-\infty}^{\infty} e^{-Bt^2} e^{-jvt} dt \\
 &= C \int_{-\infty}^{\infty} e^{-\left(Bt^2 + jvt - \frac{v^2}{4B}\right) - \frac{v^2}{4B}} dt \\
 &= C e^{\frac{v^2}{4B}} \int_{-\infty}^{\infty} e^{-\left(\sqrt{B}t + j\frac{v}{2\sqrt{B}}\right)^2} dt \\
 &= C \sqrt{\frac{\pi}{B}} e^{-\frac{v^2}{4B}} \tag{4.4}
 \end{aligned}$$

Similarly, a uniformly-spaced discrete function $F[n]$ (N-dimensional sampling), its Fourier transform $f[\xi]$, called discrete Fourier transform, is written

$$f[\xi] = DFT \{F[n]\} = \sum_{n=0}^{N-1} F[n] e^{-j\frac{2\pi\xi}{N}n} \tag{4.5}$$

And, the inverse discrete Fourier transform is described by

$$F[n] = DFT^{-1} \{f[\xi]\} = \frac{1}{N} \sum_{\xi=0}^{N-1} f[\xi] e^{+j\frac{2\pi\xi}{N}n} \tag{4.6}$$

Where n are integers defined as $n \in [0, N - 1]$.

STRUCTURE CODES

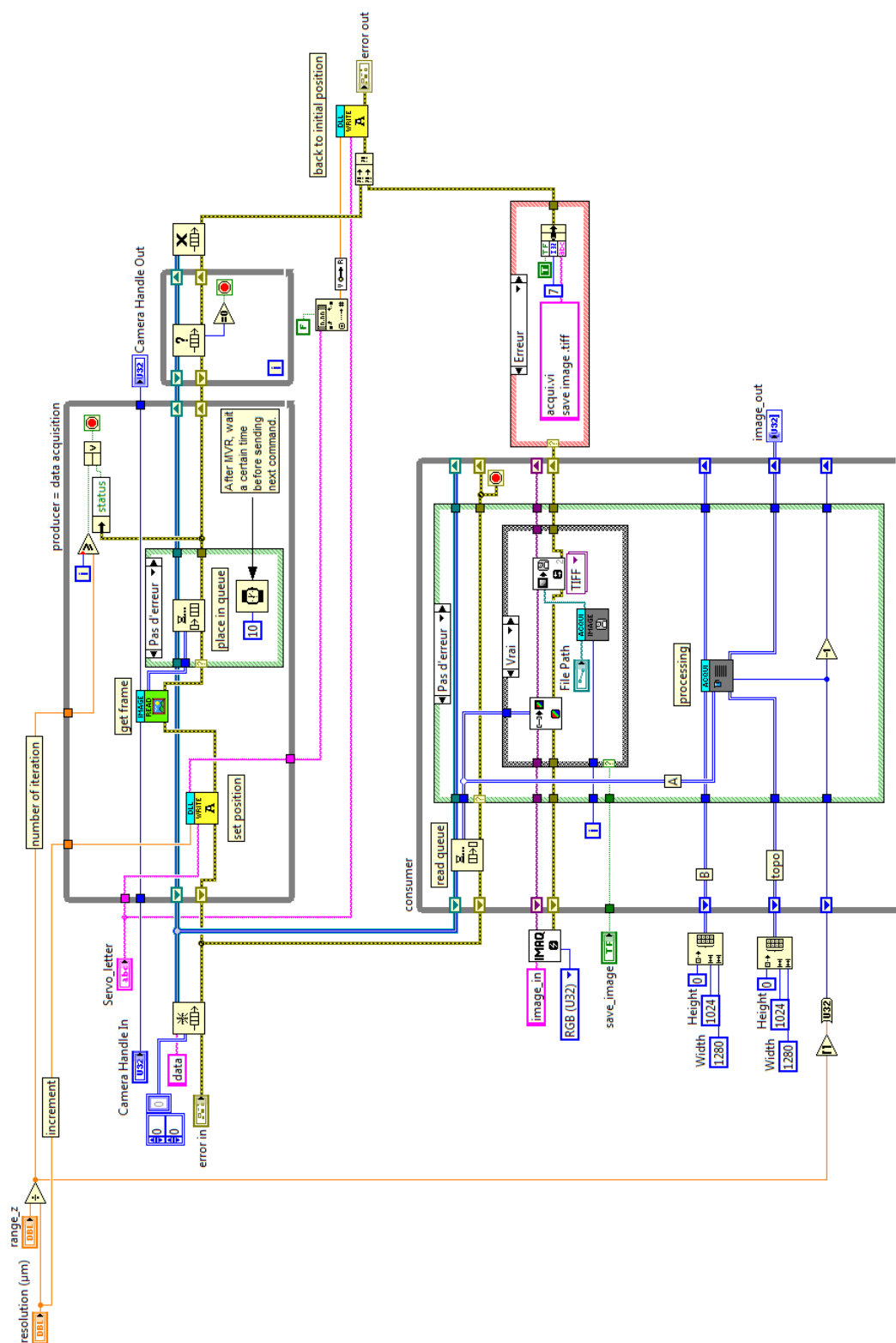


Figure 4.16: Producer consumer structure for the coherence scanning interference microscope.

MATHEMATICAL DESCRIPTION OF SINPSI

This chapter of the Annex is extracted from the Sasaki *et al.*'s works [138, 142]. In FD-OCT, the intensity of the sinusoidally phase shifted spectral interferogram, resulting on interference between both reference and object arms, is expressed as,

$$I_{sinPSI}(k, t) = \eta \frac{S(k)}{4} \left[\left(R_r + \sum_{m=1}^M R_m \right) + 2 \sum_{m=1}^M \sqrt{R_r R_m} \cos [2k (z_r - z_m) + 2ka \cos (\omega t + \beta)] \right], \quad (4.7)$$

where $S(k)$ is the spectral density of the light source depending on the wavenumber k and R_r and R_m are the reflective power of reference mirror and m^{th} interface of the sample, which consists of M layers. The term $z_r - z_m$ is the optical path difference. To simplify the equations, the OPD is now written Δz_n . The function $2ka \cos (\omega t + \beta)$ is related to the sinusoidal phase shifting actuation. a and ω are the amplitude and the angular frequency ($2\pi\Omega$) of the oscillation, respectively. β is the initial phase. From this point forward, the cosin function is called $\phi(\omega, t)$. The interferograms are acquired following the time t and the wavenumber k . A two dimensional representation of recorded interferograms is exposed in Fig. 2.11. The spectral intensity signal $I_{sinPSI}(k, t)$ can also be written as

$$I_{sinPSI}(k, t) = \eta \frac{S(k)}{4} \left[\left(R_r + \sum_{m=1}^M R_m \right) + 2 \sum_{m=1}^M \sqrt{R_r R_m} [\cos (2k\Delta z) \cos (2\phi(\omega, t)) - \sin (2k\Delta z) \sin (2\phi(\omega, t))] \right] \quad (4.8)$$

Then, the Fourier transform along the time of the interferograms allows expressing it as a function of ω and is given by

$$\tilde{I}_{sinPSI}(k, \omega) = \eta \frac{S(k)}{4} \left[\left(R_r + \sum_{m=1}^M R_m \right) \delta(\omega) + \mathcal{F}_t \left\{ 2 \sum_{m=1}^M \sqrt{R_r R_m} [\cos (2k\Delta z) \cos (2\phi(\omega, t)) - \sin (2k\Delta z) \sin (2\phi(\omega, t))] \right\} \right] \quad (4.9)$$

Jacobi Anger expansion [219] is employed to reduce and simplify both terms $\cos (2\phi(\omega, t))$ and $\sin (2\phi(\omega, t))$ through the following mathematical treatment,

$$\exp (ju \cos \alpha) = J_0 (u) + 2 \sum_{q=1}^{\infty} j^q J_q (u) \cos (q\alpha) \quad (4.10)$$

Where $J_q(u)$ is the q^{th} order Bessel function of the first kind with the variable u . The two last expressions of Eq. 4.9 can thus be formulated

$$\sum_{m=1}^M \sqrt{R_r R_m} \cos(2k\Delta z) \cos(2\phi(\omega, t)) = \sum_{m=1}^M \sqrt{R_r R_m} \cos(2k\Delta z) \left[\sum_{q=-\infty}^{\infty} (-1)^q J_{2q}(2ka) \exp(j2q\beta) \delta(\omega - 2q\Omega) \right] \quad (4.11)$$

And,

$$\sum_{m=1}^M \sqrt{R_r R_m} \sin(2k\Delta z) \sin(2\phi(\omega, t)) = \sum_{m=1}^M \sqrt{R_r R_m} \sin(2k\Delta z) \left[\sum_{q=-\infty}^{\infty} (-1)^q J_{2q-1}(2ka) \exp(j(2q-1)\beta) \delta(\omega - (2q-1)\Omega) \right] \quad (4.12)$$

At the frequency components of the two first harmonics of the Fourier transform - i.e., when $\omega = 2\Omega$ and $\omega = \Omega$ - and at $q=1$, the real part of both Eq. 4.11 and Eq. 4.12 leads to

$$\Re \left\{ \tilde{I}_{\sin PSI}(k, 2\Omega) \right\} = \sum_{m=1}^M \eta \frac{S(k)}{2} \sqrt{R_r R_m} \cos(2k\Delta z) (-1) J_2(2ka) \cos(2\beta) \quad (4.13)$$

And to

$$\Re \left\{ \tilde{I}_{\sin PSI}(k, \Omega) \right\} = \sum_{m=1}^M \eta \frac{S(k)}{2} \sqrt{R_r R_m} \sin(2k\Delta z) (-1) J_1(2ka) \cos(\beta) \quad (4.14)$$

Afterwards, the complex interferometric signal $I(k)$ is given by $I(k) = A(k) \exp(-j\Phi(k))$ with the magnitude term

$$A(k) = \eta \frac{S(k)}{2} \left[\left(\frac{\Re \left\{ \tilde{I}_{\sin PSI}(k, \Omega) \right\}}{J_1(2ka) \cos(\beta)} \right)^2 + \left(\frac{\Re \left\{ \tilde{I}_{\sin PSI}(k, 2\Omega) \right\}}{J_2(2ka) \cos(2\beta)} \right)^2 \right]^{1/2} \quad (4.15)$$

and the phase term

$$\tan(\Phi(k)) = \frac{\Re \left\{ \tilde{I}_{\sin PSI}(k, \Omega) \right\}}{J_1(2ka) \cos(\beta)} \times \frac{J_1(2ka) \cos(2\beta)}{\Re \left\{ \tilde{I}_{\sin PSI}(k, 2\Omega) \right\}} \quad (4.16)$$

By inverse Fourier transform $I(k)$ with respect to the wavenumber, the depth profile free of artifacts occurs.

ZERNIKE POLYNOMIAL DECOMPOSITION

For the evaluation of a single optical element or complete system, the retrieval of optical aberrations is essential. Therefore, after the extraction of the two dimensional phase distribution $\phi(\rho, \theta)$, using interferometry or phase retrieval techniques, the decomposition of the wavefront in N-number Zernike polynomials $Z_n(\rho, \theta)$ can be performed [220, 221]. This leads to the imaging quality characterization through the values of the coefficients c_n . The phase distribution can be written as

$$\phi(\rho, \theta) = \sum_{n=0}^N c_n Z_n(\rho, \theta) \quad (4.17)$$

With ρ and θ , the normalized radial and azimuthal coordinates. And, the first eleven Zernike functions $Z_n(\rho, \theta)$ are summarized in Tab.4.2.

This amounts to write the wavefront distribution as a two dimensional matrix [222]. For the characterization of micro-optical elements (see Sec. 3.1.3), a MATLAB code (MathWorks) has been developed in order to estimate the coefficients c_n of the optical aberrations.

Algorithm 3 Aberration coefficients calculation. This simplified algorithm is inspired on the Zernike decomposition MATLAB code from Mathworks file exchange website. The pseudo-inverse function is only due to the non-square coefficient matrix.

1: $Z A = W$

2: $Z^T Z A = Z^T W$

3: $A = (Z^T Z)^{-1} Z^T W$

4: $A = Z^{-1} W$

▷ with Z^{-1} , the pseudo inverse matrix

Zernike term Z_n	Name	Zernike polynomial
Z_1	Piston	1
Z_2	Vertical tilt x	$\rho \cos(\theta)$
Z_3	Horizontal tilt y	$\rho \sin(\theta)$
Z_4	Defocus	$2\rho^2 - 1$
Z_5	Primary vertical astigmatism (0° and 90°)	$\rho^2 \cos(2\theta)$
Z_6	Primary oblique astigmatism ($+45^\circ$)	$\cos^2 \cos(2\theta)$
Z_7	Primary vertical coma x	$(3\rho^3 - 2\rho) \cos(\theta)$
Z_8	Primary horizontal coma y	$(3\rho^3 - 2\rho) \sin(\theta)$
Z_9	Vertical triangular astigmatism (trefoil)	$\rho^3 \cos(3\theta)$
Z_{10}	Oblique triangular astigmatism (trefoil)	$\rho^3 \sin(3\theta)$
Z_{11}	Primary spherical	$6\rho^4 - 6\rho^2 + 1$

Table 4.2: Zernike orthogonal circle polynomials. Excepted the piston, the mean of each polynomial is zero. To be note that $Z_n(\rho, \theta)$ is the simply denotation of Zernike polynomial.

MODULATION TRANSFER FUNCTION

Performances of an optical system, such as a microscope objective, can be quantified by knowing its transfer function, also called frequency transfer function. Furthermore, it is often used to design an optical system. The transfer function of a complete system is equivalent to the product of the transfer functions of each optical element [223]. Based on the diffraction theory, it is the ability for an optical system to reproduce the image of a continuous sinusoidal object at a specific frequency. This is the way of an imaging system to transfer the sinusoidal spatial frequency components (Fourier decomposition) of an object to the image. However, the naming conventions and the mathematical treatment depend on the coherent nature of the illumination beam. In this annex chapter, the incoherent transfer function - i.e., object illuminated with an incoherent light source - is summarized and the expressions of the resolution are defined. Nevertheless, a short description of the coherent transfer function is exposed. Gauss approximations are considered - i.e., small incident angles and point light sources close to the optical axis. Formerly, an image, formed from these approximations, used to be named Gaussian image [224].

In incoherent imaging, the transfer function, called optical transfer function (OTF), is expressed as a function of object intensity and image irradiance. Mathematically, the OTF is the Fourier transform of the point spread function (PSF) which is the spatial response of the optical system. Moreover, OTF can be seen as the normalized auto-correlation of the pupil function $P(p, q)$ of the optical system.

$$OTF(\eta, \zeta) = \mathcal{F}\{PSF(x, y)\} = \mathcal{F}\left\{\left[\mathcal{F}\{P(p, q)\}\right]^2\right\} \quad (4.18)$$

Assuming an aberration-free circular system, the PSF is an Airy disk (squared Bessel function of the first kind of order one) and the OTF is a real function. However, since the imaging system introduces optical aberrations, the pupil function is written $P(p, q) = T(p, q) \exp[j\phi(p, q)]$ with $T(p, q)$, the transmission over the pupil, and $\phi(p, q)$, the wavefront aberration. Hence, the OTF expression becomes complex and results in a modulus, the modulation transfer function (MTF), and, an argument, the phase transfer function (PTF).

$$OTF(\eta, \zeta) = MTF(\eta, \zeta) \exp[jPTF(\eta, \zeta)] \quad (4.19)$$

The PTF is linear with the frequency response and can be seen as a simple lateral shift of the image. For example, defocus aberrations leads to a π phase shifted image.

Figure 4.18 exposes the concept of incoherent transfer function through a square wave

motif. In the spatial domain, on the left of the figure, the image results from the convolution between the object and the PSF of the optical components. Whereas, in frequency domain, on the right, the image is the product of the spectrum object (Fourier transform of the object) and the OTF.

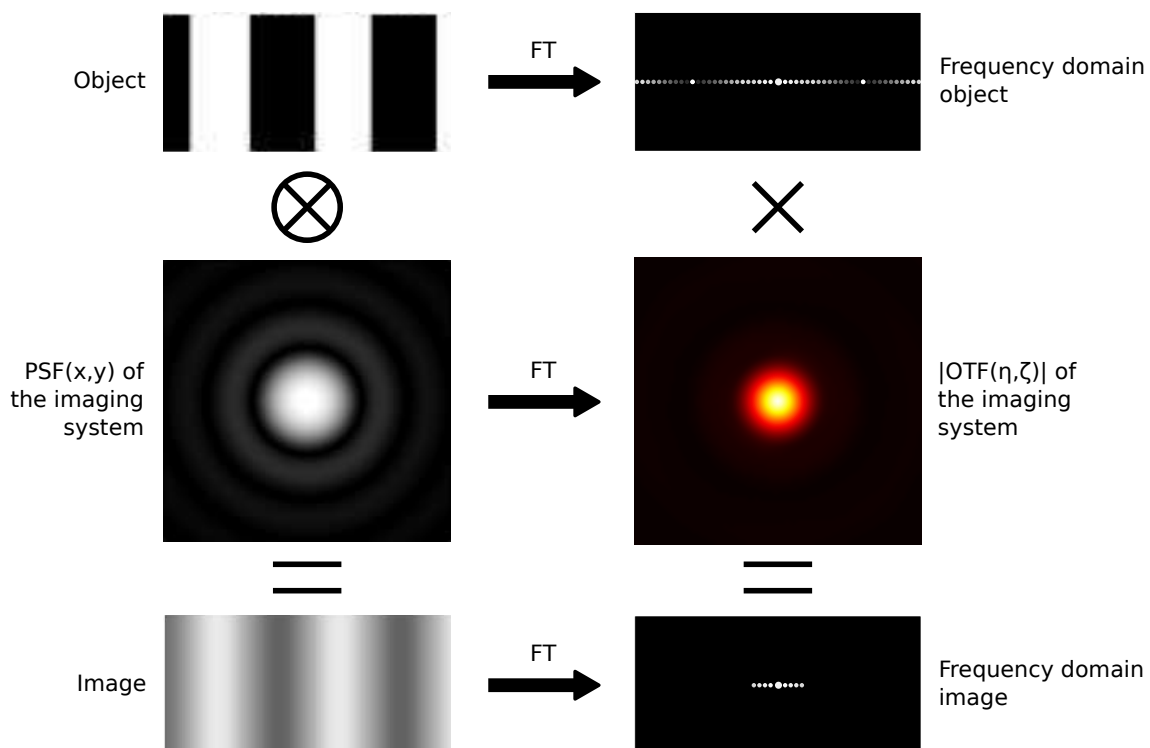


Figure 4.18: Two dimensional incoherent transfer function concept of an aberration-free optical system. Both both spatial (left) and frequency (right) domains are represented.

MTF is referred as the frequency response, the sine wave response or the contrast transfer function (CTF). However, the MTF expression should be only employed to make measurement through a sinusoidal grey-scale object. Whereas, more often used experimentally, the CTF is needed for square waves pattern object - i.e., black and white lines - which can be seen as an infinite summation of sinusoidal waves. A mathematical relation between MTF and CTF has been reported in [225]. It has been shown that, for high frequencies, the relative change in contrast transfer are similar between MTF and CTF. However, variations occur for low frequencies. This could be explained by the Fourier sinusoidal decomposition of the square function .

The MTF is expressed as the ratio of the image contrast over the object contrast

depending on the spatial frequencies.

$$MTF(f) = \frac{MTF_{image}(f)}{MTF_{object}(f)} \quad (4.20)$$

Assuming a perfect sinusoidal object - i.e., $MTF_{object} = 1$ -, the transfer function is described by the relation

$$MTF(f) = \frac{I_{max} - I_{min}}{I_{max} + I_{min}}(f) \quad (4.21)$$

Where, I_{max} and I_{min} are the maximal and minimal irradiances at a given spatial frequency or resolution. In a majority of situations, the transfer function is represented in one-dimensional form. Hence, by determining the contrast value at each spatial frequency f , the MTF curve is plotted.

From the frequency transfer function, the lateral resolution of the optical system can be derived. Indeed, the cut-off frequency f_c of the incoherent transfer function is one resolution criterion among so many others and is quite similar to the Abbe criterion. In absence of aberrations, the Abbe resolution depends onto the wavelength of the light λ and the numerical aperture NA . Resolution criteria [66] are listed in Tab.4.3.

Both Rayleigh and Sparrow incoherent criteria are based on this two-points source which provide equally bright Airy disks. By definition, Rayleigh resolution is defined as the distance between the first zero and the maximum of the PSF [226]. The contrast value results of 10.5%. Whereas, the Sparrow criterion requires a zero gradient at the peak of the summed Airy disks [227, 228]. The Houston criterion, which is used in this manuscript, is the width at half maximum of the PSF - e.g., an Airy disk for an aberration-free element.

Criterion	Resolution	Definition
Abbe (incoherent), 1873	$\frac{\lambda}{2 \sin(\alpha)}$	Minimal resolvable distance of eye in air. Although non explicit in this formula, Abbe coined the term of numerical aperture NA.
Rayleigh (incoherent), 1874	$\frac{3.83}{2\pi} \frac{\lambda_0}{NA}$	Distance between the images of two point sources when the central minimum is 80 %.
Sparrow (incoherent), 1916	$0.47 \frac{\lambda_0}{NA}$	Distance for which the resulting irradiance pattern has no curvature in the center.
Houston (incoherent), 1926	$\frac{1.03}{2} \frac{\lambda_0}{NA}$	Full width at half maximum of the PSF.
Cut-off frequency of MTF	$0.5 \frac{\lambda_0}{NA}$	P.M. Duffieux introduced the notion of an optical system which acts as a linear filter on the image frequency pattern in 1946.
Sparrow (coherent), 1967	$0.73 \frac{\lambda}{NA}$	Ultimate limit for a photodiode to resolve two irradiance peaks.
Cut-off frequency of ATF	$\frac{\lambda}{NA}$	This is the equivalent of Abbe resolution with a coherent illumination.

Table 4.3: Summary of the resolution criteria in microscopy using an incoherent or a coherent light source.

In case of spatially coherent light source (point light source), the amplitude have to be taken into account for the calculation of the transfer function [229]. This is due to the presence of phase term in the calculation. Coherent transfer function is less employed for imaging quality estimation than incoherent transfer function. To be note that, experimentally, sinusoidal amplitude distribution objects are preferred to square objects because of the diffraction blurred effect on the edges. The transfer function, called amplitude transfer function (ATF), is the Fourier transform of the amplitude spread function (ASF) which is the Fourier transform of the entrance pupil. Assuming a circular pupil, the ASF is a cardinal sine function (Bessel function of the first kind of order one).

$$ATF(\eta, \zeta) = \mathcal{F}\{ASF(x, y)\} = \mathcal{F}\{\mathcal{F}\{P(p, q)\}\} \quad (4.22)$$

Thus, the shape of the transfer function is equivalent to the one of the pupil function. This explains the lower resolution power with a coherent light source than with an incoherent light source.

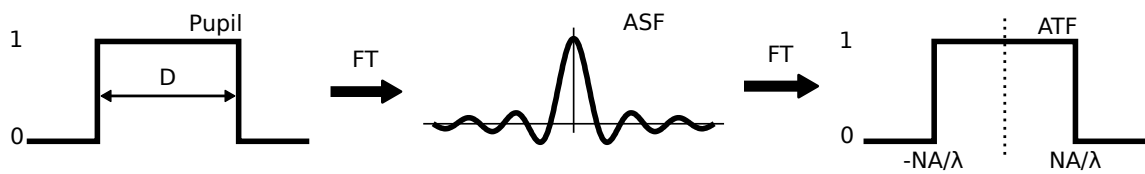


Figure 4.19: Coherent transfer function concept of an aberration-free system.

In spatial domain, the amplitude of the image is the convolution product of the amplitude object over the ASF. By squaring this amplitude, the image irradiance is found. Moreover, in frequency domain, the spectrum irradiance image results of the squared product between the object frequency spectrum (Fourier transform of the amplitude object) and the ATF. The cut-off frequency of the amplitude transfer function - i.e., Abbe resolution limit - equals λ/D .

BIBLIOGRAPHY

- [1] D.M. Parkin, J. Ferlay, M.P. Curado, F. Bray, B. Edwards, H.R. Shin, and D. Forman, "Cancer Incidence in Five Continents," IARC Cancer Base **12**, IARC Press, (2014).
- [2] Les cancers en France en 2013, INCa, Boulogne-Billancourt (2014).
- [3] B.J. Katz, M. Oliviero, and H. Rabinovitz, "Dermoscopy and its impact on skin cancer diagnostics," *Journal of Drugs in Dermatology* **9**, pp. 129-130 (2010).
- [4] D. Kapsokalyvas, N. Brusino, D. Alfieri, V. de Giorgi, G. Cannarozzo, R. Cicchi, D. Massi, N. Pimpinelli, and F.S. Pavone, "Spectral morphological analysis of skin lesions with a polarization multispectral dermoscope," *Optics Express* **21**, pp. 4826-4840 (2013).
- [5] F. Vasefi, N. MacKinnon, R.B. Saager, A.J. Durkin, R. Chave, E.H. Lindsley, and D.L. Farkas, "Polarization-Sensitive Hyperspectral Imaging in vivo: A Multimode Dermoscope for Skin Analysis," *Scientific Reports* **4**, 4924 (2014).
- [6] Y. Pan, D.S. Gareau, A. Scope, M. Rajadhyaksha, and N.A. Mullani, A.A. Marghoob, "Polarized and Nonpolarized Dermoscopy The Explanation for the Observed Differences," *Archives of dermatology* **144**, pp. 828-829 (2008).
- [7] A.A. Marghoob, R.P. Usatine, and N. Jaimes, "Dermoscopy for the Family Physician," *American Family Physician* **88**, pp. 441-450 (2013).
- [8] R. Soltani-Arabshahi, C. Sweeney, B. Jones, S.R. Florell, N. Hu, and D. Grossman, "Predictive value of biopsy specimens suspicious for melanoma: Support for 6-mm criterion in the ABCD rule," *Journal of American Academic Dermatology*, " **72**, pp. 412-418 (2015).
- [9] H. Skvara, L. Teban, M. Fiebiger, M. Binder, and H. Kittler, "Limitations of Dermoscopy in the Recognition of Melanoma," *Archives of Dermatology* **141**, pp. 155-160 (2005).
- [10] G. Goldenberg et al., "Histopathology of Skin Cancer," in "*Managing Skin Cancer*" Edited by E. Stockfleth, T. Rosen, and S. Schumaak, Springer-Verlag Berlin Heidelberg (2010).

- [11] "Non Invasive Diagnostic Techniques in Clinical Dermatology," Edited by E. Berardesca, H. Maibach, and K. Wilhelm, Springer-Verlag Berlin Heidelberg (2014).
- [12] R. Kleinerman, T.B. Whang, R.L. Bard, and E.S. Marmur, "Ultrasound in dermatology: Principles and applications," *Journal of the American Academy of Dermatology* **67**, pp. 478-487 (2012).
- [13] D. Rallan and C.C. Harland, "Skin imaging: is it clinically useful?," *Clinical and Experimental Dermatology* **29**, pp. 453-459 (2004).
- [14] H.F. Zhang, K. Maslov, G. Stoica, and L.V. Wang, "Functional photoacoustic microscopy for high-resolution and noninvasive in vivo imaging," *Nature Biotechnology* **24**, pp. 848-851 (2006).
- [15] A.G. Bell, "On the production and reproduction of sound by light," *American Journal of Science* **20**, pp.305-324 (1880).
- [16] M. Xu and L.V. Wang, "Photoacoustic imaging in biomedicine," *Review of Scientific Instruments* **77**, 041101 (2006).
- [17] R.J. Zemp, L. Song, R. Bitton, K. Kirk Shung, and L.V. Wang, "Realtime photoacoustic microscopy in vivo with a 30-MHz ultrasound array transducer," *Optics Express* **16**, pp. 7915-7928 (2008).
- [18] L.V. Wang, "Multiscale photoacoustic microscopy and computed tomography," *Nature Photonics* **3**, pp. 503-509 (2009).
- [19] M. Rajadhyaksha, M. Grossman, D. Esterowitz, R.H. Webb, and R.R. Anderson, "In Vivo Confocal Scanning Laser Microscopy of Human Skin: Melanin Provides Strong Contrast," *Journal of Investigative Dermatology* **104**, pp. 946-952 (1995).
- [20] Vivascope®, *in-vivo* confocal microscopy devices, "[http : // www.vivascope.de/en/products/devices/in - vivo - devices.html](http://www.vivascope.de/en/products/devices/in-vivo-devices.html)" [Online]. This is the commercial website of the MAVIG Vivascope company (2015).
- [21] A. Nwaneshiudu, C. Kuschal, F.H. Sakamoto, R.R. Anderson, K Schwarzenberger, and R.C. Young, "Introduction to Confocal Microscopy," *Journal of Investigative Dermatology* **132** (2012).
- [22] A.N. Yaroslavsky, J. Barbosa, V. Neel, C. DiMarzio, and R.R. Anderson, "Combining multispectral polarized light imaging and confocal microscopy for localization of nonmelanoma skin cancer," *Journal of Biomedical Optics* **10**, 014011 (2005).
- [23] "Non Invasive Diagnostic Techniques in Clinical Dermatology," Edited by E. Berardesca, H. Maibach, and K. Wilhelm, Springer-Verlag Berlin Heidelberg (2014).

- [24] Vivosight, VivoSight OCT scanner, "[http : //www.vivosight.com/products/](http://www.vivosight.com/products/)" [Online]. This is the commercial website of the VivoSight OCT system from Michelson Diagnostics company (2016).
- [25] Skintell, Non-invasive high-definition Optical Coherence Tomography solution, "[http : //www.agfahealthcare.com/global/en/main/news_events/news/archive/he20120926_skintell.jsp](http://www.agfahealthcare.com/global/en/main/news_events/news/archive/he20120926_skintell.jsp)" [Online]. This is the commercial website of the Skintell OCT system from AGFA HealthCare company (2016).
- [26] DAMAE Medical - le diagnostic dans la peau, "[http : //www.damaemedical.fr](http://www.damaemedical.fr)" [Online]. This is the website of the start-up DAMAE Medical (2016).
- [27] Dermalumics, "[http : //http : //www.dermalumics.com/](http://www.dermalumics.com/)" [Online]. This is the commercial website of the NITID OCT system from Dermalumics company (2016).
- [28] S. Perrin, L. Froehly, N. Passilly, and C. Gorecki, "Optical coherence tomography microsystem for early diagnosis of skin pathologies," Summer School Biophotonics 13, Sweden (2013).
- [29] S. Bargiel, C. Jia, M. Baranski, J. Fromel, N. Passilly, C. Gorecki, and M. Wiemer, "Vertical integration technologies for optical transmissive 3-D micro-scanner based on glass microlenses," *Procedia Engineering* **47**, pp. 1133-1136 (2012).
- [30] J.M. Palmer, "Getting Intense on Intensity ," *Metrologia* **30**, pp. 371-372 (1993).
- [31] A.F. Fercher, K. Mengedoht, and W. Werner, "Eye length measurement by interferometry with partially coherent light," *Optics Letters* **13**, pp. 186-188 (1988).
- [32] D. Huang, E.A. Swanson, C.P Lin, J.S. Schuma, W.G. Stinson, W. Chang, M.R. Hee, T. Flotte, K. Gregory, C.A. Puliafito, and J.G. Fujimoto, "Optical coherence tomography," *Science* **254**, pp. 1178-1181 (1991).
- [33] J. Welzel, E. Lankenau, R. Birngruber, and R. Engelhardt, "Optical coherence tomography of the human skin," *Journal of the American Academy of Dermatology* **37**, pp. 958-963 (1997).
- [34] N.D Gladkova, G.A Petrova, N.K. Nikulin, S.G. Radenska-Lopovok, L.B. Snopova, Y.P. Chumakov, V.A. Nasonova, V.M. Gelikonov, G.V. Gelikonov, R.V. Kuranov, A.M. Sergeev, and F.I. Feldchtein, "In vivo op-tical coherence tomography imaging of human skin: normand pathology," *Skin Research and Technology* **6**, pp. 6-16 (2000).
- [35] "Optical coherence tomography, Technology and Applications," Edited by W. Drexler and J.G. Fujimoto, Springer Berlin Heidelberg (2008).

- [36] "Fundamentals of Photonics," Edited by B.E.A. Saleh and M.C. Teich, Wiley-Interscience (2007).
- [37] D. Gabor, "A new microscopic principle," *Nature* **161**, 777 (1948).
- [38] A.F. Fercher, C.K. Hitzenberger, G. Kamp, and S.Y. El-Zaiat, "Measurement of intraocular distances by backscattering spectral interferometry," *Optics Communications* **117**, pp. 43-48 (1995).
- [39] M. Wojtkowski, R. Leitgeb, A. Kowalczyk, T. Bajraszewski, and A.F. Fercher, "In vivo human retinal imaging by Fourier domain optical coherence tomography," *Journal of Biomedical Optics* **7**, pp. 457-463 (2002).
- [40] N. Wiener, "Generalized harmonic analysis," *Acta mathematica* **55**, pp. 117-258 (1930).
- [41] A. Khintchine, "Korrelationstheorie der stationären stochastischen Prozesse," *Mathematische annalen* **109**, pp. 604-615 (1934).
- [42] S.R. Chinn, E.A. Swanson, and J.G. Fujimoto, "Optical coherence tomography using a frequency-tunable optical source," *Optics Letters* **22**, pp. 340-342 (1997).
- [43] G. Hausler and M.W. Lindner, "Coherence radar and spectral radar - New tools for dermatological diagnosis," *Journal of Biomedical Optics* **3**, pp. 21-31 (1998).
- [44] S. Perrin, J. Kuhn, and C. Depeursinge, "Microscopie holographique digitale à faible cohérence," Master of science thesis, Université de Bourgogne (2010).
- [45] M.V. Sarunic, S. Weinberg, and J.A. Izatt, "Full-field swept-source phase microscopy," *Optics Letters* **31**, pp. 1462-1464 (2006).
- [46] R. Leitgeb, C.K. Hitzenberger, and A.F. Fercher, "Performance of fourier domain vs. time domain optical coherence tomography," *Optics Express* **11**, pp. 889-894 (2003).
- [47] J. Zhang, J.S. Nelson, and Z. Chen, "Removal of a mirror image and enhancement of the signal-to-noise ratio in Fourier-domain optical coherence tomography using an electro-optic phase modulator," *Optics Letters* **30**, pp. 147-149 (2005).
- [48] M. Wojtkowski, A. Kowalczyk, R. Leitgeb, and A.F. Fercher, "Full range complex spectral optical coherence tomography technique in eye imaging," *Optics Letters* **27**, pp. 1415-1417 (2002).
- [49] B. Vakoc, S. Yun, G. Tearney, and B. Bouma, "Elimination of depth degeneracy in optical frequency-domain imaging through polarization-based optical demodulation," *Optics Letters* **31**, pp. 362-364 (2006).

- [50] A.M. Davis, M.A. Choma, and J.A. Izatt, "Heterodyne swept-source optical coherence tomography for complete complex conjugate ambiguity removal," *Journal of Biomedical Optics* **10**, 064005 (2005).
- [51] M. Sarunic, M.A. Choma, C. Yang, and J.A. Izatt, "Instantaneous complex conjugate resolved spectral domain and swept-source OCT using 3x3 fiber couplers," *Optics Express* **13**, pp. 957-967 (2005).
- [52] "Interferogram analysis of optical testing, Second Edition," Edited by D. Malacara, M. Servín, and Z. Malacara, CRC Press (2005).
- [53] H. Schreiber and J.H. Bruning, "Phase shifting interferometry," in "*Optical shop testing*" Edited by D. Malacara, Wiley-Interscience (2007).
- [54] D.Y. Kim, J.S. Werner, and R.J. Zawadzki, "Comparison of phase-shifting techniques for in vivo full-range, high-speed Fourier-domain optical coherence tomography," *Journal of Biomedical Optics* **15**, 056011 (2010).
- [55] J.T. Oh and B.M. Kim, "Artifact removal in complex frequency domain optical coherence tomography with an iterative least-squares phase-shifting algorithm," *Applied Optics* **45**, pp. 4157-4164 (2006).
- [56] K. Wang, Z. Ding, Y. Zeng, J. Meng, and M. Chen, "Sinusoidal B-M method based spectral domain optical coherence tomography for the elimination of complex-conjugate artifact," *Optics Express* **17**, pp. 16820-16832 (2009).
- [57] S. Bourquin, "Low-coherence interferometry based on customized detector arrays," Ph.D thesis, École Polytechnique Fédérale de Lausanne (2010).
- [58] M.H. Frosz, M. Juhl, and M.H. Lang, "Optical coherence tomography: System design and noise analysis," Risø National Laboratory (2001).
- [59] S. Beer, "Real-time photon-noise limited optical coherence tomography based on pixel-level analog signal processing," Ph.D thesis, Université de Neuchâtel and Centre suisse d'électronique et de microtechnique (2006).
- [60] "The Fourier Transform and Its Applications," Edited by R.N. Bracewell, McGraw Hill (1965).
- [61] S. Shin, U. Sharma, H. Tu, W. Jung, and S.A. Boppart, "Characterization and analysis of relative intensity noise in broadband optical sources for optical coherence tomography," *IEEE Photonics Technology Letters* **22**, pp. 1057-1059 (2010).

- [62] M. Choma, M. Sarunic, C. Yang, and J. Izatt, "Sensitivity advantage of swept source and Fourier domain optical coherence tomography," *Optics Express* **11**, pp. 2183-2189 (2003).
- [63] J.F. de Boer, B. Cense, B.H. Park, M.C. Pierce, G.J. Tearney, and B.E. Bouma, "Improved signal-to-noise ratio in spectral-domain compared with time-domain optical coherence tomography," *Optics Letters* **28**, pp. 2067-2069 (2003).
- [64] "Hologscopy," Edited by D. Hillmann, Springer Vieweg (2013).
- [65] Z. Yaqoob, J. Wu, and C. Yang, "Spectral domain optical coherence tomography: a better OCT imaging strategy," *BioTechniques* **39**, pp. S6-S13 (2005).
- [66] X.C. de Lega and P.J. de Groot, "Lateral resolution and instrument transfer function as criteria for selecting surface metrology instruments," *OSA Imaging and Applied Optics Technical Papers*, OTu1D.4 (2012).
- [67] "Principles of optics - Electromagnetic theory of propagation, Interference and Diffraction of light, Sixth edition," Edited by M. Born and E. Wolf, Pergamon Press (1980).
- [68] J.G. Fujimoto, "Biomedical optical imaging," *Progress Report* **151**, pp. 2008-2009.
- [69] C. Akcay, P. Parrein, and J.P. Rolland, "Estimation of longitudinal resolution in optical coherence imaging," *Applied Optics* **41**, pp. 5256-5262 (2002).
- [70] B. Povazay, K. Bizheva, A. Unterhuber, B. Hermann, H. Sattmann, A.F. Fercher, W. Drexler, A. Apolonski, W.J. Wadsworth, J.C. Knight, P.St.J. Russell, M. Vetterlein, and E. Scherzer, "Submicrometer axial resolution optical coherence tomography," *Optics Letters* **27**, pp. 1800-1802 (2002).
- [71] E. Salomatina, B. Jiang, J. Novak, and A.N. Yaroslavsky, "Optical properties of normal and cancerous human skin in the visible and near-infrared spectral range," *Journal of Biomedical Optics* **11**, 064026 (2006).
- [72] J.G. Fujimoto, C. Pitris, S.A. Boppart, and M.E. Brezinski, "Optical coherence tomography: an emerging technology for biomedical imaging and optical biopsy," *Neoplasia* **2**, pp. 9-25 (2000).
- [73] J.R. Sheppard, "Depth of field in optical microscopy," *Journal of Microscopy* **149**, pp. 73-75 (1987).
- [74] J. Mo, M. de Groot, and J.F. de Boer, "Focus-extension by depth-encoded synthetic aperture in Optical Coherence Tomography," *Optics Express* **21**, pp. 10048-10061 (2013).

- [75] S.W. Lee, H.W. Jeong, B.M. Kim, Y.C. Ahn, W. Jung, and Z. Chen, "Optimization for axial resolution, depth range, and sensitivity of spectral domain optical coherence tomography at 1.3 μm ," *Journal of the Korean Physical Society* **55**, pp. 2354-2360 (2009).
- [76] M.J. Cobb, X. Liu, and X. Li, "Continuous focus tracking for real-time optical coherence tomography," *Optics Letters* **30**, pp. 1680-1682 (2005).
- [77] J. Jang, J. Lim, H. Yu, H. Choi, J. Ha, J.H. Park, W.Y. Oh, W. Jang W, S. Lee S, and Y. Park, "Complex wavefront shaping for optimal depth-selective focusing in optical coherence tomography," *Optics Express* **21**, pp. 2890-2902 (2013).
- [78] A. Kumar, W. Drexler, and R.A. Leitgeb, "Subaperture correlation based digital adaptive optics for full field optical coherence tomography," *Optics Express* **21**, pp. 10850-10566 (2013).
- [79] B. Povazay, A. Unterhuber, B. Hermann, H. Sattmann, H. Arthaber, and W. Drexler, "Full-field time-encoded frequency-domain optical coherence tomography," *Optics Express* **14**, pp. 7661-7669 (2006).
- [80] M. Strathman, Y. Liu, E.G. Keeler, M. Song, U. Baran, J. Xi, M.T. Sun, R. Wang, X. Li, and L.Y. Lin, "MEMS scanning micro-mirror for optical coherence tomography," *Biomedical Optics Express* **6**, pp. 211-224 (2015).
- [81] Y. Watanabe and M. Sato, "Three-dimensional wide-field optical coherence tomography using an ultrahigh-speed CMOS camera," *Optics Communications* **281**, pp. 1889-1895 (2008).
- [82] A. Dubois, G. Moneron, K. Grieve, and A.C. Boccara, "Three-dimensional cellular-level imaging using full-field optical coherence tomography," *Physics in Medicine and Biology* **49**, pp. 1227-1234 (2004).
- [83] J. Fergusson, "Full Field Swept Source Optical Coherence Tomography ," Ph.D thesis, Cardiff University (2013).
- [84] B. Grajciar, M. Pircher, A.F. Fercher, and R.A. Leitgeb, "Parallel Fourier domain optical coherence tomography for in vivo measurement of the human eye," *Optics Express* **13**, pp. 1131-1137 (2005).
- [85] T. Bonin, G. Franke, M. Hagen-Eggert, P. Koch, and G. Huttmann, "In vivo Fourier-domain full-field OCT of the human retina with 1.5 million A-lines/s," *Optics Letters* **35**, pp. 3432-3434 (2010).

- [86] A.H. Dhalla, J.V. Migacz, and J.A. Izatt, "Crosstalk rejection in parallel optical coherence tomography using spatially incoherent illumination with partially coherent sources," *Optics Letters* **35**, pp. 2305-2307 (2010).
- [87] A. Kohler, "Ein neues Beleuchtungsverfahren für mikrographische Zwecke," *Zeitschrift für wissenschaftliche Mikroskopie und für Mikroskopische Technik* **10**, pp. 433-440 (1893).
- [88] T. Gambichler, V. Jaedicke, and S. Terras, "Optical coherence tomography in dermatology: technical and clinical aspects," *Archives of Dermatological Research* **303**, pp. 457-473 (2011).
- [89] A.H. Mirau, "Interferometer," US patent **152,151** (1952).
- [90] "MOEMS: Micro-Opto-Electro-Mechanical Systems," Edited by M.E. Motamedi, SPIE Press (2005).
- [91] M Baranski, S. Bargiel, N. Passilly, C. Gorecki, C. Jia, J. Frömel, and M. Wiemer, "Micro-optical design of a three-dimensional microlens scanner for vertically integrated micro-opto-electro-mechanical systems," *Applied Optics* **54**, pp. 6924-6934 (2015).
- [92] B. Redding, Y. Bromberg, M.A. Choma, and H. Cao, "Full-field interferometric confocal microscopy using a VCSEL array," *Optics Letters* **39**, pp. 4446-4449 (2014).
- [93] Y. Lu, Y. Liu, and T.K. Lau, "Simple, portable, and low-cost microscope based on off-axis digital holography using two spherical waves," *Optics Letters* **39**, pp. 4549-4552 (2014).
- [94] J. Albero, S. Bargiel, N. Passilly, P. Dannberg, M. Stumpf, U.D. Zeitner, C. Rousselot, K. Gastinger, and C Gorecki, "Micromachined array-type Mirau interferometer for parallel inspection of MEMS," *Journal of Micromechanics and Microengineering* **21**, 065005 (2011).
- [95] A. Orth and K. Crozier "Microscopy with microlens arrays: high throughput, high resolution and light-field imaging," *Optics Express* **20**, pp. 13522-13531 (2012).
- [96] "Microoptics, Second Edition," Edited by S. Sinzinger and J. Jahns, Wiley VCH (2003).
- [97] Y. Zhou, W. Xing, K.I. Maslov, L.A. Cornelius, and L.V. Wang, "Handheld photoacoustic microscopy to detect melanoma depth in vivo," *Optics Express* **39**, pp. 4731-4734 (2014).

- [98] G.J. Tearney, S.A. Boppart, B.E. Bouma, M.E. Brezinski, N.J. Weissmann, J.F. Southern, and J.G. Fujimoto, "Scanning single-mode fiber optic catheter-endoscope for optical coherence tomography," *Optics Letters* **21**, pp. 543-545 (1996).
- [99] N. Iftimia, G. Maguluri, E.W. Chang, S. Chang, J. Magill, and W. Brugge, "Hand scanning optical coherence tomography imaging using encoder feedback," *Optics Letters* **39**, pp. 6807-6810 (2014).
- [100] C.D. Lu, M.F. Kraus, B. Potsaid, J.J. Liu, W. Choi, V. Jayaraman, A.E. Cable, J. Hornegger, J.S. Duker, and J.G. Fujimoto, "Handheld ultrahigh speed swept source optical coherence tomography instrument using a MEMS scanning mirror," *Biomedical Optics Express* **5**, pp. 293-311 (2014).
- [101] T. Xie, H. Xie, G.K. Fedder, M. Zeidel, Y. Pan, "Endoscopic optical coherence tomography with a micromachined mirror," *Proc. IEEE in Microtechnologies in Medicine and Biology*, pp. 208-211 (2002).
- [102] K.H. Kim, B.H. Park, G.N. Maguluri, T.W. Lee, F.J. Rogomentich, M.G. Bancu, B.E. Bouma, J.F. de Boer, and J.J. Bernstein, "Two-axis magnetically-driven MEMS scanning catheter for endoscopic high-speed optical coherence tomography," *Optics Express* **15**, pp. 18130-18140 (2007).
- [103] I. Grulkowski, K. Szulzycki, and M. Wojtkowski, "Microscopic OCT imaging with focus extension by ultrahigh-speed acousto-optic tunable lens and stroboscopic illumination," *Optics Express* **22**, pp. 31746-31760 (2014).
- [104] H.M. Subhash, J.N. Hogan, and M.J. Leahy, "Multiple reference optical coherence tomography for smartphone applications," *SPIE Newsroom* (2015).
- [105] "Optical System Design, Second Edition," Edited by R.E. Fischer, B. Tadic-Galeb, P.R. Yoder, McGraw-Hill (2008).
- [106] "Modern Lens Design," Edited by W.J. Smith, McGraw-Hill, Inc. (1992).
- [107] J. Sandby-Moller, T. Poulsen, and H.C. Wulf, "Epidermal Thickness at Different Body Sites: Relationship to Age, Gender, Pigmentation, Blood Content, Skin Type and Smoking Habits," *Acta Dermato-Venereologica* **83**, pp. 410-413 (2003).
- [108] G-E. Costin and V.J. Hearing, "Human skin pigmentation: melanocytes modulate skin color in response to stress," *FASEB Journal* **21**, pp. 976-994 (2007).
- [109] J. Krauter, T. Boettcher, K. Korner, M. Gronle, W. Osten, N. Passilly, L. Froehly, S. Perrin, and C. Gorecki, "Full-field swept-source optical coherence tomography with phase-shifting techniques for skin cancer detection," *Proc. SPIE* **9529**, 952913 (2015).

- [110] P.J. de Groot and J.F. Biegen, "A new class of wide-field objectives for 3D interference microscopy," *Proc. SPIE* **9525**, 95250N (2015).
- [111] J. Schmit, K. Creath, and J.C. Wyant, "Surface profilers, multiple wavelength, and white light interferometry," in *"Optical shop testing"* Edited by D. Malacara, Wiley-Interscience (2007).
- [112] W.S. Wang, J. Lullin, J. Froemel, M. Wiemer, S. Bargiel, N. Passilly, C. Gorecki and T. Gessner, "Multi-wafer bonding technology for the integration of a micromachined Mirau interferometer," *Proc. SPIE* **9375**, 93750P (2015).
- [113] J. Albero, S. Perrin, N. Passilly, J. Krauter, L. Gauthier-Manuel, J. Lullin, S. Bargiel, L. Froehly, W. Osten, and C. Gorecki, "Wafer-level fabrication of Multi-element Glass Microlenses: Lens Doublet with Improved Optical performances", *Optics Letters* **41**, pp. 96-99 (2016).
- [114] S.H. Yun, G.J. Tearney, J.F. de Boer, N. Iftimia, and B.E. Bouma, "High-speed optical frequency-domain imaging," *Optics Express* **11**, pp. 2953-2963 (2003).
- [115] S.H. Yun, C. Boudoux, M.C. Pierce, J.F. de Boer, G.J. Tearney, and B.E. Bouma, "Extended-cavity semiconductor wavelength-swept laser for biomedical imaging," *IEEE Photonics Technology Letters* **16**, pp. 293-295 (2004).
- [116] S.H. Yun, C. Boudoux, G.J. Tearney, and B.E. Bouma, "High-speed wavelength-swept semiconductor laser with a polygon-scanner-based wavelength filter," *Optics Letters* **28**, pp. 1981-1983 (2003).
- [117] M. Choma, M. Sarunic, C. Yang, and J. Izatt, "Sensitivity advantage of swept source and Fourier domain optical coherence tomography," *Optics Express* **11**, pp. 2183-2189 (2003).
- [118] M. Blomberg, H. Kattelus, and A. Miranto, "Electrically tunable surface micromachined Fabry-Perot interferometer for visible light," *Sensors and Actuators A: Physical* **162**, pp. 184-188 (2010).
- [119] Superluminescent Diodes, "<https://www.superlumdiodes.com/superluminescent-diodes>" [Online]. This is the commercial website of the Superlum company (2015).
- [120] H. Saari, V.V. Aallos, A. Akujarvi, T. Antila, C. Holmlund, U. Kantajarvi, J. Makyonen, and J. Ollila, "Novel miniaturized hyperspectral sensor for UAV and space applications," *Proc. SPIE* **7474**, 74741M (2009).
- [121] A.H. Dhalla, J.V. Migacz, and J.A. Izatt, "Crosstalk rejection in parallel optical coherence tomography using spatially incoherent illumination with partially coherent sources," *Optics Letters* **35**, pp. 2305-2307 (2010).

- [122] B. Karamata, P. Lambelet, M. Laubscher, R.P. Salathé, and T. Lasser, "Spatially incoherent illumination as a mechanism for cross-talk suppression in wide-field optical coherence tomography," *Optics Letters* **29**, pp. 736-738 (2004).
- [123] W. Ha, S. Lee, Y. Jung, J.K. Kim, and K. Oh, "Acousto-optic control of speckle contrast in multimode fibers with a cylindrical piezoelectric transducer oscillating in the radial direction," *Optics Express* **17**, pp. 17536-17546 (2009). Oh2009,Scott2005
- [124] M. McGill and V.S. Scott, "Vibrating Optical Fibers To Make Laser Speckle Disappear," *NASA Tech Briefs GSC-14680-1* (2005).
- [125] LASER speckle reducer, "<http://www.optotune.com/products/laser-speckle-reducers/lsr-3005-series/>" [Online]. This is the commercial website of the Optotune company (2015).
- [126] Condenser combination, "<https://www.qioptiq-shop.com/en/Precision-Optics/LINOS-Achromats-Lens-Systems/Condensers/Condenser-combination-f-16-mm-crown-glass.html/>" [Online]. This is the commercial website of the Qioptic company (2015).
- [127] J.C. Wyant and J. Schmit, "Large FOV and high spatial resolution surface measurements," *International Journal of Machine Tools and Manufacture* **38**, pp. 691-698 (1998).
- [128] M. Zhenhe, R.K. Wang, Z. Fan, and Y. Jianquan, "Three-phase shifting method for full range spectral optical coherence tomography," *Proc. SPIE* **6085**, pp. 22-28 (2006).
- [129] D.G. Fischer and B. Ovrzyn, "Phase shifting optical coherence tomography," *Proc. SPIE* **4251** (2001).
- [130] M. Wojtkowski, A. Kowalczyk, R. Leitgeb, and A.F. Fercher, "Full range complex spectral optical coherence tomography technique in eye imaging," *Optics Letters* **27**, pp. 1415-1417 (2002).
- [131] A. Federici, H.S. Gutierrez da Costa, J. Ogien, A.K. Ellerbee, and A. Dubois, "Wide-field, full-field optical coherence microscopy for high-axial-resolution phase and amplitude imaging," *Applied Optics* **54**, pp. 8212-8220 (2015).
- [132] D.Y. Kim, J.S. Werner, and R.J. Zawadzki, "Comparison of phase-shifting techniques for in vivo full-range, high-speed Fourier-domain optical coherence tomography," *Journal of Biomedical Optics* **15**, 056011 (2010).
- [133] J. Krauter, T. Boettcher, K. Körner, M. Gronle, W. Osten, N. Passilly, L. Froehly, S. Perrin, and C. Gorecki, "Performance analysis of a full-field and full-range swept-source OCT system," *Proceeding SPIE* **9576**, Applied Advanced Optical Metrology Solutions, 957609 (2015).

- [134] K. Wang, Z. Ding, Y. Zeng, J. Meng, and Minghui Chen, "Sinusoidal B-M method based spectral domain optical coherence tomography for the elimination of complex-conjugate artifact," *Optics Express* **17**, pp. 16820-16833 (2009).
- [135] Y.Y. Cheng and J.C. Wyant, "Phase shifter calibration in phase-shifting interferometry," *Applied Optics* **24**, pp. 3049-3052 (1985).
- [136] C. Ai and J.C. Wyant, "Effect of piezoelectric transducer nonlinearity on phase shift interferometry," *Applied Optics* **26**, pp. 1112-1116 (1987).
- [137] P.J. de Groot, L.L. Deck, "New algorithms and error analysis for sinusoidal phase shifting interferometry," *Proc. SPIE* **7063**, 70630K (2008).
- [138] O. Sasaki and H. Okazaki, "Sinusoidal phase modulating interferometry for surface profile measurement," *Applied Optics* **25**, pp. 3137-3140 (1986).
- [139] O. Sasaki and H. Okazaki, "Analysis of measurement accuracy in sinusoidal phase modulating interferometry," *Applied Optics* **25**, pp. 3152-3158 (1986).
- [140] O. Sasaki, H. Okazaki, and M. Sakai, "Sinusoidal phase modulating interferometer using the integrating-bucket method," *Applied Optics* **26**, pp. 1089-1093 (1987).
- [141] P. Bu, X. Wang, O. Sasaki, "Dynamic full-range fourier-domain optical coherence tomography using sinusoidal phase-modulating interferometry," *Optical Engineering* **46**, 105603 (2007).
- [142] P. Bu, X. Wang, O. Sasaki, "Full-range parallel Fourier-domain optical coherence tomography using sinusoidal phase-modulating interferometry," *Journal of Optics A: Pure and Applied Optics* **9**, pp. 422 (2007).
- [143] N. Nan, X. Wang, P. Bu, Z. Li, X. Guo, Y. Chen, X. Wang, F. Yuan, and O. Sasaki, "Full-range Fourier domain Doppler optical coherence tomography based on sinusoidal phase modulation," *Applied Optics* **53**, pp. 2669-2676 (2014).
- [144] J. Lullin, S. Bargiel, P. Lemoal, S. Perrin, J. Albero, N. Passilly, L. Froehly, F. Lardet-Vieudrin and C. Gorecki, "An electrostatic vertical micro-scanner for phase modulating array-type Mirau microinterferometry," *Journal of Micromechanics and Microengineering* **25**, 115013 (2015).
- [145] J. Lullin, S. Perrin, M. Baranski, S. Bargiel, L. Froehly, N. Passilly, J. Albero, and C. Gorecki, "Impact of mirror spider legs on imaging quality in Mirau microinterferometry," *Optics Letters* **40**, pp. 2209-2212 (2015).

- [146] P. Merz, H.J. Quenzer, H. Bernt, B. Wagner, and M. Zoberbier, "A novel micromachining technology for structuring borosilicate glass substrates," *Proc. IEEE, Conference on Solid State Sensors, Actuators and Microsystems*, pp. 258-261 (2003).
- [147] J. Albero, S. Perrin, S. Bargiel, N. Passilly, M. Baranski, L. Gauthier-Manuel, F. Bernard, J. Lullin, L. Froehly, J. Krauter, W. Osten, and C. Gorecki, "Dense arrays of millimeter-sized glass lenses fabricated at wafer-level," *Optics Express* **23**, pp. 11702-11712 (2015).
- [148] J. Albero, S. Perrin, S. Bargiel, M. Baranski, N. Passilly, L. Gauthier-Manuel, and C. Gorecki, "Arrays of millimeter-sized glass lenses for miniature inspection systems," *Proc. SPIE* **9130**, 91300U (2014).
- [149] X. Wei, A. Bosseboeuf, F. Parrain, and E. Martincic, "Design of a long range bidirectional MEMS scanner for a tunable 3D Integrated Mirau interferometer," *Proc. IEEE in Design, Test, Integration and Packaging of MEMS/MOEMS*, pp. 1-6 (2014).
- [150] J. Lullin, "Design, simulation and fabrication of a vertical micro-scanner for phase modulation interferometry," Ph.D thesis, Université Bourgogne Franche-Comté (2015).
- [151] M.S. Kim, L. Allegre, J. Sunarjo, W. Noell, and R. Voelkel, "Overview of characterization and metrology techniques for microlenses and microlens arrays," *Proc. SPIE* **9525**, 95251D (2015).
- [152] R. Leach, "The measurement of surface texture using stylus instruments," *Measurement Good Practice Guide* **37**, National Physical Laboratory (2014).
- [153] G. Binnig, C.F. Quate, and C. Gerber, "Atomic Force Microscope", *Physical Review Letters* **56**, pp. 930-933 (1986).
- [154] G. Binnig and H. Rohrer, "Scanning tunneling microscopy", *IBM Journal of Research and Development* **30** (1986).
- [155] J.M. Bennett, V. Elings, and K. Kjoller, "Precision metrology for studying optical surfaces," *Optics and Photonics News* **2**, pp. 14-18 (1991).
- [156] "Optical measurement of surface topography," Edited by R. Leach, Springer-Verlag (2011).
- [157] G. Udupa, M. Singaperumal, R.S. Sirohi, and M.P. Kothiyal, "Characterization of surface topography by confocal microscopy: I. Principles and the measurement system," *Measurement Science and Technology* **11**, pp. 305-314 (2000).

- [158] P. de Groot, "Principles of interference microscopy for the measurement of surface topography," *Advances in Optics and Photonics* **7**, pp. 1-65 (2015).
- [159] M. Davidson, K. Kaufman, I. Mazor, and F. Cohen, "An application of interference microscopy to integrated circuit inspection and metrology," *Proc. SPIE* **0775**, pp. 233-247 (1987).
- [160] A. Dubois and A.C. Boccara, "Full-field optical coherence tomography," in "*Optical coherence tomography, Technology and Applications*" Edited by W. Drexler and J.G. Fujimoto, Springer Berlin Heidelberg (2008).
- [161] G.S. Kino and S.C. Chim, "Mirau correlation microscope," *Applied Optics* **29**, pp. 3775-3783 (1990).
- [162] Application Design Patterns: Producer/Consumer, "<http://www.ni.com/white-paper/3023/en/>" [Online]. This is the tutorial of the producer/consumer design from the National Instruments website.
- [163] N. Balasubramanian, "Optical system for surface topography measurement," US patent **US4340306 A** (1982).
- [164] P.C. Montgomery and J.P. Fillard, "Peak fringe scanning microscopy: submicron 3D measurement of semiconductor components," *Proc. SPIE* **1755**, pp. 12-23 (1993).
- [165] M.K. Baranski, "Optical design and development of building blocks for a new generation of vertically integrated on-chip confocal microscopes," Ph.D thesis, Université de Franche-Comté (2013).
- [166] "Surface Texture Parameters", Report from Zygo Corporation (2013).
- [167] C.J.R. Sheppard and K.G. Larkin, "Effect of numerical aperture on interference fringe spacing," *Applied Optics* **34**, pp. 4731-4734 (1995).
- [168] E. Botcherby, R. Juskaitis, M. Booth, and T. Wilson, "An optical technique for remote focusing in microscopy," *Optical Communication* **281**, pp. 880-887 (2008).
- [169] R.W. Cole, T. Jinadasa, and C.M. Brown, "Measuring and interpreting point spread functions to determine confocal microscope resolution and ensure quality control," *Nature Protocols* **6**, pp. 1929-1941 (2011).
- [170] N. Bobroff and A.E. Rosenbluth, "Evaluation of highly corrected optics by measurement of the Strehl ratio," *Applied Optics* **31**, pp. 1523-1536 (1992).

- [171] F. Charriere, A. Marian, T. Colomb, P. Marquet and C. Depeursinge, "Amplitude point-spread function measurement of high-NA microscope objectives by digital holographic microscopy," *Optics Letters* **32**, pp. 2456-2458 (2007).
- [172] T.E. Oliphant, "Python for scientific computing," *Computer Sciences Engineering* **9**, pp. 10-20 (2007).
- [173] M. A. Robertson, S. Borman and R. Stevenson, "Dynamic range improvement through multiple exposures," *Proc. IEEE, International Conference on Image Processing*, pp. 159-163 (1999).
- [174] "The Optical Transfer Function of Imaging Systems," Edited by T. Williams, CRC Press (1998).
- [175] "Modulation Transfer Function in Optical and Electro-Optical Systems," Edited by G.D. Boreman, SPIE Press Book (2001).
- [176] K. Strehl, "Aplanatische und fehlerhafte Abbildung im Fernrohr," *Zeitschrift für Instrumentenkunde* **15**, pp. 362-370 (1895).
- [177] M. Baranski, S. Perrin, N. Passilly, L. Froehly, J. Albero, S. Bargiel, and C. Gorecki, "A simple method for quality evaluation of micro-optical components based on 3D IPSF measurement," *Optics Express* **22**, pp. 13202-13212 (2014).
- [178] A Better Method of Measuring Optical Performance, "<http://www.rfroyce.com/standards.htm>" [Online]. This is the short course on the Strehl ratio and the relationship with the wavefront.
- [179] Effect of wavefront aberrations, "<http://www.telescope-optics.net/effects1.htm>" [Online]. This is a course of the effects on optical aberrations onto the image quality.
- [180] H. Ottevaere, R. Cox, H. P. Herzig, T. Miyashita, K. Naessens, M. Taghizadeh, R. Völkel, H. J. Woo, and H. Thienpont, "Comparing glass and plastic refractive microlenses fabricated with different technologies," *Journal of Optics A: Pure and Applied Optics* **8**, S407-S429 (2006).
- [181] V.N. Mahajan, "Strehl ratio for primary aberrations in terms of their aberration variance," *Journal of the Optical Society of America* **73**, pp. 860-861 (1983).
- [182] J. Yang, L. Qiu, W. Zhao, R. Shao, and Z. Li, "Measuring the lens focal length by laser reflection-confocal technology," *Applied Optics* **52**, pp. 3812-3817 (2013).
- [183] G.R. Brady, "Application of Phase Retrieval to the Measurement of Optical Surfaces and Wavefronts," Ph.D thesis, University of Rochester (2008).

- [184] F. Charriere, J. Kuhn, T. Colomb, F. Montfort, E. Cucho, Y. Emery, K. Weible, P. Marquet, and C. Depeursinge, "Characterization of microlenses by digital holographic microscopy," *Applied Optics* **45**, pp. 829-835 (2006).
- [185] P. Pulaski, James P. Roller, Daniel R. Neal, and Keith Ratte, "Measurement of aberrations in microlenses using a Shack-Hartmann wavefront sensor," *Proc. SPIE* **4767**, pp. 44-52 (2002).
- [186] Wavefront and surface measurement, "<http://www.trioptics.com/knowledge-base/wavefront-and-surface-measurement/>" [Online]. This knowledge base lists the wavefront and the surface measurement techniques through interferometers and Shack-Hartmann sensors.
- [187] R. W. Gerchberg and W. O. Saxton, "A practical algorithm for the determination of the phase from image and diffraction plane pictures," *Optik* **35**, pp. 237-246 (1972).
- [188] D.L. Misell, "An examination of an iterative method for the solution of the phase problem in optics and electron optics," *Journal of Physics D: Applied Physics*. **6**, pp. 2200-2216 (1973).
- [189] L.J. Allen and M.P. Oxley, "Phase retrieval from series of images obtained by defocus variation," *Optical Communication* **199**, pp. 65-75 (2001).
- [190] J.R. Fienup, "Phase retrieval algorithms: A comparison," *Appl. Opt.* **21**, 2758-2769 (1982).
- [191] G.R. Brady and J.R. Fienup, "Measurement range of phase retrieval in optical surface and wavefront metrology," *Applied Optics* **48**, pp. 442-449 (2009).
- [192] I.A. Shevkunov, N.S. Balbekin, and N.V. Petrov, "Comparison of digital holography and iterative phase retrieval methods for wavefront reconstruction," *Proc. SPIE* **9271**, 927128 (2014).
- [193] V.N. Mahajan, "Zernike polynomials and wavefront fitting," in "*Optical Shop Testing, 3rd ed.*", Edited by D. Malacara, John Wiley and Sons (2007).
- [194] "Principles of Optics: Electromagnetic Theory of Propagation, Interference and Diffraction of Light," Edited by M. Born, E. Wolf, and A. Bhatia, Cambridge U. Press (1999).
- [195] "Computer Techniques for Image Processing in Electron Microscopy," Edited by W.O. Saxton, Academic Press Inc. (1978).

- [196] "Adaptive Optics for Vision Science: Principles, Practices, Design and Applications," Edited by J. Porter, H. Queener, J. Lin, K. Thorn, and A. A. S. Awwal, Wiley-Blackwell (2006).
- [197] J.Y. Wang and D.E. Silva, "Wave-front interpretation with Zernike polynomials," *Appl. Opt.* **19**, 1510-1518 (1980).
- [198] Z. Jingshan, R.A. Claus, J. Dauwels, L. Tian, and L. Waller, "Transport of intensity phase imaging by intensity spectrum fitting of exponentially spaced defocus planes," *Optics Express* **22**, pp. 10661-10674 (2014).
- [199] J. Martinez-Carranza, K. Falaggis, M. Jozwik, and T. Kozacki, "Comparison of phase retrieval techniques based on the transport of intensity equation using equally and unequally spaced plane separation criteria," *Proc. SPIE* **9204**, 92040G (2014).
- [200] G.R. Brady and J.R. Fienup, "Measurement range of phase retrieval in optical surface and wavefront metrology," *Appl. Opt.* **48**, 442-449 (2009).
- [201] "Two Dimensional Phase Unwrapping. Theory, Algorithms and Software," Edited by D.C. Ghiglia and M.D. Pritt, Wiley-Blackwell (1998).
- [202] H. Takajo and T. Takahashi, "Noniterative method of obtaining the exact solution for the normal equation in least-squares phase estimation from the phase difference," *Journal of Optical Society of America A.* **5**, pp.1818-1827 (1988).
- [203] "Modern Optical Engineering 4th edition," Edited by W.J. Smith, SPIE Press (2008).
- [204] Q. Li, X. Shao, "Spherical aberration and modulation transfer function," *Proc. SPIE* **9124**, 91241B (2014).
- [205] "Glass: Nature, Structure and Properties," Edited by H. Scholze, Springer-Verlag (1991).
- [206] MSA-500 Micro-system analyzer, Polytec, "[http : //www.polytec.com/us/products/vibration - sensors/microscope - based - systems/msa - 500 - micro - system - analyzer/](http://www.polytec.com/us/products/vibration-sensors/microscope-based-systems/msa-500-micro-system-analyzer/)" [Online]. This is the commercial website of the MSA-500 Micro-system analyzer from Polytec company (2015).
- [207] M. Baranski, N. Passilly, S. Bargiel, L. Froehly, and C. Gorecki, "Miniature Schwarzschild objective as a micro-optical component free of main aberrations: concept, design, and first realization with silicon-glass micromachining," *Applied Optics* **55**, pp. 2771-2779 (2016).

- [208] A. Federici, "Developpement de systemes de microscopie par coherence optique plein champ etendus spatialement et spectralement," Ph.D thesis, Institut d'Optique Graduate School - Université Paris-Sud (2015).
- [209] Z. Hu and A.M. Rollins, "Fourier domain optical coherence tomography with a linear-in-wavenumber spectrometer," *Optics Letters* **32**, pp. 3525-3527 (2007).
- [210] N.R. Lomb, "Least-squares frequency analysis of unequally spaced data," *Astrophysics and Space Science* **39**, pp. 447-462 (1976).
- [211] D. Hillmann, G. Huttmann, and P. Koch, "Using nonequispaced fast Fourier transformation to process optical coherence tomography signals," *Proc. SPIE-OSA Biomedical Optics* **7372**, 73720R (2009).
- [212] A.V. Zvyagin, P. Blazkiewicz, and J. Vintrou, "Image reconstruction in full-field Fourier-domain optical coherence tomography," *Journal of Optics A: Pure Applied Optics* **7**, pp 350-356 (2005).
- [213] S. Chang, Y. Mao, and C. Flueraru, "Labview programming for swept-source full-field optical coherence tomography," *Proc. SPIE* **8007**, 800705 (2011).
- [214] H. Hiro-Oka, "Use of cosine tapered window to improve dynamic range of OCT without loss of resolution," *Proc. SPIE* **6847** (2008).
- [215] M. Bayleyegn, H. Makhlof, C. Crotti, K. Plamann, and A. Dubois, "High resolution spectral-domain optical coherence tomography at 1.3 micron center wavelength using a broadband superluminescent diode light source," *Optics Communications, Elsevier*, pp. 5564 (2012).
- [216] "The Analytical Theory of Heat," Edited by J.B.J Fourier, Translated by Alexander Freeman, The University Press Cambridge (1878).
- [217] "Handbook of Mathematical Functions with Formulas, Graphs, and Mathematical Tables, 9th printing," Edited by M. Abramowitz and I.A. Stegun, New York Dover Publications (1972).
- [218] J. Lein, "Spectral linewidth and coherence," Master of science thesis, University of Oslo (2010).
- [219] "Handbook of Mathematical Functions with Formulas, Graphs, and Mathematical Tables," Edited by M. Abramowitz, and I.A. Stegun, Dover Publications (1972).
- [220] F. Zernike, "Beugungstheorie des schneidenver-fahrens und seiner verbesserten form, der phasenkontrastmethode," *Physica* **1**, pp. 689-704 (1934).

- [221] J.C. Wyant and K. Creath, "Basic Wavefront Aberration Theory for Optical Metrology," *Applied Optics and Optical Engineering* **11** (1992).
- [222] V.N. Mahajan and G.M. Dai, "Orthonormal polynomials in wavefront analysis: analytical solution," *Journal of the Optical Society of America A* **24**, pp. 2994-3016 (2007).
- [223] "Optics and photonics - Optical transfer function - Definitions and mathematical relationships," British Standards Institution, BS ISO 9334 (2012).
- [224] "Handbook of Optical Design, Second Edition," Edited by Z. Malacara, CRC Press (2003).
- [225] J.W. Coltman, "The Specification of Imaging Properties by Response to a Sine Wave Input," *Journal of the Optical Society of America* **44**, pp. 468-471 (1954).
- [226] Lord Rayleigh, "Investigations in optics, with special reference to the spectroscope," *Philosophical magazine*. **8**, pp. 261-274 (1879).
- [227] C.M. Sparrow, "On Spectroscopic Resolving Power," *Astrophysical Journal* **44**, pp. 76-87 (1916).
- [228] A.W. Jones, J. Bland-Hawthorn, and P.L. Shopbell, "Towards a General Definition for Spectroscopic Resolution," *Proc. ASP Astronomical Data Analysis Software and Systems IV* **77** (1995).
- [229] D.A. Tichenor and J.W. Goodman, "Coherent Transfer Function," *Journal of the Optical Society of America* **62**, pp. 293-295 (1972).

INDEX

- aberrations
 - spherical, 45, 85, 94, 100, 133
 - Zernike, 86, 88, 133
- coherence
 - length, 16, 33, 74
 - spatial, 32, 38, 110
 - temporal, 16, 74
- MOEMS
 - micro-scanner, 56, 65, 95
 - microlens, 44, 63, 92
 - Mirau-interferometer, 43, 97, 106
- optical coherence tomography
 - frequency domain, 20, 41
 - frequency domain, 24, 51
 - full-field swept-source, 36, 41, 71, 105
 - noise, 28, 60
 - resolution, 9, 32
 - swept source, 20, 106
 - time domain, 18, 74
- phase
 - phase retrieval, 86
 - phase shifting, 25, 57, 109
- propagation, 16, 52, 87
- refractive index, 33, 48, 62, 94
- resolution
 - Abbe criterion, 32, 44, 82
 - diffraction-limited, 83, 93
 - FWHM criterion, 82, 92, 98, 137
 - measurement, 80, 137
- topography, 72, 92, 99
- transfer function
 - coherent, 138
 - contrast, 100, 136
 - modulation, 32, 45, 82, 93, 135

Stéphane Perrin - Résumé

Address	53B Rue de Belfort, FR-25000 Besançon	Date of Birth	22 th April 1986
Mobile Phone	+33 (0)6 85 49 60 67	Nationality	French
		Email	stephane.perrin@femto-st.fr

Summary

I obtained my MSc degree, in Physics, Laser and Materials, at the University of Bourgogne (Dijon, France) and my BSc, in Optical Instrumentation, at the University Louis Pasteur (Strasbourg I, France). In 2010, I joined Prof. Christian Depeursinge's Microvision and Microdiagnostics Group, at the Swiss Institute of Technology in Lausanne (EPFL). I worked as Scientific Assistant for the development of a new low coherence digital holographic microscopy technique. Then, from 2011 to 2012, I was Research Engineer in a private research laboratory, Dynamic 3D. I made special machines for the optical metrology and the non-destructive testing. Since October 2012, I'm PhD student at FEMTO-ST Institute under Prof. Christophe Gorecki's supervision. I work on optical coherence tomography (OCT) for the diagnosis of skin pathologies and the characterization of micro-optical components.

EDUCATION

- 2012-2016 **PhD in Engineering Sciences**
University Bourgogne Franche-Comté (UBFC), FR
Topic: Micro-optics for optical coherence tomography micro-system
- 2008-2010 **Master in Physics Laser and Materials**
University of Bourgogne (UB), FR, and EPFL, CH
Master topic: Low coherence digital holography microscope
- 2007-2008 **Bachelor in Optical Instrumentation**
University Louis Pasteur (ULP), FR
- 2005-2007 **Advanced technician's certificate in Photonics**
Lycée Victor Bérard, FR

PROFESSIONAL EXPERIENCE

- 2012-2016 **Research assistant**
FEMTO-ST (UMR 6174 CNRS, University Bourgogne Franche-Comté), FR
Development of a new full field swept source optical coherence tomography micro-system for the diagnosis of skin pathologies and characterization of micro-optical components.
- 2011-2012 **Research engineer**
Dynamic 3D, FR
Manufacturing of non-invasive and non-destructive special devices for industry.
- 2010-2011 **Research assistant**
Swiss Institute of Technology in Lausanne, CH
Development of digital holography microscope based on low coherence involving real-time visualizing of biological application.
- Intern**
- 2009 ICB (University of Bourgogne), FR. Microwave microscopy
- 2008 LSP (University Louis Pasteur), FR. Stereo-microscopy
- 2008 LSP (University Louis Pasteur), FR. Laser marking with diffractive optical elements
- 2007 University of Technology of Troyes, FR. Near-field scanning optical microscopy
- 2006 HOLOLAB (University of Liège), BE. Imaging holography

COMPUTER SKILLS

OS	Windows XP and 7, Unix
Publishing	MS Office Suite, LaTeX, Inkscape, Adobe Illustrator
Programming languages	Labview Core 3, Python, Matlab
Simulation	Matlab, Python, Comsol Multiphysics, Zemax
CAD	AutoCAD, Solidworks, SwCAD

EXTERNAL ACTIVITIES

Organizations: Treasurer of FEMTO-ST SPIE and OSA Student Chapter (2013-2015)

Sports: Basket-ball, hand-ball, swimming, hiking, skiing

PUBLICATIONS

PEER-REVIEWED PUBLICATIONS

- J. Albero, S. Perrin, N. Passilly, J. Krauter, L. Gauthier-Manuel, L. Froehly, J. Lullin, S. Bargiel, W. Osten, and C. Gorecki, "Wafer-level fabrication of multi-element glass lenses: lens doublet with improved optical performances," *Optics Letters* **41**, pp. 96-99 (2016).
- S. Perrin, M. Baranski, L. Froehly, J. Albero, N. Passilly, and C. Gorecki, "Simple method based on intensity measurements for characterization of aberrations from micro-optical components," *Applied Optics* **54**, pp. 9060-9064 (2015).
- J. Lullin, S. Bargiel, P. Lemoal, S. Perrin, J. Albero, N. Passilly, L. Froehly, F. Lardet-Vieudrin and C. Gorecki, "An electrostatic vertical micro-scanner for phase modulating array-type Mirau micro-interferometry," *Journal of Micromechanics and Microengineering* **25**, pp. 115013 (2015).
- J. Lullin, S. Perrin, M. Baranski, S. Bargiel, L. Froehly, N. Passilly, J. Albero, and C. Gorecki, "Impact of mirror spider legs on imaging quality in Mirau micro-interferometry," *Optics Letters* **40**, pp. 2209-2212 (2015).
- J. Albero, S. Perrin, S. Bargiel, N. Passilly, M. Baranski, L. Gauthier-Manuel, F. Bernard, J. Lullin, L. Froehly, J. Krauter, W. Osten, and C. Gorecki, "Dense arrays of millimeter-sized glass lenses fabricated at wafer-level," *Optics Express* **23**, pp. 11702-11712 (2015).
- M. Baranski, S. Perrin, N. Passilly, L. Froehly, J. Albero, S. Bargiel, and C. Gorecki, "A simple method for quality evaluation of micro-optical components based on 3D IPSF measurement," *Optics Express* **22**, pp. 13202-13212 (2014).

PROCEEDINGS

- S. Perrin, N. Passilly, L. Froehly, and C. Gorecki, "Aberration retrieval for the characterization of micro-optical components," *Proceeding SPIE 9890, Optical Micro and Nanometrology V* (2016).
- N. Passilly, S. Perrin, J. Albero, J. Krauter, O. Gaiffe, L. Gauthier-Manuel, L. Froehly, J. Lullin, S. Bargiel, W. Osten, and C. Gorecki, "Wafer-level fabrication of arrays of glass lens doublets," *Proceeding SPIE 9888, Optical Micro and Nanometrology V* (2016).

- N. Passilly, S. Perrin, J. Lullin, J. Albero, S. Bargiel, L. Froehly, C. Gorecki, J. Krauter, W. Osten, W.S. Wang, and M. Wiemer, "Array-type miniature interferometer as the core optical microsystem of an optical coherence tomography device for tissue inspection," *Proceeding SPIE 9890, Optical Micro and Nanometrology V* (2016).
- J. Krauter, T. Boettcher, K. Körner, M. Gronle, W. Osten, N. Passilly, L. Froehly, S. Perrin, and C. Gorecki, "Performance analysis of a full-field and full-range swept-source OCT system," *Proceeding SPIE 9576, Applied Advanced Optical Metrology Solutions*, 957609 (2015).
- J. Krauter, T. Boettcher, K. Körner, M. Gronle, W. Osten, N. Passilly, L. Froehly, S. Perrin, and C. Gorecki, "Full-field swept-source optical coherence tomography with phase-shifting techniques for skin cancer detection," *Proceeding SPIE 9529, Optical Methods for Inspection, Characterization, and Imaging of Biomaterials II*, 952913 (2015).
- S. Perrin, M. Baranski, N. Passilly, L. Froehly, J. Albero, S. Bargiel, and C. Gorecki, "Simple setup for optical characterization of microlenses," *Proceeding SPIE 9204, Interferometry XVII: Advanced Applications*, 92040D (2014).
- J. Lullin, S. Bargiel, E. Courjon, S. Perrin, M. Baranski, N. Passilly, and C. Gorecki, "Monolithic integration of a glass membrane on silicon micro-actuator for micro-interferometry," *IEEE International Conference, Optical MEMS and Nanophotonics (OMN)*, pp. 87-88 (2014).
- J. Albero, S. Perrin, S. Bargiel, M. Baranski, N. Passilly, L. Gauthier-Manuel, and C. Gorecki, "Arrays of millimeter-sized glass lenses for miniature inspection systems," *Proceeding SPIE 9130, Micro-Optics*, 91300U (2014).
- J. Krauter, T. Boettcher, W. Lyda, W. Osten, N. Passilly, L. Froehly, S. Bargiel, J. Albero, S. Perrin, J. Lullin, and C. Gorecki, "Optical design of a vertically integrated array-type Mirau-based OCT system," *Proceeding SPIE 9132, Optical Micro- and Nanometrology V*, 91320L (2014).
- M. Baranski, S. Perrin, N. Passilly, L. Froehly, S. Bargiel, J. Albero, and C. Gorecki, "Metrology of micro-optical components quality using direct measurement of 3D intensity point spread function," *Proceeding SPIE 9132, Optical Micro- and Nanometrology V*, 913216 (2014).

INTERNATIONAL CONFERENCE PRESENTATIONS

- S. Perrin, N. Passilly, L. Froehly, and C. Gorecki, "Aberration retrieval for the characterization of micro-optical components," SPIE Photonics Europe, Brussels, Belgium, April 2016.
- S. Perrin, J. Lullin, L. Froehly, N. Passilly, and C. Gorecki, "Optical Coherence Tomography for Early Diagnosis of Skin Pathologies," Neuchâtel, Switzerland, September 2014.
- S. Perrin, M. Baranski, N. Passilly, L. Froehly, J. Albero, S. Bargiel, and C. Gorecki, "Simple setup for optical characterization of microlenses," SPIE Optics and Photonics, San Diego, United States, August 2014.

Abstract:

The manuscript concerns the optical design and the development of a non-invasive new imaging system for the early diagnosis of skin pathologies. Indeed, an early diagnosis can make the difference between malignant and benign skin lesion in order to minimize unnecessary surgical procedure. Furthermore, prognosis for the year 2015 was that more than three millions new skin cancer cases will be diagnosed in the United States. Based on the swept source optical coherence tomography technique in full-field and multiple channels configuration, the imaging system is able to perform a volumetric image of the subsurface of the skin, and thus can help in taking a better medical decision. Furthermore, for a batch-fabrication of the hand-held device, micro-optical components were made at wafer-level and vertically assembled using multi-wafer bonding. This miniaturized system requires specific characterization. Thus, two systems were also developed for imaging quality evaluation of micro-optical elements. This work has been supported by the VIAMOS (Vertically Integrated Array-type Mirau-based OCT System) European project.

Keywords: Full-field swept-source optical coherence tomography, MOEMS, Micro-optics, Optical characterization, Phase retrieval, Sinusoidal phase shifting interferometry, Three dimensional imaging, Interferometry.

Résumé :

Ce manuscrit de thèse de doctorat présente la conception et la réalisation d'un système d'imagerie pour le diagnostic précoce des pathologies de la peau. Un diagnostic précoce permet de réduire les actes chirurgicaux inutiles. Il est important de mettre en avant que seulement 20% des pathologies faisant office d'une opération chirurgicale, sont malignes. De plus, les pronostics de l'année 2015 avançaient trois millions de nouveaux cas de cancer de la peau diagnostiqués aux États-Unis. Basé sur la tomographie par cohérence optique à balayage en longueur d'onde et une configuration plein champ et multi-canaux, le système d'imagerie médicale est capable d'imager en volume les couches internes de la peau et donc de fournir un diagnostic médical pour le professionnel de santé. Pour une fabrication en série du système portatif, les composants optiques sont micro-fabriqués sur des substrats et assemblés verticalement. Ces micro-composants optiques requièrent une caractérisation spécifique. Pour cela, deux systèmes ont ainsi été développés pour estimer leurs performances optiques. Ce travail a été réalisé dans le cadre du projet Européen VIAMOS (Vertically Integrated Array-type Mirau-based OCT System).

Mots-clés : Tomographie par cohérence optique plein champ à balayage en longueur d'onde, MOEMS, Micro-composants optiques, Caractérisation optique, Récupération de phase, Interférométrie à décalage de phase sinusoïdale, Imagerie tri-dimensionnelle, Interférométrie.